CHEMICAL REVIEWS

pubs.acs.org/CR

Review

Non-adiabatic Excited-State Molecular Dynamics: Theory and Applications for Modeling Photophysics in Extended Molecular Materials

Tammie R. Nelson, Alexander J. White, Josiah A. Bjorgaard, Andrew E. Sifain, Yu Zhang, Benjamin Nebgen, Sebastian Fernandez-Alberti, Dmitry Mozyrsky, Adrian E. Roitberg,* and Sergei Tretiak*

Cite This: *Chem. Rev.* 2020, 120, 2215−2287

Read Online

ACCESS | Metrics & More | Article Recommendations

ABSTRACT: Optically active molecular materials, such as organic conjugated polymers and biological systems, are characterized by strong coupling between electronic and vibrational degrees of freedom. Typically, simulations must go beyond the Born−Oppenheimer approximation to account for non-adiabatic coupling between excited states. Indeed, non-adiabatic dynamics is commonly associated with exciton dynamics and photophysics involving charge and energy transfer, as well as exciton dissociation and charge recombination. Understanding the photoinduced dynamics in such materials is vital to providing an accurate description of exciton formation, evolution, and decay. This interdisciplinary field has matured significantly over the past decades. Formulation of new theoretical frameworks, development of more efficient and accurate computational algorithms, and evolution of high-performance computer hardware has extended these simulations to very large molecular systems with hundreds of atoms, including numerous studies of organic semiconductors and biomolecules. In this Review, we will describe recent theoretical advances including treatment of electronic decoherence in surface-hopping methods, the role of solvent effects, trivial unavoided crossings, analysis of data based on transition densities, and efficient computational implementations of these numerical methods. We also emphasize newly developed semiclassical approaches, based on the Gaussian approximation, which retain phase and width information to account for significant decoherence and interference effects while maintaining the high efficiency of surface-hopping approaches. The above developments have been employed to successfully describe photophysics in a variety of molecular materials.

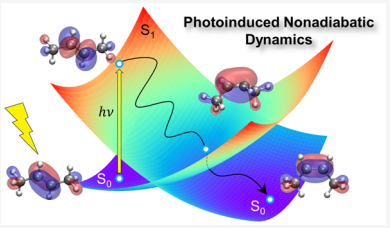

CONTENTS

Received: July 15, 2019
Published: February 10, 2020

https://dx.doi.org/10.1021/acs.chemrev.9b00447
Chem. Rev. 2020, 120, 2215−2287

1. INTRODUCTION

Ab initio molecular dynamics (MD) simulation methods provide a universal tool to model materials at the atomistic scale directly from the first principles of quantum mechanics. As a rule, MD techniques that include electronic excited-state effects in a non-equilibrium regime should invoke solutions of Schrödinger's equation on-the-fly for the electronic levels and the molecular forces (interatomic potentials). The problem central to this work is schematically outlined in Figure 1. Here, a manifold of electronically excited states in a prototypical molecular system is a function of multidimensional coordinates, **R**, spanning the space of vibrational (nuclear) degrees of freedom. Excited states are usually (but not necessarily) separated by a gap from the ground state. The potential energy surfaces (PESs) of these states are topologically complex and frequently cross each other, and perhaps even the ground state, as a function of **R**. Since the excited-state PESs are generally not known, their modeling requires elaborate quantum chemical techniques. The underlying model electronic structure can span the range from high accuracy wavefunction approaches,[1−5] to density functional theory (DFT)[6−10] and to effective reduced Hamiltonian methods.[11−13]

Excited-state processes such as photophysics and photochemistry in molecular and solid-state materials of practical interest necessarily involve multiple, and frequently dense, electronic states. For example, an initial non-equilibrium state (or an electronically excited wavepacket, Figure 1) can be created by optical excitation, by charge injection, or by shock means. This electron-vibrational (or vibronic) excitation evolves across the excited-state manifold, gradually losing its electronic energy into molecular vibrations (or heat), a process called internal conversion or non-radiative relaxation. In such a case, the excited-state molecular dynamics (ESMD) is non-adiabatic and occurs beyond the Born−Oppenheimer (BO) regime. Within the BO framework, electrons and nuclei evolve on significantly different time scales, allowing the system Hamiltonian to be split into "fast" (electrons) and "slow" (nuclei) degrees of freedom. Indeed, in the BO picture, all many-body electronic states are orthogonal to each other and there is no physically allowed way for the system to decay to a lower state unless electrons couple to nuclear motions, thus allowing for energy dissipation and a change of excited-state identity. In fact, such non-radiative relaxation is a very common process in materials that provide channeling of electronic energy into heat, which leads, for example, to Kasha's rule which states that molecules typically fluoresce from the lowest singlet excited electronic state. The non-adiabatic process occurs in the regions where excited states get close to each other or cross (Figure 1).[14−18] The outcome of the dynamics can be a return to the equilibrium ground state (or quenching), i.e., a complete loss of the initial electronic energy into heat. Alternative scenarios with specific products emphasizing useful electronic functionalities of the material are illustrated in Figure 1. For example, light emission applications[19−26] require formation of a low-lying fluorescent state, frequently described by a bound electron−hole pair (or exciton). Light harvesting usually includes spatial electronic energy (exciton) transfer followed by charge

https://dx.doi.org/10.1021/acs.chemrev.9b00447
Chem. Rev. 2020, 120, 2215−2287

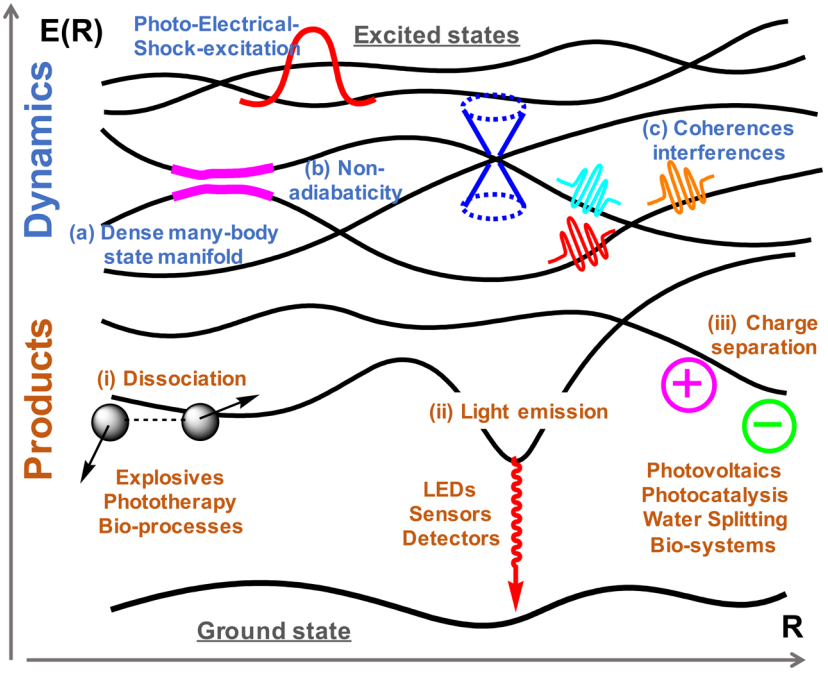

Figure 1. Schematic representation of complex excited-state potential energy surfaces as a function of multi-dimensional reactive coordinate **R**. Excited-state non-adiabatic molecular dynamics (NAMD) samples this manifold following photoexcitation, electrical excitation, or shock excitation. The NAMD techniques typically calculate energy E as a function of time t (i.e., trajectory $E(\mathbf{R}(t))$) along structural coordinates **R** of the system. The dense manifold of electronic states gives rise to complex non-adiabatic dynamics in the vicinity of avoided crossings and conical intersections when states are dense and cross, with coherences and interferences appearing. Products of NAMD such as dissociation, light emission, and charge separation are key processes in many applications.

separation.[27−35] Alternatively, dynamics can trigger chemical processes involving molecular decomposition and bond breaking/formation, as commonly occurs in explosives and various photochemical processes.[36−41] Finally, non-radiative crossing back to the ground state can lead to electron-transfer reactions,[42] as exploited in a primary process of vision (photoisomerization)[43−47] and the photosynthetic reaction center.[48,49]

Modeling the underlying non-adiabatic molecular dynamics (NAMD) complements experimental spectroscopic investigations by supplying detailed atomistic insights into the concomitant evolution of electronic wavefunctions and vibrational degrees of freedom. Besides providing fundamental insights, dominating factors and structure−property relationships, as identified by simulations, can be further used to optimize the product outcome and to design better materials. One modern example is the use of coherence arising from concerted vibronic dynamics (Figure 1) to enhance functionalities,[50] such as more efficient energy transfer (ET)[51−53] or desired photochemical reactions in laser-control experiments.[54−58]

The NAMD modeling is nontrivial and is based on two basic components: electronic structure methodology able to adequately describe the energetics and topology of excited-state PESs, and MD algorithms accounting for non-adiabatic phenomena and trajectory propagation. The other complications include modeling the excessively broad conformational space that large or flexible molecules can occupy at ambient conditions and assessing the effects of dielectric environment such as a solvent or a solid-state matrix. Existing theoretical methods are necessarily approximate and involve significant numerical expense when applied to realistic molecular systems (with sizes of tens to hundreds of atoms) to simulate dynamical time scales of interest (tens of femtoseconds to picoseconds). Subsequently, the method of choice is always a compromise between accuracy and computational expense, where the "individual contributions" to the "total error bar" are not well defined and/or are unknown. For instance, when describing non-radiative relaxation time scales, it is frequently unclear whether electronic structure methodology results in inaccurate gaps between electronic states or whether the NAMD driver evaluates incorrect transfer rates due to a common problem of missing coherence phenomena. Subsequently, the NAMD simulations are typically qualitative and verification of computational results based on spectroscopic data is highly desirable when possible.

Accounting for specific physical phenomena controlling the NAMD is critical. For example, for molecular materials, the electronic structure technique should assess electronic correlations (e.g., leading to excitonic phenomena).[59] Moreover, due to large vibronic couplings, excited-state PESs vary significantly,[60] so that simulations of gradients native to individual states are imperative. In the area of NAMD algorithms, numerous methods have been developed for the treatment of quantum effects arising from slow nuclear motions. These methods range from fully quantum treatment of nuclei[61,62] to semiclassical[63−67] to mixed quantum-classical (MQC)[68] approaches. The latter two classes are particularly suitable for simulating large molecular systems. Within the MQC family, the Ehrenfest[69−73] and surface-hopping methods[74] are the most widely used.[75] They do, however, have critical limitations arising from the fundamental inconsistencies between quantum and classical mechanics.[76] Consequently, the use of improved numerically efficient algorithms for treating electronic coherences[76−103] and the trivial crossing problem,[104−117] becomes desirable. Finally, the particular computational implementation matters: the choice of convergence criteria, time steps for electronic

https://dx.doi.org/10.1021/acs.chemrev.9b00447
Chem. Rev. 2020, 120, 2215−2287

dynamics, and the number of statistically independent trajectories all affect the final outcome and should be taken into consideration.

The present Review is specifically focused on the NAMD methodologies and applications to large, finite molecular systems aiming to model light-induced dynamics and concurrent non-radiative relaxation and ET processes. We limit ourselves by reviewing the latest developments in the area of semiclassical and MQC theoretical methodologies for NAMD and the practical computational implementations of these approaches within the scope of time-dependent self-consistent field (TD-SCF) methods such as time-dependent Hartree−Fock (TD-HF)[118,119] and time-dependent density functional theory (TD-DFT)[6] techniques. Further, we provide an overview of multiple examples showing how simulations using these computational frameworks help us to understand fundamental excited-state processes and their connections to experimental observables in a broad range of organic chromophores including conjugated polymers and dendrimers, molecular aggregates, and chlorophylls (Chls). Previous reviews on closely related subjects are refs 3,10,76,78,120−123. Topics excluded from this Review are high-accuracy, computationally expensive NAMD approaches such as multiconfigurational time-dependent Hartree (MC-TDH), ab initio full multiple spawning (AIMS), density matrix, quantum Liouville, and quantum trajectory techniques (see relevant reviews in refs 120,124−131); high-fidelity electronic structure methodologies beyond TD-SCF such as coupled-clusters and GW techniques (see relevant reviews in refs 132−135); and simpler schemes such as mono-electronic (or single-partial orbital) approximation for electronic transitions and Classical Path approximations (see relevant reviews in refs 74 and 136). We will not overview a variety of modern NAMD codes developed over the years, and refer the reader to a recent review by Crespo-Otero and Barbatti et al.[121] Because of their relationship with Semiclassical Ehrenfest, and lack of any recent review, here we also address ab initio multiple cloning (AIMC), multiconfigurational Ehrenfest (MCE), and other semiclassical Gaussian wavepacket methods. We illustrate computational aspects of NAMD in the context of Ehrenfest and surface-hopping approaches as well as a variety of applications to many molecular systems using mostly the nonadiabatic excited-state molecular dynamics (NEXMD) package developed in our group.[137]

The structure of our Review is the following: Section 2 outlines methodological aspects of NAMD algorithms including Ehrenfest, MCE with cloning, and surface-hopping approaches, paying particular attention to their advantages and deficiencies. We then delineate a standard model test suite for benchmarking the algorithms against exact solutions. This is followed by a description of several techniques allowing the electronic decoherence phenomenon to be addressed, a major challenge for many NAMD schemes. We close by overviewing the latest developments of NAMD algorithms in the area of wavepacket dynamics, which promises higher accuracy, albeit with a moderate increase of numerical cost. Section 3 is devoted to practical implementation aspects of NAMD algorithms. We start by describing the main features of electronic structure methodology underlying the TD-SCF methods and incorporation of essential dielectric medium effects including state-specific (SS) solvation. We further discuss various convergence criteria, number of electronic states and statistically independent trajectories, proper time steps, trivial crossing artifacts, and various truncation schemes. A new family of extended Lagrangian schemes, allowing significant acceleration of the dynamics, is also described. Finally, we discuss some typical methodologies for analysis of excited-state dynamics processes in terms of the spatial extent of the electronic wavefunction via transition density matrices (TDMs), which are practical for large systems generating a voluminous amount of dynamical data. Section 4 exemplifies modeling of internal conversion across a range of molecular chromophores. We also consider effects of non-adiabatic couplings (NACs) on the excited-state vibrational normal modes and present a few examples of photochemistry involving molecular decomposition. Section 5 illustrates simulations of extended coupled molecular systems where non-radiative relaxation is typically concomitant to a spatial ET process. Connections between modeling results and spectroscopic data are conveyed through several examples. Finally, in section 6, we summarize the scope of the Review and outline future perspectives of the field.

2. THEORETICAL DEVELOPMENTS AND NON-ADIABATIC EXCITED-STATE MOLECULAR DYNAMICS ALGORITHMS

2.1. Full Quantum Mechanics: The Time-Dependent Schrödinger Equation

In order to exactly calculate time-dependent non-adiabatic MD of an isolated system, one must solve, numerically or analytically, the time-dependent Schrödinger equation (TDSE):

$$i\hbar\frac{\partial\Psi(\boldsymbol{R},\boldsymbol{r},t)}{\partial t} = \hat{H}(\boldsymbol{R},\boldsymbol{r})\Psi(\boldsymbol{R},\boldsymbol{r},t) \tag{2.1}$$

$$\begin{aligned}\hat{H}(\boldsymbol{R},\boldsymbol{r}) &= -\frac{1}{2}\hbar^2\nabla_{\boldsymbol{R}}\cdot\hat{\boldsymbol{m}}_{\boldsymbol{R}}^{-1}\cdot\nabla_{\boldsymbol{R}} - \frac{1}{2}\hbar^2\frac{\nabla_r^2}{m_e} + \hat{U}(\boldsymbol{R},\boldsymbol{r})\\ &= \hat{T}(\boldsymbol{R}) + \hat{H}_{el}(\boldsymbol{R},\boldsymbol{r})\end{aligned} \tag{2.2}$$

where $\boldsymbol{r}$ and $\boldsymbol{R}$ are the positions of all electrons and nuclei with their respective masses m_e and $\hat{\boldsymbol{m}}_{\boldsymbol{R}}$, and the potential $\hat{U}(\boldsymbol{R},\boldsymbol{r})$ includes the electron−electron, electron−nuclei, and nuclei−nuclei interaction terms. All terms in the molecular Hamiltonian $\hat{H}(\boldsymbol{r},\boldsymbol{R})$, except the nuclear kinetic energy operator, $\hat{T}(\boldsymbol{R})$, are collected into the electronic Hamiltonian, $\hat{H}_{el}(\boldsymbol{r},\boldsymbol{R})$. One can exactly represent the total wavefunction $\Psi(\boldsymbol{r},\boldsymbol{R},t)$ in terms of coupled electronic and nuclear wavefunctions through the Born−Huang/Born−Oppenheimer expansion:[138,139]

$$\Psi(\boldsymbol{r},\boldsymbol{R},t) = \sum_a \phi_a(\boldsymbol{r})\chi_a'(\boldsymbol{R},t) = \sum_a \psi_a(\boldsymbol{r},\boldsymbol{R})\chi_a(\boldsymbol{R},t) \tag{2.3}$$

where $\psi_a(\boldsymbol{r},\boldsymbol{R})$ and $\phi_a(\boldsymbol{r})$ are the ath electronic wavefunctions in the *adiabatic* and *diabatic* representations, respectively.

In the *diabatic* representation, the first expansion in eq 2.3 is inserted into eq 2.1. Usually the diabatic wavefunctions are defined to be orthogonal, $\langle\phi_a(\boldsymbol{r})|\phi_b(\boldsymbol{r})\rangle_r = \delta_{ab}$. By definition the diabatic electronic wavefunction does not depend parametrically on $\boldsymbol{R}$: $\nabla_{\boldsymbol{R}}|\phi(\boldsymbol{r})\rangle \equiv 0$. Thus, the diabatic matrix elements of the Hamiltonian operator, eq 2.2, include only diagonal kinetic energy matrix elements, $\langle\phi_a(\boldsymbol{r})|\nabla_{\boldsymbol{R}}^2|\phi_b(\boldsymbol{r})\rangle \equiv 0$, and both diagonal and non-diagonal potential matrix elements, $H_{ab}(\boldsymbol{R}) \equiv \langle\phi_a(\boldsymbol{r})|\hat{H}_{el}(\boldsymbol{r},\boldsymbol{R})|\phi_b(\boldsymbol{r})\rangle \neq 0$. Diagonal elements of the potential, $H_{aa}(\boldsymbol{R}) = \langle\phi_a(\boldsymbol{r})|\hat{H}_{el}(\boldsymbol{r},\boldsymbol{R})|\phi_a(\boldsymbol{r})\rangle$, are $3N$-dimensional diabatic PESs, where N is the number of atoms. In the *adiabatic* representation, $\psi_a(\boldsymbol{r},\boldsymbol{R})$ and $E_a(\boldsymbol{R})$ are the ath eigenvector and

https://dx.doi.org/10.1021/acs.chemrev.9b00447
Chem. Rev. 2020, 120, 2215−2287

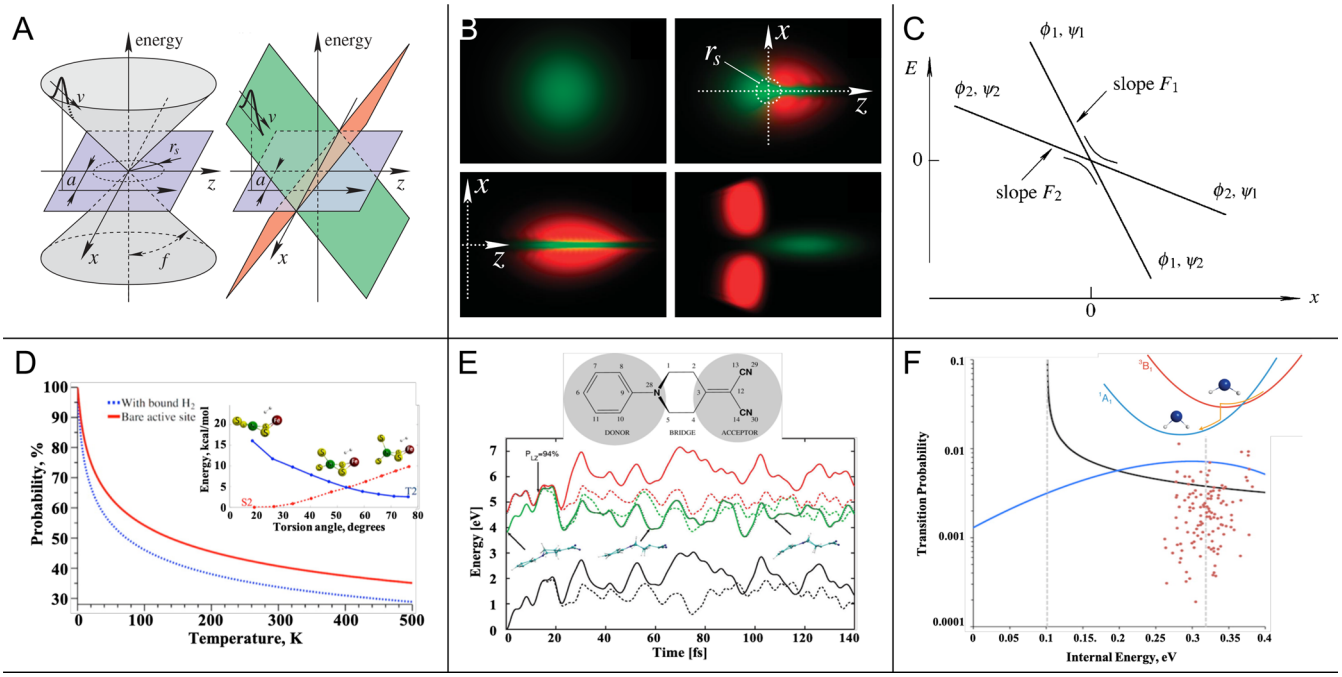

Figure 2. (A) Topology of a 2-D conical intersection in adiabatic (left) and diabatic (right) bases. (B) Snapshots at different times for semiclassical wavepacket scattering from the upper (green) to lower (red) surface through a conical intersection. (C) Level crossing for the Landau−Zener (LZ) model, with linear diabatic potential energies and constant coupling. (D) LZ probabilities of spin-forbidden singlet−triplet non-adiabatic transition in [NiFe]-hydrogenase model system with (blue) and without (red) H_2 binding. The 1-D reaction coordinate (torsion angle) PES is obtained from DFT (shown top right) and multi-reference methods. (E) Excited- and ground-state energies for a model donor−bridge−acceptor molecule along a non-adiabatic MD trajectory. LZ is used to calculate transition probabilities at avoided crossings on-the-fly. (F) Comparison of LZ (black line), Delos (blue line), and surface-hopping transition probabilities (dots) for SiH_2 intersystem crossing for different initial energies. Panels A and B: Reproduced with permission from ref 141. Copyright 2005 American Physical Society. Panel C: Reproduced with permission from ref 175. Copyright 2005 American Chemical Society. Panel D: Reproduced with permission from ref 181. Copyright 2015 American Chemical Society. Panel E: Reproduced with permission from ref 182. Copyright 2009 American Chemical Society. Panel F: Reproduced with permission from ref 183. Copyright 2015 American Chemical Society.

eigenvalue, respectively, of $\hat{H}_{el}(\boldsymbol{r},\boldsymbol{R})$, the static Schrödinger equations typically solved by electronic structure methods:

$$\hat{H}_{el}(\boldsymbol{r},\boldsymbol{R})\psi_a(\boldsymbol{r},\boldsymbol{R}) = E_a(\boldsymbol{R})\psi_a(\boldsymbol{r},\boldsymbol{R}) \tag{2.4}$$

The functions $E_a(\boldsymbol{R})$ are the 3N-dimensional adiabatic PESs. Diabatic and adiabatic PESs corresponding to a one-dimensional (1-D) seam and conical intersection, respectively, are shown in Figure 2A. A representation in which neither $\hat{H}_{el}(\boldsymbol{r},\boldsymbol{R})$ nor $\nabla_{\boldsymbol{R}}^2$ matrix elements are diagonal is called a *mixed* representation.

The choice of an adiabatic representation is convenient for multiple reasons. First, as eigenfunctions, the adiabatic electronic wavefunctions are always orthogonal, $\langle\psi_a(\boldsymbol{r},\boldsymbol{R})|\psi_b(\boldsymbol{r},\boldsymbol{R})\rangle_r = \delta_{ab}$. Another, modern quantum chemistry methods for solving eq 2.4, from post Hartree−Fock to DFT techniques, are well developed for directly resolving the adiabatic electronic wavefunctions. Finally, there is no rigorous diabatic representation for polyatomic molecules, only approximately diabatic representations exist.[140] In this adiabatic basis, the TDSE *for the nuclear wavefunction* can be written as

$$\begin{aligned} i\hbar\frac{\partial\chi_a(\boldsymbol{R},t)}{\partial t} = &\left[-\frac{1}{2}\hbar^2\nabla_{\boldsymbol{R}}\cdot\hat{\boldsymbol{m}}_{\boldsymbol{R}}^{-1}\cdot\nabla_{\boldsymbol{R}} + E_a(\boldsymbol{R})\right.\\ &\left. - \sum_b \frac{1}{2}\hbar^2\boldsymbol{d}_{ab}(\boldsymbol{R})\cdot\hat{\boldsymbol{m}}_{\boldsymbol{R}}^{-1}\cdot\boldsymbol{d}_{ab}(\boldsymbol{R})\right]\chi_a(\boldsymbol{R},t)\\ &+ \sum_b \frac{1}{2}\hbar^2[\boldsymbol{d}_{ab}(\boldsymbol{R})\cdot\hat{\boldsymbol{m}}_{\boldsymbol{R}}^{-1}\cdot\nabla_{\boldsymbol{R}} + \nabla_{\boldsymbol{R}}\cdot\hat{\boldsymbol{m}}_{\boldsymbol{R}}^{-1}\cdot\boldsymbol{d}_{ab}(\boldsymbol{R})]\chi_b(\boldsymbol{R},t) \end{aligned} \tag{2.5}$$

The rotation of the nuclear kinetic energy operator into the adiabatic basis leads to a new term: the non-adiabatic coupling vector (frequently abbreviated as NACV or NACR), also called the derivative coupling vector, which depends on $\boldsymbol{R}$, is given by $\boldsymbol{d}_{ab}(\boldsymbol{R}) = \langle\psi_a(\boldsymbol{r},\boldsymbol{R})|\nabla_{\boldsymbol{R}}|\psi_b(\boldsymbol{r},\boldsymbol{R})\rangle_r$. The NACR can be determined from the Hellman−Feynman theorem:

$$\boldsymbol{d}_{ab}(\boldsymbol{R}) = \frac{\langle\psi_a(\boldsymbol{r},\boldsymbol{R})|\nabla_{\boldsymbol{R}}\hat{H}_{el}(\boldsymbol{r},\boldsymbol{R})|\psi_b(\boldsymbol{r},\boldsymbol{R})\rangle_r}{E_b(\boldsymbol{R}) - E_a(\boldsymbol{R})}, \quad \boldsymbol{d}_{aa}(\boldsymbol{R}) = 0 \tag{2.6}$$

Within the constraint of the adiabatic or diabatic representation, the total wavefunction can, in limiting cases, be factorized into a single product of electronic and nuclear wavefunctions, $\Psi(\boldsymbol{r},\boldsymbol{R},t) = \psi(\boldsymbol{r})\chi(\boldsymbol{R},t)$ or $\Psi(\boldsymbol{r},\boldsymbol{R},t) = \phi(\boldsymbol{r})\chi'(\boldsymbol{R},t)$. In the diabatic representation, this requires that $H_{ab}(\boldsymbol{R}) \ll [|H_{aa}(\boldsymbol{R}) - H_{bb}(\boldsymbol{R})| + \hat{T}(\boldsymbol{R})]$. In the adiabatic representation, this assumes that the $\boldsymbol{d}_{ab}(\boldsymbol{R})$ terms in eq 2.5 can be ignored due

https://dx.doi.org/10.1021/acs.chemrev.9b00447
Chem. Rev. 2020, 120, 2215−2287

to the time scale separation of the electronic (fast) and nuclear (slow) motions, or equivalently the large energy separation between electronic PESs compared to the nuclear kinetic energy. This is known as the Born−Oppenheimer[139] approximation. Alternatively, the Born−Huang approximation[138] retains the $\boldsymbol{d}_{ab}^2(\boldsymbol{R})$ terms in eq 2.5 ($\boldsymbol{d}_{ab}(\boldsymbol{R})\cdot\hat{\boldsymbol{m}}_{\boldsymbol{R}}^{-1}\cdot\boldsymbol{d}_{ab}(\boldsymbol{R})$). These terms are referred to as the diagonal Born−Oppenheimer correction, which manifests as a correction to the PES. In both cases, the nuclear wavefunction, $\chi(\boldsymbol{R},t)$, propagates adiabatically on a single PES. The single product approximations in either the adiabatic or diabatic representation are valid in opposite limits with regard to time scales. The adiabatic limit (or adiabatic passage) requires that nuclei move much slower than the electron time scale. In terms of energy ($\hbar$/time) this implies that the energy gap between states is much larger than the state-to-state coupling, i.e., $|E_b(\boldsymbol{R}) - E_a(\boldsymbol{R})| \gg [\boldsymbol{d}_{ab}(\boldsymbol{R})\cdot\hat{\boldsymbol{m}}_{\boldsymbol{R}}^{-1}\cdot\nabla_{\boldsymbol{R}} + \nabla_{\boldsymbol{R}}\cdot\hat{\boldsymbol{m}}_{\boldsymbol{R}}^{-1}\cdot\boldsymbol{d}_{ab}(\boldsymbol{R})]$. This is often valid due to the large mass of nuclei compared to electrons. The diabatic limit (or diabatic passage) requires the opposite; the nuclei must move much faster than the electron time scale, which is less common.

Beyond the BO or Born−Huang approximations, one can picture a wavefunction that propagates on a PES, but also branches to other PESs in regions of non-zero NACRs or $\boldsymbol{H}_{ab}(\boldsymbol{R})$. From eq 2.6, one sees that the NAC terms couple PESs when their energy gaps become small. Note that when PESs are weakly coupled, $\langle\boldsymbol{\psi}_a(\boldsymbol{r},\boldsymbol{R})|\nabla_{\boldsymbol{R}}\hat{\boldsymbol{H}}_{\mathrm{el}}(\boldsymbol{r},\boldsymbol{R})|\boldsymbol{\psi}_b(\boldsymbol{r},\boldsymbol{R})\rangle \approx 0$, the NAC has delta-function-like behavior at the PES degeneracy point. This is discussed and exemplified in detail in section 3.4. Figure 2B shows the effect of crossing a conical intersection[141] (Figure 2A), one such degenerate point between two or more multidimensional PESs, on a wavepacket that is nonlocal in space, $\chi_2(\boldsymbol{R},t)$. The dimensionality of the degeneracy is always the nuclear dimension minus two; i.e., it is at a single point for two-dimensional adiabatic PESs, a seam for three dimensions, a plane for four dimensions, etc. The wavepacket that remains on the upper surface (shown in green) is split by the conical intersection, with the portion of the wavepacket closer to the intersection transitioning to the lower surface (shown in red).[141] This demonstrates that regions with small adiabatic energy gaps play a dominant role in non-adiabatic dynamics.

Direct numerical solution of the nuclear TDSE for a single surface, a $3N-6$-dimensional linear partial differential equation (PDE), scales exponentially with dimension. This limits exact solution to very small molecules, typically with less than 5 atoms.[142−157] By reducing the vibrational space in large molecules to a few key degrees of freedom, i.e., reaction coordinates, direct numerical simulation can still be informative.[158] Various techniques for direct numerical solutions of PDEs were utilized when solving the Schrödinger equation in eq 2.5. These include implicit,[159] explicit,[160] and mixed methods[161] such as Crank−Nicolson. Particularly, the latter nicely preserves the wavefunction normalization exactly.[162] Polynomial expansions, such as the Chebychev polynomials,[163] the use of discrete variable representation (DVR) basis,[164] or the application of the Trotter expansion and the split-operator Fourier transform,[165−168] to name a few methods, have greatly aided the exact numerical propagation of the TDSE. Among these approaches, the MC-TDH technique has been broadly used owing to its high efficiency.[61,169,170] However, this is still a grid based numerical method with exponential scaling for solving exact quantum dynamics.[171] All these approaches are also applicable beyond the adiabatic approximation, where the nuclear TDSE has to propagate M coupled linear PDEs, where M is the number of included PESs. Thus, non-adiabaticity introduces an additional scaling factor of $O(M^2)$, in addition to the exponential scaling with dimensions. Just as with the adiabatic case, here direct numerical solutions are useful in understanding non-adiabatic dynamics of small molecules.

2.1.1. Early Developments: Tunneling Models. Early attempts to understand and calculate non-adiabatic processes analytically started in the 1930s and were focused on transition probabilities for atomic collisions. Landau and Zener (LZ) used analytical continuation theory to find an analytic function for the transmission probability of a single passage through an avoided crossing, specifically linear *diabatic* PESs.[172,173] Landau considered the near-adiabatic and near-diabatic (near-sudden) limits, while Zener solved the time-dependent coupled electronic and nuclear equations, both for constant H_{12}.[174,175] The resulting probability P_{LZ} is known as the LZ formula, which gives the probability of transition between two crossing diabatic electronic states, 1 and 2 ($\phi_{1/2}$ in Figure 2C) assumed to have a linear potential energy $H_{11/22}$ and constant coupling H_{12}:

$$P_{\mathrm{LZ}} = \exp\left[-\frac{2\pi}{\hbar}H_{12}^2\Big/\left|\left(\frac{\partial H_{11}}{\partial x} - \frac{\partial H_{22}}{\partial x}\right)\dot{x}\right|\right] \tag{2.7}$$

The most remarkable feature of the LZ formula is that it captures the transition from fully diabatic to fully adiabatic passages with decreased rate of passage, $\dot{x}$. In the adiabatic representation, the Massey parameter,[176] $|\hbar\boldsymbol{d}_{12}\dot{x}/(E_1 - E_2)|$, provides a criterion to estimate the importance of non-adiabaticity in passage through an avoided crossing ($\psi_{1/2}$ in Figure 2C). Neither the exponent in eq 2.7 nor the Massey parameter depends on the nuclear mass, only the velocity. It is clear that for large adiabatic energy gaps or large diabatic coupling, low velocity, and weak NAC, $\boldsymbol{d}_{12}$, the passage will be adiabatic. Both Landau[173] and Stuckelburg[177] considered the problem of multiple crossings through non-adiabatic regions. In such a case, interference patterns appear in the transition probability, so-called Stuckelburg oscillations.[177] Alternative non-adiabatic crossing models, such as the Rosen−Zener[178] or Demkov[179] models, with constant diabatic energies and localized coupling, were also solved analytically. Teller generalized the LZ method for a 1-D avoided crossing to multiple dimensions, in particular conical intersections.[180]

Since these earliest works, further generalizations,[184] for example by Nikitin[185−190] and Nakamura,[191−195] to name a few, have advanced the treatment of non-adiabatic scattering to include energies near turning points and more general potentials. Nikitin's review article[196] and the book by Nakamura[197] provide more detailed overviews of these early ideas and current advancements. Furthermore, an extension of the LZ analytic approach to the case of conical intersections (Figure 2A) was derived in ref 141.

Among practical applications, the LZ framework has been frequently used to calculate transition probabilities assuming a 1-D reaction coordinate (Figure 2D). This approach can make use of high quality electronic structure simulations, however, in a reduced dynamical model.[181] Additionally, the LZ probabilities have been utilized to calculate transition rates at minima in adiabatic energy gaps, which was implemented in on-the-fly MD (Figure 2E).[182] Zaari and Varganove have compared double passage LZ and Delos[184,198] transition probabilities (which account for tunneling) against modern surface-hopping probabilities (to be discussed below) for SiH_2 intersystem crossing (Figure 2F). Delos probabilities differ from LZ and

https://dx.doi.org/10.1021/acs.chemrev.9b00447
Chem. Rev. 2020, 120, 2215−2287

surface-hopping near turning-points (low kinetic energy).[198] Unfortunately, such analytic solutions require crude approximations to the shape of the PESs. Therefore, approximate quantum dynamics which can use the real PES, but are more computationally affordable than numerical solutions to the TDSE, are desirable.

2.1.2. Semiclassical Dynamics. While solutions of quantum mechanical (QM) equations of motion (EOMs) for the nuclear wavefunctions, eq 2.5, scale exponentially with dimension, the classical EOMs for the time-dependent nuclear positions, $\boldsymbol{R}_t$, and momenta, $\boldsymbol{P}_t$,

$$\dot{\boldsymbol{R}}_t = \hat{m}_{\boldsymbol{R}}^{-1}\cdot\boldsymbol{P}_t \quad \dot{\boldsymbol{P}}_t = -\nabla_{\boldsymbol{R}}E(\boldsymbol{R}_t) \tag{2.8}$$

scale linearly with the number of degrees of freedom. We use the subscript to distinguish time-dependent nuclear positions and momentums, i.e., a moving point in phase space, from the general nuclear position and momentum variable, i.e., the full phase space. These coupled ordinary differential equations are almost trivial to solve for even thousands of degrees of freedom, assuming rapid calculation of the energy gradients (or forces, $-\nabla_{\boldsymbol{R}}E(\boldsymbol{R}_t)$). Thus, great effort has been spent to determine *semiclassical* equations for the propagation of nuclear wavepackets on single or coupled surfaces, where nuclear motions are essentially based on eq 2.8. Early efforts include the development of time-dependent Wentzel−Kramers−Brillouin (WKB) and Van Vleck−Gutwiller propagation,[199] which use path integration to define the dynamics of the nuclear wavefunction:

$$\begin{aligned}
\chi(\boldsymbol{R},t) &\approx \int \mathrm{d}\boldsymbol{R}' G_{\mathrm{sc}}(\boldsymbol{R},\boldsymbol{R}',t,0)\chi(\boldsymbol{R}',0)\\
G_{\mathrm{sc}}(\boldsymbol{R},\boldsymbol{R}',t,0) &= \left[\frac{1}{2\pi i\hbar}\right]^{\frac{D}{2}}\sum_j \left|\frac{\partial^2 S_j(\boldsymbol{R},\boldsymbol{R}',t,0)}{\partial\boldsymbol{R}\partial\boldsymbol{R}'}\right|^{\frac{1}{2}}\\
&\quad\times\exp\left[\frac{iS_j(\boldsymbol{R},\boldsymbol{R}',t,0)}{\hbar}-\frac{1}{2}i\pi\nu_j\right]\\
S_j(\boldsymbol{R},\boldsymbol{R}',t,0) &= \int_0^t \mathrm{d}t'[\boldsymbol{P}_{t'}\cdot\dot{\boldsymbol{R}}_{t'}-H_{\mathrm{cl}}(\boldsymbol{P}_{t'},\boldsymbol{R}_{t'})]
\end{aligned} \tag{2.9}$$

Here, G_{sc} is the semiclassical propagator of the nuclear wavefunction, S is the action, i.e., the time integral of the Lagrangian, H_{cl} is the classical Hamiltonian, D is the dimensionality, and ν_j is the Maslov index.[199] Inside the action integral, the initial and final variables are defined by $\boldsymbol{R}_0 \equiv \boldsymbol{R}'$, $\boldsymbol{R}_t \equiv \boldsymbol{R}$, and $\boldsymbol{P}_0 = \frac{\partial S_j(\boldsymbol{R}',0)}{\partial \boldsymbol{R}'}$. This semiclassical path integral based approach recovers classical mechanics (Hamilton's equations) in the $\hbar\to 0$ limit. However, they are difficult to implement, due to caustics, and they are boundary value (root-search) problems that require full exploration of the position space, i.e., all possible paths, j, through phase space, $(\boldsymbol{P}_{t'},\boldsymbol{R}_{t'})$, that satisfy the boundary conditions connecting $\boldsymbol{R}$ and $\boldsymbol{R}'$; see ref 199 for details. Miller transformed this propagator into a purely initial-value problem by transferring dependence on the final position to a dependence on initial momentum, known as the semiclassical initial value representation (SC-IVR).[200−203] This allows for sampling of only the initial conditions $(\boldsymbol{P}_0,\boldsymbol{R}_0)$, rather than finding the paths via root search.

Complementary to the semiclassical path integral approaches, in 1975, Heller suggested a very simple scheme allowing the introduction of classical trajectories into the solution of the TDSE.[204−206] If one assumes that the nuclear wavefunction has the form of a Gaussian (or superposition of Gaussians) function,

$$g(\boldsymbol{R}_t,\boldsymbol{P}_t,\boldsymbol{R},t) = \exp\left[\frac{i}{\hbar}[\gamma_t+\boldsymbol{P}_t\cdot(\boldsymbol{R}-\boldsymbol{R}_t)+(\boldsymbol{R}-\boldsymbol{R}_t)\cdot\hat{\boldsymbol{\alpha}}\cdot(\boldsymbol{R}-\boldsymbol{R}_t)]\right] \tag{2.10}$$

and expands the PES, $E(\boldsymbol{R})$, in a Taylor series around the center of the Gaussian(s) up to second order, then the EOM of the Gaussian(s) can be determined analytically:

$$\begin{aligned}
\dot{\boldsymbol{R}}_t &= \hat{\boldsymbol{m}}_{\boldsymbol{R}}^{-1}\cdot\boldsymbol{P}_t\\
\dot{\boldsymbol{P}}_t &= \boldsymbol{F}_t = -\nabla_{\boldsymbol{R}}E(\boldsymbol{R}_t)\\
\dot{\hat{\boldsymbol{\alpha}}} &= -2\hat{\boldsymbol{\alpha}}\cdot\hat{\boldsymbol{m}}_{\boldsymbol{R}}{}^{-1}\cdot\hat{\boldsymbol{\alpha}}-\frac{1}{2}\nabla_{\boldsymbol{R}}(\nabla_{\boldsymbol{R}}E(\boldsymbol{R}_t))\\
\dot{\gamma}_t &= i\hbar Tr\left[\frac{\hat{\boldsymbol{\alpha}}}{M}\right]+\frac{1}{2}\boldsymbol{P}_t\cdot\hat{\boldsymbol{m}}_{\boldsymbol{R}}{}^{-1}\cdot\boldsymbol{P}_t-E(\boldsymbol{R}_t)
\end{aligned} \tag{2.11}$$

In Gaussian wavepacket dynamics (GWD), the center, $\boldsymbol{R}_t$ and $\boldsymbol{P}_t$, of the wavepacket moves according to classical Newtonian mechanics. Additionally, the EOMs for the normalizing phase, γ_t, and complex widths, $\hat{\boldsymbol{\alpha}}_t = \hat{\boldsymbol{\alpha}}_R + i\hat{\boldsymbol{\alpha}}_I$, are introduced. The steady-state solution of the $\hat{\boldsymbol{\alpha}}$ EOM in a harmonic potential leads to frozen Gaussians. The Taylor series expansion is exact for globally harmonic potentials, and is also valid for slowly varying PESs, when $\hat{\boldsymbol{\alpha}}_I \gg \nabla_{\boldsymbol{R}}(\nabla_{\boldsymbol{R}}E(\boldsymbol{R}_t))$, i.e., locally harmonic potentials. In a harmonic potential within the steady-state limit, there is a balance between the first term of eq 2.11, $-2\hat{\boldsymbol{\alpha}}\cdot\hat{\boldsymbol{m}}_{\boldsymbol{R}}^{-1}\cdot\hat{\boldsymbol{\alpha}}$, which leads to a broadening of the wavepacket due to quantum uncertainty, and the binding of the wavepacket due to the potential walls in the second term of eq 2.11, $-\frac{1}{2}\nabla_{\boldsymbol{R}}(\nabla_{\boldsymbol{R}}E(\boldsymbol{R}_t))$, leading to a frozen Gaussian, i.e., ground-state wavefunction of the harmonic oscillator. In a general potential, the Gaussian is *thawed* with a time-dependent $\hat{\boldsymbol{\alpha}}_t$. Kong, Markmann, and Batista[207] recently showed the extension of the GWD to the exact quantum propagation limit through time-slicing, which consists of periodic re-expansion of the wide Gaussians into narrower ones. Extension of the thawed GWD to non-adiabatic situations will be discussed in section 2.5.5.

Introduction of the so-called coherent-state, or a frozen Gaussian representation, to the semiclassical propagator leads to the Herman−Kluk (HK) propagator:[208−210]

$$\begin{aligned}
\chi(\boldsymbol{R},t) &\approx \int \mathrm{d}\boldsymbol{R}_i\,\mathrm{d}\boldsymbol{P}_i\left[\frac{1}{2\pi\hbar}\right]^D \hat{K}(\boldsymbol{R}_i,\boldsymbol{P}_i,t)g(\boldsymbol{R}_t,\boldsymbol{P}_t,\boldsymbol{R},t)\\
&\quad\times\exp\left[\frac{iS(\boldsymbol{R}_i,\boldsymbol{P}_i,t)}{\hbar}\right]\langle g(\boldsymbol{R}_i,\boldsymbol{P}_i,\boldsymbol{R}')|\chi(\boldsymbol{R}',0)\rangle_{\boldsymbol{R}'}\\
K(\boldsymbol{R}_i,\boldsymbol{P}_i,t) &= \frac{1}{2}\left|\frac{\partial\boldsymbol{R}_t}{\partial\boldsymbol{R}_i}+\frac{\partial\boldsymbol{P}_t}{\partial\boldsymbol{P}_i}-2\alpha\hbar\frac{\partial\boldsymbol{R}_t}{\partial\boldsymbol{P}_i}-\frac{1}{2\alpha\hbar}\frac{\partial\boldsymbol{P}_t}{\partial\boldsymbol{R}_i}\right|^{\frac{1}{2}}\\
g(\boldsymbol{R}_t,\boldsymbol{P}_t,\boldsymbol{R},t) &= \exp\left[\frac{i}{\hbar}[S+\boldsymbol{P}_t\cdot(\boldsymbol{R}-\boldsymbol{R}_t)+\right.\\
&\quad\left.(\boldsymbol{R}-\boldsymbol{R}_t)\cdot\hat{\boldsymbol{\alpha}}\cdot(\boldsymbol{R}-\boldsymbol{R}_t)]\right]
\end{aligned} \tag{2.12}$$

This integral can be sampled by Monte Carlo algorithms, resulting in a distribution of trajectories which are then propagated classically. Here, g is a trajectory guided Gaussian

https://dx.doi.org/10.1021/acs.chemrev.9b00447
Chem. Rev. 2020, 120, 2215−2287

function with a phase space center, $\boldsymbol{R}_t$ and $\boldsymbol{P}_t$, and a complex width, $\hat{\boldsymbol{\alpha}}$. The action, S, and the Mondromedy matrix, $\hat{\boldsymbol{K}}$, are propagated along with trajectories.[208] Note that the HK method propagates a swarm of Gaussian wavepackets in order to go beyond harmonic potentials. Additionally, the Miller−Meyer−Stock−Thoss[64,65,200] (MMST) Hamiltonian was developed to generalize this method to the non-adiabatic case by introducing additional degrees of freedom for each electronic state and an action-angle representation. This representation results in a mean-field description of non-adiabatic dynamics.

The HK propagator has also been extended to non-adiabatic cases without using the MMST Hamiltonian. In this case, the HK propagator is expanded as a series with different orders of the NAC.[165,211−214] In general, these approaches involve swarms of classical or coherent-state trajectories propagating in time, acquiring complex coefficients, which can be difficult to calculate. Each trajectory is a sample of a Monte Carlo approximation to the total path integral, eq 2.12. Since the total wavefunction is usually a highly oscillatory function, this Monte Carlo approach suffers from the well-known sign problem,[215] leading to difficulties in convergence and numerical instability. For both adiabatic and non-adiabatic semiclassical methods, additional approximations, such as linearization and the forward−backward IVR, have improved stability and convergence costs, but they can reduce accuracy.[203,216−218]

In general, the methods outlined above have been shown to be highly accurate in small molecular systems of up to tens of atoms, or for reduced systems. However, in the study of large molecular systems (tens to hundreds of atoms or even nanoscale structures) the simulation of non-adiabatic dynamics is dominated by less rigorous, but more computationally tractable and simple, MQC methods.

2.2. Mixed Quantum-Classical Equations

MQC dynamics methods attempt to retain a multidimensional, fully classical treatment for the nuclei, eq 2.8, while the other degrees of freedom, such as electrons and selected vibrations, are computed quantum mechanically. Ehrenfest and surface-hopping approaches, described in the following sections (sections 2.2.1 and 2.2.2, respectively), are the most popular MQC methods that have been broadly applied to a variety of molecular and solid systems due to their computational affordability, robustness, and relatively simple numerical implementation. Here, the non-adiabatic coupling vector (NACR, $\boldsymbol{d}_{ab}(\boldsymbol{R}) = \langle \psi_a(\boldsymbol{r},\boldsymbol{R})|\nabla_{\boldsymbol{R}}|\psi_b(\boldsymbol{r},\boldsymbol{R})\rangle_{\boldsymbol{r}}$) and its counterpart, the time-dependent scalar (NACT, $\dot{\boldsymbol{R}}_t\cdot\boldsymbol{d}_{ab}(\boldsymbol{R}) = \left\langle \psi_a(\boldsymbol{r},\boldsymbol{R})\middle|\frac{\mathrm{d}}{\mathrm{d}t}\middle|\psi_b(\boldsymbol{r},\boldsymbol{R})\right\rangle_{\boldsymbol{r}}$), are essential ingredients in all MQC methods.

2.2.1. Ehrenfest Dynamics. The *Ehrenfest*, or mean-field trajectory method,[72,219] is the simplest extension of classical mechanics that also includes the quantum-mechanical effect of non-adiabaticity. The major assumption is that the nuclear and electronic parts of the wavefunction in eq 2.3 are uncorrelated. Thus, for either the adiabatic or diabatic representations, eq 2.3 can be rewritten as

$$\Psi(\boldsymbol{r},\boldsymbol{R},t) = \chi_0(\boldsymbol{R},t)\sum_a c_a(t)\psi_a(\boldsymbol{r},\boldsymbol{R}) \tag{2.13}$$

where $\chi_0(\boldsymbol{R},t)$ is a normalized single phase-less Gaussian wavepacket, i.e., eq 2.10 with $\gamma(t) \equiv -(i\hbar/4\ \ln[2\ \mathrm{Tr}[\hat{\boldsymbol{\alpha}}_I]/(\hbar\pi)]$, and $c_a(t)$ is the state-dependent complex coefficient. Inserting eq 2.13 into the TDSE, eq 2.1, and assuming a complete basis of electronic wavefunctions, gives

$$\begin{aligned}\frac{i\partial\Psi(\boldsymbol{r},\boldsymbol{R},t)}{\partial t} = \sum_a [&-\psi_a(\boldsymbol{r},\boldsymbol{R})\times\hbar^2\nabla_{\boldsymbol{R}}\cdot\hat{\boldsymbol{m}}_{\boldsymbol{R}}^{-1}\cdot\nabla_{\boldsymbol{R}}\chi_0(\boldsymbol{R},t)/2\\ &+\chi_0(\boldsymbol{R},t)\hat{H}_{\mathrm{el}}(\boldsymbol{R})\psi_a(\boldsymbol{r},\boldsymbol{R})\\ &-\sum_b\{\psi_b(\boldsymbol{r},\boldsymbol{R})\{\hbar^2\hat{\boldsymbol{m}}_{\boldsymbol{R}}^{-1}\cdot\nabla_{\boldsymbol{R}}\chi_0(\boldsymbol{R},t)\}\cdot\boldsymbol{d}_{ba}(\boldsymbol{R})\\ &+\chi_0(\boldsymbol{R},t)\psi_b(\boldsymbol{r},\boldsymbol{R})\hbar^2\tilde{\boldsymbol{d}}_{ba}^2(\boldsymbol{R})/2\}]c_a(t)\end{aligned} \tag{2.14}$$

The next approximation is to assume that the wavepacket (see eq 2.10) is highly localized in nuclear space. The electronic Hamiltonian can then be assumed to be nearly constant near the mean position of $\chi_0(\boldsymbol{R},t)$, i.e., $\hat{H}_{\mathrm{el}}(\boldsymbol{R}) \approx [\hat{H}_{\mathrm{el}}(\boldsymbol{R}_t) + \nabla_{\boldsymbol{R}}\hat{H}_{\mathrm{el}}(\boldsymbol{R}_t)(\boldsymbol{R}-\boldsymbol{R}_t)]$, $\boldsymbol{d}_{ba}(\boldsymbol{R}) \approx \boldsymbol{d}_{ba}(\boldsymbol{R}_t)$, and $\boldsymbol{d}_{ba}^2(\boldsymbol{R}) \approx 0$. Multiplying both sides of eq 2.14 by $\chi_0^*(\boldsymbol{R},t)$ and $\psi_a^*(\boldsymbol{r},\boldsymbol{R})$, and integrating over all nuclear space, $\boldsymbol{R}$, and electronic space, $\boldsymbol{r}$, leads to the EOM for the complex coefficients:

$$\begin{aligned}i\hbar\frac{\partial c_a(t)}{\partial t} = &[E_a(\boldsymbol{R}_t) + \boldsymbol{P}_t\cdot\hat{\boldsymbol{m}}_{\boldsymbol{R}}^{-1}\cdot\boldsymbol{P}_t/2\\ &+\mathrm{Tr}[\hat{\boldsymbol{m}}_{\boldsymbol{R}}^{-1}\cdot(\hat{\boldsymbol{\alpha}}_{\mathrm{Im}} + \hat{\boldsymbol{\alpha}}_{\mathrm{Re}}\hat{\boldsymbol{\alpha}}_{\mathrm{Im}}{}^{-1}\hat{\boldsymbol{\alpha}}_{\mathrm{Re}})]/\hbar]c_a(t)\\ &-i\hbar\sum_b\boldsymbol{d}_{ab}(\boldsymbol{R}_t)\cdot\hat{\boldsymbol{m}}_{\boldsymbol{R}}^{-1}\cdot\boldsymbol{P}_t c_b(t)\end{aligned} \tag{2.15}$$

Subscripts Re and Im represent real and imaginary parts, respectively. Due to the assumption of a single uncorrelated nuclear wavepacket, the kinetic contribution in eq 2.15, $\boldsymbol{P}_t\cdot\hat{\boldsymbol{m}}_{\boldsymbol{R}}^{-1}\cdot\boldsymbol{P}_t/2 + \frac{\mathrm{Tr}[\hat{\boldsymbol{m}}_{\boldsymbol{R}}^{-1}\cdot(\hat{\boldsymbol{\alpha}}_{\mathrm{Im}} + \hat{\boldsymbol{\alpha}}_{\mathrm{Re}}\hat{\boldsymbol{\alpha}}_{\mathrm{Im}}{}^{-1}\hat{\boldsymbol{\alpha}}_{\mathrm{Re}})]}{\hbar}$, can be ignored since it is constant across the different electronic states. This leads to the more common form,

$$i\hbar\frac{\partial c_a(t)}{\partial t} = E_a(\boldsymbol{R}_t)c_a(t) - \frac{i\hbar}{m_{\boldsymbol{R}}}\sum_b\boldsymbol{d}_{ab}(\boldsymbol{R}_t)\cdot\boldsymbol{P}_t c_b(t) \tag{2.16}$$

The EOMs for $\boldsymbol{R}_t$ and $\boldsymbol{P}_t$ are then obtained by the Ehrenfest theorem[219,220] and the local approximation for $\hat{H}_{\mathrm{el}}$:

$$\begin{aligned}\frac{\partial\boldsymbol{R}_t}{\partial t} &= \langle\Psi|i[\hat{H},\boldsymbol{R}]|\Psi\rangle = \hat{\boldsymbol{m}}_{\boldsymbol{R}}^{-1}\cdot\boldsymbol{P}_t\\ \frac{\partial\boldsymbol{P}_t}{\partial t} &= \langle\Psi|i[\hat{H},-i\nabla]|\Psi\rangle = -\langle\Psi|\nabla\hat{H}_{\mathrm{el}}(\boldsymbol{R}_t)|\Psi\rangle,\end{aligned} \tag{2.17}$$

where $[X,Y]$ is the commutator of X and Y. In practical implementations, the NACT scalars, $\dot{\boldsymbol{R}}_t\cdot\boldsymbol{d}_{ab}(\boldsymbol{R}) = \left\langle \psi_a(\boldsymbol{r},\boldsymbol{R})\middle|\frac{\mathrm{d}}{\mathrm{d}t}\middle|\psi_b(\boldsymbol{r},\boldsymbol{R})\right\rangle_{\boldsymbol{r}}$, are frequently used for numerical propagation of eq 2.16 without explicit calculation of the respective NACRs, $\boldsymbol{d}_{ab}(\boldsymbol{R}_t)$.

Note that the simplicity of the EOMs, eqs 2.16 and 2.17, is a direct result of the assumption that the nuclear wavefunction is well represented by a single Gaussian wavepacket basis. A more accurate representation of $\chi(\boldsymbol{R},t)$, through either a sum of Gaussians or functions with higher-order moments, would add significant complication since the kinetic contributions could no longer be ignored. Note that the same approximations can be made in the diabatic representation, leading to the identical result, $i\hbar\frac{\partial c_a'(t)}{\partial t} = \sum_b H_{\mathrm{el};a,b}(\boldsymbol{R}_t)c_b'(t)$, where $c_a'(t)$ and $c_b'(t)$ are coefficients for the diabatic electronic wavefunctions. For an

https://dx.doi.org/10.1021/acs.chemrev.9b00447
Chem. Rev. 2020, 120, 2215−2287

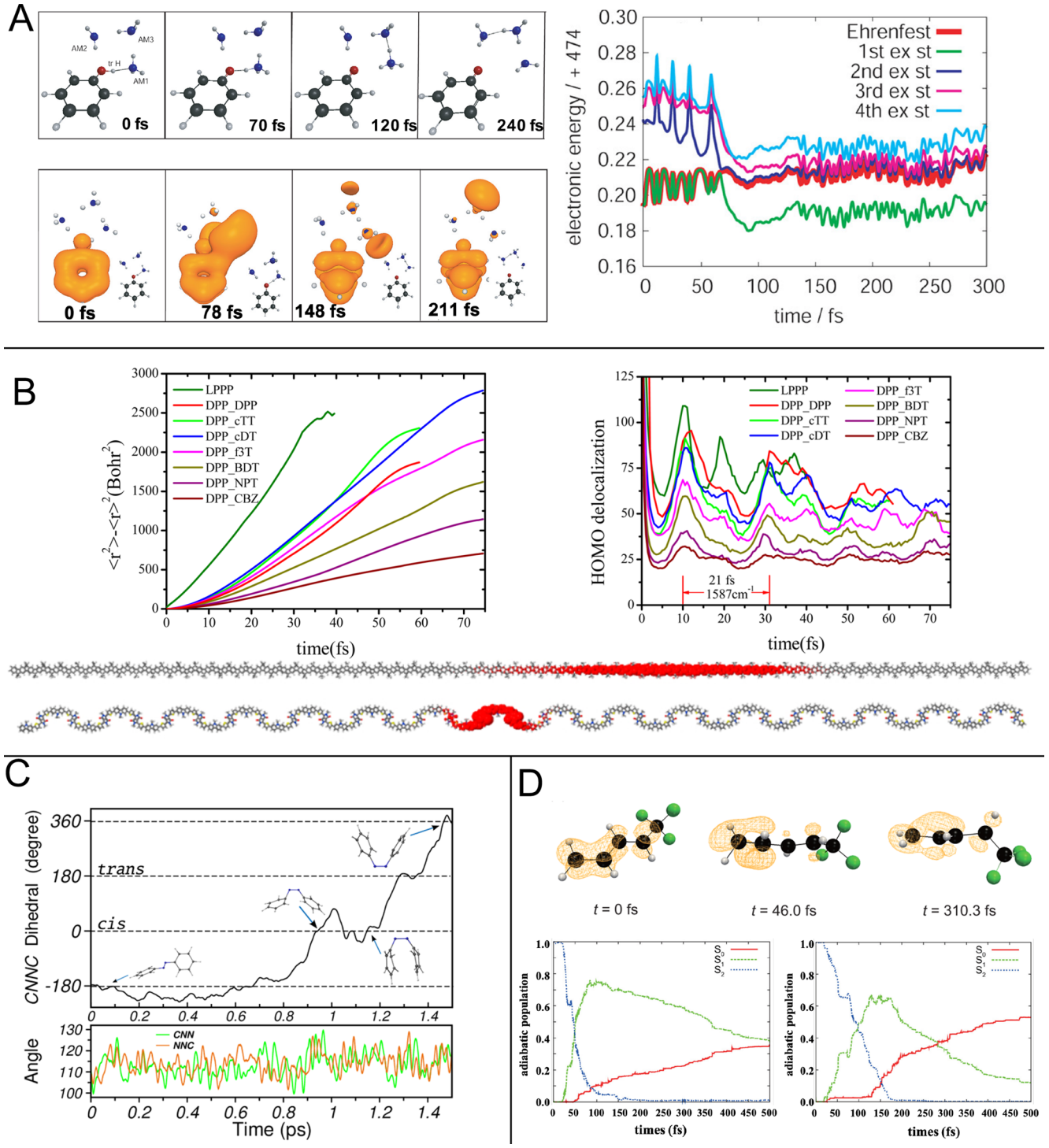

Figure 3. Examples of applications of Ehrenfest dynamics. (A) Coupled proton−electron transfer from phenol to ammonia cluster. Snapshots of the nuclei positions and unpaired electron density are shown (left). Time-dependent adiabatic energies and Ehrenfest mean energy are shown over 300 fs (right). (B) Ehrenfest dynamics with density functional tight binding used to simulate charge transport and localization/delocalization in semiconducting polymers. Averaged variances of diffusion distance (left) and HOMO delocalization (right) for diketopyrrolo-pyrrole (DPP) and various copolymers are shown. Charge distributions for pure DPP and DPP carbazole (DPP-CBZ) (bottom) are also shown. (C) Azobenzene isomerization simulated with extended Hückel semiempirical Hamiltonian. Bridge dihedral and angles are shown. (D) Path-branching Ehrenfest simulations of photoinduced successive isomerization (top) in butadiene with corresponding population dynamics (left) compared to that of CF_3-substituted butadiene (right). Panel A: Reproduced with permission from ref 222. Copyright 2012 American Chemical Society. Panel B: Reproduced with permission from ref 223. Copyright 2014 American Chemical Society. Panel C: Reproduced with permission from ref 224. Copyright 2016 American Chemical Society. Panel D: Reproduced with permission from ref 225. Copyright 2017 American Chemical Society.

alternative derivation of the Ehrenfest method, see the discussion by Tully in ref 221.

While the simplicity of a classical description is also the primary goal of the approach, the Ehrenfest method is limited by

https://dx.doi.org/10.1021/acs.chemrev.9b00447
Chem. Rev. 2020, 120, 2215−2287

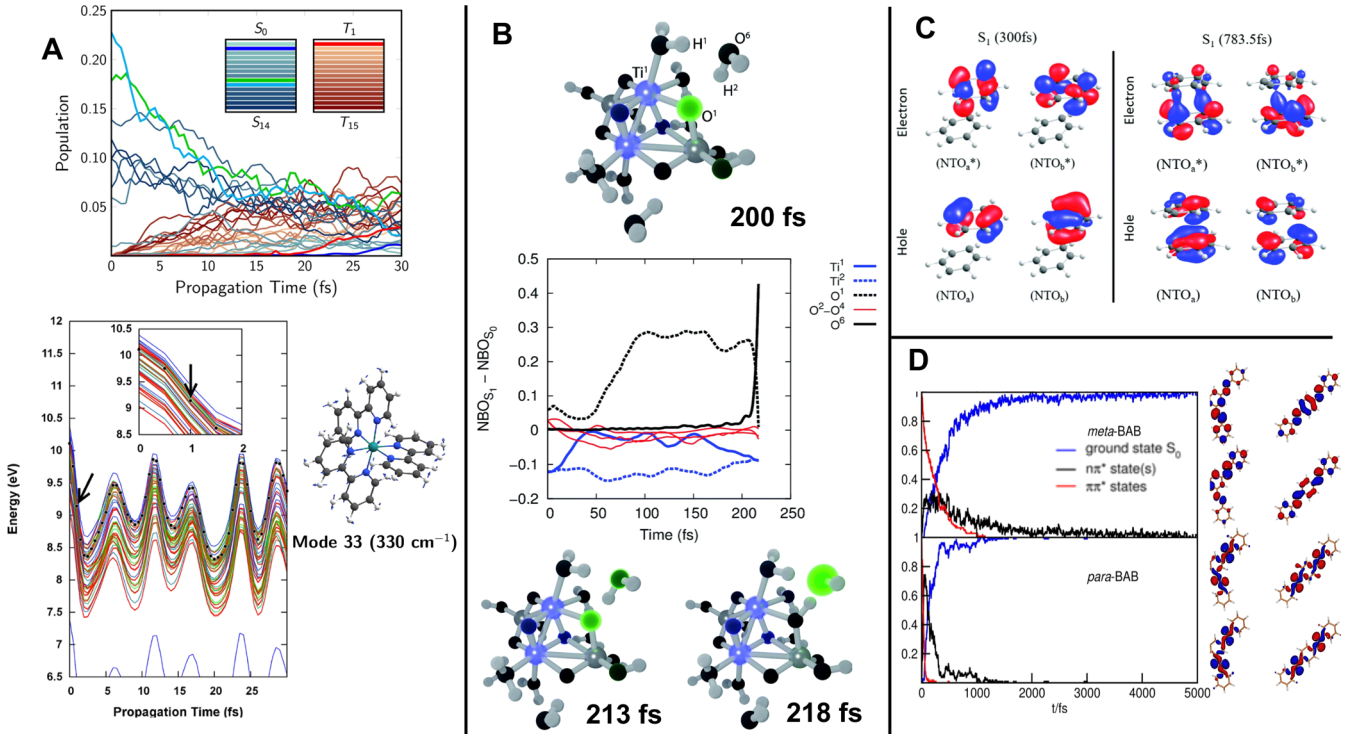

Figure 4. Examples of applications of surface-hopping NAMD. (A) Relaxation, including intersystem crossing, of metal-to-ligand transfer excitation in a ruthenium organometallic complex requiring 14 singlet (S) and 15 triplet (T) states. Adiabatic populations (top), energies (bottom), including trajectory energy (black dots), and molecular geometry are shown. (B) TiO_2 photocatalytic reduction and splitting of water: Natural Bonding Orbital (NBO) population analysis of first excited state and ground state shows exciton dynamics. Nuclear snapshots are also shown, with green spheres indicating the exciton positions. (C) Delocalization of electron and hole in benzene excimer.[242] Snapshots of natural transition orbitals (NTOs) show localized (left) and delocalized (right) excitation. (D) Photoinduced zusammen and entgegen (E-Z) isomerization of bisazobenzene (BAB): population dynamics and frontier NTOs are shown. Panel A: Reproduced with permission from ref 243. Copyright 2017 American Chemical Society. Panel B: Reproduced with permission from ref 244. Copyright 2017 The Royal Society of Chemistry. Panel C: Reproduced with permission from ref 242. Copyright 2019 The Royal Society of Chemistry. Panel D: Reproduced with permission from ref 245. Copyright 2015 American Chemical Society.

the two approximations. First, the classical treatment of the trajectory neglects both differences in zero-point energy (ZPE) for different states and tunneling. The second limitation is that nuclei "feel" the mean-field potential across the distribution of electronic states, i.e., the force acting on the classical trajectory is given by (in the adiabatic representation):

$$\boldsymbol{F}_t = \sum_a |c_a(t)|^2 \nabla_{\boldsymbol{R}} E_a(\boldsymbol{R}_t) + \sum_{a<b} 2\mathrm{Re}\{c_a^*(t)c_b(t)\}\boldsymbol{d}_{ab}(\boldsymbol{R}_t)[E_b(\boldsymbol{R}_t) - E_a(\boldsymbol{R}_t)] \quad (2.18)$$

Branching of the wavepacket is not possible (see sections 2.4 and 2.5.4 on overcoming this limitation). However, the exact nuclear TDSE, eq 2.5, i.e., $\chi(\boldsymbol{R},t)$ may have multiple localized regions of significant magnitude, while a classical trajectory is completely local. Despite this, Ehrenfest dynamics is widely used and is quite appropriate when nuclei are heavy and the range of motion is minimal, i.e., for nanostructures such as quantum dots and carbon nanotubes or other systems with weak correlation of the nuclear motion and the particular electronic states. While the Ehrenfest method is derived from unitary quantum dynamics, not quantum statistical mechanics, the classical nuclear dynamics are often, in practice, coupled to a finite-temperature bath, i.e., in the canonical ensemble or with a thermostat. In the Ehrenfest method, this will result in a continuous heating of the quantum subsystem, i.e., the electrons. Thus, in long time dynamics, the Ehrenfest dynamics does not recover equilibrium electronic population distributions (detailed balance is violated).[226,227] However, the Ehrenfest algorithm correctly conserves the total energy of the isolated system. Thus, for simulations in the microcanonical ensemble or short times, detailed balance is not a concern.

The Ehrenfest approach, in either the standard or multi-configurational techniques, is widely used in non-adiabatic simulations.[228−233] Excited-state hydrogen atom transfer between phenol and ammonia is simulated in ref 222, shown in Figure 3A. In this work, the computational efficiency of the single trajectory Ehrenfest approach allowed for the utilization of high-accuracy Configuration Interaction Singles and Doubles (CISD) electronic structure methods, albeit for a reduced electron active space, required to simulate the proton transfer.[222] The transfer was shown to be a non-adiabatic coupled proton−electron transfer, rather than an adiabatic excited-state proton transfer. The low cost of the Ehrenfest approach also allows for very large systems to be studied. In ref 223, the relatively low cost density functional tight binding (DFTB) approach with Ehrenfest dynamics allows for the simulation of charge migration in very large polymer molecules with about 2000 atoms. The charge localization is strongly affected by the structure of the polymer; see Figure 3B. Linear polymers exhibit delocalization over hundreds of atoms, while "kinked" polymers show significant localization. Similarly, seeking low-cost options for NAMD, Oloboni et al. have presented a combination of

https://dx.doi.org/10.1021/acs.chemrev.9b00447
Chem. Rev. 2020, 120, 2215−2287

Ehrenfest with an extended Hückel model for the electronic structure.[224] This leads to an excited-state nuclear force which consists of the approximate ground-state (molecular mechanics based) force plus a simple electron−hole pair potential force, which approximates the back-reaction of the nuclei due to the electronic states. A variety of well-studied photodynamic processes, including the photoisomerization of azobenzene, shown in Figure 3C,[224] have been studied within this framework. This approach can lead to accurate dynamics on very large systems and tens of picoseconds time scales.

Extensions of the Ehrenfest approach to account for trajectory branching, or more generally electron−nuclear correlation, are critical to the simulation of many chemical problems (section 2.5.4). Ehrenfest dynamics can be restricted to regions of strong non-adiabatic coupling, while allowing branching into separate trajectories when leaving a strong coupling region. Such a *path-branching* approach has been used to simulate photoisomerization dynamics of butadiene derivatives; see Figure 3D and ref 225. The bonds most closely correlated with the passage through two conical intersections could then be determined.

2.2.2. Surface Hopping. In an attempt to address the loss of electron−nuclear correlation in the Ehrenfest method, Tully developed the surface-hopping MD scheme.[234,235] In this approach, the classical trajectory does not "feel" an effective mean-field force but rather it propagates on a single electronic PES, as in the BO case. However, the trajectory has a finite probability to "hop" to another surface. An original hopping probability was designed to simply maintain the equality between the quantum population, from propagation of the electronic coefficients along the trajectory, eq 2.16, and the actual number of trajectories on the surfaces.[235] The problem with this approach is that it introduces an excessive number of hopping events, effectively becoming mean-field dynamics which is inadequate for chemical processes exhibiting branching along different reaction pathways. Tully later introduced a hopping rate that accomplished this balance (mostly) with the fewest number of hops. This results in the so-called fewest-switches surface-hopping (FSSH) method.[76,234] Here the probability for a hop is given by

$$P_{a\to b}(t) = \max\left[0, -\frac{\delta t \frac{2}{\hbar}\mathrm{Re}[c_a^*(t)c_b(t)[\boldsymbol{d}_{ab}(\boldsymbol{R}_t)\cdot\dot{\boldsymbol{R}}_t]]}{c_a c_a^*}\right] \tag{2.19}$$

where δt is the numerical time step and $\boldsymbol{d}_{ab}(\boldsymbol{R}_t)\cdot\dot{\boldsymbol{R}}_t$ is a NACT scalar in the time-dependent trajectory. The evolution of $c(t)$ follows the same EOM, eq 2.16, as in the Ehrenfest method. The "hop" proceeds after each MD step as follows: (1) The probability to hop to all included states is determined. If the probability to hop to a state is negative, it is set to zero. (2) A random number is compared to these probabilities to determine if a hop occurs and to which state. (3) If a hop occurs, the nuclear velocity $\dot{\boldsymbol{R}}_t$ is adjusted along the direction of the NACR $\boldsymbol{d}_{ab}(\boldsymbol{R}_t)$ such that the total energy is conserved. For hops which increase the potential energy, if there is not enough kinetic energy in this direction, then the hop is "frustrated" and does not occur. Multiple alternative schemes have been subsequently developed, including reversal of the direction of the motion along the NACR,[236] introduction of time uncertainty to allow flexibility in energy conservation,[237] or total neglect of the velocity adjustment.[238] Recently there has been emphasis that only the full swarm should be forced to conserve energy.[239−241]

The FSSH method is the most widespread method for non-adiabatic dynamics for both gas- and condensed-phase simulations.[157,246−256] A few characteristic applications are shown in Figure 4. Detailed analysis of photoinduced dynamics calculated using the FSSH-like approaches is exemplified across several molecular systems in sections 4 and 5. For many systems, the number of relevant excited states can be large. Surface hopping is an efficient approach for such systems. In systems with many excited states, it can even be more efficient than Ehrenfest, because forces on the nuclei need to be calculated only for the single "active" state, rather than averaged across all states. For example, Figure 4A summarizes simulations by Atkins and Gonzalez of the excited-state dynamics occurring in the organometallic $Ru(bpy)_3$ complex.[243] Accurate simulation of the intersystem crossing in this system requires many states from both the singlet and triplet manifold. Here, intersystem crossing and internal conversion are directly competing. Additionally, higher excited triplet and singlet states remain populated even after 30 fs, in contrast to organic molecules which typically follow Kasha's rule.[257] In addition to handling large numbers of electronic states, many applications require long trajectories which may be inaccessible to less efficient approaches. In an example simulation of the photocatalytic water splitting by a TiO_2 nanoparticle, little is observed until about 200 fs, when excitonic energy is finally transferred to the water and reaction occurs (Figure 4B). This long time scale allows for non-radiative relaxation back to the ground state to dominate over the exciton transfer, limiting the catalytic efficiency of TiO_2.[244] Figure 4C shows the transient formation of an isolated benzene eximer, taking about 0.5−1 ps. In isolation, the dimer cannot redistribute excess vibrational energy, and the lifetime of the excimer is short compared to observations in the condensed phase.[258]

The efficiency of surface hopping is also critical when systems require high accuracy correlated electronic structure methods. Surface-hopping calculations at the complete active space self-consistent field or perturbation theory (CASSCF/CASPT2) levels have become standard for molecules with tens of atoms. Recent simulations including isomerization of azobenzene[259] and animal rhodopsin[260] have demonstrated the importance of high-quality electronic structure and full treatment of electron−nuclear dynamics, i.e., going beyond 1-D LZ models. Multi-reference complete active space configuration interaction (CAS-CI) and Floating Occupation CI can be used in combination with trajectory surface hopping.[245] An example is the zusammen and entgegen (E-Z) photoisomerization of azobenzene oligomers, a prototypical example of linked molecular switches, shown in Figure 4D. Photoisomerization, like photochemistry, may lead to highly correlated electron−nuclear dynamics, necessitating a beyond mean-field approach like surface hopping. Note that mean-field dynamics can potentially provide accurate simulations of photoisomerization, provided that there is only a single dominant pathway for the dynamics. This may be the case for recent simulations,[261,262] but comparison to experiment, or another method which would allow bifurcation, is prudent. Dynamics of the two switches in bisazobenzene (BAB) was found to depend strongly on whether the coupled switches are *para*-BAB or *meta*-BAB, with *meta*-BAB having a higher switching yield. Additionally the efficiency of a switch was found to be higher if the other switch was initially in the Z configuration.[245]

The key to the success of the surface-hopping approach is that it includes non-adiabatic effects, beyond the mean field, with

https://dx.doi.org/10.1021/acs.chemrev.9b00447
Chem. Rev. 2020, 120, 2215−2287

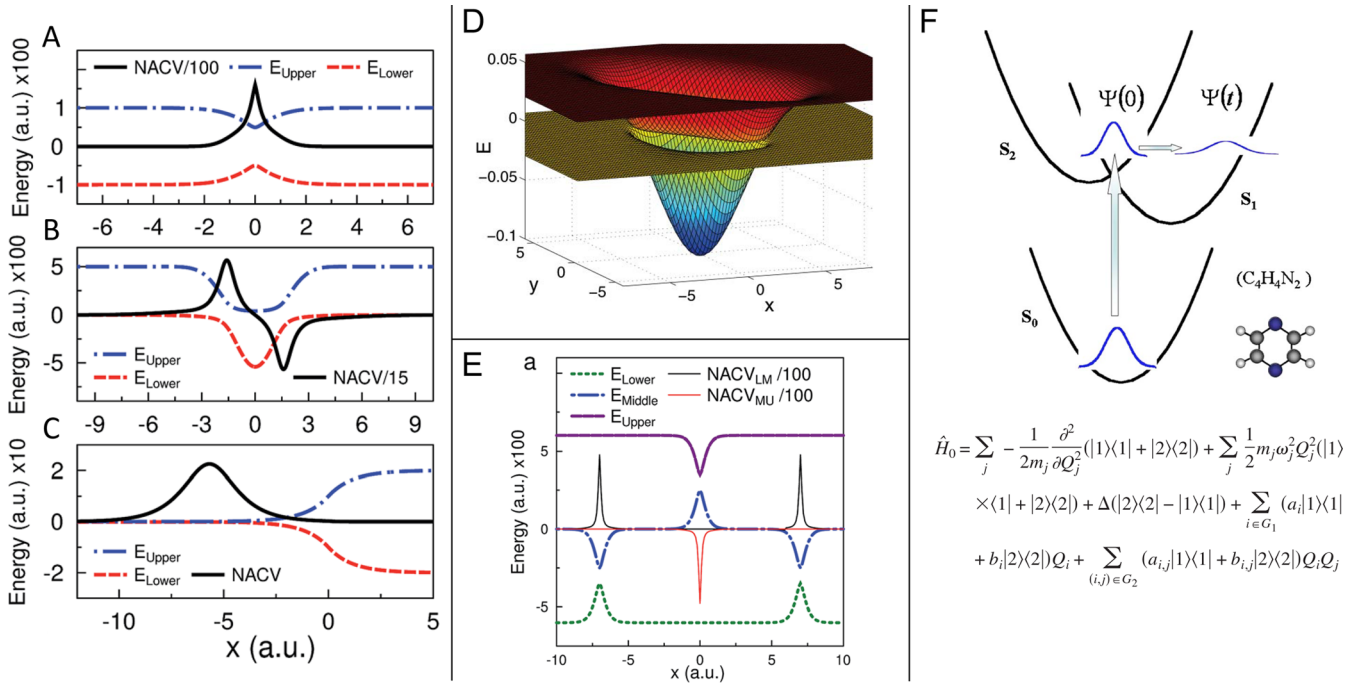

$$\hat{H}_0 = \sum_j -\frac{1}{2m_j}\frac{\partial^2}{\partial Q_j^2}(|1\rangle\langle 1| + |2\rangle\langle 2|) + \sum_j \frac{1}{2}m_j\omega_j^2 Q_j^2(|1\rangle \times\langle 1| + |2\rangle\langle 2|) + \Delta(|2\rangle\langle 2| - |1\rangle\langle 1|) + \sum_{i\in G_1}(a_i|1\rangle\langle 1| + b_i|2\rangle\langle 2|)Q_i + \sum_{(i,j)\in G_2}(a_{i,j}|1\rangle\langle 1| + b_{i,j}|2\rangle\langle 2|)Q_iQ_j$$

Figure 5. Model systems for non-adiabatic algorithm testing. NACV is the non-adiabatic coupling vector, also known as NACR (eq 2.6). (A−C) Tully's original 1-D models: (A) single avoided crossing, (B) dual avoided crossing, and (C) extended coupling with reflection. (D) 2-D well. (E) "Model X", a series of three avoided crossings between three levels. (F) 24-dimensional and reduced four-dimensional, two-level spin-boson-type model, parametrized to model a pyrazine molecule. See ref 263 for the model parameters. Panels A−C: Reproduced with permission from ref 234. Copyright 1990 AIP Publishing. Panel D: Reproduced with permission from ref 264. Copyright 2011 AIP Publishing. Panel E: Reproduced with permission from ref 96. Copyright 2011 American Chemical Society. Panel F: Reproduced with permission from ref 263. Copyright 2010 AIP Publishing.

independent trajectories, without the difficulty to converge interference between trajectories, and without the quantum Bohmian potential. This leads to a simple and naturally parallel algorithm for simulations with minimal extensions beyond adiabatic MD, and efficient statistical convergence. However, this also leads to some well-known issues with the method, as described in the next section.

2.3. Model Scattering Problems: A Standard Test Suite for Non-adiabatic Algorithms

Both Ehrenfest and FSSH approaches are necessarily approximate. The most significant approximations are the *neglect* of electron−nuclear correlation in the Ehrenfest approach, and the *inconsistent* treatment of electron−nuclear correlation in FSSH. For Ehrenfest, this prohibits branching. For surface hopping, this leads to closely related *decoherence* and *recoherence/interference* problems. Both result in errors in the transfer of population between electronic states, and thus in the dynamics of the nuclei. These issues are specifically related to non-adiabatic dynamics, and are considered separately from issues inherent to classical trajectories (ZPE, tunneling, etc.). By comparing the approximate results to exact QM solutions for simple models, these limitations can be demonstrated.

Tully used three test problems[221] (see Figure 5A−C) to demonstrate the successes and failures of the surface-hopping methods and Ehrenfest. More than 25 years later, these models are still widely used to test novel approaches for non-adiabatic dynamics. The popularity of these models stems from the simplicity of interpretation combined with relevance to observed phenomena in molecular systems, e.g., decoherence, Stückelberg oscillations, etc. Additional models have also been introduced to further evaluate methods. These models are typically one-dimensional (1-D) or two-dimensional (2-D) for three reasons: ease of testing, ease of interpretation of results, and the ability to compare to readily available, numerically exact, TDSE solutions.

2.3.1. Single Avoided Crossing. The first of the three "Tully test problems" is a single avoided crossing (SAC) model (Figure 5A). This problem cannot be exactly solved by the LZ approximation, as neither the diabatic state energies nor the coupling are linear or constant, respectively, near the crossing region at $x = 0$. A wavepacket entering the scattering region with total energy (in arbitrary units) $E < 0.004$ will completely reflect on the lower surface. For $0.004 < E < 0.015$ a wavepacket will overcome the barrier in the lower adiabatic surface, but not significantly transfer to the upper. For $0.015 < E < 0.02$ a wavepacket has some probability to transfer to the upper adiabatic surface, but cannot reach the asymptotic region and will reflect. This effect is not reproducible in a mean-field trajectory, as it is based on a strong correlation between the nuclear dynamics and the specific adiabatic PES. For higher energies, the wavepacket will partially transmit on the upper and lower adiabatic surfaces. In addition to comparing quantitative difference between approaches, the model demonstrates the ability of FSSH to capture both diabatic and adiabatic limits (see section 2.1) at least when utilized in the adiabatic representation (see Figure 4 in ref 221). Once the threshold energy ($E > 0.02$) is reached, there is little separation between wavepackets on the upper or lower surfaces, i.e., there is minimal correlation between the nuclear motion and the electronic state. This ensures excellent results in the Ehrenfest and surface-hopping methods for the high-energy case.

https://dx.doi.org/10.1021/acs.chemrev.9b00447
Chem. Rev. 2020, 120, 2215−2287

2.3.2. Dual Avoided Crossing. The dual avoided crossing model (Figure 5B) is designed to demonstrate the consequences of the mean-field nature of eqs 2.16 and 2.17 on QM interference. In this model, wavepackets with initial $E > 0.05$ have two paths for transmitting through the crossing on either surface. A wavepacket that branches from the lower adiabatic surface to the upper surface in the first crossing and then branches from the upper surface to the lower surface in the second crossing will interfere with the wavepacket that remained on the lower surface throughout the scattering process. This interference leads to an oscillation in the momentum dependent transmission probability on the lower surface, i.e., Stückelberg oscillations. In eq 2.16, the EOM of the amplitudes, c_a, carry partial information regarding the difference in their phases through the energy dependence in the first term on the right-hand side. This is more easily seen by determining the EOM of the matrix, $c_b^* c_a$. However, comparing to the EOM for wavepackets, eq 2.15, one sees that there is a lack of kinetic energy dependence in eq 2.16. Stated in simple terms, the trajectories "think" that their own specific momentum is the momentum for all trajectories representing the quantum wavepacket. If the kinetic energy for trajectories on the upper and lower surfaces is small, or the time of separation is low (time spent on upper surface in this case), the error is negligible. This is the case for wavepackets with initial $E > 0.2$, or so. For lower energies, the phase differences in eq 2.16 are incorrect leading to a shift in the peak positions of the Stückelberg oscillations. As mentioned, the error will grow with the increase in time spent on the upper surface, one can see this by extending the distance between the crossings as shown in ref 265.

2.3.3. Extended Coupling with Reflection. This model (Figure 5C) highlights the *overcoherence* or *decoherence* problem in Tully's surface-hopping scheme. For wavepackets with $E < 0.02$, the wavepacket will branch onto both upper and lower adiabatic surfaces, with the wavepacket on the lower surface transmitting ($x \rightarrow \infty$) and the wavepacket on the upper surface reflecting and re-entering the non-adiabatic coupling region. Mean-field trajectories cannot resolve such a bifurcation and will erroneously transmit for all energies, albeit with a lower momentum. The FSSH method can resolve the nuclear dependence on the electronic state, by propagating trajectories on the individual adiabatic states, however the evolution of the electronic coefficients in eq 2.16 assumed the mean-field back action of the nuclei on the electronic system. Thus, the trajectories on the upper surface "think" that the wavepacket on the lower adiabatic surface also reflects and interferes with the returning wavepacket on the upper surface, i.e., that all other trajectories have the same position in time. Thus, wavepackets with $E < 0.02$ show false interference oscillations in the reflection probabilities on the upper and lower surfaces, i.e., upon the second entry into the region of non-adiabatic coupling.

2.3.4. Two-Dimensional Well. Originally utilized by Shenvi and Subotnik,[264] the 2-D well model (Figure 5D) is essentially a 2-D extension of the dual avoided crossing model. It is useful in testing changes in efficiency and accuracy of methods when going from single to higher dimensional problems, especially when interference effects are playing a role. Additionally, by including two dimensions, it allows for the testing of directional dependence in, for example, the phase propagation or in velocity adjustment after surface hops.

2.3.5. Model X. Model X (Figure 5E) consists of three avoided crossings between three surfaces. It was proposed by Subotnik[96] to provide a test for surface hopping when there are multiple pathways. Some pathways interfere, as in the double avoided crossing, while others do not, as in the extended coupling with reflection, depending on the initial nuclear kinetic energy. It also provides a more rigorous test of the quantitative accuracy and convergence of NAMD methods. The more rapid change of the PES with position induces stronger differences in the forces associated with the different surfaces compared to the SAC above.

2.3.6. Pyrazine Molecule. The vibronic absorption spectrum of pyrazine has been extensively modeled.[217,266−270] Typically, the related PESs are represented in either full 24 dimensions or reduced four-dimensional models (Figure 5F), with two excited electronic states (S_1, S_2). The vibronic Hamiltonian is approximated as linearly[266] or quadratically[271,272] coupled harmonic oscillators using the ground-state normal mode coordinates basis. Linear coupling neglects the shift of vibrational frequencies with respect to electronic state. Absorption spectra for these models have been calculated using the high accuracy MC-TDH approach,[171,269,273] creating a good reference for comparison with new methods.[271] The availability of parameters for this Hamiltonian[266,271] with the simplicity of the quadratic model have made the pyrazine molecule attractive for transitioning from test models to "realistic" molecules, albeit while neglecting anharmonicities.

2.4. Treatment of Electron−Nuclear Correlation in Surface Hopping

Introducing decoherence corrections into surface-hopping-like algorithms such as FSSH is critical. Since the interference between the quantum amplitudes of branching subpackets is neglected, the electronic states tend to be more coherent than they should be. This affects not only the correct physical description of the dynamics, but also introduces severe internal numerical inconsistencies in the method.[76,77,79,80] Indeed, along the trajectory, classically occupied states gradually relax to the lower energies via hopping, whereas the quantum wavepacket with amplitudes c_a gets broader and "left behind" remaining at higher energy compared to the classical trajectory, as illustrated in Figure 1 in ref 93. Subsequently, the probability of a hop, eq 2.19 is decided by quantum coefficients with small amplitudes c_a on the very wing of the wavepacket, defying the underpinning foundation of surface hopping. Moreover, persistent broadening of the quantum wavepacket makes the result dependent on the number of electronic states included in the simulations.

Several attempts have been made to include decoherence, proper interference, and other corrections into surface-hopping algorithms. Many of these methods were recently described in the review by Subotnik et al.[78] Decoherence can be introduced by occasionally resetting the quantum amplitudes, $c_k \rightarrow \delta_{k\gamma}$ (where γ is the occupied state), or by adding terms that decay in time the off-diagonal elements in the density matrix representation, as originally proposed by Tully.[234] The question becomes, when and how to enforce such a projection, or what terms to add to the density matrix EOM. The simplest approach is to project after every time step, as proposed by Webster, Rossky, and Friesner.[274] While this may be drastic, it is consistent with a stationary-phase approximation applied to Pechukas' classical scattering theory.[275]

Other early efforts[82,275] by Rossky, Bittner, Schwartz, Prezhdo, Jansen, Zhu, Truhlar, et al. focused on finding a decoherence rate from the approach of frozen Gaussian wavepackets, with widths based either on a harmonic approximation at the initial geometry or a thermal distribution

https://dx.doi.org/10.1021/acs.chemrev.9b00447
Chem. Rev. 2020, 120, 2215−2287

of the initial state.[84] Care must be taken, however, as frozen Gaussians can overestimate decoherence by neglecting the spread of the wavepacket in time, which incorrectly maintains full coherence in constant PESs regardless of the energy gap. Rates based on the energy gap between states and the total kinetic energy have been proposed by Truhlar et al.[81] and implemented by Granucci et al.[83−87] These energy-based decoherence correction (EDC) and/or coherent switching with decay of mixing (CSDM) methods, have the benefit of being more easily calculated, and are the most widely used decoherence corrections. Often, the parameter suggested by Granucci et al.[84] is used regardless of the system being studied.[247,249,251,276−300] While simulations using EDC and CSDM performed on models and small molecular systems lead to results that are relatively independent of the predefined set of decoherence time and parameters, this was shown not to be true when applying the methods to large conjugated molecular systems. Results obtained in simulations of non-radiative relaxation in two conjugated oligomer systems, poly(phenylene-vinylene) (PPV) and poly(phenylene-ethynylene) (PPE), have shown a drastic dependence on which parameters are used.[93] This reveals that methods successfully used for treating small systems cannot be straightforwardly translated to large molecular systems using equivalent parameters. Besides, their success depends on the particular system under study.

Subotnik has proposed an *augmented* fewest-switches surface-hopping (A-FSSH) algorithm, in which the moments (as well as the average) of the position and momenta of the wavepacket are propagated along the trajectory in order to estimate a decoherence rate based on thawed Gaussians.[95,96,301−304] Propagation of the higher moments of the position and momenta adds computational expense since the Hessian of the PES is required. However, recent additional approximations have been applied, with the method remaining quite accurate while gaining numerical efficiency.[117] In addition, Subotnik proposed an alternative to estimating decoherence rates. In the simultaneous-trajectory surface-hopping approach, a surface-hopping trajectory "spawns" extra trajectories with the sole purpose of determining the rate of their separation from the decay of their overlap (assuming GWD).[305]

Introduction of decoherence rates into mean-field dynamics can drive propagation from a mixed electronic surface back to a single surface.[98] This can be done directly, as in the coherence penalty functional approach and the decay of mixing methods, by setting an exponential decay of the off-diagonal density matrix elements.[306] Alternatively, the collapse to an adiabatic state can be stochastic, resulting in a surface-hopping-type scheme, as in the decoherence-induced surface-hopping (DISH) scheme proposed by Jaeger and Prezhdo.[99,307,308]

Methods without decoherence rates have also been proposed. Hammes-Schiffer argued that the projection could be applied when the non-adiabatic coupling drops below a certain threshold,[103] but the determination of the threshold and potentially slow changes between different coupling regions poses a challenge. The use of minima in the non-adiabatic coupling provides a similar criterion, with no threshold. Parlant and Gislason used such a method, but allowed hopping to *only* occur at the minima.[309] We have proposed a simple method, based on no parameters, to include the occasional projection $c_k \rightarrow \delta_{kj}$. In this *instantaneous decoherence* (ID) method, we enforce the projection after each successful (ID-S) or each attempted (ID-A) hop.[93,310,311] It is similar to the method by Webster, Rossky, and Friesner[274] but with a time scale enforced stochastically with the same order as the average time between hops.[93] Another set of methods introduces a coherence time as a parameter in the simulations.[92] If the parametrization of different coherence times is required for different pairs of electronic excited states, these methods become impractical for large systems involving many coupled electronic states.[80,88−91]

Correct treatment of the quantum interference effects, i.e., the phase of the trajectory, usually requires a semiclassical treatment of the dynamics discussed earlier. However, some attempts have been made to correct the phase propagation within the surface-hopping method. Subotnik and Shenvi developed a phase corrected surface-hopping approach.[264] The approach takes into account the difference in the magnitude of the momentum of energy conserving trajectories on each surface, but it cannot fully account for the difference in the dynamics, i.e., direction of the momentum, on each surface. This is a necessary limitation for the trajectories to maintain their independence. Shenvi and Wang showed that phase correction can also aid in decoherence.[94,312]

An important aspect of exact quantum dynamics is the independence of expectation values from the choice of the electronic representation, i.e., adiabatic, diabatic, or other, for the electronic wavefunction. For the Ehrenfest approach, if the electronic basis is complete (not necessarily true in practice), then the results are representation independent (though highly approximate). This is not true for surface hopping. Surface hopping in the adiabatic representation is well defined, and many aspects, such as the rescaling of nuclear momentum along the direction of the NACR in order to conserve total energy, are justified by comparison to other methods. However, analysis of electronic dynamics and their use in interpretation of experimental results, is often clearer in an electronically diabatic basis. For example, the concept of superexchange is lost in the adiabatic representation, but often of interest in electronic dynamics in the diabatic basis. In surface hopping, within the diabatic basis, superexchange is not allowed due to the enforcement of energy conservation on hops. Methods such as time-uncertainty surface hopping soften such requirements.[237] The Prezhdo group[74] has recently developed a number of methods to recover superexchange in diabatic surface hopping, including second-quantization surface hopping,[239] global-flux surface hopping (GFSH),[313] and surface hopping in Liouville space (SHLS).[314] Note that for FSSH in the diabatic representation, energy conservation of hops is *not* justified by comparison to rigorous semiclassical methods. Results for the Tully dual avoided crossing (see Figure 5B) for the Liouville space hopping are shown below in Figure 7A. GFSH and SHLS have been shown to reduce differences between adiabatic and diabatic dynamics.[313,314]

2.5. Alternative Mixed Quantum-Classical Approaches beyond Surface Hopping and Ehrenfest

Overall, the need for the many variations discussed above (section 2.4) to correct the surface-hopping or Ehrenfest methods stems from the respective ad hoc and mean-field treatment of the electron−nuclear correlation. The previously mentioned quantum (section 2.1) and semiclassical (section 2.2) methods based on *first-principles*, do not rely on such approximations but are, in general, not sufficiently numerically efficient to routinely simulate many-atom systems, as can be accomplished using surface-hopping or Ehrenfest techniques. Thus, development of new methods continues through targeting well controlled approximations.

https://dx.doi.org/10.1021/acs.chemrev.9b00447
Chem. Rev. 2020, 120, 2215−2287

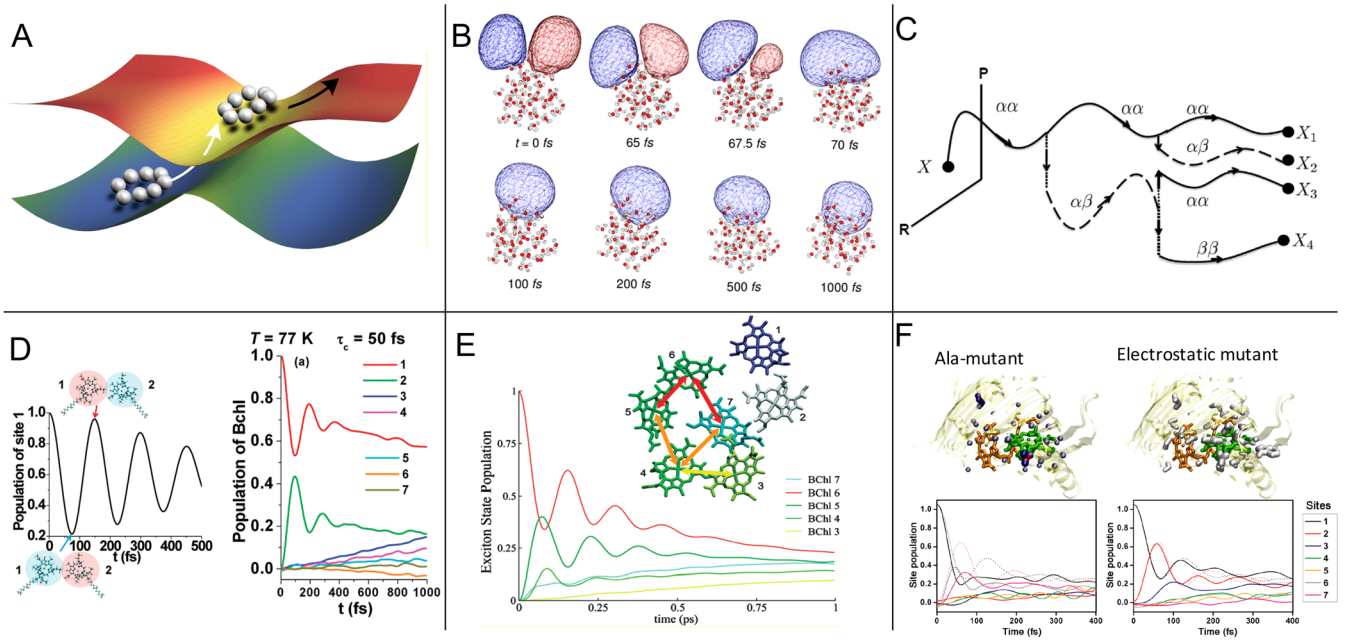

Figure 6. (A) Cartoon representation of non-adiabatic ring-polymer molecular dynamics (RPMD). (B) Non-adiabatic RPMD simulation of relaxation of "excess solvated electron wavefunction", shown by isosurface, in photoexcited water cluster. Excited state shows "p-like" wavefunction, while ground state shows "s-like" wavefunction. (C) Cartoon of Monte Carlo-based quantum-classical Liouville equation solution, with characteristic phase space trajectories and population/coherence hops. (D) Semiclassical simulations of a two-level spin-boson model of a bacteriochlorophyll dimer (left) and a seven-state model of a Fenna−Mathews−Olson (FMO) complex (right). Diabatic "site" populations are shown. Initially a single chromophore is excited. (E) Same seven-state FMO model simulation but using PBME approach. (F) Similar to panel E, but with mutated FMO-type complexes. Panel A: Reproduced with permission from ref 315. Copyright 2017 American Chemical Society. Panel B: Reproduced with permission from ref 316. Copyright 2013 Elsevier. Panel C: Reproduced with permission from ref 317. Copyright 2016 Elsevier. Panel D: Reproduced with permission from ref 151. Copyright 2010 American Chemical Society. Panel E: Reproduced with permission from ref 318. Copyright 2011 American Chemical Society. Panel F: Reproduced with permission from ref 319. Copyright 2012 American Chemical Society.

2.5.1. Ring-Polymer/Path Integral Molecular Dynamics. Interesting developments include the ring-polymer and centroid MD. These methods have been recently reviewed for molecular systems.[128] Both are based on an imaginary time path integral approach to find the *equilibrium* thermal density matrix.[128] By slicing the partition function into imaginary time slices, a single slice for each monomer or bead in the Ring-polymer, one can develop a MD scheme with harmonically coupled trajectories. Thus, every atom in a molecular system is interacting with N_{bead} versions of itself, called "beads" of the ring polymer, through a harmonic force, $\omega_{RPMD} = \frac{m_R N_{bead}^2}{2\hbar^2\beta^2}$, as well as with the $N_{atom} - 1$ other atoms in the system. In the very high temperature limit $\frac{1}{T} = \beta \to 0$, the spring becomes very stiff and $N_{bead} \to 1$. For lower temperatures, the spring becomes very loose and the N_{bead} required to converge results increases. Requiring N_{bead} additional trajectories instead of a single trajectory is limiting for many *ab initio* on-the-fly methods, but is reasonable for classical force-field or quantum derived force-field approaches. The centroid approximation, a mean-field average over the beads, is a more affordable, but more approximate, alternative.

Ad hoc extensions of the method to non-adiabatic dynamics (see Figure 6A) have recently been developed,[74,315,320,321] though interference effects are ignored. Figure 7F (below) shows a comparison of ring-polymer molecular dynamics (RPMD) and TDSE calculations of the time-dependent probabilities for the standard Tully models. In this case, the spring constant is taken to be related to the wavepacket width or ZPE. While the method is formally an equilibrium method (where temperature is well defined), not a real-time propagation, the method was also applied to non-equilibrium situations with some promising results,[322,323] as well as to solvated electron dynamics in a water cluster (Figure 6B).[316] Quantum tunneling (included approximately through the RPMD scheme) leads to approximately twice faster relaxation of the photoexcited solvated electron.

2.5.2. Quantum-Classical Liouville Equation. Instead of working with the TDSE, multiple methods focus instead on the EOM for the density matrix[324] using the Von Neumann equation:

$$i\hbar\frac{\partial\hat{\rho}(t)}{\partial t} = [\hat{H}, \hat{\rho}(t)] \tag{2.20}$$

Treating the nuclei as a "bath" of heavy atoms, performing a partial Wigner transformation over the bath variables, and taking the semiclassical limit leads to Kapral's quantum-classical Liouville equation (QCLE).[325] The use of this method in non-adiabatic dynamics has been recently reviewed in refs 127 and 326. Similar to complex Gaussian wavepackets, the approach introduces an intuitive phase-space picture of the quantum-classical dynamics. Like the semiclassical approaches mentioned above (section 2.2), accounting for non-adiabatic effects requires a Monte Carlo approach for sampling oscillatory functions, which can be inefficient. Figure 6C shows how a diagram for a Monte Carlo "hopping" scheme for the QCLE works. Trajectories undergo stochastic transitions from representing population matrix elements, which propagate on adiabatic PESs, to representing coherence elements, which propagate on average surfaces.[317,327] Since the Wigner density is

https://dx.doi.org/10.1021/acs.chemrev.9b00447
Chem. Rev. 2020, 120, 2215−2287

not always positive,[327] Linearization,[328] forward−backward propagation,[329] and filtering[330] have been introduced (similar to the SC-IVR propagator) in an attempt to improve stability and efficiency. A transfer tensor method has also been developed to extend accuracy and feasibility of the QCLE to long times using short-time trajectories.[331] Implementation of the QCLE in the mapping basis,[332] leads to a the Poisson-bracket mapping equation (PBME), which is mean-field in nature, significantly extending applicability at the cost of accuracy.[326] Application of the PBME, SC-IVR, and MMST models to study electronic ET in biological chromophores is shown in Figure 6D−F. Figure 6D shows the SC-IVR/MMST calculated ET in a two-state bacteriochlorophyll dimer and a seven-state model for the Fenna−Mathews−Olson (FMO) complex.[151] PBME simulations of the FMO and mutations (shown in Figure 6E,F) are in good agreement with the SC-IVR/MMST results[318,319] but more closely resemble simulations based on full hierarchical equations; see ref 151. These results support the role of electronic quantum coherence in ET in these systems at physiological temperatures.[151] However, recent experimental/theoretical results[333] indicate that previous simulations may have underestimated decoherence rates due to the environment and molecular vibrations, leading to overestimation of electronic coherence effects.

The Liouville space approach, and its semiclassical limit, is also the starting point for the consensus surface hopping (CSH) and fully coherent approach proposed by Martens.[241,334,335] The main purpose of the development of CSH is to connect surface-hopping "schemes" to the quantum Liouville equation through clear approximations. Thus, CSH provides a prescription for "hopping" in the *diabatic* representation, the difficulties of which were discussed in section 2.4. The most notable difference between traditional surface hopping and CSH is that there is no forced energy conservation of individual trajectories in CSH.[335]

2.5.3. Quantum Hydrodynamics, Bohmian Mechanics, and Exact Factorization. An alternative to the semiclassical path integral based approach to quantum dynamics is semiclassical Bohmian dynamics. In this hydrodynamic formulation of quantum mechanics, classical trajectories propagate in a nonlinear fashion, with a quantum potential $Q(\boldsymbol{R})$:

$$\begin{aligned}\dot{\boldsymbol{R}}_t &= \hat{\boldsymbol{m}}_{\boldsymbol{R}}^{-1}\cdot\boldsymbol{P}_t\\ \dot{\boldsymbol{P}}_t &= -\nabla_{\boldsymbol{R}}(E(\boldsymbol{R}_t) + Q(\boldsymbol{R}_t))\\ Q(\boldsymbol{R}) &= -|\chi(\boldsymbol{R})|^{-\frac{1}{2}}(\hbar^2/2)\nabla_{\boldsymbol{R}}\cdot\hat{\boldsymbol{m}}_{\boldsymbol{R}}^{-1}\cdot(\nabla_{\boldsymbol{R}}|\chi(\boldsymbol{R})|^{\frac{1}{2}})\end{aligned} \tag{2.21}$$

determined from the dynamics of the full swarm of trajectories.[336−338] Of course, a significant number of trajectories is required to generate an accurate quantum potential, and divergence when the density goes to zero can lead to difficulties. This limits the application of Bohmian dynamics to small systems. Similarly, the exact factorization method also introduces a quantum potential for semiclassical dynamics.[126,339,340] The exact factorization approach extended to non-adiabatic dynamics, the coupled trajectory mixed quantum/classical method, was recently applied to the photochemical ring opening reaction of oxirane. Ehrenfest, decoherence-corrected surface hopping,[126] and multiple spawning[341] show that the exact factorization approach can successfully capture decoherence effects in conical intersections. The Bohmian dynamics and exact factorization methods were thoroughly reviewed by Barbatti and Crespo-Otero.[121]

2.5.4. Multiconfigurational Approaches: Multiconfigurational Ehrenfest and Ab Initio Multiple Cloning. As has been previously mentioned (section 2.1), Gaussian wavepackets are widespread through quantum dynamics methods.[165−167,204−206,208,211−213,342,343] In particular, a class of dynamical methods based on the solution to the time-dependent Dirac−Frenkel variational principle,[69]

$$\left\langle \partial\Psi(\boldsymbol{R},\boldsymbol{r},t)\middle|\hat{H}(\boldsymbol{R},\boldsymbol{r}) - i\hbar\frac{\partial}{\partial t}\middle|\Psi(\boldsymbol{R},\boldsymbol{r},t)\right\rangle = 0 \tag{2.22}$$

or the TDSE, using a Gaussian basis set, leads to coupled equations for the time-dependent parameters of a swarm of Gaussian wavepackets. This class includes the variational multiconfigurational Gaussian (v-MCG) method,[344] the direct dynamics MCG,[345] the coupled coherent states, the MCE,[263,346] and the AIMS methods.[43,125,347,348] In the first three, the dynamics of the Gaussians are coupled through the solution of eq 2.22 or the TDSE. In the AIMS and MCE methods, only complex coefficients for each time-dependent Gaussian basis function are then determined from the TDSE. The MCE uses Ehrenfest equations to propagate the wavepacket in regions of NAC, while the AIMS method propagates it adiabatically on the PES, and "spawns" new Gaussians on coupled PESs in NAC regions.[349] For a more in-depth look at spawning and Gaussian wavepacket methods see the review by Barbatti and Crespo-Otero.[121] Here, we will focus on the MCE and AIMC methods.

For the MCE method, the wavefunction is written as a linear combination of Ehrenfest configurations (eq 2.13):

$$\Psi(\boldsymbol{r},\boldsymbol{R},t) = \sum_n d^{(n)}(t)\Psi^{(n)}(\boldsymbol{r},\boldsymbol{R},t) \tag{2.23}$$

$$\Psi^{(n)}(\boldsymbol{r},\boldsymbol{R},t) \equiv \chi^{(n)}(\boldsymbol{R},t)\sum_a c_a^{(n)}(t)\psi_a^{(n)}(\boldsymbol{r},\boldsymbol{R}) \tag{2.24}$$

where the subindex n denotes the nth Ehrenfest configuration and $c_a^{(n)}(t)$ is the electronic wavefunction coefficient (eqs 2.13 and 2.16) for the nth configuration. The additional configurational coefficient, $d^{(n)}(t)$, is solved using the TDSE:

$$i\hbar\frac{\partial}{\partial t}d^{(n)} = \sum_m (\hat{S}^{-1})_{nm}\times \sum_l \left\langle \Psi^{(m)}(\boldsymbol{r},\boldsymbol{R},t)\middle|\hat{H}(\boldsymbol{R},\boldsymbol{r}) - i\hbar\frac{\partial}{\partial t}\middle|\Psi(l)(\boldsymbol{r},\boldsymbol{R},t)\right\rangle d^{(l)}(t) \tag{2.25}$$

with

$$S_{ml} = \langle\Psi^{(m)}(\boldsymbol{r},\boldsymbol{R},t)|\Psi^{(l)}(\boldsymbol{r},\boldsymbol{R},t)\rangle \tag{2.26}$$

Each configuration is assumed to follow its own Ehrenfest (mean-field) trajectory (eqs 2.18 and 2.11). $\chi^{(n)}(\boldsymbol{R},t)$ is still a Gaussian wavepacket (see section 2.5.5), but with a fixed, purely imaginary width, $\hat{\boldsymbol{\alpha}}(t) = i\hat{\boldsymbol{\alpha}}_I(0)$, and with a time-dependent phase factor: $\dot{\gamma}_t = \boldsymbol{P}_t\cdot\hat{\boldsymbol{m}}_{\boldsymbol{R}}^{-1}\cdot\boldsymbol{P}_t/2$. Thus, the wavepacket is referred to as a coherent state (CS). In practical application, $\hat{H}(\boldsymbol{R},\boldsymbol{r})$ and $\psi_a^{(n)}(\boldsymbol{r},\boldsymbol{R})$ need to be expanded around a nuclear geometry, typically near the center of either the bra or ket of Ψ in eq 2.25, their midpoint or some other linear combination. In large systems, adiabatic states can change significantly within the CS width and the electronic overlaps must be taken into account. Subsequently, accounting for trivial unavoided crossings (section 3.4.3) is a concern which can be addressed by

https://dx.doi.org/10.1021/acs.chemrev.9b00447
Chem. Rev. 2020, 120, 2215−2287

representing the electronic parts of the wavefunction in the time-dependent diabatic basis (TDDB).[350]

Each configuration evolves on its own mean-field PES driven by force eq 2.18, allowing a highly efficient trivial parallelization in the numerical implementation with the appropriate post-processing of the results. The mechanism by which configurations are generated does not affect the results when enough of the configurational space is sampled such that the basis is complete. Configuration amplitudes and electronic overlaps can be calculated and post-processed after propagation of the trajectories. However, for systems having different relaxation pathways, the average Ehrenfest PES does not represent its individual contributions to the overall relaxation process and will not lead to a complete basis of CSs. A more adequate treatment of these individual contributions can be achieved by using the AIMC,[349,353] that allows situations in which the average Ehrenfest potential becomes unphysical to be taken into account. That is, regions of low non-adiabatic couplings presenting significant differences between the shapes of the PESs of two or more substantially populated electronic states. This typically happens when a configuration passes through (or near) a conical intersection or a region of strong non-adiabatic coupling. In this case, a sole nuclear wavepacket splits into multiple parts, each dominated by a single electronic state.

The AIMC procedure quantifies how well the mean field represents the individual excited-state dynamics. Whenever the mean-field fails, the corresponding configuration is replaced by two new configurations, having the same nuclear wavefunction but different electronic populations and, therefore, their own distinct mean fields. Amplitudes corresponding to these new configurations are defined such that the wavefunction remains continuous at the cloning point. After the cloning procedure, each new configuration follows its own mean field and separates from the other, providing the desired bifurcation effect. More details and technical implementations of the AIMC method can be found elsewhere.[349,353,354] While initial applications of this approach are encouraging, systematic future studies on numerical convergence of the trajectory swarm and optimal cloning schemes are needed in the realm of large molecular systems. If a diabatic representation is assumed, cloning can be formulated without non-adiabatic couplings and adiabatic states, though the cloning criteria will be different.[355]

2.5.5. First-Principles Non-adiabatic Dynamics Based on Monte Carlo Integration and Coupled Wavepackets. Our group has sought to develop a numerically efficient non-adiabatic dynamics method, based on *controllable* approximations to the TDSE, eq 2.5. In formulating a new method, we seek to retain the simplicity of *on-the-fly* classical dynamics, i.e., no root-search or PES generation. We only require variables that can be calculated from standard quantum-chemistry packages, such as the force on the nuclei (PES gradients) and the electronic wavefunction. Finally, the method must have better (or at least equivalent) efficiency and scalability compared to FSSH, such that the approach would be applicable to many-atom molecules.

Before describing the computational approach, let us revisit the mathematical foundations of the adiabatic dynamics. In particular, when deriving eq 2.5, we have assumed that the adiabatic states, $\psi_a(\boldsymbol{r},\boldsymbol{R})$, in eq 2.3 are functions of the nuclear coordinates, $\boldsymbol{R}$. In MD simulations, the nuclei follow a classical trajectory and, therefore, their coordinates are actually functions of time. Thus, when substituting eq 2.3 into the Schrödinger equation, eq 2.4, one should assume that ψ_a are explicit functions of t, $\psi_a = \psi_a(\boldsymbol{r},\boldsymbol{R}_t)$. Following such assumption, the substitution of eq 2.3 into eq 2.4 gives[351,356]

$$i\hbar\frac{\partial\chi_a(\boldsymbol{R},t)}{\partial t} = -\frac{1}{2}\hbar^2\nabla_{\boldsymbol{R}}\cdot\hat{\boldsymbol{m}}_{\boldsymbol{R}}^{-1}\cdot\nabla_{\boldsymbol{R}}\chi_a(\boldsymbol{R},t) + \sum_b V_{ab}\chi_b(\boldsymbol{R},t) \tag{2.27}$$

with

$$V_{ab}(\boldsymbol{R},t) = i\left\langle \psi_b(\boldsymbol{R}(t))\left|\frac{\partial}{\partial t}\right|\psi_a(\boldsymbol{R}(t))\right\rangle + \langle\psi_b(\boldsymbol{R}(t))|\hat{H}_{\mathrm{el}}(\boldsymbol{R})|\psi_a(\boldsymbol{R}(t))\rangle \tag{2.28}$$

Note that in the expression for V_{ab} the Hamiltonian, $\hat{H}_{\mathrm{el}}$, contains $\boldsymbol{R}$ as an operator, while $\boldsymbol{R}_t$ is a variable. Expansion of $\hat{H}_{\mathrm{el}}(\boldsymbol{R})$ in the vicinity of $\boldsymbol{R}_t$ leads to an effective Hamiltonian,

$$\hat{H}_{\mathrm{eff}}(\boldsymbol{R},\boldsymbol{R}_t) \approx -\frac{1}{2}\hbar^2\nabla_{\boldsymbol{R}}\cdot\hat{\boldsymbol{m}}_{\boldsymbol{R}}^{-1}\cdot\nabla_{\boldsymbol{R}} + \sum_a V_a(\boldsymbol{R})|a\rangle\langle a| + \sum_{a\neq b} V_{ab}(\boldsymbol{R})|a\rangle\langle b| \tag{2.29}$$

with

$$V_a(\boldsymbol{R}) = E_a(\boldsymbol{R}_t) + f_a(\boldsymbol{R}_t)\cdot(\boldsymbol{R}-\boldsymbol{R}_t) + \frac{1}{2}(\boldsymbol{R}-\boldsymbol{R}_t)\cdot\hat{\kappa}_a(\boldsymbol{R}_t)\cdot(\boldsymbol{R}-\boldsymbol{R}_t) \tag{2.30}$$

$$V_{ab}(\boldsymbol{R}) = i\boldsymbol{d}_{ab}(\boldsymbol{R}_t)\cdot\dot{\boldsymbol{R}}_t + (E_a - E_b)\boldsymbol{d}_{ab}(\boldsymbol{R}_t)\cdot(\boldsymbol{R}-\boldsymbol{R}_t) \tag{2.31}$$

In eq 2.30, parameters E_a,$\boldsymbol{f}_a$, and $\hat{\kappa}_a$ are the ath expectation values of the electronic Hamiltonian, $\hat{H}_{\mathrm{el}}(\boldsymbol{R}_t)$, and its first and second derivatives, respectively. In eq 2.31, we used eq 2.10 to get the last term on the right-hand side and neglected the second-order term.

The off-diagonal couplings, V_{ab}, generate transitions between different PESs. Upon application of operator $V_{ab}(\boldsymbol{R})$ in eq 2.31 to a Gaussian in eq 2.10, the latter, generally speaking, becomes a non-Gaussian function. We recall, however, that the nuclear wavepackets are quite narrow, and therefore we can rewrite eq 2.31 as

$$V_{ab}(\boldsymbol{R}) \approx i\boldsymbol{d}_{ab}\cdot\dot{\boldsymbol{R}}_t\, \mathrm{e}^{-i\Delta\boldsymbol{p}_{ab}\cdot(\boldsymbol{R}-\boldsymbol{R}_t)} \tag{2.32}$$

where

$$\Delta\boldsymbol{p}_{ab} = (E_a - E_b)\boldsymbol{d}_{ab}/(\boldsymbol{d}_{ab}\cdot\dot{\boldsymbol{R}}_t) \tag{2.33}$$

The exponential dependence of $V_{ab}(\boldsymbol{R})$ on $\boldsymbol{R}-\boldsymbol{R}_t$ greatly simplifies the picture. Indeed, now application of operator $V_{ab}(\boldsymbol{R})$ in eq 2.32 to a Gaussian in eq 2.10 leads to a new Gaussian, with a new amplitude (proportional to NACT scalar $\boldsymbol{d}_{ab}\cdot\dot{\boldsymbol{R}}_t$) and a changed momentum. The difference in the momenta of the old and new wavepackets, $\Delta\boldsymbol{p}_{ab}$, has a direction along the NACR. The magnitude of $\Delta\boldsymbol{p}_{ab}$ obviously depends on $\dot{\boldsymbol{R}}_t$, which is not uniquely defined. Indeed, while it was implicitly assumed that $\boldsymbol{R}_t$ is the classical coordinate of the nuclei, $\boldsymbol{R}_t$ only defines the point at which we evaluate the electronic basis functions (and thus the parameters of the effective Hamiltonian in eq 2.29). If we consider the following choice,

$$\dot{\boldsymbol{R}}_t = \hat{\boldsymbol{m}}_{\boldsymbol{R}}^{-1}\cdot(\boldsymbol{P}_{0,a} + \boldsymbol{P}_{1,b}) \tag{2.34}$$

where $\boldsymbol{P}_{0,a(1,b)}$ is the momentum of the "parent" ("offspring") wavepacket, then classical energy conservation is satisfied,

https://dx.doi.org/10.1021/acs.chemrev.9b00447
Chem. Rev. 2020, 120, 2215−2287

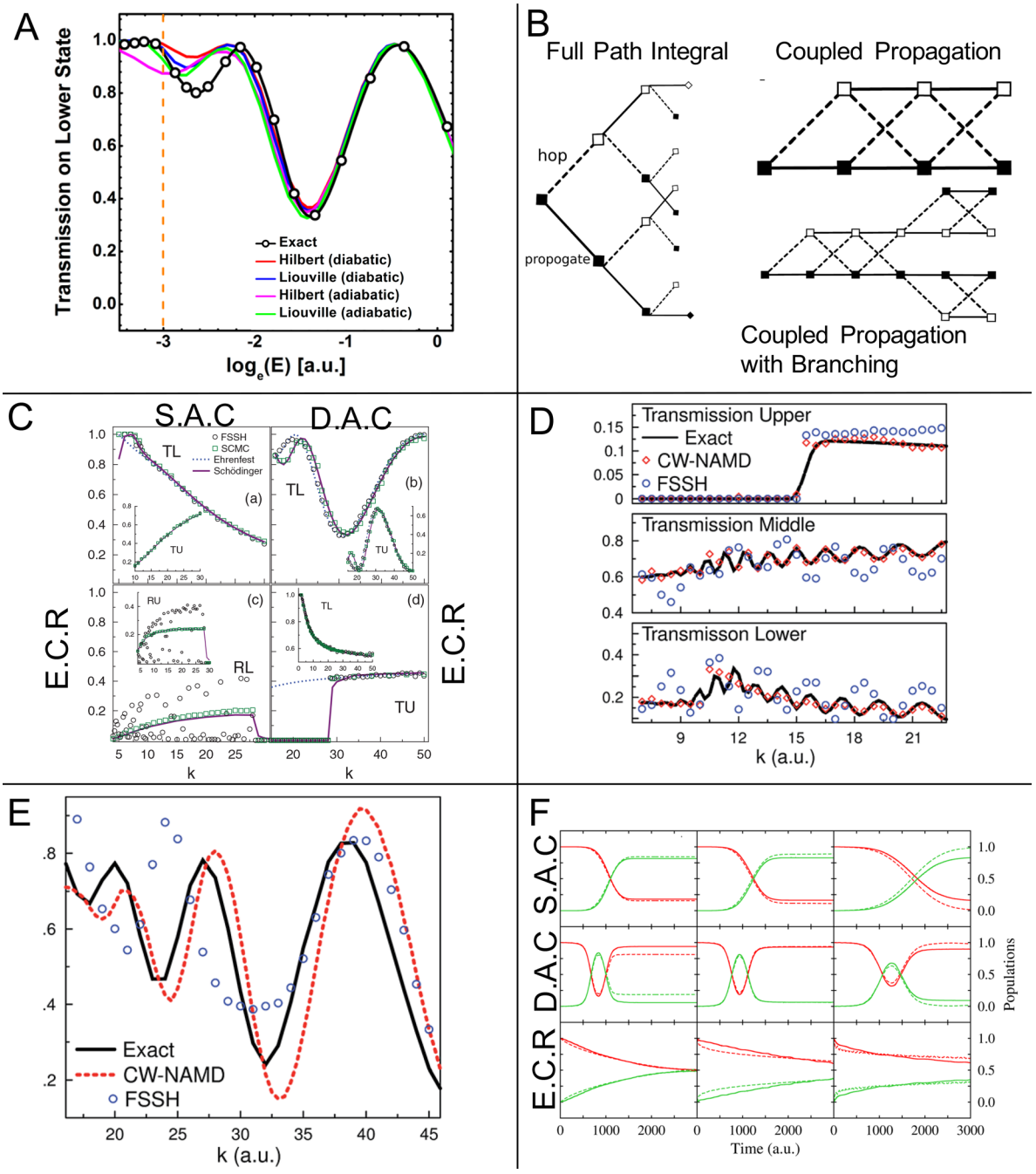

Figure 7. (A) Standard and Liouville space surface-hopping results: transmission on lowest PES vs initial scattering energy for the dual avoided crossing model compared to exact solution. (B) Diagram representation of semiclassical wavepacket approaches. The full path integral (branching at each time point) can be sampled stochastically ("hopping", semiclassical Monte Carlo (SCMC)), or the basis functions can be propagated "coupled" together, as in Ehrenfest dynamics, and occasionally "branch" by projection onto specific eigenstates, as in ab initio multiple cloning and coupled-wavepacket (CW) methods. (C) SCMC scattering results: transition (T) or reflection (R) on upper (U) or lower (L) vs initial wavepacket momentum (k) of Tully models (see Figure 5A–C), compared to surface hopping, Ehrenfest, and exact solution. (D) CW, surface hopping, and exact results for scattering through the three-state "Model X". (E) CW, surface hopping, and exact results for scattering through the 2-D well model; probability on the lower surface is shown.[271,273,351] (F) Time-dependent populations for scattering in the three Tully models (top to bottom): comparison for non-adiabatic RPMD (solid) with exact (dashed) for three different initial momenta (left to right); green is upper and red is lower state probability. Panel A: Reproduced with permission from ref 314. Copyright 2015 American Chemical Society. Panels B, D, and E: Reproduced with permission from ref 351. Copyright 2016 The Royal Society of Chemistry. Panel C: Reproduced with permission from ref 352. Copyright 2014 AIP Publishing. Panel F: Reproduced with permission from ref 323. Copyright 2015 American Chemical Society.

$$\frac{1}{2}\boldsymbol{P}_{0,a}\cdot\hat{\boldsymbol{m}}_{\boldsymbol{R}}^{-1}\cdot\boldsymbol{P}_{0,a}+E_a=\frac{1}{2}\boldsymbol{P}_{1,b}\cdot\hat{\boldsymbol{m}}_{\boldsymbol{R}}^{-1}\cdot\boldsymbol{P}_{1,b}+E_b \tag{2.35}$$

The energy conservation condition in eq 2.35 is standard for the surface-hopping algorithm, where hops between PESs are accompanied by momentum rescaling that conserves energy. The condition is motivated, in particular, by the semiclassical arguments.[234] Alternatively, $\boldsymbol{R}_t$ can follow the QM expectation value of the total wavefunction, in concurrence with the

https://dx.doi.org/10.1021/acs.chemrev.9b00447
Chem. Rev. 2020, 120, 2215−2287

Ehrenfest theorem.[356] The form of the effective Hamiltonian in eq 2.29 suggests a simple computational approach to describe the non-adiabatic propagation of Gaussian wavepackets. Propagation proceeds similarly to eq 2.11, but the wavepackets transfer amplitude at each time step to any coupled surfaces, here called offspring. As in the standard surface-hopping procedure, the momentum is changed along the direction of NACR, such that the classical energy, $\boldsymbol{P}_t\cdot\hat{\boldsymbol{m}}_R^{-1}\cdot\boldsymbol{P}_t/2 + E(\boldsymbol{R}_t)$, of the trajectory is conserved,[351] or nearly conserved.[356] The repetition of the process, i.e., the propagation of both the "parent" and the "offspring" Gaussians leads to an infinitely branching tree, represented for a two-state (TS) system in Figure 7B. We have developed two approaches to handle this expanding basis set, the semiclassical Monte Carlo (SCMC) and the coupled-wavepacket (CW) methods.

In an attempt to retain the simplicity of surface-hopping dynamics, one can use a Markov-chain Monte Carlo approach with importance sampling to approximate this branching tree. In this approach, a swarm of wavepackets is propagated, each following classical dynamics, while the EOMs for α_t and γ_t are also integrated. After each time step, the wavepacket has a probability to hop to another surface given by

$$\text{Prob}_{a\to b} = \frac{|\boldsymbol{d}_{ab}(\boldsymbol{R}_0)\cdot\dot{\boldsymbol{R}}_t|\Delta t}{1 + \sum_c |\boldsymbol{d}_{ac}(\boldsymbol{R}_0)\cdot\dot{\boldsymbol{R}}_t|\Delta t} \equiv \frac{|D_{ab}|}{1 + \sum_c |D_{ac}|} \tag{2.36}$$

As in conventional surface hopping, eq 2.36 excludes hops forbidden by the energy conservation, eq 2.35. After a successful hop, the weight of the wavepacket, N, must be scaled, $N_1 = N_0 \times [D_{ab}/|D_{ab}|] \times [1 + \sum_c |D_{ac}|]$. At any given time, the wavefunction is given by the simple sum of Gaussian functions (one for each trajectory).

We have applied the SCMC approach to the model problems described in section 2.3. The method provides excellent agreement with exact quantum dynamics for the scattering probabilities shown in Figure 7C. In practice, for computational efficiency, we neglect $\hat{\kappa}$ everywhere. We call this the *free thawed Gaussian* approximation. The method does not suffer from the decoherence problems of traditional surface hopping, as the finite width of the wavepackets will prevent false interference effects. Additionally, the action of the individual trajectories is calculated along with the classical dynamics; thus, Stückelberg oscillations are accurately reproduced, see Figure 7C.

Like other semiclassical path integral methods which rely on Monte Carlo sampling of complex integrals, such as the non-adiabatic SC-IVR and HK methods, the SCMC approach suffers from the "sign problem" of Monte Carlo. That is, the final wavefunction is the superposition of many wavepackets with complex valued coefficient. The SCMC method requires an order of magnitude more trajectories for the SAC problem compared to surface hopping. The required number of trajectories increases for systems with additional complexity, i.e., multiple interfering paths such as the dual avoided crossing and the Model X. However, dimensionality of the system does not have an effect on the required number of trajectories, as seen by comparing the number of trajectories required for convergence in the 1-D and 2-D dual avoided crossing models. An in-depth analysis of the sign problem in SCMC is presented in ref 352. Advanced sampling techniques can be used to alleviate the inefficiencies of the SCMC method. The accelerated SCMC approach removes all redundant calculations from SCMC by mixing deterministic branching with Monte Carlo hops.[265]

While the SCMC[352,357] and accelerated SCMC[265] approaches provide excellent agreement for the model scattering problems (section 2.3), they are not sufficiently efficient for the simulation of large molecular systems routinely treated with surface-hopping techniques. The branching tree in Figure 7B corresponds to branching at each time step on two coupled PESs. It reveals that after two time steps, the original wavepacket has created four new packets, two on each surface. One of the two wavepackets on the lower surface has propagated adiabatically for both time steps; the other has transferred to the upper surface and returned back. While the phase space shift in these two wavepackets is infinitesimally small, the returning wavepacket has acquired a new weight and a negative sign. Both wavepackets will proceed similarly as the dynamics continues, but the change in their sign (or more generally any phase shift) leads to the inefficiency of Monte Carlo sampling.

To create a more efficient approach, we have developed the CW algorithm, where we apply a *re-Gaussianization* approximation. We assume that, since the shift in the wavepackets is infinitesimally small, after one δt, one can approximate their linear superposition by a new Gaussian function (here we assume only two functions):

$$\begin{aligned} &N_{0,a} g_{(a,a)}(\boldsymbol{R}_{1,(a,a)}, \boldsymbol{P}_{1,(a,a)}, \boldsymbol{R}, \delta t)|\chi_a(\boldsymbol{R}_{1,(a,a)})\rangle \\ &\quad + \sum_{b\neq a} N_{1,a} g_{(a,b)}(\boldsymbol{R}_{1,(a,b)}, \boldsymbol{P}_{1,(a,b)}, \boldsymbol{R}, \delta t)|\chi_a(\boldsymbol{R}_{1,(a,b)})\rangle \\ &\quad \approx \tilde{N}_1 g_a(\boldsymbol{R}_1, \boldsymbol{P}_1, \boldsymbol{R}, 0)|\chi_a(\boldsymbol{R}_1)\rangle \end{aligned} \tag{2.37}$$

$\tilde{N}_1$ is complex, containing the real weight and phase of g_a. It is found by projecting the sum of all Gaussians on a onto g_a. The new phase space center of the Gaussian, $\boldsymbol{R}_1$,$\boldsymbol{P}_1$, is chosen to be the expectation values, $\langle\boldsymbol{R}\rangle$ and $\langle\boldsymbol{P}\rangle$, of the superposition, while the new complex width is given by the moments, $\langle\boldsymbol{R}^2\rangle$ and $\langle\boldsymbol{P}^2\rangle$. Details can be found in the Supporting Information of ref 351. This leads to a coupled propagation, also represented diagrammatically in Figure 7B. This approximate *re-Gaussianization* breaks down when the overlap between the Gaussian functions in the sum in eq 2.37 becomes significantly less than 1. Thus, we propose to monitor the overlap and allow separation of the coupled wavepackets when their overlap is lower than a threshold.[351] This leads to a coarse-grained branching, as shown in Figure 7B. We have applied this method to the Model X, Figure 7D, and the 2-D well, Figure 7E, with excellent results compared to the exact solution and substantially exceeding FSSH in terms of both accuracy and computational cost.[351] For example, converged results are obtained in the models above using only tens of trajectories. More recently, we have developed an approach where all the Gaussian variables are continuously propagated rather than having discrete re-Gaussianization steps, and we utilized the Ehrenfest theorem to determine the classical trajectory: $\dot{\boldsymbol{R}}_t$ and $\dot{\boldsymbol{P}}_t$.[356] This has improved the accuracy, efficiency, and stability of the algorithm which we call Ehrenfest-plus (EP). This efficiency makes the EP algorithm feasible for realistic molecular systems, while retaining *ab initio* treatment of electronic decoherence and interference.

Methods based on the time-dependent variational principle (section 2.5.4) and the SCMC, CW, or EP approaches are all based on the propagation and generation of Gaussian wavepackets, but their differences should be elucidated. To summarize, the approach of the SCMC/CW methods is to

https://dx.doi.org/10.1021/acs.chemrev.9b00447
Chem. Rev. 2020, 120, 2215−2287

generate an approximate wavefunction, which is the sum of Gaussian functions, by best approximating the EOM for those functions in correspondence with quantum dynamics in a local harmonic approximation. Thus, the simulated wavefunction is a direct sum of complex Gaussian functions, without the *a priori* assumption that the particular set of functions creates a complete basis. The dynamics are not forced to be unitary, thus total probability is only conserved in a converged simulation. The Gaussian methods discussed earlier such as AIMS, AIMC, and MCE, (section 2.5.4) involve the solution of the exact TDSE in the basis of moving Gaussian functions. However, the accuracy of the exact Schrödinger solution is limited by the completeness of the basis. In practice, it is impossible to obtain a fully complete basis, leading to error in the simulated wavefunction. However, dynamics are unitary and total probability is conserved, but not necessarily correct. The EP is a compromise between these two, using unitary electronic dynamics, and an optimized nuclear equation of motion, but independently propagating after separation of the wavepackets.[356] Generally, one approach is not preferable over the others in every case, and one should keep the differences in mind and apply the most appropriate approximation based on available computational resources and any available information on the PESs. For example, if the number of crossings is known to be small, then a branching based method (AIMC, CW, EP, AIMS) would be desirable. If there are many crossings, a stochastic approach such as SCMC would likely be preferable. If correlations are present, but weak, then MCE may be suitable and simpler. If the dynamics inside a non-adiabatic coupling region are of particular interest, the EP may be preferable over AIMC/AIMS since it includes beyond mean-field terms in the force due to non-adiabatic coupling.

3. PRACTICAL COMPUTATIONAL IMPLEMENTATION OF NON-ADIABATIC EXCITED-STATE MOLECULAR DYNAMICS

3.1. Electronic Excitations and Potential Energy Surfaces from TD-SCF Methods

Electronic structure calculations have been the bedrock of quantum chemistry for many years. Building from the BO approximation, electronic structure methods seek to solve the time-independent electronic Schrödinger equation, eq 2.4, for a given configuration of nuclei, $\boldsymbol{R}$. This provides a single point (energy) and a respective wavefunction of an adiabatic state for a multidimensional PES in the space of $\boldsymbol{R}$. The NAMD simulations require calculations of energies, $E_a(\boldsymbol{R})$, of multiple PESs (a manifold of electronic states here labeled with index a), gradients (or forces), $\frac{\partial E_a(\boldsymbol{R})}{\partial \boldsymbol{R}}$, for at least one (or more) PES, and a matrix of NACRs, $\boldsymbol{d}_{ab}(\boldsymbol{R})$ (eq 2.6). For practical NAMD implementations, these quantities are required to be calculated on-the-fly to enable running dynamical trajectories. The calculation of forces and NACRs are frequently done with an analytic gradient method (as opposed to the much slower numerical differentiation) to be exemplified in section 3.1.3. Altogether, energies, gradients, and NACRs typically suffice as an input to the basic NAMD algorithms such as Ehrenfest (section 2.2.1) and surface hopping (section 2.2.2). Other algorithms briefly discussed in section 2 (frequently methods accounting for decoherence corrections) require the Hessian matrix (the derivative of gradients $\frac{\partial^2 E_a(\boldsymbol{R})}{\partial^2 \boldsymbol{R}}$), which may increase numerical cost.

One of the simplest and earliest approaches for ground-state electronic structure is the Hartree−Fock (HF) approximation,[358] which laid the foundation for so-called single-reference *ab initio* methods. These methods use a single Slater determinant to describe the many-body electronic wavefunction and solve for the self-consistent field (SCF) (or mean field) potential acting on an electron from the other charges. Despite known issues with these methods, they have found widespread use thanks to their ability to describe a variety of chemical systems. Where single-reference *ab initio* methods fail, higher-order electronic correlation effects can be included in a systematic way by using a variety of methods, such as Møller−Plesset perturbation theory[359−364] or coupled-cluster theory[365−370] (these high accuracy wavefunction methodologies are outside of the scope of the present Review).

On the other hand, it is, in principle, possible to form an exact electronic structure description using DFT[371−379] based on a single reference Slater determinant, but practical calculations require approximating the exact exchange-correlation functional.[380−382] Such DFT formulation in the Kohn−Sham (KS) form[372,383] is convenient due to the use of numerical procedures similar to HF, and has become the most widely used electronic structure method in quantum chemistry because of its speed and reasonable compromise for accuracy. Further numerical efficiency toward larger systems is accessible using a family of parametrized reduced tight-binding-like single-reference methods such as DFTB,[384−389] or semiempirical methods.[11,13,390−393] These methods allow calculations on the order of 10,000 atoms to be performed for static structures[394] or permit long time scale dynamics simulations of molecules in the range of up to 1000 atoms.[395,396]

Simulations of electronically excited states can subsequently follow the ground-state SCF calculations, for example, in the form of configuration interaction (CI) methods.[358,397−399] Among the most popular and numerically accessible approaches for calculating excited-state PESs and optical responses of large molecules is a family of TD-SCF methods,[6,400−402] ranging from TD-HF to TD-DFT. The TD-SCF approach can be formulated using classical dynamics with EOMs for the density matrix satisfying the Hamilton−Liouville form.[403] We further exemplify how the basic ingredients for NAMD simulations can be obtained for TD-SCF methodologies.

3.1.1. SCF Methods for Ground-State Calculations. SCF methods, including HF, DFT (commonly in the KS form), and various semiempirical methods, solve for a single Slater determinant of a system of non-interacting electrons. Here, the electronic Schrödinger equation for a given configuration of nuclei, $\boldsymbol{R}$, can be written as an eigenproblem (we will further omit the parametric dependence of functions and operators on $\boldsymbol{R}$ for brevity):

$$\hat{\boldsymbol{F}}(\hat{\boldsymbol{\rho}})\boldsymbol{\theta} = \lambda\boldsymbol{\theta} \tag{3.1}$$

The quantities calculated are the single-electron molecular orbitals (MO) $|\theta_i\rangle$, MO energies λ_i, and i is the MO index. These values are calculated self-consistently using the HF or KS Hamiltonian matrix $\hat{\boldsymbol{F}}(\hat{\boldsymbol{\rho}})$, given as

$$\hat{\boldsymbol{F}}(\hat{\boldsymbol{\rho}}) = \hat{\boldsymbol{t}} + \hat{\boldsymbol{V}}(\hat{\boldsymbol{\rho}}) \tag{3.2}$$

where $\hat{\boldsymbol{\rho}} = \sum_{i\in\mathbf{occ}}|\theta_i\rangle\langle\theta_i|$ is the ground-state single-electron density matrix obtained from MOs by summing over the occupied space. Here and throughout this Review, an orthogonal atomic orbital (AO) basis is assumed. This could

https://dx.doi.org/10.1021/acs.chemrev.9b00447
Chem. Rev. 2020, 120, 2215−2287

be performed, for instance, by the Löwdin decomposition of the overlap matrix $\hat{\mathbf{S}}$.[404]

In eq 3.2, the elements of $\hat{\boldsymbol{t}}$ are one-electron integrals accounting for the kinetic energy and nuclear attraction of an electron.[358] The elements of the Coulomb operator $\hat{\boldsymbol{V}}(\hat{\boldsymbol{\rho}})$ acting on an arbitrary density matrix $\hat{\boldsymbol{\rho}}$ are generally given by

$$\boldsymbol{V}(\hat{\boldsymbol{\rho}}) = \boldsymbol{J}(\hat{\boldsymbol{\rho}}) - \boldsymbol{K}(\hat{\boldsymbol{\rho}}) + \boldsymbol{V}^{\mathrm{xc}}(\hat{\boldsymbol{\rho}}) \tag{3.3}$$

where $\boldsymbol{V}^{\mathrm{xc}}(\hat{\boldsymbol{\rho}})$ is the exchange-correlation potential from KS-DFT in the matrix form[405] and the Hartree and exchange terms are represented as

$$J_{ij\sigma}(\hat{\boldsymbol{\rho}}) - K_{ij\sigma}(\hat{\boldsymbol{\rho}}) = \sum_{kl\sigma'} (ij\sigma|kl\sigma')\rho_{kl\sigma'} - C_x(ik\sigma|jl\sigma')\rho_{kl\sigma}\delta_{\sigma\sigma'} \tag{3.4}$$

The parameter C_x allows mixing of pure KS-DFT and HF theories, e.g., in the case of Becke's hybrid functionals.[406] The indices i, j, k, l refer to the orbital spatial indices (running up to the number of basis functions N), and σ refers to the spin index. $(ij\sigma|kl\sigma')$ are conventional two-electron integrals representing the Coulombic interaction.[405]

The HF theory assumes $\boldsymbol{V}^{\mathrm{xc}}(\hat{\boldsymbol{\rho}}) = 0$ and $C_x = 1$. The key approximation in KS-DFT ($C_x = 0$) is the form of $\hat{\boldsymbol{V}}^{\mathrm{xc}}(\hat{\boldsymbol{\rho}})$, which is not known exactly. The first approximation used was the local density approximation (LDA), which applied the free electron gas to give expressions for exchange and correlation in $\hat{\boldsymbol{V}}^{\mathrm{xc}}(\hat{\boldsymbol{\rho}})$.[382,407] Another important approximation is the generalized gradient approximation (GGA).[374,381,408] The original DFT models still show widespread use, both in their pure form for periodic systems, and as components for more complex approximations. For example, approximations for molecular systems now combine LDA and GGA with HF exchange in various ratios to form so-called hybrid functionals. Notable examples of hybrid functionals are B3LYP (Becke's exchange functional with 20% HF exchange ($C_x = 0.2$) paired with Lee, Yang, and Parr's functional for correlation)[406] and PBE0 (the Perdue, Becke, and Ernzerhof functional coupled with $C_x = 0.25$).[409] These functionals provide results that are in excellent agreement with experimental quantities for a wide spectrum of chemical systems.[410−412] A well-known problem with DFT is electronic over-delocalization and the appearance of spurious charge-transfer states.[413−415] This has been addressed using long-range corrected functionals,[416,417] which offer improved accuracy for the calculation of spectroscopic properties and excited states, and range-separated functionals,[418−421] where the fraction of HF exchange (C_x) varies depending on the distance.

While many hybrid functionals rely on some semiempirical parametrization (such as B3LYP), another class of methods involves empirically approximated $\hat{\boldsymbol{t}}$ and $\hat{\boldsymbol{V}}(\hat{\boldsymbol{\rho}})$, eq 3.3. Popular semiempirical parametrizations are AM1, PM3, PM5, ZINDO, and a number of other varieties.[11,13,390−392,422,423] These methodologies typically severely truncate the four-index tensor of the two-electron integrals, $(ik\sigma|jl\sigma')$, so that this array effectively becomes 2-D and can fit in the computer memory. For example, the AM1 model originally parametrized for ground-state properties[11] has been extensively used for ESMD methods of conjugated molecules and provided reasonably accurate results.[424,425] DFTB is another family of methods that uses a tight-binding approximation effective reduced representation derived from DFT models.[384−389] Both methods allow for large calculations to be performed with less memory and higher speed. Finally, we note that linear-scaling SCF methods have been extensively developed over the past decades enabling access to larger systems.[426,427]

The total electron energy of the molecule in the SCF methods is $E_{\mathrm{el}} = \mathrm{TR}[(\hat{\boldsymbol{t}} + \hat{\boldsymbol{F}}(\hat{\boldsymbol{\rho}}))\hat{\boldsymbol{\rho}}]$, where the trace includes both spatial and spin variables. To calculate $\hat{\boldsymbol{\rho}}$ and E_{el} self-consistently, $\hat{\boldsymbol{F}}(\hat{\boldsymbol{\rho}})$ is prepared with trial $\hat{\boldsymbol{\rho}}$, and $|\theta\rangle$'s are calculated using eq 3.1. A new $\hat{\boldsymbol{\rho}}$ is used to prepare a new iteration of $\hat{\boldsymbol{F}}(\hat{\boldsymbol{\rho}})$. This cycle is repeated until a convergence criterion is achieved for $\hat{\boldsymbol{\rho}}$ and E_{el}. Thus, the SCF iterations converge toward solution $\hat{\boldsymbol{\rho}}_{\mathrm{g}}$, with $[\hat{\boldsymbol{F}}(\hat{\boldsymbol{\rho}}_{\mathrm{g}}),\hat{\boldsymbol{\rho}}_{\mathrm{g}}] = 0$, where square parentheses denote the Fermionic anticommutator of two matrices. E_{el} obeys the variational principle, establishing convergence of the energy toward a lower limit of the true electronic energy. For both HF and KS theories or their hybrid mixtures, it ensures that the wavefunction and charge density are variational quantities.[372] In particular, owing to the variational principle, the gradients of the mean-field ground-state energy, $E_{\mathrm{el}} = \mathrm{Tr}[(\hat{\boldsymbol{t}} + \hat{\boldsymbol{F}}(\boldsymbol{\rho}_g))\boldsymbol{\rho}_g]$, become (for derivation see Appendix C in ref 358)

$$\frac{\partial E_{\mathrm{el}}}{\partial \boldsymbol{R}} = \frac{1}{2}\mathrm{Tr}\left[\left(\frac{\partial \hat{\boldsymbol{t}}}{\partial \boldsymbol{R}} + \frac{\partial \hat{\boldsymbol{F}}(\hat{\boldsymbol{\rho}}_g)}{\partial \boldsymbol{R}}\right)\hat{\boldsymbol{\rho}}_g\right] \tag{3.5}$$

The derivatives of $\hat{\boldsymbol{t}}$ and $\hat{\boldsymbol{F}}(\hat{\boldsymbol{\rho}}_{\mathrm{g}})$ with respect to the nuclear degrees of freedom apply only to the matrix elements of one-electron and two-electron operators (eqs 3.2−3.4), which are routinely calculated in all quantum-chemical packages. This exemplifies the analytic gradient method (as opposed to slower numerical differentiation) where the energy gradients are expressed in terms of derivatives of the Hamiltonian matrix elements and thus bypassing differentiation of other quantities such as the density matrix $\hat{\boldsymbol{\rho}}_{\mathrm{g}}$. The total ground-state energy is $E_0(\boldsymbol{R}) = E_{\mathrm{el}}(\boldsymbol{R}) + E_{\mathrm{nuc}}(\boldsymbol{R})$, where the latter term is the Coulombic energy of nuclear repulsion, which is calculated straightforwardly. Thus, the solution of the SCF equations provides the ground-state PES, $E_0(\boldsymbol{R})$, and its gradients, $\frac{\partial E_0}{\partial \boldsymbol{R}}$.

3.1.2. Excited Electronic States within Linear Response Formalism. Calculation of excited electronic states is a subsequent step following the SCF ground-state procedure in the family of single-reference methods. Among the simple and practical techniques able to account for electronic correlation effects present in excited states (such as excitonic effects) are the Configuration Interaction Singles (CIS) and the TD-HF theory.[428] The respective DFT analogs are the Tamm−Dancoff approximation (TDA) and TD-DFT methods.[429] All these approaches are flavors of the TD-SCF method, which computes dynamics of the single-electron density matrix of the system subject to an external perturbation.[430] The working equations of TD-SCF methods in the frequency domain are variations of the random-phase approximation (RPA) eigenvalue equations, which involve finding the eigenvalues of a tetradic matrix (the flattened Liouville super-operator $\hat{\boldsymbol{L}}$) of dimension $N^2 \times N^2$, where N is the number of basis functions:[430]

$$\hat{\boldsymbol{L}}\xi = \Omega\boldsymbol{\xi} \tag{3.6}$$

Here $\boldsymbol{\xi}$ is the TDM mapped to a vector $\hat{\boldsymbol{\xi}}$; see discussion below in section 3.1.2. The action of an operator $\hat{\boldsymbol{L}}$ on an arbitrary matrix $\hat{\boldsymbol{x}}$ is defined as

$$\hat{\boldsymbol{L}}(\hat{\boldsymbol{x}}) = [\hat{\boldsymbol{F}}(\hat{\boldsymbol{\rho}}_g), \hat{\boldsymbol{x}}] + [\hat{\boldsymbol{G}}(\hat{\boldsymbol{x}}), \hat{\boldsymbol{\rho}}_g] \tag{3.7}$$

where $\hat{\boldsymbol{F}}(\hat{\boldsymbol{\rho}}_{\mathrm{g}})$ is given by eqs 3.2−3.4, and the operator $\hat{\boldsymbol{G}}(\boldsymbol{x})$ is defined as (compare to eq 3.4)

https://dx.doi.org/10.1021/acs.chemrev.9b00447
Chem. Rev. 2020, 120, 2215−2287

$$G_{ij\sigma}(\hat{\boldsymbol{x}}) = J_{ij\sigma}(\hat{\boldsymbol{x}}) - K_{ij\sigma}(\hat{\boldsymbol{x}}) + \sum_{kl\sigma'} f_{ij\sigma,kl\sigma'} x_{kl\sigma'} \tag{3.8}$$

Here, $f_{ij\sigma,kl\sigma'}$ is a functional derivative of $\hat{\boldsymbol{V}}^{xc}(\hat{\boldsymbol{\rho}}_g$ with respect to the density projected to a given basis. The formal numerical cost of diagonalizing the RPA matrix scales as $O(N^6)$, but effective Krylov subspace algorithms and iterative diagonalization techniques have been developed.[431,432] This allows for efficient calculation of the lower portion of the eigenspectrum of the RPA matrix necessary for modeling electronic excitations. Recently, methods have been developed to determine various eigenbands of the matrix, allowing for calculations of a selective excitation range.[433] Overall, standard computation of excited-state properties for molecular systems (e.g., excitation energies, spectra, and hyperpolarizabilities)[401] are numerically efficient with $O(N^2) - O(N^4)$ complexity. Sparse matrix algebra has been used to provide $O(N)$ scaling for excited-state calculations in the AO basis.[401]

Conventionally, the RPA eigenvalue problem is solved in the MO representation,[430]

$$\begin{pmatrix} \hat{\boldsymbol{A}} & \hat{\boldsymbol{B}} \\ -\hat{\boldsymbol{B}} & -\hat{\boldsymbol{A}} \end{pmatrix} \begin{pmatrix} \boldsymbol{X} \\ \boldsymbol{Y} \end{pmatrix} = \Omega \begin{pmatrix} \boldsymbol{X} \\ \boldsymbol{Y} \end{pmatrix} \tag{3.9}$$

The submatrices $\hat{\boldsymbol{A}}$ and $\hat{\boldsymbol{B}}$ are fourth-order tensors flattened to matrices; i.e., they have a super-operator structure defined on the Liouville space $(N_{occ}N_{virt}) \times (N_{occ}N_{virt})$, where N_{occ} and N_{virt} denote the Hilbert spaces of occupied and virtual MOs, respectively, with $N = N_{occ} + N_{virt}$. The tetradic elements of these matrices can always be chosen to be real. They are given in the canonical MO basis as[430]

$$A_{ik\sigma,jl\sigma'} = (\lambda_{k\sigma} - \lambda_{i\sigma})\delta_{ij}\delta_{kl}\delta_{\sigma\sigma'} + (ik\sigma|jl\sigma') + f_{ik\sigma,jl\sigma'} - C_x(kl\sigma|ij\sigma')\delta_{\sigma\sigma'} \tag{3.10}$$

$$B_{ik\sigma,jl\sigma'} = (ik\sigma|jl\sigma') + f_{ik\sigma,jl\sigma'} - C_x(jk\sigma|il\sigma')\delta_{\sigma\sigma'} \tag{3.11}$$

where indices $i,j(k,l)$ run over occupied (virtual) MOs. In eq 3.9, the matrices $\hat{\boldsymbol{A}}$ and $\hat{\boldsymbol{B}}$ are Hermitian. The matrix $\hat{\boldsymbol{A}}$ is identical to the CIS matrix, being diagonally dominant for typical molecules. When neglecting $\hat{\boldsymbol{B}}$, diagonalization of $\hat{\boldsymbol{A}}$ gives the CIS excitation energies for a HF approach, while for DFT methodologies, it is known as the TDA.[429] The first term of $\hat{\boldsymbol{A}}$ in eq 3.10 gives a zeroth-order approximation to the excitation energies as the differences between the single-particle excitation energies, i.e., differences between MO eigenvalues from HF or KS. The rest of the elements of $\hat{\boldsymbol{A}}$ and $\hat{\boldsymbol{B}}$ are additional Coulomb and exchange-correlation terms.

The $\boldsymbol{X}_a$ and $\boldsymbol{Y}_a$ in eq 3.9 are, respectively, the particle−hole (ph) and hole−particle (hp) interband components of the TDM $\boldsymbol{\xi}_a$ for a given eigenstate a. We will use the TDM extensively for analysis of properties of electronic excitations (see section 3.5). For now, we will give its matrix form in MO representation as

$$\hat{\boldsymbol{\xi}}_a = \begin{bmatrix} 0 & \hat{\boldsymbol{Y}}_a \\ \hat{\boldsymbol{X}}_a & 0 \end{bmatrix} \tag{3.12}$$

where $\hat{\mathbf{X}}_a$ and $\hat{\mathbf{Y}}_a$ (tensorially mapped to arrays $\boldsymbol{X}_a$ and $\boldsymbol{Y}_a$) are $N_{occ}\times N_{virt}$ and $N_{virt}\times N_{occ}$ matrices, respectively. The eigenvectors $\boldsymbol{\xi}_a$ are normalized as

$$\langle\hat{\boldsymbol{\xi}}_a|\hat{\boldsymbol{\xi}}_b\rangle = \mathrm{Tr}(\hat{\boldsymbol{\rho}}_g\,[\hat{\boldsymbol{\xi}}_a^{\mathrm{T}}\hat{\boldsymbol{\xi}}_b]) = \delta_{ab} \tag{3.13}$$

where superscript T stands for transpose matrix, square parentheses denote Fermionic anticommutator of two matrices, and δ is a Kronecker delta. The TDM, $\hat{\boldsymbol{\xi}}_a$, between the ground state and ath excited state is representative of a family of single-electron density matrices,

$$(\pi_{ab})_{ij} = \langle\psi_a|c_i^\dagger c_j|\psi_b\rangle \tag{3.14}$$

where indices a and b label the adiabatic electronic eigenstates of the system (solutions of the static electronic Schrödinger equation, eq 2.4), and indices i and j run over the basis functions. c and $c^\dagger$ are the electron creation and annihilation operators, respectively. Thus, $\hat{\boldsymbol{\pi}}_{00} = \hat{\boldsymbol{\rho}}_g$ is the ground-state density matrix, $\hat{\boldsymbol{\pi}}_{aa}$ is the density matrix of the ath excited state, $\hat{\boldsymbol{\pi}}_{0a} = \hat{\boldsymbol{\xi}}_a$ is a TDM corresponding to the $|\psi_0\rangle\rightarrow|\psi_a\rangle$ electronic transition, and the rest $\hat{\boldsymbol{\pi}}_{ab}$ are TDMs between excited states. Notably, for the majority of molecules, the $\boldsymbol{X}$ component (originating from the prevailing CIS term) in the TDM dominates because elements of $\hat{\boldsymbol{B}}$ represent higher-order electronic correlations and their magnitudes are small compared to those of matrix $\hat{\boldsymbol{A}}$. Consequently, the CIS or TDA ($\hat{\boldsymbol{B}} = 0$, $\hat{\boldsymbol{Y}} = 0$ in eq 3.9) is considered a good approximation for computing excited states and is widely used as a simplification for the original RPA problem.

To this end, the solution of the RPA eigenproblem (eq 3.9) results in a manifold of excited states with transition energies, $\Omega_a(\boldsymbol{R})$, and their respective TDMs, $\hat{\boldsymbol{\xi}}_a(\boldsymbol{R})$, for a given nuclear geometry, $\boldsymbol{R}$. The excited-state energies are determined as $E_a(\boldsymbol{R}) = E_0(\boldsymbol{R}) + \Omega_a(\boldsymbol{R})$.

3.1.3. Excited-State Gradients and Non-adiabatic Couplings. Finally, energy gradients (forces) and NACs in TD-SCF methods are the remaining ingredients for NAMD techniques,[434,435] which can also be calculated analytically. A detailed formalism for calculating these quantities is involved, and it has become the subject of numerous technical reports.[434−442] Here, we provide only an outline and ideas of numerical procedures developed for this purpose.

Analytic gradients require a variational formulation for the excited-state energy.[443−445] In TD-SCF methods, the excited-state energy is formally not a variational quantity with respect to the ground-state density matrix, $\hat{\boldsymbol{\rho}}_g$. A variational formalism for the excited-state energy[446] introduces the difference density matrix, $\boldsymbol{\delta\hat{\rho}}_{aa}$, which being added to $\hat{\boldsymbol{\rho}}_g$ results in the excited-state density matrix $\hat{\boldsymbol{\rho}}_{aa} = \hat{\boldsymbol{\rho}}_g + \boldsymbol{\delta\hat{\rho}}_{aa}$ for state a. The difference density matrix $\boldsymbol{\delta\hat{\rho}}_{aa} = \hat{\boldsymbol{T}}_{aa} + \hat{\boldsymbol{Z}}_{aa}$ consists of so-called unrelaxed $\hat{\boldsymbol{T}}_{aa}$ and relaxed $\hat{\boldsymbol{Z}}_{aa}$ components determined using Lagrange multipliers in a free energy functional. For example, the unrelaxed density matrix $\hat{\boldsymbol{T}}_{aa}$ can be calculated as[403]

$$\hat{\boldsymbol{T}}_{aa} = \frac{1}{2}[[\hat{\boldsymbol{\xi}}_a^{\mathrm{T}}, \hat{\boldsymbol{\rho}}_g], \hat{\boldsymbol{\xi}}_a] \tag{3.15}$$

where intraband particle−particle (pp) and hole−hole (hh) components $\hat{\boldsymbol{T}}_{aa}^{pp}$ and $\hat{\boldsymbol{T}}_{aa}^{hh}$ are $N_{occ}\times N_{occ}$ and $N_{virt}\times N_{virt}$ matrices, respectively. The unrelaxed part is calculated with the $\boldsymbol{Z}$-vector matrix equation (not shown) after the excitation energies have been calculated.[403,446,447] Overall, this adds a relatively minor numerical cost compared to solution of RPA eq 3.6 or 3.7. Provided calculated difference density matrix $\boldsymbol{\delta\hat{\rho}}_{aa}$, the gradients of the transition energy $\Omega_a(\boldsymbol{R})$ for state a in the orthogonal basis can be calculated as[447]

https://dx.doi.org/10.1021/acs.chemrev.9b00447
Chem. Rev. 2020, 120, 2215−2287

$$\frac{\partial \Omega_a(\boldsymbol{R})}{\partial \boldsymbol{R}} = \mathrm{Tr}\left[\frac{\partial \hat{\boldsymbol{F}}(\hat{\boldsymbol{\rho}}_g)}{\partial \boldsymbol{R}}\hat{\boldsymbol{\rho}}_{aa}\right] + \mathrm{Tr}\left[\frac{\partial \hat{\boldsymbol{V}}(\hat{\boldsymbol{\xi}}_a^{\mathrm{T}})}{\partial \boldsymbol{R}}\hat{\boldsymbol{\xi}}_a\right] \tag{3.16}$$

where $\frac{\partial \hat{\boldsymbol{F}}(\hat{\boldsymbol{\rho}}_g)}{\partial \boldsymbol{R}}$ and $\frac{\partial \hat{\boldsymbol{V}}(\hat{\boldsymbol{\xi}}_c^{\mathrm{T}})}{\partial \boldsymbol{R}}$ are derivatives of the Fock and Coulomb Hamiltonian matrix elements defined by eqs 3.2 and 3.3 with respect to the nuclear degrees of freedom, similar to the case for ground-state gradients in eq 3.5.

As discussed in section 2.1, the NACRs, $\boldsymbol{d}_{ab}(\boldsymbol{R}) = \langle \psi_a(\boldsymbol{r},\boldsymbol{R})|\nabla_{\boldsymbol{R}}|\psi_b(\boldsymbol{r},\boldsymbol{R})\rangle_{\boldsymbol{r}}$ (eqs 2.5 and 2.6), describe the mixing of two *adiabatic* wavefunctions due to vibrational nuclear motions. NACRs are the final essential ingredient for NAMD simulations. Propagating dynamical trajectories, such as solving the TDSE (using Ehrenfest eqs 2.17 and 2.19), frequently requires computing only the time-dependent NACT scalars, $\dot{\boldsymbol{R}}_t \cdot \boldsymbol{d}_{ab}(\boldsymbol{R}) = \left\langle \psi_a(\boldsymbol{r},\boldsymbol{R})\middle|\frac{\partial}{\partial t}\middle|\psi_b(\boldsymbol{r},\boldsymbol{R})\right\rangle_{\boldsymbol{r}}$. Notably, both NACR and NACT values can be calculated directly from the overlaps of the adiabatic electronic wavefunctions (finite difference approach).[448,449] While seemingly straightforward, such an approach requires careful evaluation of the overlap of formal excited-state wavefunctions related to TDMs. Additionally, it needs to account for rotation of the atomic basis (Pulay forces).[450] Alternatively, a route similar to that which is used for gradients can be applied for NACR and NACT which leads to analytic techniques. Calculating NACs analytically in TD-SCF approaches, where there are no explicit wavefunctions, is challenging. The first step is calculation of TDMs between excited states a and b, $\hat{\boldsymbol{\pi}}_{ab} = \hat{\boldsymbol{T}}_{ab} + \hat{\boldsymbol{Z}}_{ab}$, which has unrelaxed $\hat{\boldsymbol{T}}_{ab}$ and relaxed $\hat{\boldsymbol{Z}}_{ab}$ components. Similar to the calculation of state density matrices, the unrelaxed component is given by $\hat{\boldsymbol{T}}_{ab} = \frac{1}{2}[[\hat{\boldsymbol{\xi}}_a^{\mathrm{T}}, \hat{\boldsymbol{\rho}}_g], \hat{\boldsymbol{\xi}}_b]$, whereas calculation of the relaxed component is numerically involved and $\hat{\boldsymbol{Z}}_{ab}$ can be determined using a variety of techniques and different approximations.[401,439,451−453] For example, in our group we have been using an approximate expansion of $\hat{\boldsymbol{Z}}_{ab}$ into a set of ground- to excited-state TDMs $\boldsymbol{\xi}$ derived from the nonlinear optical response formalism.[401,454−456]

Once TDMs between excited states $\hat{\boldsymbol{\pi}}_{ab}$ are known, analytic NACRs and NACTs in the TD-SCF approaches can be represented in the Hellmann−Feynman form, given in the orthogonal orbital basis as[401,435]

$$\boldsymbol{d}_{ab}(\boldsymbol{R}) = \mathrm{Tr}\left[\frac{\partial \hat{\boldsymbol{F}}(\hat{\boldsymbol{\rho}}_g)}{\partial \boldsymbol{R}}\hat{\boldsymbol{\pi}}_{ab}\right][\Omega_b(\boldsymbol{R}) - \Omega_a(\boldsymbol{R})]^{-1},$$
$$\boldsymbol{b} \neq \boldsymbol{a},\ \boldsymbol{d}_{aa}(\boldsymbol{R}) = 0 \tag{3.17}$$

$$\dot{\boldsymbol{R}}_t \cdot \boldsymbol{d}_{ab}(\boldsymbol{R}_t) = \mathrm{Tr}\left[\frac{\partial \hat{\boldsymbol{F}}(\hat{\boldsymbol{\rho}}_g)}{\partial t}\hat{\boldsymbol{\pi}}_{ab}\right][\Omega_b(\boldsymbol{R}) - \Omega_a(\boldsymbol{R})]^{-1}, \quad \boldsymbol{b} \neq \boldsymbol{a} \tag{3.18}$$

where $\frac{\partial \hat{\boldsymbol{F}}(\hat{\boldsymbol{\rho}}_g)}{\partial \boldsymbol{R}}$ and $\frac{\partial \hat{\boldsymbol{F}}(\hat{\boldsymbol{\rho}}_g)}{\partial t}$ are the derivatives of the Hamiltonian matrix elements from eq 3.2 with respect to nuclear coordinates and time, respectively.

For more details, we refer the reader to a summary of methods and considerations in computing NACs in TD-SCF methods in a review.[140] Chernyak and Mukamel were the first to show how NACs could be calculated analytically using linear response (LR) TD-SCF methods based on the Hellmann−Feynman theorem.[435,436] Practical implementations required, however, exploration of multiple aspects. Initially, the focus has been on computing couplings between the ground and excited states, for which expressions exist and have continued to be developed both for the plane-wave pseudopotential[457] and AO basis.[458] More recently, the analytic form for NACs between excited states has been derived for TD-DFT,[459,460] thus allowing further research in areas of photochemistry and photoexcitation dynamics that involve excited state-to-excited state transitions. For example, Furche and co-workers have performed FSSH simulations using atom-centered Gaussian basis sets coupled with hybrid TD-DFT methods. They successfully demonstrated the approach to model photochemical reactions in several large molecular systems.[10] Unlike the plane-wave basis sets, computing the exact gradients and NACs using the local basis set requires Pulay corrections[435] to account for the coordinate dependence of the basis functions. The translational and rotational variance of the NAC matrix elements[461] is another important consideration. The absence of translational invariance, previously dealt with using electron translation factors that impose a fixed reference origin for each electronic state,[462] has been solved by Subotnik and co-workers who realized that ignoring all matrix elements involving the antisymmetrized derivative of the overlap matrix recovers translational invariance and momentum conservation during dynamics.[463] Thus, the need for accurate NACs in TD-SCF has been recognized and is now essentially solved.

3.2. Solvation Effects in Excited-State Dynamics

Another important aspect in NAMD simulations of realistic molecular systems are the interactions of the system with a dielectric or solid-state environment. Possible interactions between the solute and solvent include charge-transfer, dispersion, polarization, and Coulombic interactions.[464,465] Solvent can have a drastic effect on optical properties and photoexcited dynamics of molecular chromophores,[466,467] yet modeling the excited-state properties of solute−solvent systems remains a difficult task for quantum chemistry.[468] Here, we are concerned with modifications of excited-state energies, their gradients, and the respective NACs due to presence of the dielectric environment. A full QM treatment of a solute in a solvent is prohibitively expensive for most methods. Therefore, models of reduced complexity have been used to describe the solvent or other environment. In general, these approaches can be divided into two classes, namely implicit and explicit solvation models.

In the continuum (implicit) approach, the solute is modeled as a system embedded in a dielectric cavity.[469] The system-environment interaction is then mediated by an environment dielectric constant. Consequently, the Coulomb interactions in the solute Hamiltonian are effectively screened by the cavity polarization caused by the solute charge density. The dielectric continuum model has the added advantage of being an effective average over solvent configurations. This averaging is reflective of most experimental measurements and would otherwise need to be performed by simulating multiple distinct molecular configurations. Across many variations of implicit solvent models,[469−472] the most popular is the polarizable continuum model (PCM) which uses a self-consistent reaction field to determine the ideal cavity charges.[472] A numerically less expensive scheme is the conductor-like polarizable continuum model (CPCM)[471] frequently denoted as the conductor-like

https://dx.doi.org/10.1021/acs.chemrev.9b00447
Chem. Rev. 2020, 120, 2215−2287

screening model (COSMO),[473] where the cavity charges are determined directly from a single system of linear equations at each SCF iteration. In contrast, determining the cavity charges in PCM is more complex and computationally demanding. While numerical simulations rely on the realistic molecular cavity shape, simpler spherical or elliptical shapes (Onsager models) allow for an analytic solution for an effective solvent potential.[474,475]

In contrast, the hybrid quantum mechanics/molecular mechanics (QM/MM) approach embeds the QM part of the system into an explicit solvent or MM part described by a chosen classical force field.[476] Here, treatment of the solvent−solute interaction is conceptually similar to the implicit methods. For example, mutual polarization of QM and MM partitions requires that the solute charge density and solvent polarization terms be determined self-consistently.[477] While, numerically involved compared to PCM, the QM/MM methods are more accurate and have been taking a leading role in MD simulations for both ground and excited states.[478] The QM/MM method is also commonly used to treat large biological complexes, such as proteins, in explicit environments. In these simulations, a selected site of interest (usually a few amino acids or a chromophore) is treated at the QM level while the larger remainder of the protein is treated at the lower MM level.[479,480] For example, QM/MM strategies were recently used to study photodynamics of retinal in the presence of the surrounding opsin protein.[481] Surface hopping has also been combined with QM/MM approaches. Early work on fitting molecular mechanics valence bonding force fields to CASSCF/CASPT2 data lead to some of the first NAMD simulations using multireference electronic structure.[482−485] As computational capabilities increased, *on-the-fly* QM/MM, where a portion of the system is treated explicitly with high cost electronic structure, e.g., CASSCF, while environment is treated by a force field, have been combined with surface hopping.[486−489] When a clear system and environment separation exists, this allows for high accuracy excited-state properties with explicit treatment of solvent and environmental effects. The QM/MM NAMD method has been successfully applied to study photoinduced processes in biological chromophores and photoreceptors in their explicit native environments providing experimentally accurate modeling of spectroscopic data and vibrational coherences.[260,486,487,489−491]

Although wavefunction (many-body) variations of both implicit and explicit solvation methods exist for both ground and excited-state calculations, we seek to review their application to excited-state dynamics within TD-SCF methods.

3.2.1. Solvent Effects and Analytic Gradients in TD-SCF Methods. Overall, implicit solvation methods are well established for ground-state electronic structure calculations using SCF methods, such as HF and DFT. Here the Fock matrix $\hat{\boldsymbol{F}}(\hat{\boldsymbol{\rho}})$ of a molecule in a vacuum (eq 3.2) is modified by the addition of an effective solvent potential, $\hat{\boldsymbol{V}}_s(\hat{\boldsymbol{\rho}})$, as[492]

$$\hat{\boldsymbol{F}}_{LR}(\hat{\boldsymbol{\rho}}) = \hat{\boldsymbol{F}}(\hat{\boldsymbol{\rho}}) + \hat{\boldsymbol{V}}_s(\hat{\boldsymbol{\rho}}) \tag{3.19}$$

The operator $\hat{\boldsymbol{V}}_s(\hat{\boldsymbol{\rho}})$ describes an electrostatic interaction between the solute and solvent charge densities and is well determined within QM/MM or PCM methods. For example, it is explicitly defined in the case of the COSMO framework[473] and in the Onsager spherical cavity model with radius R, dielectric constant ε, and dipole $\hat{\boldsymbol{\mu}}$, it is given as $\hat{\boldsymbol{V}}_s(\hat{\boldsymbol{\rho}}) = \frac{\varepsilon - 1}{\varepsilon + 0.5} R^{-3} \hat{\boldsymbol{\mu}} \mathrm{Tr}(\hat{\boldsymbol{\mu}}\hat{\boldsymbol{\rho}})$. Consequently, the mean-field (solute) and reaction field (solute−solvent) solution $[\hat{\boldsymbol{F}}_{LR}(\hat{\boldsymbol{\rho}}_g), \hat{\boldsymbol{\rho}}_g] = 0$ is achieved self-consistently within the same iteration cycle.

In contrast, TD-SCF methods require both ground- and excited-state calculations (CIS, TD-DFT, etc.). Here, the mutual polarization involves the excited-state electronic density, which complicates the TD-SCF equations. Much work has gone into developing methods to take this polarization into account to achieve self-consistency between solute charge density and effective solvent potential. Developed methods involve different relationships between solvent effects in the ground state and excited states.[492−494] So far, several schemes were offered for simulating solvent effects for the excited states in TD-SCF methods. In the linear response (LR) model, the solvent is polarized by the transition density (TD).[492,495,496] It describes solvent effects for electronic excitations with permanent dipoles similar to the ground state, which have significant transition dipole moments (bright states) or higher-order transition multipoles. Here, after the completion of the ground-state SCF cycle, the modified Liouville operator $\hat{\boldsymbol{L}}_{\boldsymbol{LR}}$ is defined as[494]

$$\hat{\boldsymbol{L}}_{LR}(\hat{\boldsymbol{x}}) = [\hat{\boldsymbol{F}}_{LR}(\hat{\boldsymbol{\rho}}_g), \hat{\boldsymbol{x}}] + [\hat{\boldsymbol{G}}(\hat{\boldsymbol{x}}), \hat{\boldsymbol{\rho}}_g] + [\hat{\boldsymbol{V}}_s(\hat{\boldsymbol{x}}), \hat{\boldsymbol{\rho}}_g] \tag{3.20}$$

Similar to the isolated molecule case, the calculations within the LR formalism proceed in a two-step fashion; i.e., the ground-state SCF loop is followed by RPA diagonalization for excited states (eq 3.9). Consequently, the gradients for the excited states can be calculated in the LR scheme. For instance, analytic gradients were formulated for the LR model in TD-DFT by Scalmani et al.[492]

Despite the computational simplicity of the LR scheme, the lack of effects from the excited-state electronic density has serious drawbacks. For example, excited states with significantly different permanent dipole moments are expected to have dissimilar stabilization by a solvent. In particular, this is the case for charge-transfer excitations, for example, in organic semiconductors.[497−500] Moreover, with the LR model, the time-dependent Stokes shift and thus fluorescence solvatochromism cannot be described adequately.[501−505] Subsequently, so-called state-specific (SS) solvation models introduced by Improta et al.[501,506] allow inclusion of an excited-state polarization. This approach involves the choice of a specific state to form the solvent potential by its unique electronic density. However, upon addition of an effective potential that depends on the excited-state density of a specific electronic state to the SCF loop and the RPA eigenvalue equation, a coupled system of nonlinear equations emerges. For example, the state-specific Fock operator becomes

$$\hat{\boldsymbol{F}}_{SS}(\hat{\boldsymbol{\rho}}, \hat{\boldsymbol{\rho}}_{aa}) = \hat{\boldsymbol{F}}(\hat{\boldsymbol{\rho}}) + \hat{\boldsymbol{V}}_s(\hat{\boldsymbol{\rho}}_{aa}) \tag{3.21}$$

where $\hat{\boldsymbol{\rho}}_{aa}$ is a density matrix of the excited state of interest obtained after solving the RPA eigenproblem with the state-specific Liouville operator $\hat{\boldsymbol{L}}_{SS}$, defined as[494]

$$\hat{\boldsymbol{L}}_{SS}(\hat{\boldsymbol{x}}) = [\hat{\boldsymbol{F}}_{SS}(\hat{\boldsymbol{\rho}}, \hat{\boldsymbol{\rho}}_{aa}), \hat{\boldsymbol{x}}] + [\hat{\boldsymbol{G}}(\hat{\boldsymbol{x}}), \hat{\boldsymbol{\rho}}] + [\hat{\boldsymbol{V}}_s(\hat{\boldsymbol{x}}), \hat{\boldsymbol{\rho}}] \tag{3.22}$$

An iterative solution including the ground-state SCF and RPA eigenvalue equation to obtain both $\hat{\boldsymbol{\rho}}_g$ and $\hat{\boldsymbol{\rho}}_{aa}$ is then necessary with self-consistency occurring in the excited-state charge density and effective solvent potential. It is important to note that the variational principle of the ground-state SCF equations is not necessarily applicable when a potential dependent on the excited-state density matrix is added to the ground-state Fock or KS matrix and thus significantly complicates the calculation of

https://dx.doi.org/10.1021/acs.chemrev.9b00447
Chem. Rev. 2020, 120, 2215−2287

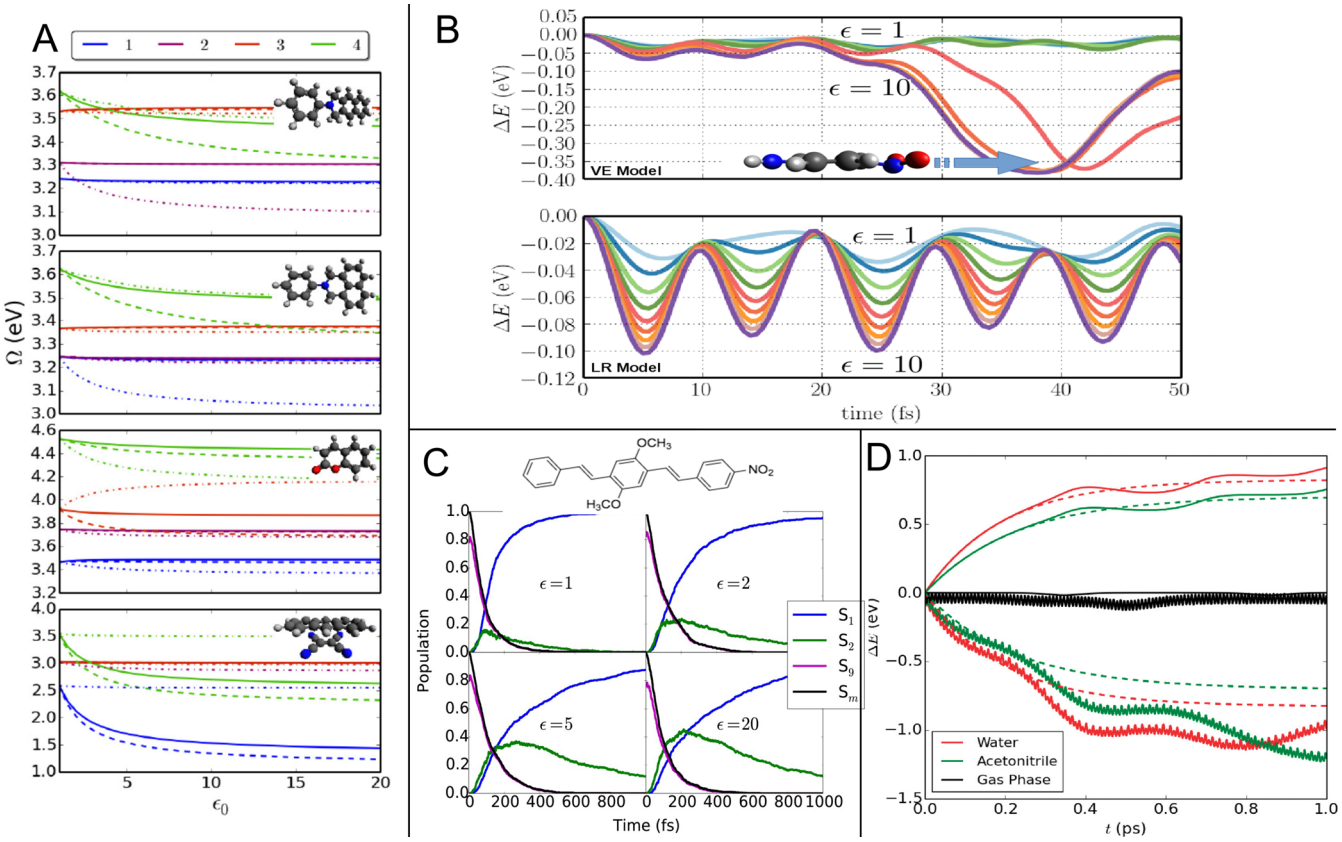

Figure 8. Demonstration of various solvent models. (A) Lowest four excitation energies (Ω) denoted with blue, purple, red, and green colors calculated using linear response (LR, dot-dash), vertical excitation (VE, dash), and state-specific (SS, solid) solvent models as a function of dielectric constant ε. For VE and SS models, each ground state-to-excited state transition is calculated using the SS charge density such that each transition is fully relaxed within the effective solvent potential for state k = 1, ..., 4. (B) Change in potential energy ΔE of the first singlet excited state during dynamics after photoexcitation for *p*-nitroaniline using VE (top) and LR (bottom) with an Onsager-type potential as a function of dielectric constant ε. (C) Time-dependent populations in non-radiative relaxation of a prototypical donor−acceptor substituted *p*-phenylene-vinylene oligomer (inset) obtained with non-adiabatic molecular dynamics simulations with LR solvent model as a function of dielectric constant ε. (D) Change in the potential energy ΔE of acetaldehyde during excited-state molecular dynamics. Solvent parameters for acetonitrile and water are used. Dashed lines correspond to frozen nuclei. Initially increasing lines correspond to post-photoemission simulations, and initially decreasing lines represent post-photoabsorption simulations. For post-photoabsorption simulations, $\Delta E = \Delta E_{es}$, while for post-photoemission simulations, $\Delta E = \Delta E_{gs}$. Panel A: Reproduced with permission from ref 494. Copyright 2015 AIP Publishing. Panel B: Reproduced with permission from ref 513. Copyright 2015 AIP Publishing. Panel C: Reproduced with permission from ref 137. Copyright 2018 American Chemical Society. Panel D: Reproduced with permission from refs 494 and 514. Copyright 2016 AIP Publishing.

gradients in this model, in practice, making it numerically intractable for analytic gradient methods.

Consequently, intermediate schemes, referred to as the vertical excitation (VE) model[507−512] and corrected linear response (cLR) model,[493] have also been developed. In the VE model, the effective solvent potential in the ground state depends only on the ground-state density matrix, but in the ground state-to-excited state transitions it depends on the excited-state density matrix.[507] Here the modified Liouville operator adopts the form[494]

$$\hat{\boldsymbol{L}}_{\mathrm{VE}}(\hat{\boldsymbol{x}}) = [\hat{\boldsymbol{F}}_{\mathrm{LR}}(\hat{\boldsymbol{\rho}}_{\mathrm{g}}), \hat{\boldsymbol{x}}] + [\hat{\boldsymbol{G}}(\hat{\boldsymbol{x}}), \hat{\boldsymbol{\rho}}_{\mathrm{g}}] + [\hat{\boldsymbol{V}}_{\mathrm{s}}(\hat{\boldsymbol{T}}_{aa}), \hat{\boldsymbol{\rho}}_{\mathrm{g}}] \tag{3.23}$$

An artificial separation of the ground- and exited-state parts of $\hat{\boldsymbol{\rho}}_{aa}$ is performed so that the SCF iterated ground-state density matrix has no dependence on the excited-state density. In addition, the relaxed $\hat{\boldsymbol{Z}}_{aa}$ component of $\hat{\boldsymbol{\rho}}_{aa}$ is neglected. The VE model can be thought of as being SS in the excitation calculation and similarly solved self-consistently with iteration only over the RPA eigenvalue equation. The cLR model is essentially a single iteration of the VE model using a relaxed excited-state density and has similar properties, but is not a self-consistent method.

Thus, in the SS approach and its approximate VE and cLR models, the solvent is polarized by the excited-state charge density. This allows modeling of energetics of charge-transfer states in comparison with excitonic electronic states with no permanent dipole moment, which cannot be achieved with LR solvation.[417,515] Moreover, the simplification introduced in the VE method restoring sequential simulations of ground and excited states in the TD-SCF methods, allows for a variational formulation and calculations of analytic gradients. The analytic gradient of the VE model was developed by Bjorgaard et al.[513] A similar formalism was further adapted and implemented in a standard TD-DFT framework by Guido et al.[516] and is used to develop analytic gradients for polarizable QM/MM simulations.[517] In addition, the analytic gradients of the VE model in equation of motion coupled-cluster theory[508] and of the SS model in a symmetry-adapted cluster-configuration interaction theory[509] have been formulated.

To exemplify performance of these models for excited states in four molecules of different polarity, Figure 8A shows

https://dx.doi.org/10.1021/acs.chemrev.9b00447
Chem. Rev. 2020, 120, 2215−2287

dependence of excitation energies as a function of the dielectric constant.[494] Here COSMO model was used with the same dielectric constant for both ground- and excited-state calculations. For example, transition 2 (top panel) and 1 (second panel from the top) exhibit solvent shifts in the LR method owing to the larger transition dipole. In contrast, transitions 1 and 4 (bottom panel) have significant solvatochromism in VE and SS models because of their large permanent-state dipole moments, and can be identified as excitations with charge-transfer character. The microcanonical dynamics (with total energy conserved) of the first excited state of *p*-nitroaniline within LE and VE models is shown in Figure 8B.[513] The molecular conformation associated with the large decrease in energy with the VE model at 40 fs appears due to out of plane bending of the nitro group. Thus, accurate simulations of fluorescence solvatochromism includes relaxation of the molecular structure on the excited-state PES and thus mandates the use of the solvation models.[497,518,519]

In NAMD simulations, NACs are affected by the solvent and are effectively "screened". A recent study reported implicit solvent effects in excited-state NAMD using the LR solvent model exemplifying modifications of the PESs and NACs.[137] The relaxation dynamics of substituted oligomers was found to be highly dependent on the solvent, and the effect increases with the polarity and electron-withdrawing strength of the substitution group. Shown in Figure 8C is the population of essential excited states in the internal conversion process using several dielectric constants. A large dielectric constant slows down the overall relaxation rate owing to the increased participation of the S_2 state in the relaxation process due to the solvent screening effect.[137] Multi-state NAMD simulations with SS-type models are yet to be studied for realistic molecular systems due to lack of analytic gradients and different SS stabilization of excited states participating in the dynamics (e.g., excitonic vs charge-transfer types of excitations). The PESs and NACs are expected to be substantially modified by solute−solvent interactions in these cases.

3.2.2. Non-equilibrium Solvent Effects. As described above, modeling excited-state dynamics in the presence of solvent may be complicated due to a formal lack of analytic gradients and different solvent stabilization for various excited states. An additional important dynamical aspect is that the solvent response is not instantaneous. When a fast process occurs in a solute, such as electronic excitation, a polar solvent will usually not reach an equilibrium with the solute on the same fast time scale. The solute−solvent system evolves in a non-equilibrium state.[502,520−522] Generally, such response of the solvent can be described by its complex dielectric permittivity, which frequently is approximated using a combination of fast and slow time scale limits. Here optical and static dielectric constants are related to the solvent response to oscillating electric fields of infinite and zero frequency, respectively.[464,465,523] This approximation, however, fails in dynamical simulations where the evolution of both solute and solvent subsystems occurs on a range of time scales, and the memory effects in the dynamic responses are present and can be important. Photoisomerization and dynamic Stokes shift in solution[497,520,521,524] exemplify solvent effects on the solute charge redistribution processes, which happen in many chemical reactions. Within explicit solvation, the solvent inherently carries information about the past configuration being rearranged by the solute. In implicit models, the solvent relaxation is frequently approximated by the Debye model based on a single exponential function.[525] Here frequency-dependent permittivity $\varepsilon(\omega)$ is given by

$$\varepsilon(\omega) = \varepsilon_\infty + \frac{\varepsilon_0 - \varepsilon_\infty}{1 + i\omega\tau_D} \tag{3.24}$$

where ε_0 and ε_∞ are the static and optical dielectric constants, respectively, and τ_D is the Debye relaxation time for a given solvent. Subsequently, the solvent reaction potential, $\mathcal{R}(t)$, induced by the time-dependent molecular charge density has a memory component, $\mathcal{R}_M(t)$, related to previous time steps expressed within a Debye model as

$$\mathcal{R}_M(t + \Delta t) = e^{-\Delta t/\tau_L}\mathcal{R}(t) \tag{3.25}$$

where the parameter $\tau_L = \tau_D\varepsilon_0/\varepsilon_\infty$ is called the longitudinal relaxation time. This introduces the effective solvent relaxation time which may have a complex interplay with NAMD time scales.

Other models generalize the solvent response to multi-exponential or nonexponential behavior such as the Cole−Davidson model.[526] Overall, derivation of the solvent reaction potential, $\mathcal{R}(t)$, is nontrivial and is subject to many approximations, which were the focus for the development of theoretical methodologies over many years.[502,522,527,528] In the context of TD-SCF methods, Ingrosso, Mennucci, and Tomasi extended these methods to a more realistic model of the solute cavity with the integral equation formalism of PCM in LR-TD-DFT.[529] Following this, Caricato et al. presented a multistep integration procedure for the same model, again with frozen nuclei.[530] Recently, Ding, Lingerfelt, Mennucci, and Li extended these methods to real-time TD-DFT simulations of electronic dynamics with the CPCM[531] while Corni, Pipolo, and Cammi formulated time-dependent solvent effects for several versions of PCM, including CPCM, and applied them to real-time TD-DFT.[532] Subsequently, the energy gradients and forces for the non-equilibrium solvent effects were formulated and applied to excited-state BOMD to model these dynamic solvent effects.[514] Figure 8D summarizes the results for the latter formalism for excited-state dynamics of acetaldehyde in the gas phase and solvents following light absorption or emission events on the lowest excited state or ground state, respectively. When the nuclei are frozen, the potential energy reaches an equilibrium on a τ_L time scale. A similar trend is seen in simulations with moving nuclei, although the signatures of vibrational modes coupled to the electronic system are pronounced.[514] Overall, a combination of SS and non-equilibrium implicit solvation models may potentially overcome the issue of the lack of SS analytic gradients by allowing the excited-state BOMD to be followed with lagging solvent response. Conducting the NAMD simulations with non-equilibrium solvation is an important future direction toward quantitative modeling of chemical dynamics in the condensed phase.

3.3. Propagation of Dynamical Trajectories in NAMD

We outlined how to obtain excited-state energies, gradients, and NACs in the framework of TD-SCF methods in section 3.1, and in the presence of dielectric environment (solvent) in section 3.2. Here, we discuss some practical numerical aspects of performing the NAMD simulations using one of the techniques described in section 2 (Ehrenfest, FSSH, MCE/AIMC, etc.). while keeping in mind the importance of comparisons with experimental spectroscopies typically probing time-evolution of an ensemble of molecular systems in a certain solvent (or solid-state) at specific thermodynamics conditions.

https://dx.doi.org/10.1021/acs.chemrev.9b00447
Chem. Rev. 2020, 120, 2215−2287

3.3.1. Initial Conditions and Thermostat. Typical NAMD simulations propagate a swarm of trajectories. This frequently addresses both the complex conformations that soft molecular structures sample at given conditions, as well as stochasticity and branching of individual trajectories common for non-adiabatic regions. Sampling of initial conditions (or phase space of initial coordinates and momenta) is thus the first step in the NAMD modeling. Different procedures can be followed to achieve this task. One way to perform such sampling is via Wigner distribution (or quantum sampling) that requires calculation of vibrational normal modes and assumes that the molecule is at its ZPE level where each vibrational degree of freedom α has energy $\hbar\omega_\alpha/2$. Another common approach is to sample the phase space from classical MD trajectories under the assumption that the system is in a thermal equilibrium with its environment. In this temperature sampling, each vibrational degree of freedom has kT energy. Typically, for room temperature, the quantum sampling has broader vibrational amplitude compared to that obtained from MD run at a given temperature.[533] The ultimate answer for a superior way to represent the initial condition for excited-state NAMD is unclear. One report[533] argues the advantage of Wigner distribution for a small molecule example. On the other hand, temperature sampling may be more exhaustive and representative for flexible molecular systems by sampling multiple metastable minima at ambient conditions. Below, we exemplify the numerical procedure for obtaining temperature sampling.

Our goal is to obtain a set of initial snapshots (coordinates and momenta) that are representative of the entire conformational space embraced by the equilibrated ensemble of molecules at given thermodynamic conditions. These can be obtained from the sufficiently long ground-state classical MD trajectories in the presence of a thermostat that accounts for simple thermal bath effects.[534] For example, in the case of the Langevin thermostat, nuclei evolve along the ground-state PES, $E_g(\boldsymbol{R}_t)$, according to constant-temperature Langevin dynamics:[535,536]

$$\hat{\boldsymbol{m}}_{\boldsymbol{R}}\cdot\ddot{\boldsymbol{R}}_t = -\nabla E_g(\boldsymbol{R}_t) - \gamma\dot{\boldsymbol{P}}_t + \boldsymbol{A}_t \tag{3.26}$$

where $\ddot{\boldsymbol{R}}_t$ is the nuclear acceleration vector. $\boldsymbol{A}_t$ is the stochastic force that depends on the bath temperature, T, and the friction coefficient, γ (ps^{-1}). Obviously, translational and rotational degrees of freedom need to be excluded in the Cartesian coordinates to consider $3N-6$ nuclear degrees of freedom. In energy-conserving dynamics (eq 2.8) or thermostat (eq 3.26) conditions, nuclear degrees of freedom are propagated using Verlet integration in a microcanonical scheme.[534]

As an alternative, different thermostat models[537−540] can be applied to the classical Newton equations to attain the desired temperature. For example, the Berendsen thermostat[541] involves the rescaling of velocities at each time step, Δt, according to a certain bath time relaxation constant, τ_T (ps^{-1}), in order to achieve a desired T_0 temperature according to

$$\dot{\boldsymbol{R}}'_t = \chi\dot{\boldsymbol{R}}_t \tag{3.27}$$

$$\chi = \left[1 + \frac{\Delta t}{\tau_T}\left(\frac{T}{T_0} - 1\right)\right]^{1/2} \tag{3.28}$$

In contrast, the Andersen thermostat[537] randomly assigns particles new velocities. It should be noted here that neither the Berendsen nor the Andersen thermostats conserve the canonical phase space ensemble[542] while the Nosé−Hoover thermostat, in contrast, does preserve such a distribution.[543]

For relatively small (10−50 atoms) and semirigid molecular systems, sufficient conformational sampling can be attained with long (typically up to 10 ns) ground-state simulations performed using the *native* electronic structure methodology to be used later for excited states. In practical terms, several such trajectories can be started in parallel from slightly different geometries and the snapshots can be further sampled every 1−10 ps after sufficient equilibration.[544] The next subsection (section 3.3.2) discusses statistical convergence of these simulations. Moreover, larger molecules with many conformational degrees of freedom may not be easily sampled with such on-the-fly ground-state dynamics. In such cases, the simulations can proceed in two steps. First, MD with classical force fields such as AMBER, CHARMM, GROMOS, OPLS, etc.[545] can be conducted to identify and sample possible PES basins corresponding to molecular conformers. Since the ground-state PES in the desired electronic structure methodology and classical force field are generally different, the molecular system should be adapted to this new level of approximation: The second step is then to run ground-state trajectories with an electronic structure code starting from the broad set of initial conformational snapshots derived from classical MD. Here the trajectories can be relatively short aiming to attain equilibrium toward collecting a snapshot. For example, this technique was applied to sample diverse ground-state conformations (Figure 9A) at ambient conditions for subsequent NAMD simulations in the case of a large dendrimer.[310,546] Moreover, the presence of directional interactions and weak bonds between the solute and solvent molecules can have significant effects on the conformational sampling. Because of that, introducing selected explicit solvent molecules is recommended. Ideally, the respective QM/MM simulations should be applied to achieve an accurate temperature sampling.

The NAMD simulations can then start after Franck−Condon excitations to the excited-state manifold using coordinates and momenta obtained from the collected snapshots. Here, a frequent initial step is to benchmark against the experimentally measured optical absorption spectrum, which can be calculated as a histogram of the excited-state energy values, obtained from each snapshot, weighted by their corresponding oscillator strengths.[547] The initial conditions for NAMD simulations are completed once the initial excited states are populated according to a laser excitation wavelength, pulse width, excited-state transition dipole moments/oscillator strengths, etc. For example, in Ehrenfest or FSSH simulations, this corresponds to assignment of the initial values of the quantum coefficients. The initial excited states can be chosen according to a Gaussian-shaped Franck−Condon window defined as

$$W_a = f_a \exp\left[\frac{-(E_{\text{laser}} - \Omega_a)^2}{2\sigma^2}\right] \tag{3.29}$$

where Ω_a and f_a represent the energy and the normalized oscillator strength of the ath excited state, respectively, E_{laser} is the central energy of a laser pulse, and σ is related to the full width at half-maximum (fwhm), defined by fwhm $= 2\sqrt{2\ln 2}\,\sigma$.

The subsequent NAMD simulations can be run either at constant energy (eq 2.8) or constant-temperature (eq 3.26). Typically, inclusion of a thermostat is critical for ground-state conformational sampling, and has less effect on the electronic energy relaxation rates in ultrafast non-radiative excited-state dynamics in large molecules.[548]

https://dx.doi.org/10.1021/acs.chemrev.9b00447
Chem. Rev. 2020, 120, 2215−2287

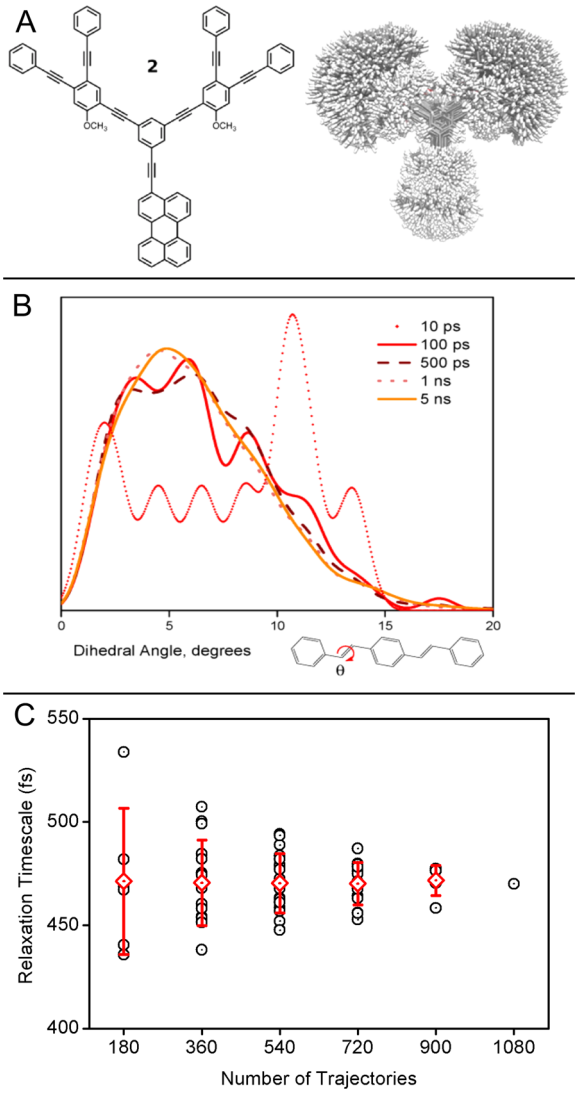

Figure 9. (A) Ground-state conformational disorder of 1000 configurations of a branched dendrimer. (B) Convergence of conformational sampling of distyrylbenzene indicated by the relative probability of torsion angles, θ, in different ensemble sizes. The distribution of initial geometries depends on the length of the sampled ground-state trajectory (shorter trajectory yields narrower ensemble). Constant 1 ps sampling interval was used in the current example. (C) Calculated internal conversion time constants for the S_1 population growth in distyrylbenzene for trajectory ensembles of different sizes. The average time constant (red pulses) and standard deviation (red bars) are shown. Panel A: Reproduced with permission from ref 549. Copyright 2015 American Chemical Society. Panels B and C: Reproduced with permission from ref 544. Copyright 2012 AIP Publishing.

3.3.2. Statistical Averages and Number of Trajectories. Propagation of the swarm of trajectories underpins many NAMD approaches (section 2). Depending on the system complexity and diversity of photoinduced pathways, a large number of trajectories may be needed for statistical averaging. The numerical cost of computing an ensemble of trajectories can impose limitations. The independent trajectory approximation featured in FSSH[234,544] (section 2.2.2) provides the advantage of running computations on multiple processors in a trivially parallelizable fashion. Dynamical trajectory cloning and dependent trajectory methods[68,346,353] (section 2.5.4) may be challenging for parallel implementation and scaling up. Here, we demonstrate convergence of the non-radiative relaxation rate toward an average value in the FSSH approach for a polyatomic molecule, where photoexcited dynamics follows a singular pathway.

An ensemble of trajectories typically reflects the initial condition including geometry distributions (molecular conformations; Figure 9A) and classical nuclear velocities, as discussed in section 3.3.1. The realistic ensemble should sample distinct distributions, including classical phase space (conformations and velocities), quantum sampling via stochasticity (divergent trajectories originating from the same phase space point but following separate paths), and an initial electronic state since more than one state can be initially populated given the finite laser pulse width. In the FSSH approach, these distributions are sampled simultaneously by starting the dynamics from different initial conditions (conformation, velocity, and excited state) and propagating trajectories in a Monte Carlo-like stochastic fashion.[74,76,437,550]

Sampling of initial conditions for molecular systems featuring shallow PESs, such as torsions and librations, is challenging.[533] For example, PPV oligomers (Figure 9B, inset) have such torsional degrees of freedom. Figure 9B exemplifies convergence of torsional angle distribution for an ensemble of ground-state MD trajectories of distyrylbenzene. In that case, the geometry sampling for soft torsional motions requires about 1000 statistically quasi-independent points (1 ns ground-state trajectory sampled at 1 ps intervals). With sufficient initial sampling, the next goal is ensuring statistical convergence of hopping distributions in the NAMD simulations. Convergence studies,[544] Figure 9C, have revealed the time scale dependence on the number of independent trajectories. Compared to the reference ensemble of 1080 trajectories, 720 trajectories are needed to reach a standard deviation of less than 2%. An ensemble of 400−500 trajectories is sufficient to reach convergence within 10−20% accuracy, which is a reasonable compromise for numerical expense. Finally, the use of less than 100 trajectories is statistically inaccurate and, at best, only qualitatively represents dynamical time scales. These studies underscore only a specific molecular example and the FSSH NAMD methodology. Different NAMD methods require different numbers of trajectories to achieve statistical convergence depending on the electronic structure methods, complexity of the system, and sampling methods. For example, such investigation for AIMC-MCE approach[349,353,354] (section 2.5.4) is yet to be done. Overall, reaching statistical convergence in terms of trajectories is an important consideration that should not be overlooked.

3.3.3. Extended Lagrangian Methods for Excited-State MD (XL-ESMD). The time step is an essential parameter in any MD simulation. A relatively large time step (typically $\Delta t \approx 0.5$ fs) can be used for the propagation of nuclei in ground-state Born−Oppenheimer molecular dynamics (BOMD) simulations. In contrast, NAMD simulations require shorter values ($\Delta t \leq 0.1$ fs) owing to steep gradients of the excited-state PESs and ultrafast electronic dynamics occurring in the non-adiabatic regions. While these issues are discussed in detail in sections 3.4.2 and 3.4.3, here we outline algorithmic tools that can potentially lower the numerical expense for MD simulations in SCF and TD-SCF methods.

Most of NAMD methodologies (section 2) involve piece-wise propagation of BO trajectories on a certain excited state. Consequently, reusing the initial guess of the ground-state

https://dx.doi.org/10.1021/acs.chemrev.9b00447
Chem. Rev. 2020, 120, 2215−2287

density matrix and excited-state TDMs to the respective iterative SCF and TD-SCF optimizations from previous time steps seems to be a practical and efficient solution. However, it is well established that for SCF (and TD-SCF) the forces are not conservative and the electronic degrees of freedom act like a heat sink or heat source. The MD propagation then has broken time-reversibility and results in unphysical energy drifts, unless very accurate convergence of the electronic ground state is reached.[552−554] Car−Parrinello molecular dynamics (CPMD) was the first approach overcoming this limitation. CPMD enabled practical ab initio MD simulations for a broad range of problems in chemistry and materials science[555−557] including some excited-state applications.[558,559] This was followed by the development of extended Lagrangian BOMD (XL-BOMD), a parameter free method lifting the CPMD limitations on the electronic steps.[560] Finally, the XL-BOMD framework was recently extended to excited-state BOMD (XL-ESMD) within TD-SCF techniques.[551]

In the XL methods, the initial guesses are not extrapolated, but rather propagated as extended degrees of freedom, allowing time-reversibility to be recovered. This is achieved by introducing the extended variables into Euler−Lagrange EOMs. Briefly, for excited-state BOMD, the Lagrangian is given by

$$\mathcal{L}^{\mathrm{ES}}(\boldsymbol{R}_t, \dot{\boldsymbol{R}}_t) = \frac{1}{2}\dot{\boldsymbol{R}}_t \cdot \hat{\boldsymbol{m}}_{\boldsymbol{R}} \cdot \dot{\boldsymbol{R}}_t - E_{\mathrm{g}}[\boldsymbol{R}_t, \hat{\boldsymbol{\rho}}_{\mathrm{g}}] - \Omega[\boldsymbol{R}_t, \hat{\boldsymbol{\rho}}_{\mathrm{g}}, \hat{\boldsymbol{\xi}}] \tag{3.30}$$

where E_{g} and Ω are ground-state and transition energies, respectively, depending on nuclear coordinates, $\boldsymbol{R}_t$. The ground-state density matrix is $\hat{\boldsymbol{\rho}}_g$, and the TDM is $\hat{\boldsymbol{\xi}}$. The extended Lagrangian for XL-ESMD is then

$$\begin{aligned}\mathcal{L}^{\mathrm{XES}}(\boldsymbol{R}_t, \dot{\boldsymbol{R}}_t, \hat{\boldsymbol{P}}, \dot{\hat{\boldsymbol{P}}}, \hat{\boldsymbol{\zeta}}, \dot{\hat{\boldsymbol{\zeta}}}) = \mathcal{L}^{\mathrm{ES}}(\boldsymbol{R}_t, \dot{\boldsymbol{R}}_t) + \frac{\mu_{\mathrm{gs}}}{2}\mathrm{Tr}[\dot{\hat{\boldsymbol{P}}}^2] \\ - \frac{\mu_{\mathrm{gs}}\omega_{\mathrm{gs}}^2}{2}\mathrm{Tr}[(\hat{\boldsymbol{\rho}}_{\mathrm{g}} - \hat{\mathrm{P}})^2] + \frac{\mu_{\mathrm{es}}}{2}\mathrm{Tr}[\dot{\hat{\boldsymbol{\xi}}}^2] \\ - \frac{\mu_{\mathrm{es}}\omega_{\mathrm{es}}^2}{2}\mathrm{Tr}\,\hat{\xi}[(\hat{\boldsymbol{\xi}} - \hat{\boldsymbol{\zeta}})^2]\end{aligned} \tag{3.31}$$

Here density matrices $\hat{\boldsymbol{P}}$ and $\hat{\boldsymbol{\zeta}}$ are new extended dynamical variables that oscillate in harmonic wells centered around $\hat{\boldsymbol{\rho}}_{\mathrm{g}}$ and $\hat{\boldsymbol{\xi}}$, respectively. μ_{gs}, μ_{es}, ω_{gs}^2, and ω_{es}^2 are the fictitious electronic mass and frequency parameters of the extended harmonic oscillators for the ground state (gs) and the excited state (es), respectively. In the limit of vanishing masses, the Euler−Lagrange equations become decoupled.[551] These correspond to the original Newtonian EOM for the nuclei and two equations for harmonic oscillators for extended variables $\hat{\boldsymbol{P}}$ and $\hat{\boldsymbol{\zeta}}$ (Figure 10A). The latter variables can be integrated into the propagation scheme with the time-reversibility (e.g., through a modified Verlet integration scheme[561,562]) and provide accurate approximations to $\hat{\boldsymbol{\rho}}_{\mathrm{g}}$ and $\hat{\boldsymbol{\xi}}$ with a leading error that is only of second-order in time step.

These propagation schemes are straightforward to implement in most MD codes. Numerically, they can significantly reduce the number of iterations required to solve for $\hat{\boldsymbol{\rho}}_{\mathrm{g}}$ and $\hat{\boldsymbol{\xi}}$ in each time step in TD-SCF, while keeping the constant of motion stable.[551] Thus, XL-ESMD can provide a significant speed-up by relaxing numerical convergence criteria and ensuring numerical stability in ESMD by eliminating unphysical energy drifts as demonstrated in Figure 10B. Applications of this method to

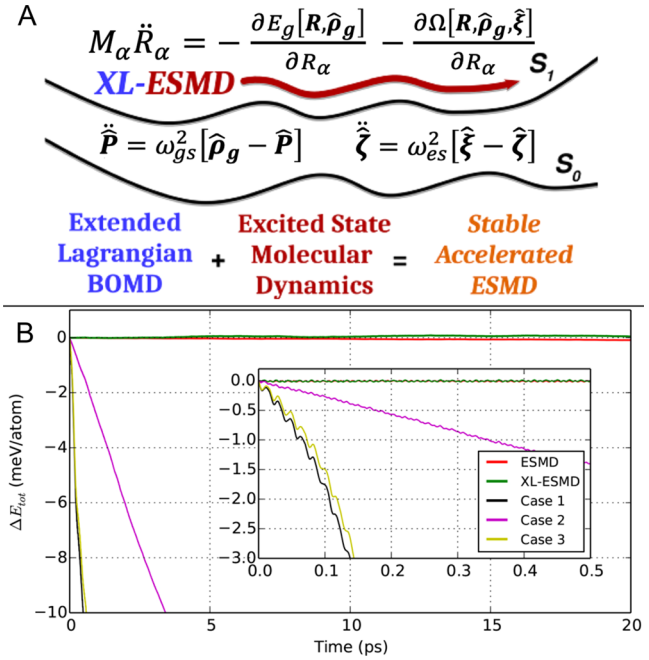

Figure 10. (A) The extended Lagrangian methods for excited-state molecular dynamics (XL-ESMD) framework in the time-dependent self-consistent field (TD-SCF) method reduces computational cost associated with iterative solutions of both ground and excited states. (B) Total energy fluctuations are shown for energy-conserving Born−Oppenheimer dynamics on the PES of the first excited electronic state (S_1) of acetaldehyde, starting from the optimal ground-state (S_0) geometry. Simulations are performed using conventional ESMD with a fully converged SCF and random-phase approximation (RPA) iterations, $\gamma = 10^{-10}$ eV, or using XL-ESMD with relaxed convergence criteria $N_{\mathrm{SCF}} = 2$ and $\gamma = 10^{-4}$ eV. γ is a numerical threshold being the absolute value of the maximal difference between subsequent $\hat{\boldsymbol{\rho}}_{\mathrm{g}}$ and $\hat{\boldsymbol{\xi}}$ in SCF and RPA iterations, respectively. N_{SCF} is the maximum number of SCF cycles at each time step regardless of γ. Three cases illustrate non-energy-conserving ESMD at low convergence thresholds γ and N_{SCF}. Case 1 corresponds to $N_{\mathrm{SCF}} = 2$ and $\gamma = 10^{-4}$ eV, i.e., conventional ESMD with no XL propagation. Case 2 is XL propagation of $\hat{\boldsymbol{\rho}}_{\mathrm{g}}$ with $N_{\mathrm{SCF}} = 2$ while using the previous solution for $\hat{\boldsymbol{\xi}}$ as an initial guess for the RPA equation iterated to $\gamma = 10^{-4}$ eV. Case 3 corresponds to no XL propagation of $\hat{\boldsymbol{\rho}}_{\mathrm{g}}$ using $N_{\mathrm{SCF}} = 2$ but with XL propagation of $\hat{\boldsymbol{\xi}}$ with $\gamma = 10^{-4}$ eV. All three cases show a noticeable drift of energy in contrast to XL-ESMD results. Reproduced with permission from ref 551. Copyright 2018 American Chemical Society.

NAMD methods, such as Eherenfest dynamics and surface-hopping techniques, can significantly improve numerical efficiency, however they have yet to be implemented and tested for NAMD simulations of realistic systems.

3.4. Non-adiabatic Coupling Terms and FSSH NAMD

The NAC vectors (NACRs; eqs 2.6 and 3.17) represent the main ingredients for the propagation of the time-dependent quantum coefficients in the TDSE. By definition, $\boldsymbol{d}_{aa} = 0$ and $\boldsymbol{d}_{ab} = -\boldsymbol{d}_{ba}$, such that there will be $N_S(N_S - 1)/2$ and $(3M - 6)N_S(N_S - 1)/2$) unique NACTs and NACRs, respectively, for a system of N_S electronic states and M nuclei. Consequently, for efficient NAMD simulations, numerical calculations of these quantities along the dynamical trajectories discussed in the previous section (section 3.1.3) is one of the primary computational bottlenecks. For example, in both FSSH and Ehrenfest dynamics NACTs need to be evaluated at each trajectory point (section 2.2). They control the surface-hopping

https://dx.doi.org/10.1021/acs.chemrev.9b00447
Chem. Rev. 2020, 120, 2215−2287

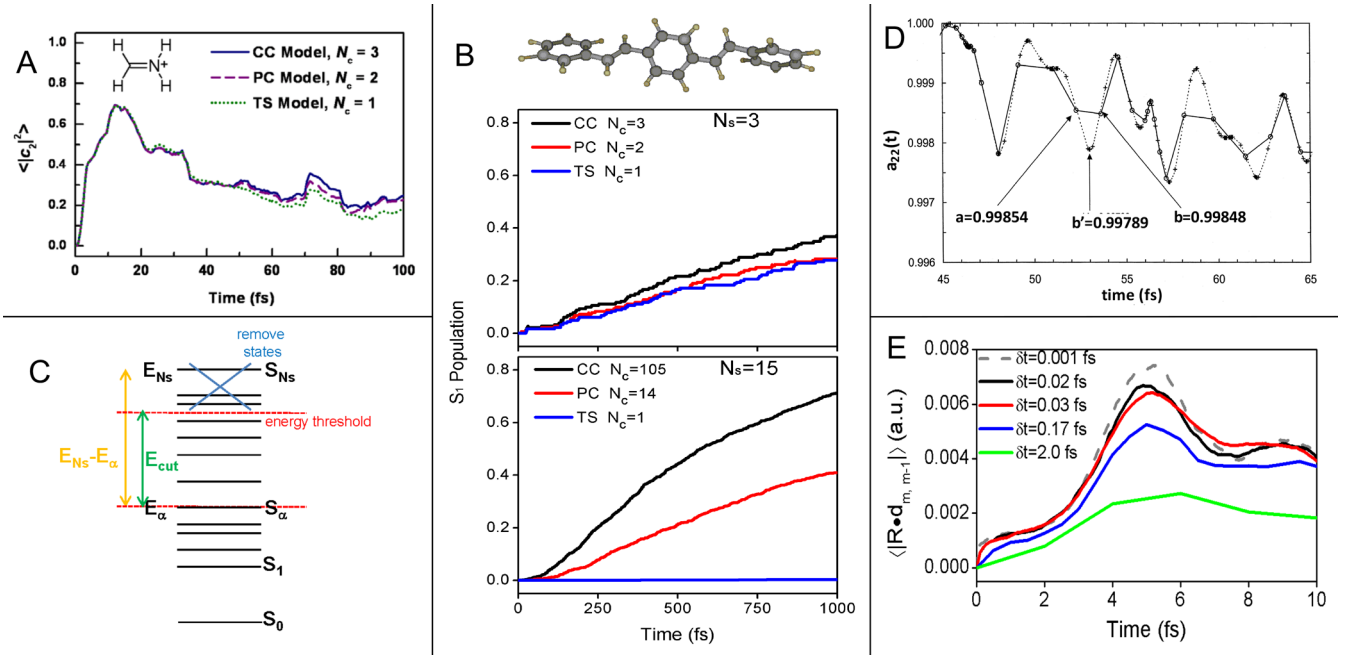

Figure 11. (A) Adiabatic-state populations computed from surface-hopping NAMD using the complete coupling (CC), partial coupling (PC), and two-state (TS) models for the three-state simulation of methaniminium cation from the initial S_2 state. (B) S_1 adiabatic-state populations computed using the CC, PC, and TS models for the three-state simulation of distyrylbenzene from the initial S_2 state (top) and for the 15-state simulation of distyrylbenzene from the initial S_m state (bottom). (C) State reduction method for on-the-fly limiting of excited states with energy cutoff based on local kinetic energy. (D) Probability of being in state 2 at time t, $a_{22}(t)$, evaluated using different integrators. The open circles and solid lines represent steps taken with the Bulirsch−Stoer (BS) integrator. The pulses and dashed lines are the integrator values using small steps near extrema. Both methods agree in values of $a_{22}(t)$, but the BS integrator cannot resolve peaks (b') that change the hopping probability. (E) Average non-adiabatic coupling scalar (NACT) for quantum transitions in distyrylbenzene computed using different numbers of classical and quantum time steps. As the quantum time step, δt, is increased, the maximum NACT value is reduced and the peak is not resolved. Panel A: Reproduced with permission from ref 563. Copyright 2009 Elsevier. Panels B and E: Reproduced with permission from ref 544. Copyright 2012 AIP Publishing. Panel C: Reproduced with permission from ref 564. Copyright 2016 Elsevier. Panel D: Reproduced with permission from ref 565. Copyright 1999 American Chemical Society.

probabilities in FSSH. Moreover, NACRs are required at each hopping event for rescaling of the velocities in FSSH. Section 3.1.3 overviews the formalism of NAC calculations in the family of TD-SCF methods. Here we outline some possible issues in the numerical NAMD simulations related to NACs.

3.4.1. NACT Simplification Schemes and Essential States. A common approach to reducing the computational load imposed by NACTs is to reduce their number since the NAC matrix (eq 2.6) is generally sparse. This can be done by either restricting the number of coupling terms computed for a fixed number of electronic states, or alternatively by reducing the number of electronic states included in the simulation. The complete coupling (CC) model includes all $N_S(N_S-1)/2$ coupling terms in order to describe coupling between all possible pairs of states. In order to reduce the computational demand, approximations of the CC model that involve only a fraction of the NACTs have been proposed. The simplifications introduce error in the propagation of electronic wavefunction coefficients (eq 2.16) and can also restrict the available relaxation pathways by decoupling states. We illustrate the consequences of such reduction on an example of FSSH simulations. Figure 11A,B summarizes the comparison of excited-state populations obtained from the FSSH NAMD simulations performed with the CC model, and crude approximations such as the partial coupling (PC) and two-state (TS) models. The PC limits NACTs only between the current state of interest (the state that defines the nuclear propagation) and all other states reducing the number of coupling terms to $N_S - 1$. The TS model is a more drastic approximation in which only one NACT is evaluated, specifically the coupling between the current state of interest and the state directly below in energy.

The simplified models have been demonstrated to work well in reproducing the CC results for small molecules with few excited states, such as the photoexcited dynamics of methaniminium cation with three electronic states[563] shown in Figure 11A. The simplified models have been also tested for a large polyatomic molecule (distyrylbenzene),[544] to model the three-state and 15-state electronic relaxation, Figure 11B. TS and PC approximations reproduce the essential features of the CC modeling for the three-state system. However, extension to the realistic 15-state system, which would provide considerable computational savings, does not provide good agreement (Figure 11B). The truncated models exclude relaxation pathways that do not involve the current state and the TS model enforces sequential downhill relaxation and eliminates upward transitions and decay pathways involving hops over multiple states. The error in the wavefunction propagation introduced by these models make them inappropriate for scaling up to large system applications. Subsequently, making assumption on the sparsity of NAC matrices is not well justified and is system-specific.

Another approach to reducing the computational demand of the NACT calculations is to eliminate high-energy excited states (and their couplings) on-the-fly when they no longer participate in the dynamics,[564] represented schematically in Figure 11C, based on kinetic energy considerations. In this way, the CC model is preserved for a dynamic excited-state manifold by

https://dx.doi.org/10.1021/acs.chemrev.9b00447
Chem. Rev. 2020, 120, 2215−2287

introducing an energy threshold defined by the local kinetic energy. This has been demonstrated to be an effective parameter free method that can be applied to any molecular system providing orders of magnitude reduction of numerical cost for the largest molecular systems with hundreds of electronic states.[564] Notably, this approach is well suited for algorithms including decoherence corrections limiting the energetic spread of the electronic wavepacket (section 2.4).

3.4.2. Time Steps and Numerical Resolution of NACT Spikes. As we discussed before, compared to BOMD, NAMD simulations must properly follow the ultrafast electronic dynamics and thus require shorter time step values (typically $\Delta t \leq 0.1$ fs). Moreover, even at such short increments, the electronic quantum coefficients in MQC dynamics (eq 2.15) may significantly change when passing regions of strong non-adiabaticity. This calls for introduction of finer time steps $\delta t \ll \Delta t$ to numerically integrate the TDSE in the form of 2.15 and capture variations in time of the real and imaginary parts of coefficients $c_a(t)$. Because the time step required for quantum integration, δt, must usually be smaller than the classical time step, Δt, used in the integration of the nuclear EOMs, the NACTs must be obtained at intermediate times. This is usually accomplished using simple linear interpolation and extrapolation schemes.[111,566] However, the NACTs typically behave as strongly localized sharp peaks that change rapidly on small time scales. This feature introduces time step dependence that can lead to large inaccuracies in evaluating hopping probabilities. Difficulties in resolving NACTs are especially relevant to the trivial unavoided crossing problem (discussed in section 3.4.3).

One way to overcome NACT resolution is the use of adaptive integration for more accurate calculations. For example, FSSH trajectories that experience long time scales relative to the total integration time and exhibit only small changes in the electronic probabilities are more sensitive to small errors in the hopping probability. In those cases, using integrators with adaptive step size control has been shown to be more efficient than using fixed step size integrators for evaluating the changes in electronic probability that enter into the hopping probability,[565] as demonstrated in Figure 11D. The appropriate quantum time step for resolving the NAC peaks must be balanced with the classical integration (Figure 11E). Adaptive time step algorithms have been proposed in which the quantum time step can be reduced on-the-fly by tracking d(NACT)/dt and/or d(NACT)/dR to indicate the presence of a coupling region. In those regions, the quantum time step would be adjusted by a given factor until the peak is resolved. The performance of such algorithm has yet to be evaluated. However, a similar approach using adaptive time steps is already employed in active space CI treatments in trajectory surface hopping. Such approaches can encounter local regions of phase space where the active and inactive orbitals can mix and switch causing discontinuities in electronic energies and gradients resulting in stability and accuracy issues. That can be overcome by applying sufficiently small time steps only in the local region where they are required. These adaptive time steps can be reduced iteratively (up to a maximum number) based on energy conservation and orbital overlap criteria.[113]

Another approach introduces flexibility by allowing NACTs to be evaluated a desired number of times, N_q, during the interval between classical time steps so that $\delta t = \Delta t/N_q$. The accuracy of interpolated values for strongly varying NACTs limits the classical integration time step. By evaluating NACTs between classical time steps, the calculation of NACTs and excited-state gradients can be separated allowing larger classical integration steps to be used. Still, the selected value of NACT evaluations must be large enough to adequately resolve peaks while maintaining the computational efficiency of the simulation. Otherwise, the coupling can be substantially underestimated causing transitions to be missed, as shown in Figure 11E where NACT resolution depends strongly on δt. The underestimated NACT changes the relaxation dynamics by reducing the hopping probability (eq 2.19). That causes non-adiabatic transitions to be missed and overall non-radiative relaxation rates will artificially slow down with time step increase.[544]

It is relevant to point out that NACT computation and resolution can be avoided altogether by performing dynamics in the diabatic representation. In this picture, diabatic states, ϕ_a, would be defined according to their electronic character and coupled through electronic or diabatic couplings given by simple matrix elements $\langle \phi_a | \hat{H}_{el} | \phi_b \rangle$. However, it is impossible to define exact diabatic states[567] and they are typically obtained from transformation of adiabatic states through various methods described in refs 14, 568, and 569. Local diabatization[106] has emerged as a particularly attractive approach for trajectory surface-hopping methods. In this approach, the nuclei are propagated on the adiabatic PESs, while the electronic amplitudes and hopping probabilities are evaluated in the diabatic basis by defining diabatic states in terms of adiabatic states at every nuclear time step. The possible benefits of using the diabatic basis in surface hopping have been demonstrated, for example, in its implementation in the SHARC software package which takes advantage of the diabatic representation for coefficient evolution in order to capture effects of spin−orbit coupling.[570−573] Multi-state diabatization is important when more than two electronic states are coupled.[569] Various other formulations of diabatic surface hopping have appeared over the years.[87,112,574−577] Methods to generate diabatic states from electronic structure have recently been reviewed by Subotnik et al.[140]

3.4.3. Trivial Unavoided Crossings. Photoinduced processes in multichromophoric extended molecular assemblies involve multiple electronic excited states that can be localized on different moieties.[104,105] These adiabatic states are commonly calculated with electronic structure methods, and are typically weakly coupled and experience multiple unavoided crossings, for example, due to thermal fluctuations. In the limit of infinitesimal time steps, their NACs have very sharp δ-function like spikes. Ideally, the interaction between states would be correctly reflected in the corresponding population transfer between states, which can be simulated, for instance, through quantum transitions using trajectory surface-hopping-like methods or Ehrenfest methods (section 2.2).[75] In practice, however, the finite time steps in the classical dynamics may miss these instantaneous NAC spikes for non-interacting state crossings resulting in severe artifacts in simulated NAMD.

Specifically, trivial unavoided crossings are defined as intersections of two non-interacting adiabatic states evidenced by a sharp peak in NAC strongly localized in time of the respective adiabatic wavefunctions occurring only at the exact energy degeneracy and becoming vanishingly small elsewhere. All direct NAMD codes taking advantage of finite time step propagators (e.g., Verlet-like algorithms)[534,578] in the adiabatic basis are vulnerable to miss trivial unavoided crossings giving rise to unphysically long population transfer time scales and unrealistic long-range ET.[105] As an example, fast torsional fluctuations between individual monomers during photo-

https://dx.doi.org/10.1021/acs.chemrev.9b00447
Chem. Rev. 2020, 120, 2215−2287

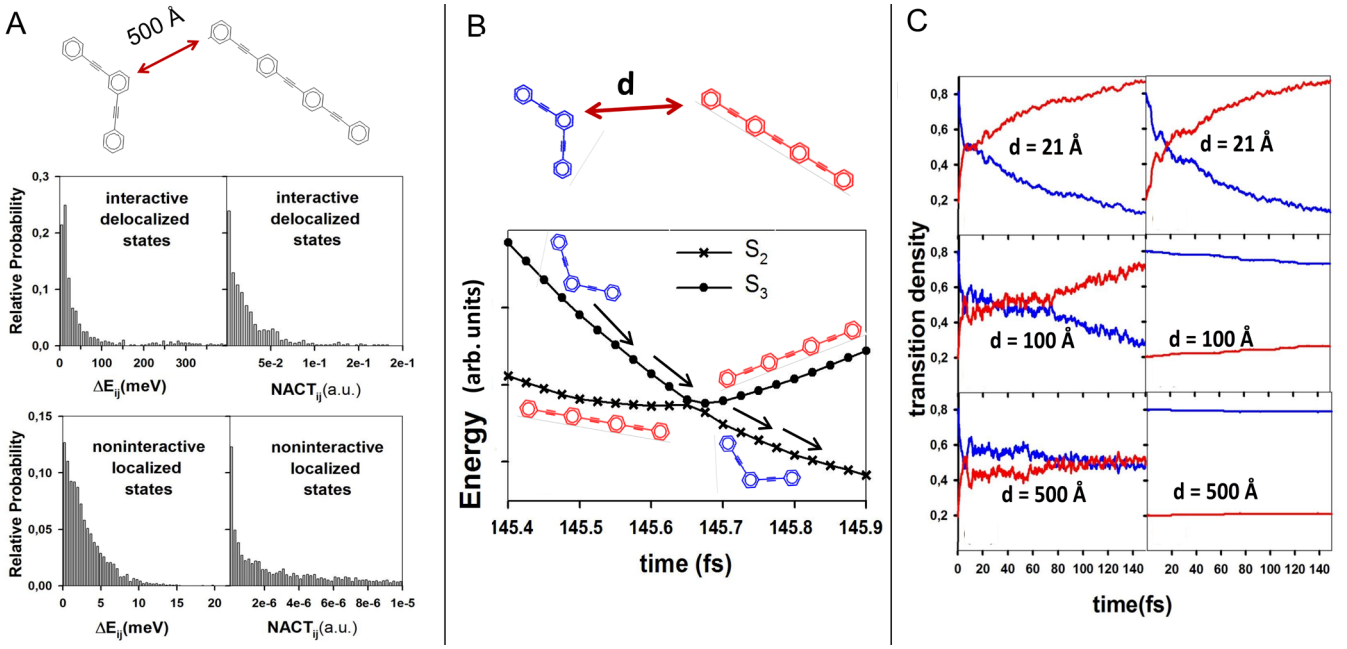

Figure 12. (A) Distribution of the energy gaps ΔE_{ij} and $NACT_{ij}$ at the moment of $S_i \rightarrow S_j$ quantum transition between interacting/delocalized states and non-interacting/delocalized states for 22-PPE and 4-PPE molecules (top) separated by 500 Å. (B) Time evolution of the adiabatic-state energies for a typical trivial unavoided crossing between non-interacting adiabatic states obtained from fewest-switches surface-hopping simulation of 22-PPE and 4-PPE molecules separated by d = 500 Å. The electronic character of the adiabatic states (plotted with black ×'s and closed circles) changes instantaneously at the moment of cross. (C) Variation of the time-dependent fraction of transition densities localized on the 22-PPE and 4-PPE molecules when they are separated by different distances, obtained with (right panels) and without (left panels) considering any specific treatment of unavoided crossings. Reproduced with permission from ref 104. Copyright 2012 AIP Publishing.

induced ET dynamics in PPV oligomers been have shown to cause extensive excited-state energy reordering[579] that can lead to a misinterpretation of multiple non-radiative relaxation pathways.

Within this context, the proper identification and treatment of trivial unavoided crossings is an important part of NAMD simulations.[104] In practice, trivial unavoided crossings are commonly recognized in regions close to the particular nuclear configurations for which the adiabatic PESs cross each other. Different strategies have been developed to deal with the trivial crossing problem during *direct* NAMD simulations, particularly in the context of surface-hopping approaches. Such algorithms typically aim to differentiate crossings between interacting states (simulated by quantum transitions), and trivial unavoided crossings between non-interacting states (detected by tracking the identity of states). Therefore, a clear numerical threshold between crossings involving interacting and non-interacting states should be defined. Generally, while the former dominate at relatively short interchromophoric distances and low density of states, the latter become noticeable at larger intermolecular distances and for processes involving high densities of states. A distinction between these two cases is illustrated in Figure 12A that compares the distribution of energy gaps and NACTs during NAMD of a system composed of PPE oligomers 22-PPE and 4-PPE, separated by 500 Å. Here adiabatic excited states of the same chromophore are interacting whereas those on the different molecules are non-interacting. We observe that trivial unavoided crossings take place in regions with an order of magnitude smaller energy gaps and with several orders of magnitude lower couplings than standard unavoided crossings.

The strategies to overcome the trivial unavoided crossing problem can be classified according to which basis set (adiabatic or diabatic) is used to expand the electronic wavefunction (eq 2.3). If the adiabatic basis set is used, the quantum transitions in the non-adiabatic region are controlled by the NAC terms. Otherwise, if a diabatic bases is chosen, the dynamics are driven by $H_{ab}(\boldsymbol{R}) \equiv \langle \phi_a(\boldsymbol{r}) | \hat{H}_{el}(\boldsymbol{r},\boldsymbol{R}) | \phi_b(\boldsymbol{r}) \rangle$ values (section 2.1). Typically, methods using an adiabatic basis representation take advantage of accurate calculations of NACTs,[435,436] whereas implementations based on diabatic basis sets require evaluations of off-diagonal terms $H_{ab}(\boldsymbol{R})$.[106,109]

For the *adiabatic basis representation*, trivial unavoided crossings are commonly recognized by tracking the adiabatic-state identities over time.[111,112] The latter are encoded into the overlap matrix $\hat{s}(t;t+\Delta t)$, defined as

$$s_{ab}(t;\, t+\Delta t) \equiv \langle \psi_a(\boldsymbol{R}_t) | \psi_b(\boldsymbol{R}_{t+\Delta t}) \rangle \tag{3.32}$$

where Δt is the classical time step used for simulations and $\psi_a(\boldsymbol{R}_t)$ is a manifold of adiabatic states. For example, the Min-Cost reassignment algorithm enables accurate identification of trivial unavoided crossings.[104] In the Min-Cost approach, at each time step during simulations, adiabatic states obtained at the current time step (i) are assigned in terms of previous adiabatic states calculated at the preceding time step $(i-1)$. The correspondence between them is determined by the maximum of the overlap matrix $\hat{s}(t;t+\Delta t)$. A trivial unavoided crossing, or switch, between states is prompted by detecting off-diagonal elements $s_{ab}(t;t+\Delta t)$, $a \neq b$ from eq 3.32 with values greater than a predefined threshold (commonly chosen as 0.9). By design, this algorithm is able to detect multiple crossing events during the same time interval, which frequently occur in extended molecular systems with a high density of states. Moreover, this technique is also suitable for Ehrenfest dynamics that requires simultaneous identification of trivial unavoided crossings for all electronic states considered during the MD simulations.[350]

https://dx.doi.org/10.1021/acs.chemrev.9b00447
Chem. Rev. 2020, 120, 2215−2287

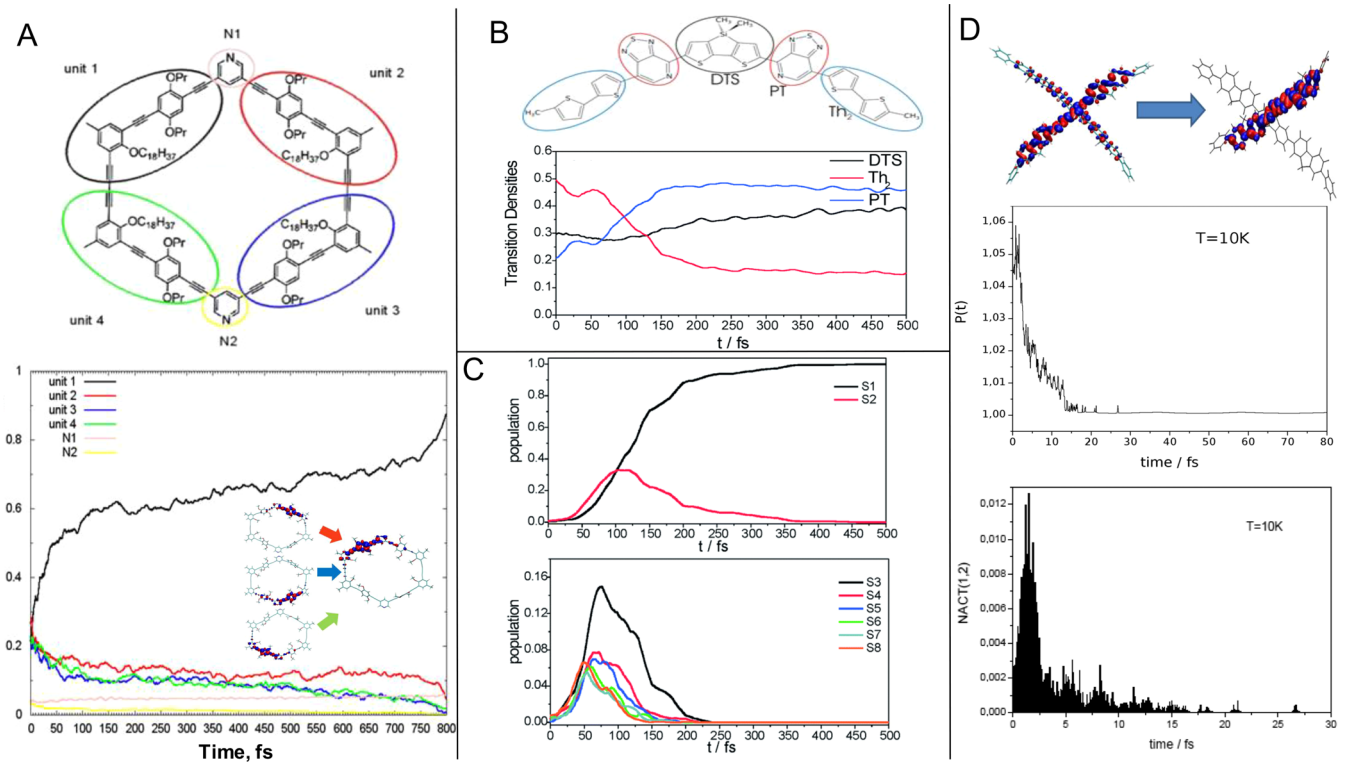

Figure 13. (A) Chemical structure of a phenylene-ethynylene macrocycle showing selection of units and evolution of the average fraction of transition density (TD) localized in each unit, signaling the flux of the TD from the different units to a final common segment. (B) Chemical structure of the p-DTS($PTTh_2$)$_2$ molecule showing the selection of units and the time-dependent average of the fraction of the TD localized in the different units. (C) Evolution of each adiabatic-state population for p-DTS($PTTh_2$)$_2$. (D) Results obtained from FSSH simulations of the photoinduced dynamics of the spiro-linked conjugated polyfluorene dimer with time dependence of the average monomer participations number, P(t), and average absolute value of NACT(1,2). Panel A: Reproduced with permission from ref 246. Copyright 2016 American Chemical Society. Panels B and C: Reproduced with permission from ref 589. Copyright 2014 The Royal Society of Chemistry. Panel D: Reproduced with permission from ref 588. Copyright 2014 American Chemical Society.

Once a trivial unavoided crossing is identified, the molecular system needs to follow the "diabatic pathway" of its parent wavefunction along the respective adiabatic PES. Figure 12B exemplifies this for the case of a trivial unavoided crossing between non-interactive adiabatic states of 22-PPE and 4-PPE molecules. Here, the populations of the corresponding adiabatic states are interchanged with unit probability. While doing that, special care should be taken in order to cancel population transfers due to inaccurate calculations of NACTs. Failure to follow the correct diabatic pathway during trivial unavoided crossings can lead to unphysical sudden changes in the spatial localization of the current excitation. Figure 12C displays results obtained from the NAMD simulations with and without considering any method to detect trivial unavoided crossings for the case of 22-PPE and 4-PPE molecules separated by different distances. At long distances the two molecules should be uncoupled. Despite that, the lack of any treatment for trivial unavoided crossings leads to unphysical long-range ET between the molecules at the longest separations.

Most trivial unavoided crossings happen between spatially localized adiabatic states that are well separated in space with no significant contribution to the dynamics. With this in mind, the flexible surface-hopping (FSH)[110] approach includes only electronic states whose coupling/energy difference are larger than a predefined threshold. This allows electronic states to be flexibly added and removed from hopping probability calculations throughout the simulations. However, the effect of constant redefinition of the active space while dealing with high density of states remains unclear.

Similar strategies have been proposed to identify switching between active and inactive MOs for dynamics based on CI expansions with a small active space of orbitals. In these cases, careful tracking of MOs becomes necessary. This requirement commonly leads to a significant reduction in the time step used in the simulations and, therefore, compromises the computational cost. Nevertheless, this drawback can be overcome using adaptive time steps (see section 3.4.2) within regions that fulfill certain energetic and/or orbital overlap criteria.[113] Adaptive time step integration schemes have also been implemented for wavepacket-based simulations like AIMS.[108] Finally, an alternative norm-preserving interpolation (NPI) scheme evaluates NACTs from a set of relatively simple analytic expressions derived from the continuous interpolation of adiabatic electronic wavefunctions.[115,116,580]

While dealing with adiabatic states necessitates tracking the state identity, in contrast, all unavoided crossings between states appear naturally in the *diabatic representation* through an increased value of off-diagonal terms $H_{ab}(t;t+\Delta t)$. For example, the direct trajectories with surface-hopping (DTSH) approach uses the *local diabatic representation*.[106] There the diabatic states are redefined at each time step via unitary transformation obtained from Löwdin's orthogonalization[581] of the overlap matrix $\hat{s}(t;t+\Delta t)$ (eq 3.32). Within the local diabatic representation, NACTs are zero and changes in quantum coefficients are driven by $H_{ab}(\boldsymbol{R})$ values. Notably, the local

https://dx.doi.org/10.1021/acs.chemrev.9b00447
Chem. Rev. 2020, 120, 2215−2287

diabatic representation collapses to the adiabatic representation in the adiabatic regions characterized by negligible non-adiabatic couplings. Despite the benefit of eliminating the spikes in NACTs, the integration of relatively small and delocalized values of off-diagonal terms $H_{ab}(\boldsymbol{R})$ can lead to inaccuracies in the prediction of quantum transitions.[100,582] An efficient assignment algorithm minimizing the difference between two local diabatic expansions was proposed to obtain an interpolated adiabatic PES during simulations.[583] Another approach based on local diabatization allows identification of trivial unavoided crossings without tracking adiabatic-state identities.[584]

Recently, an alternative approach known as self-consistent fewest-switches surface hopping (SC-FSSH)[107] was developed by Wang and Prezhdo to solve the trivial crossing problem. The method introduces a self-consistency test to the calculation of the hopping probability from the current state to the energetically closest state (eq 2.19). Trivial unavoided crossings are detected as a significant discrepancy between the summation of probabilities to hop from the current state to all other states according to the FSSH prescription, and the value of the effective change in population of the current state evaluated at the same time interval. That is, the method is limited to the identification of trivial unavoided crossings involving the current state in surface-hopping simulations. The self-consistency test proposed in SC-FSSH is naturally fulfilled using the GFSH approach[114] by eliminating dependence on NACTs for the hopping probabilities.

3.5. Analysis of Electronic Transition Densities for Spatial Excitonic Localization

The NAMD simulations of extended molecular systems produce a wealth of information on energies, spectroscopic observables, and wavefunctions along a swarm of time-dependent trajectories. It is important to analyze these data to delineate possible photoinduced relaxation pathways and establish physical processes underlying non-radiative dynamics and internal conversion. The TDMs, or so-called electronic normal modes, from the ground to excited states $\hat{\boldsymbol{\xi}}$ (eq 3.12) and between excited states $\hat{\boldsymbol{\pi}}_{ab}$ (eq 3.14) reflect the spatial delocalization of excited electronic states and are routinely calculated in all TD-SCF approaches (section 3.1). The matrix elements of $\hat{\boldsymbol{\xi}}_a$ are in fact the CIS wavefunction coefficients $\hat{\boldsymbol{X}}_a$ in the MO basis (section 3.1.2). The NACs (eqs 3.17 and 3.18) and spectroscopic observable are calculated using the respective TDMs.[437,585] For example, the transition dipoles are expectation values of the dipole moment operator on the TDMs.

TDMs in real space representation have been extensively used for analyzing and interpreting photoinduced processes in molecular systems. These are $N_{\mathrm{AO}} \times N_{\mathrm{AO}}$ matrices, where N_{AO} is the number of AO basis functions. Their elements have the following loose interpretation. Diagonal elements of TDMs $(\xi_a)_{nn}$, eq 3.14, represent light-induced changes on the electronic density distribution of the nth AO due to the excitation from ground to ath excited state.[454,586,587] For example, these diagonal elements in the AO representation directly indicate spatial localization of electronic excitations with weak charge-transfer character, Figure 13.[246,588−591] On the other hand, the off-diagonal elements $(\xi_a)_{nm}$ describe electronic coherences and charge-transfer phenomena between nth and mth AOs.[592] Thus, their characteristic spatial map indicates the delocalization and coherence lengths of the electron−hole pair (exciton) for specific excited states. This feature is particularly useful for characterizing charge-transfer excitations in multichromophoric extended conjugated molecular systems.[401,452] For example, natural transition orbitals (NTOs)[593] express the electronic TDM as essential pairs of particle and hole orbitals, thus enabling examination of electron−hole separation in excitonic wavefunctions and charge-transfer states.[87,594,595]

Here we will extensively use TDMs to analyze intra- and intermolecular spatial redistributions of time-dependent excited-state wavefunctions obtained from NAMD simulations of multichromophore molecular systems. This analysis is applicable to excited states corresponding to strongly bound excitons that can be described with the Frenkel exciton model,[596−598] a typical case for conjugated organic molecules. NTOs,[593] for example, can be applied for the analysis of charge-transfer excitations.[87,594,595,599] The starting point is partitioning the molecular system into essential moieties and/or chromophore units denoted here as X, Y, etc., depending on the structural topology. The fraction of TDM, $(\xi_a(t))^2_X$, localized on unit X at a given time can be obtained by summing the contributions of the AOs from each atom (index A) in X and occasionally contributions of the AO from atoms localized on the boundary with another unit (index B),

$$(\xi_a(t))^2_X = \sum_{n_{\mathrm{A}}m_{\mathrm{A}}} ((\xi_a)_{n_{\mathrm{A}}m_{\mathrm{A}}}(t))^2 + \frac{1}{2}\sum_{n_{\mathrm{B}}m_{\mathrm{B}}} ((\xi_a)_{n_{\mathrm{B}}m_{\mathrm{B}}}(t))^2 \tag{3.33}$$

The TDM normalization condition (eq 3.13), which becomes a simple dot product in the CIS case, justifies interpretation of $(\xi_a(t))^2_X$ as a fraction of excitation localized on segment X. This quantity can be calculated for a single representative trajectory or averaged across the entire ensemble. An example partitioning of a molecular systems and the time-evolution of the corresponding values of $(\xi_a(t))^2_X$ can be seen in Figure 13A,B.[246]

If the photoexcitation of a large conjugated molecule induces participation of tens of excited states, tracking the electronic population of each state can become a cumbersome task. The analysis of the time-evolution of the TD spatial localization provides a simple and convenient strategy to obtain a *coarse-grained* picture of the photoinduced molecular processes such as internal conversion. To exemplify this approach, consider the NAMD simulation of photoexcitation of p-DTS(PTTh$_2$)$_2$ to its broad high-energy band in the 3−4 eV range shown in Figure 13B. Figure 13C shows the analysis of the time evolution of the average electronic populations of adiabatic states that can be compared to the localization of the TD on different fragments (Figure 13B).[589] While both analysis approaches actually complement each other, the latter depicts a simplified overview of the process.

When a molecular system is composed of equivalent chromophore units (or fragments), a quantitative measure of excitonic delocalization is provided by the participation number,[546,600−602] defined for each unit as

$$P_X(t) = \left[\sum_{n_{\mathrm{A}}m_{\mathrm{A}}} ((\xi_a(t))^2_X)^2\right]^{-1} \tag{3.34}$$

If N is the number of equivalent units present, $P_X(t) \approx 1$ indicates a complete localization of the TDM on a single unit, while $P_X(t) \approx N$ correspond to the TDM fully delocalized among the N units. That is, $P_X(t)$ shows, on average, over how many equivalent chromophore units a given adiabatic excited-state wavefunction is delocalized. Further ensemble average of $P_X(t)$ tracks averaged time-dependent spatial delocalization of

https://dx.doi.org/10.1021/acs.chemrev.9b00447
Chem. Rev. 2020, 120, 2215−2287

the excitation. As an example, Figure 13D displays the time dependence of the average monomer participation number during the photoinduced dynamics of the weakly coupled spiro-linked conjugated polyfluorene dimer.[588] At early times after photoexcitation, values of $P_X(t) > 1$ indicate weak delocalization of the excitation between both monomers. This delocalization is associated with the presence of non-adiabatic coupling. After 20 fs, the states on individual monomers become energetically separated and decoupled, which leads to a complete confinement of the excited-state wavefunction on a single monomer, as indicated by values of $P_X(t) = 1$. This analysis suggests that fluorescence of the molecule originates from localized (self-trapped) excitons.

In cases of multichromophoric molecular systems, a complete description of the photoinduced intramolecular energy redistribution is not complete without the analysis of the specific energy flow between units. This can be achieved by performing a TDM flux analysis according, for example, to the statistical minimum flow (SMF) method.[246,603] Briefly, the method allows the identification of the different and simultaneous photoinduced interchromophoric ET pathways through the calculation of a flow matrix whose elements contain the amount of TD transferred between units X and Y. A detail description of how to calculate these elements can be found in ref 246 and is exemplified below in sections 4 and 5.

3.6. Common NAMD Software and the Non-adiabatic Excited-State Molecular Dynamics (NEXMD) Package

The NAMD approaches are broadly implemented across a wide range of software and are able to operate on top of a variety of electronic structure methods for calculating excited-state properties. We refer the reader to a recent review by Barbatti et al. summarizing the existing software.[121] For example, the surface-hopping method interfaced with TD-DFT is the workhorse of several open-source NAMD programs (PYXAID,[136,604] NEWTON-X,[449] SHARC,[570,605] QChem,[606] etc.). The PYXAID program,[136,604] recently added the self-consistent charge density functional tight binding (SCC-DFTB) method.[607] Newton-X[448,449] is capable of performing NAMD on-the-fly using various levels of theory including TD-DFT and multiconfigurational self-consistent field (MCSCF) theory. Real-time TD-DFT propagation (based on the Ehrenfest dynamics) has been implemented in NWChem[608] and Gaussian packages.[609] Additionally, the publicly available COBRAMM package[488] provides a surface hopping and QM/MM interface to many common computational chemistry packages, allowing NAMD simulations using CASSCF/CASPT2 or other electronic structure.

Our group has been developing the NEXMD software which incorporates many methodological advances described above. It is used for many examples of NAMD simulations present in this Review. The NEXMD software combines the Collective Electronic Oscillator (CEO) approach[401,610] with semiempirical quantum chemistry (i.e., model Hamiltonian models such as AM1, PM3, INDO/S, etc. (section 3.1.1).[11,611] It is now built on top of the SQM package from AmberTools.[612] The CEO approach[610] can be thought of as a collection of numerical algorithms for a variety of TD-SCF approaches such as TD-HF and CIS[613] (section 3.1.2) allowing for efficient calculations of excited states, their properties and spectroscopic observables in conjunction with the diverse set of semiempirical Hamiltonians. At this level, the numerical costs of computing excited states is not substantially more demanding than ground-state calculations.[431,585] Moreover, semiempirical Hamiltonians, such as AM1,[11] provide reasonably accurate ground-state geometries and energies, heats of formation, vertical excitation energies, polarizabilities, and adiabatic excited-state PESs.[614−617] Optical and excited-state properties of large systems with dense manifolds of interacting excited states may be computed as evidenced by successful application of this level of theory to systems such as polymers,[401,618,619] dendrimers,[620] light-harvesting complexes (LHCs),[621,622] and carbon nanotubes.[623,624]

Energies and forces as well as NACs in the development version of NEXMD are computed on-the-fly with nuclei evolving on native excited-state PESs.[437] Non-adiabatic transitions between electronic states are modeled with Tully's FSSH (section 2.2.2),[234] Ehrenfest dynamics (section 2.2.2) or accurate MCE/AIMC approaches (section 2.5.4).[350,353] Other essential practical aspects of calculations that are carried out with NEXMD are (1) empirical ID-S, ID-A, EDC, and CSDM decoherence corrections built on top of FSSH to alleviate inconsistencies due to the classical treatment of nuclei (section 2.4),[93] (2) advanced algorithms for tracking trivial (unavoided) crossings between non-interacting states (section 3.4.3),[104,105] (3) implicit treatment of solvation at COSMO level[473] including LR, and SS (section 3.2.1),[494,513] and non-equilibrium models (section 3.2.2),[514] (4) XL-ESMD (section 3.3.3),[551] (5) calculation and analysis of excited-state vibrational spectra and NAMD simulations along selected vibrational degrees of freedom, and (6) on-the-fly limiting to essential excited states for NAMD simulations (section 3.4.1).[564] The latter functionality significantly reduces computational time by eliminating the calculation of unnecessary excited states and NACs. More detail on the governing theory that is implemented in developmental versions of NEXMD can be found in refs 437, 544, and 625.

4. APPLICATIONS: INTERNAL CONVERSION IN CONJUGATED CHROMOPHORES

In this section, we illustrate the NAMD modeling of internal conversion on several examples of conjugated chromophores. Internal conversion is a non-radiative process of generally irreversible energy flow from electronic to vibrational degrees of freedom leading to heating of the system. Such dynamics in organic molecules with weak spin−orbit coupling is ultrafast (100 fs−1 ps time scales) and occurs across the manifold of singlet states labeled S_0, S_1, ..., S_n. In most cases presented here, the non-equilibrium population of excited electronic states initiated by photoexcitation leads to a selective excitation of specific vibrational modes due to a strong coupling of electronic and selective structural degrees of freedom. The latter can typically be represented by fast (bond stretching, e.g., C═C stretches) and slow (torsions and librations) motions. Equilibrated excitations across all vibrational modes accompanied by relaxation to the bath degrees of freedom develops at later time.

4.1. Dynamics of Excitons on Carbon Nanorings

Conjugated carbon nanorings comprise a wide variety of chemical compounds with unique optical properties provided by the nonplanar geometry of conjugated segments.[626] Within their cyclic structures, the efficiency in π-orbital overlap competes with bending strain, disorder, and steric hindrances. The NAMD simulations provide a description of how the photoinduced electronic excitation evolves within the nanoring during the first hundreds of femtoseconds to picoseconds after

https://dx.doi.org/10.1021/acs.chemrev.9b00447
Chem. Rev. 2020, 120, 2215−2287

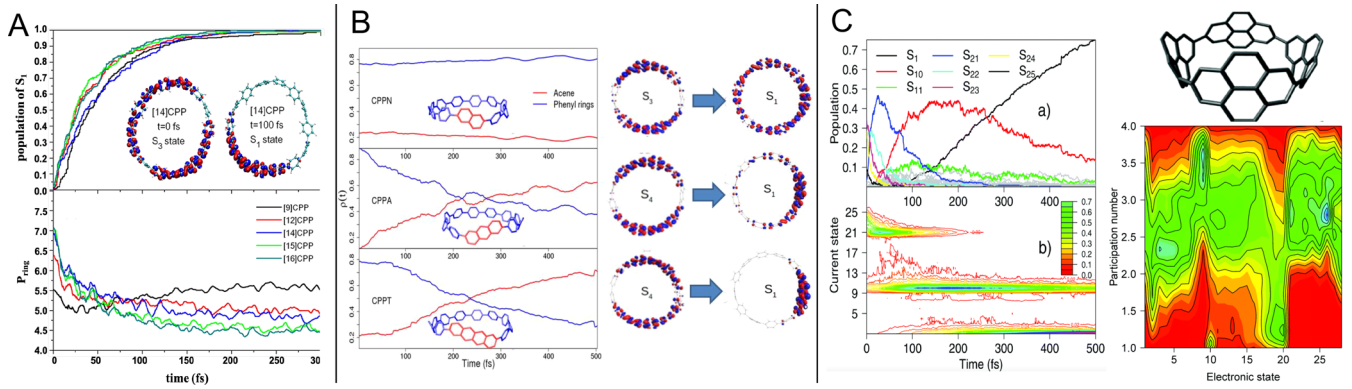

Figure 14. Fewest-switches surface-hopping simulations of excited-state NAMD in various nanorings at room temperature. (A) Internal conversion at room temperature (T = 300 K) in [9]-, [12]-, [14]-, [15]-, and [16]CPP molecules after excitation to S_2 and S_3 states. (Top) Percentage of population in S_1 state, showing rapid relaxation within 200 fs in all CPP molecules; (bottom) time dependence of the average participation number of the phenyl ring, demonstrating ultrafast spatial localization of photoexcitation within 50 fs. (B) Time dependence on the average fraction of transition density localized on the acene and phenyl rings for naphthalene (CPPN), anthracene (CPPA), and tetracene (CPPT) for the corresponding spatial redistribution of transition densities (right). (C) Evolution of electronic-state populations during relaxation of [4]CPY from the initial excitation S_{22}−S_{25} to the lowest energy state S_1 (left top), with the corresponding contour plots of the probability density of the current electronic state (left bottom) and the probability density of participation number (right) during excited-state NAMD for each state on each pyrene monomer. Panel A: Reproduced with permission from ref 627. Copyright 2014 American Chemical Society. Panel B: Reproduced with permission from ref 631. Copyright 2016 Springer Nature. Panel C: Reproduced with permission from ref 311. Copyright 2017 The Royal Society of Chemistry.

photoexcitation, before relaxation to a final lowest energy exciton state, allowing for insights into their fluorescent properties.[627] In the particular case of the cycloparaphenylenenes ([n]CPPs),[628] which consist of n phenyl units connected in a conjugated periodic chain (insets in Figure 14A), their efficient fluorescence is a consequence of an ultrafast spatial localization (or self-trapping) of the lowest excitonic state (S_1) due to electron−phonon couplings, which is facilitated by a nonadiabatic relaxation from higher energy states. This behavior breaks the Condon approximation and the optical selection rules (which state that in the homogeneous circular system the lowest excited state delocalized across the entire molecule is dipolar forbidden) are overridden. Namely, at ground-state geometries, the lowest S_1 state of CPPs is node-less and its TD (section 3.5) is mainly delocalized across the entire nanoring. Therefore, S_1 presents a weak oscillator strength in the absorption spectra at room temperature and precludes effective fluorescence. However, spontaneous symmetry breaking makes these materials superior fluorophores. A quantitative time-dependent measure of exciton delocalization across the NAMD trajectories can be provided by the participation number $P_{ring}(t)$ (see section 3.5) that evaluates the average number of phenyl units over which the excited-state wavefunction is delocalized. This scenario of an ultrafast internal conversion to S_1 is shown in Figure 14A (top) with a concomitant gradual spatial localization of the exciton in Figure 14A (bottom) for [n]CPPs nanorings of different sizes. This behavior, however, is not observed in smaller systems where the bending strain rigidifies the structure and prevents localization. Generally, the non-radiative dynamics becomes faster and is accompanied by more efficient localization with an increase of the nanoring size. Thus, the photoinduced dynamics of CPPs introduces structural distortions that localize the wavefunction enabling efficient fluorescence.

The exciton self-trapping in nanorings can be further tuned by intentionally breaking the circular symmetry of CPPs with the insertion of other organic compounds between phenyls, like acene units (insets in Figure 14B). Tracking the fraction of TD localized on the acene units after photoexcitation of these nanorings,[629,630] the NAMD results reveal that the exciton self-trapping effectiveness increases with the size of the acene unit (Figure 14B).[631] While the insertion of naphthalene (CPPN) does not essentially modify the TD localization, the insertion of anthracene (CPPA) or tetracene (CPPT) has a much stronger impact. Both CPPA and CPPT experience an ultrafast intramolecular energy redistribution after photoexcitation that implies a gradual migration of the exciton toward the acene trap, making the process more efficient and directional in CPPT, with a decreasing effect in CPPA that is further reduced in CPPN. CPPs with inserted acene units can be viewed as a "quasiparticle on a circle with a local potential well", with tetracene representing a deeper well compared to anthracene. The deeper the well, the more efficient exciton self-trapping appears on the acene defect states.

The complex interplay between transient localization/delocalization of the TD on the different electronic excited states that participate in the nanorings internal conversion is further illustrated for the case of the circular pyrene tetramer [4]cyclo-2,7-pyrenylene ([4]CPY) shown in Figure 14C.[311,632] The internal conversion of [4]CPY is dominated by an ultrafast sequential relaxation through the dense manifold of excited states with two long-lived intermediates (S_{10} and S_{21}) separated from lower states by large energy gaps. These two bottleneck states have unique features related to their TD localization. While the majority of excited states of [4]CPY within the ∼280−400 nm energy range are delocalized across multiple pyrene units, the bottleneck states are characterized by a collapse of TD on a single pyrene unit (see Figure 14C). These mismatches in the TD localizations decrease the overlap of the excited-state wavefunctions with energetically neighboring states, which, along with the large energy gap, substantially reduce the NACs. As a consequence, the lifetime and transient accumulation of population in these states become larger compared to other states. Furthermore, in analogy to photoinduced localization of the S_1 state in [n]CPPs, the transient collapses of TD in [4]CPY observed in NAMD are a consequence of structural distortions arising during the internal conversion process.[311]

https://dx.doi.org/10.1021/acs.chemrev.9b00447
Chem. Rev. 2020, 120, 2215−2287

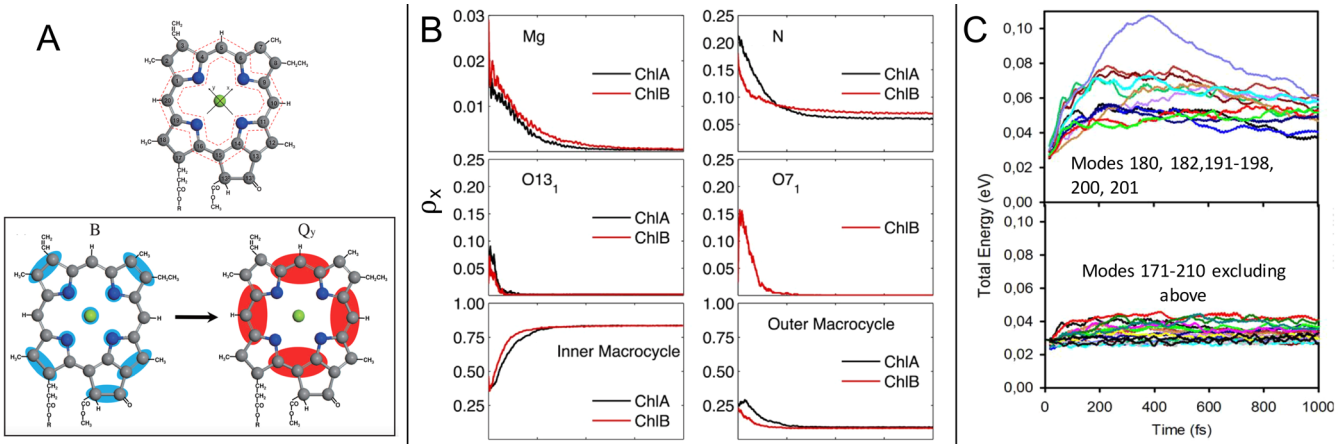

Figure 15. Fewest-switches surface-hopping simulations of excited-state NAMD in Chls at room temperature. (A) Molecular structure of chlorophyll A (ChlA). Carbon, nitrogen, and magnesium atoms are in gray, blue, and yellow, respectively. The total carbon macrocycle is defined as the carbon atoms comprising the porphyrin ring structure, whereas the "inner macrocycle" consists of the atoms between two red dashed lines excluding the N atoms, and the "outer macrocycle" is comprised of carbon atoms from the total carbon macrocycle minus those in the inner macrocycle. (B) Time dependence of the fraction of transition density in ChlA (black) and ChlB (red) localized on different regions. (C) Time evolution of the total vibrational energy associated with normal modes 180, 182, and 191−201 (top) and all the other normal modes from 171 to 210 (bottom) for ChlA. Panels A and B: Reproduced with permission from ref 644. Copyright 2015 Springer Nature. Panel C: Reproduced with permission from ref 548. Copyright 2016 American Chemical Society.

4.2. Non-radiative Relaxation of Photoexcited Chlorophylls

In natural photosynthesis, solar energy is converted into chemical energy through complex arrays of conjugated chromophores.[633,634] Because of its well-known structure, the Fenna−Matthews−Olson (FMO) complex[635] and Chl pigment dimers[636−638] have become popular systems for both experimentalists and theoreticians to study the efficient energy conversion process of natural light-harvesting organisms.[639]

Photosynthesis starts with light harvesting performed by antenna complexes in which Chl pigments play the main role.[640−642] Chls are basically composed of a porphyrin ring[643] coordinated to a Mg atom (Figure 15A). The two types of Chls that exist in the photosystems of green plants, ChlA and ChlB, differ only by an extra carbonyl oxygen at the C_7 position in ChlB. The photoexcitation and subsequent efficient non-radiative relaxation leading to intra/intermolecular energy redistribution of the excess energy initially localized on high-energy excited states, Soret (B) band, to the lowest, Q_x and Q_y, excited states in Chls is one of the initial steps in the sophisticated biological machinery that converts light into chemical energy.

The NAMD simulations can provide information about some of these processes, particularly those occurring on ultrafast time scales complementing time-resolved spectroscopic probes. For example, the slight structural difference between ChlA and ChlB leads not only to differences in their absorption spectra but also different $B \rightarrow Q_x \rightarrow Q_y$ internal conversion rates and mechanisms.[644] While $B \rightarrow Q_x$ transfer is faster in ChlB, the $Q_x \rightarrow Q_y$ transfer is faster in ChlA. The ratio of final relaxation rates, $\frac{k(B \rightarrow Q_y)_{\mathrm{ChlA}}}{k(B \rightarrow Q_y)_{\mathrm{ChlB}}} = 1.18$, obtained from FSSH modeling, indicates a slightly faster internal conversion process in ChlA than in ChlB, in good agreement with the value of 1.13 obtained from ultrafast transient absorption spectroscopy measurements.[644]

The NAMD results contain detailed insights that are not available from experiment. For example, as shown in Figure 15B, differences in internal conversion rates between ChlA and ChlB can be rationalized in terms of time-dependent localization of the wavefunction on specific atoms and groups through the analysis of TD flux (section 3.5). First, we can focus on specific atoms like Mg, N, and carbonyl O atoms. Second, we can group the atoms in an *inner carbon macrocycle* and an *outer carbon macrocycle* (see Figure 15A). The main aspects revealed by the time-evolution of the different fractions of TD during the internal conversion from $B \rightarrow Q_x \rightarrow Q_y$ in ChlA and ChlB are (a) the overall TD moves from the *outer carbon macrocycle* as well as the Mg, N, and carbonyl O atoms to the *inner carbon macrocycle*; (b) the extra carbonyl O atom ($O7_1$ in ChlB) plays a significant role in directing the TD flux.

The photoinduced intramolecular electronic energy relaxation and redistribution that takes place during the $B \rightarrow Q_x \rightarrow Q_y$ internal conversion of Chls is accompanied by vibrational energy redistribution. This intramolecular vibrational flow can be monitored by tracking the time-evolution of the vibrational energy accumulated on individual equilibrium normal modes.[548] The potential energy of individual normal modes becomes coupled during simulations at room temperature. Therefore, the total vibrational energy associated with a given mode can be approximated using the virial theorem as twice its kinetic energy. Figure 15C displays the variations of the vibrational energy for different middle- and high-frequency normal modes during the $B \rightarrow Q_x \rightarrow Q_y$ internal conversion in ChlA. It can be clearly seen that the intramolecular vibrational energy redistribution is not statistical, since the transient accumulation of vibrational energy is not the same for all modes. Only ∼12 middle- and high-frequency modes, that is, less than 5% of vibrations, actively participate in the process as indicated by a substantial increase in their vibrational energies. These active modes are characterized by the highest overlap with the NACR during electronic transitions. While the direction of NACRs correspond to the direction of the main driving force on the nuclei during electronic transitions, the active modes appear as the main nuclear degrees of freedom that couple the electronic excited states in the vicinity of level crossings. Furthermore, active modes can be classified according to their alignment with NACRs involved in either $B \rightarrow Q_x$ or $Q_x \rightarrow Q_y$ electronic ET.

https://dx.doi.org/10.1021/acs.chemrev.9b00447
Chem. Rev. 2020, 120, 2215−2287

Further statistical analysis reveals that distinct pathways for internal conversion can be identified according to the participation of different active modes.[548] The rest of the modes can be considered as a relaxation bath for the excess of vibrational energy transiently accumulated in these few active modes.

Importantly, in biological LHCs, Chls are electronically coupled. Subsequently, the typical photoexcitation is ultimately delocalized over several molecules which is concomitant to the global energy flux.[636] While we will later address the question of coupling and ET in detail (section 5), here we consider how an efficient intramolecular $B \rightarrow Q_y$ internal conversion is accompanied by ET between coupled neighboring pigments. The interplay and relative time scales of the inter- and intramolecular ET between Chls have been explored using NAMD simulations[636] selecting a ChlA dimer system (Figure 16A) from the LHCII of *Spinacia oleracea*. The overall calculated

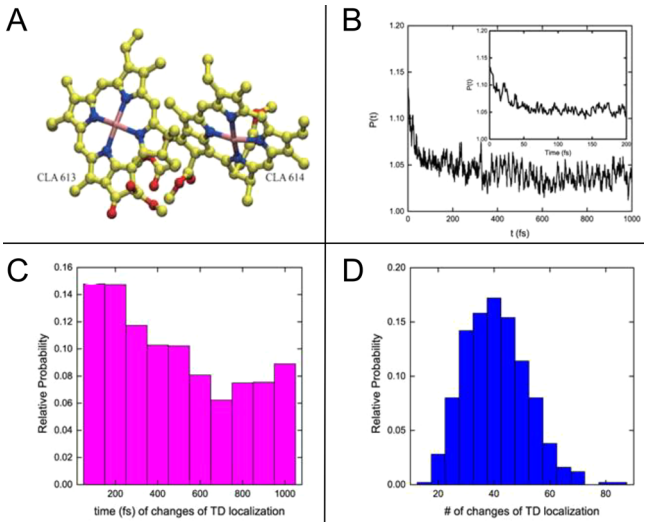

Figure 16. Fewest-switches surface-hopping simulations at room temperature of excited-state NAMD in the ChlA dimer. (A) Chemical structure of the ChlA dimer in the LHCII complex. (B) Time evolution of the participation number, P(t), of ChlA dimer. (C) Relative probability of exciton exchange between monomers as a function of time. (D) Histogram of the number of TD localization changes between monomers during the excited-state NAMD. Reproduced with permission from ref 636. Copyright 2017 American Chemical Society.

$B \rightarrow Q_y$ internal conversion in a ChlA dimer is faster than that in an isolated ChlA monomer. Indeed, dimerization induced energy level splittings in the ChlA dimer reduce the effective energy gaps between the excited states and ultimately lead to a faster relaxation rate compared to a single ChlA. Here both intra- and inter-Chl electronic exciton relaxation and redistribution compete on the same time scale. Both ChlAs are photoexcited with nearly equivalent probabilities generating a weakly delocalized state. After that, the excited-state NAMD leads to an ultrafast localization of the exciton on a single ChlA. This can be seen in Figure 16B, where the time-evolution of the participation number between monomers is depicted. The final localization of the exciton on an individual ChlA is a consequence of the thermal fluctuations at room temperature, evaluated as the average fwhm of the excitation energy distributions (~1023 cm^{-1}), which generally exceeds electronic coupling between intraband states, evaluated as half of the average energy splitting between states (~305, 224, and 398 cm^{-1} for B, Q_x, and Q_y band states, respectively). However, during the relaxation process, frequent passage through phase space domains with strong NACs promotes transient exciton delocalization and inter-ChlA energy exchanges that persist through the simulation. Figure 16C shows the time dependence of the relative probability for exciton exchange events between ChlAs. A high average number of exciton hops between ChlAs is consistently observed during relaxation dynamics (Figure 16D). Overall, each ChlA experiences an intra-ChlA internal conversion process similar to the one reported for isolated ChlAs (see Figure 15) but subjected to persistent incoherent inter-ChlA exciton hops between localized excited states.

4.3. Photochemical Processes Involving Bond Breaking

Non-radiative relaxation through multiple electronic excited states (intraband relaxation) gives rise to both photophysical and photochemical phenomena. Photophysics typically involves ET, exciton localization/delocalization, and/or charge separation, while photochemistry refers to isomerization, generation of radicals, and bond breaking/formation reactions (Figure 1). Many photochemically active materials play important roles in technological applications ranging from photovoltaics[645,646] and photodegradable plastics,[647,648] to optically sensitive explosives[649,650] and are ubiquitous in biology,[651,652] atmospheric science,[653] and environmental chemistry.[654] The complete theoretical formulation of NAMD simulations in the excited states for photochemical processes in realistically large extended molecular systems remains an ongoing challenge. Such a description should necessarily include open-shell NAMD algorithms. The majority of current NAMD codes[112] describe the system by a spin-restricted wavefunction as a closed-shell system, that is, all electrons are paired and electrons of opposite spin occupy the same orbital. This fundamental limitation excludes molecules with open-shells, or unpaired electrons, such as radical species commonly encountered during chemical reactions.[655] Open-shell treatment is also necessary for the description of high-spin states accessible during photoexcited dynamics (e.g., in photovoltaic materials,[656] water-splitting reactions,[657−659] and generally any photocatalytic process[244,660,661]).

An example of typical molecular evolution during the photochemical process is schematically presented in Figure 17A for nitromethane, a high explosive known to undergo photolysis and/or photoisomerization upon UV irradiation.[662−664] Closed-shell representations describe dynamics in *Region I* (or photophysics). Here, for example, closed-shell FSSH simulations of NAMD in nitromethane confirmed the spectroscopically measured excited-state lifetime and total photolysis quantum yield as outlined in Figure 17B.[650] In contrast, photochemical reactions in *Region II* cannot be described. Closed-shell simulations may provide useful information on intermediate species,[649] however, the subsequent dynamics of intermediates leading to additional bond breaking or recombination of fragments to form final photoproducts cannot be followed. Ultimately the system relaxes to the ground or excited state of fragments (*Region III*) where the initial conditions and probabilities of a specific product are entirely defined by *Region II*.

Despite these limitations, closed-shell simulations have proven useful in identifying intermediate species and primary photochemical pathways in several photoactive energetic materials.[649,650,665,666] For example, NAMD simulations of energetic tetrazine derivatives provide estimates on formation of

https://dx.doi.org/10.1021/acs.chemrev.9b00447
Chem. Rev. 2020, 120, 2215−2287

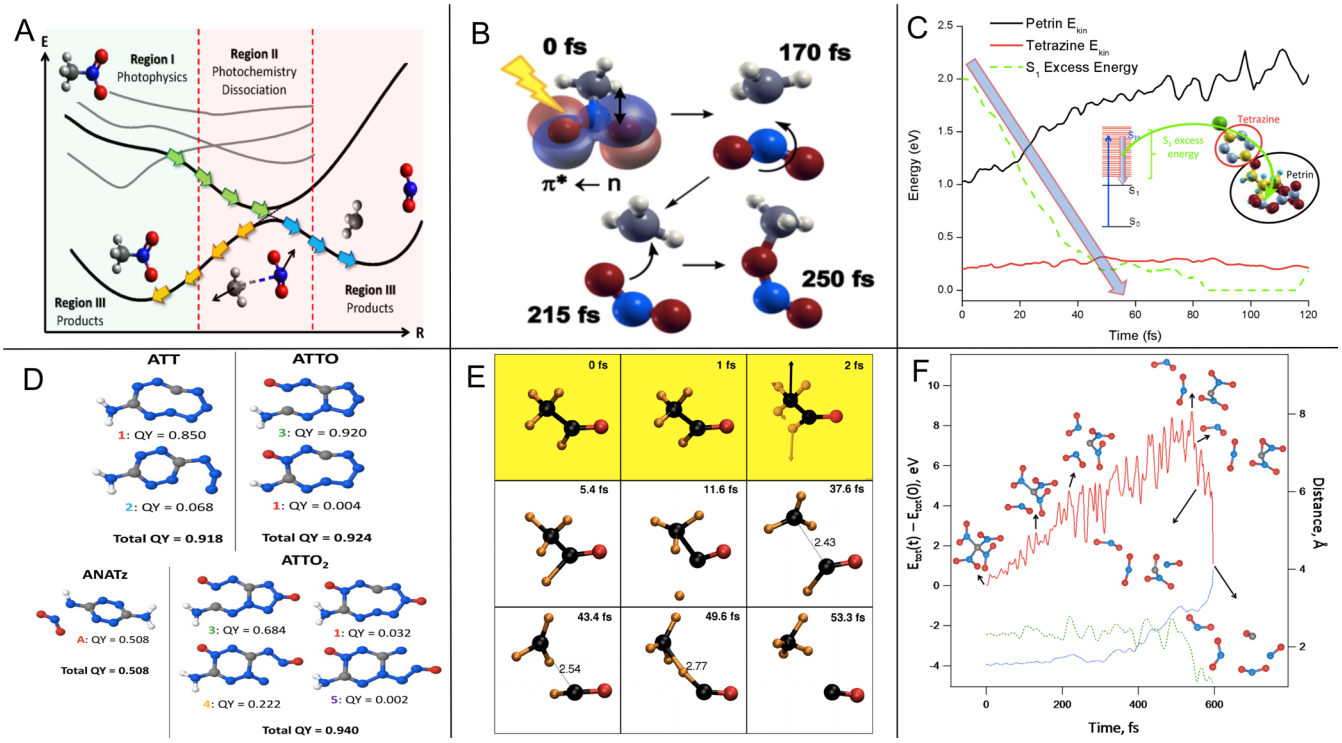

Figure 17. (A) Schematic representation of excited-state PESs involved in nitromethane dissociation. Closed-shell dynamics only describes photophysics (*Region I*). Photochemistry (*Region II*) requires open-shell description for dissociation. Dynamics of photoproducts (*Region III*) appears in the ground and/or excited states. (B) Nitromethane isomerization following excitation to the nπ^* state occurs in the excited state through bond breaking and subsequent re-formation on an ultrafast time scale. (C) Transfer of excess electronic energy in PetrinTzCl from the initially photoexcited tetrazine chromophore to an energetic PETN moiety resulting in NO_2 dissociation, modeled using closed-shell NAMD. (D) Initial bond-breaking steps and quantum yields following photoexcitation of O-substituted bicyclic conjugated energetic materials. Quantum yields are computed as the fraction of total FSSH trajectories that undergo the indicated bond cleavage as the initial step in dissociation. High atomic oxygen content opens additional photodissociation pathways targeting the oxygen-substituted sites. (E) Spin-unrestricted open-shell TD-DFT surface-hopping trajectories of non-adiabatic photodissociation of acetaldehyde showing CO + CH_4 formation. Yellow and white backgrounds indicate that the trajectory is in the S_1 and S_0 states, respectively. Spin symmetry breaking is detected by monitoring triplet instability, and S_1/S_0 transitions are enforced when the energy gap falls below a threshold. (F) Photofragmentation dynamics of tetranitromethane explored via u-TDESMD. The energy diagram shows single-point calculations for intermediates taken from u-TDESMD simulations. The red solid, blue short dashes, and green long dashes represent total energy, average C−N distance, and C−O distance for selected atoms, respectively. The diagram illustrates activation energies for several steps of ultrafast cracking reactions. Panel B: Reproduced with permission from ref 650. Copyright 2016 American Chemical Society. Panel C: Reproduced with permission from ref 649. Copyright 2015 American Chemical Society. Panel D: Reproduced with permission from ref 665. Copyright 2018 American Chemical Society. Panel E: Reproduced with permission from ref 670. Copyright 2016 American Chemical Society. Panel F: Reproduced with permission from ref 674. Copyright 2017 American Chemical Society.

photoproducts.[649] Pentaerythritol tetranitrate (PETN), a high explosive, initiates with traditional shock and thermal mechanisms. The tetrazine-substituted derivative of PETN, pentaerythritol trinitrate chlorotetrazine (PetrinTzCl), has been investigated for a photochemical initiation mechanism. Closed-shell simulations of the NAMD demonstrate that the relaxation mechanism leading to the experimentally observed photochemistry in PetrinTzCl, is due to vibrational excitation during internal conversion. The initial tetrazine localized excitation ~2.5 eV above the lowest energy excited state decays non-radiatively, and the excess electronic energy from photoexcitation is dissipated as vibrational kinetic energy in the PETN moiety leading to dissociation of NO_2 as shown in Figure 17C.[649]

Similarly, the photodissociation of conjugated energetic materials displayed in Figure 17D was also studied using closed-shell simulations of the NAMD to reveal the initial bond breaking pathways and photochemical quantum yields for O-substituted bicyclic tetrazine derivatives. The simulations revealed that O-substitution has two primary effects. First, additional O on the bicyclic framework causes the overall electronic relaxation process to become slower by enhancing intermediate excited-state lifetimes. That corresponds to a slower rate of photodissociation. Second, ring expansion occurs in all of the bicyclic compounds and is the dominant initial bond breaking event in the unsubstituted compounds. In the O-substituted compounds, the competing pathway of ring opening at the O-substituted site becomes the primary pathway. O-substitution introduces photodissociation pathways that always involve the functionalized site, suggesting a strategic chemical modification for targeting specific photochemical functionality.[665]

So far, the NAMD of open-shell systems has been achieved using spin-symmetry broken TD-DFT to describe the S_1 to S_0 transition. Spin-symmetry broken DFT has been previously used to accurately describe ground-state diradicals and for the BOMD simulations of polyradicals.[667,668] Recently, Furche and co-workers have applied the same methods to model non-adiabatic effects in photodissociation using the FSSH algorithm with spin-symmetry broken TD-DFT. The approach relies on

https://dx.doi.org/10.1021/acs.chemrev.9b00447
Chem. Rev. 2020, 120, 2215−2287

detecting triplet instabilities, according to the stability analysis of the restricted Kohn−Sham (RKS) equations.[669] At each time step in the NAMD, the stability analysis is performed for the closed-shell ground-state solution and if a triplet instability is detected, then the spin-symmetry broken ground state is used for the subsequent TD-DFT calculations, which provides a transition to *Region II* in Figure 17A. This method was applied to describe the homolytic bond cleavage in Acetaldehyde (Figure 17E)[670] and TiO_2 photocatalytic nanoparticles.[244] The photodissociation of Acetaldehyde depicted in Figure 17E was investigated using both BOMD and spin-symmetry broken NAMD. The comparison revealed that only the NAMD simulations could properly reproduce the high-energy tail in the experimental kinetic energy distributions. The occurrence of non-adiabatic transitions alters the photodissociation dynamics of acetaldehyde by enhancing kinetic energy in the direction of the NACR. The effect is strong enough to selectively enhance certain dissociation channels such as the one shown in Figure 17E. Most importantly, this work has highlighted the importance of radical pathways, *even in systems with closed-shell reactants and products*.[670]

Simultaneous efforts in the group of Kilin have led to the development of the spin-resolved electronic dynamics approach (SREDA)[671] specifically designed to model the relaxation channels in transition metal compounds that often exhibit open-shell non-singlet configurations. The method uses spin-unrestricted DFT based time-dependent excited-state molecular dynamics (u-TDESMD) algorithms for NAMD based on Rabi oscillations and principles similar to trajectory surface hopping. The spin-polarized DFT framework allows orbital energies, changes in valence and conduction bands, relaxation channels, and appearance of trap states to be analyzed separately for α and β spin projections. This approach has been successfully applied to model spin-resolved charge-transfer dynamics in doped TiO_2 nanowires,[671,672] photofragmentation in lanthanide complexes[673] and tetranitromethane (Figure 17F).[674]

Finally, in small systems (about 10 atoms) high accuracy ab initio wavefunction approaches such as AIMS[62,675] or QM simulations at the MCTDH[61] level of theory can be used to describe open-shell dynamics. For example, multireference configuration interaction (MRCI) and CASSCF have been successful in modeling dynamics of homolytic bond breaking using spin eigenstates in pyrrole[676] and adenine.[282] However, such methods quickly become prohibitively expensive for extended molecular systems when including all nuclear degrees of freedom.

5. APPLICATIONS: ENERGY TRANSFER IN MOLECULAR AGGREGATES

Designing and controlling directional ET in synthetic light-harvesting materials[677−687] that mimic natural photosynthetic complexes underpins many technological applications including organic photovoltaics,[688] light emitting diodes,[689] and sensors.[690] A typical multichromophore system or a molecular aggregate consists of coupled π-conjugated chromophores which can be molecular units in the superstructure (e.g., dendrimer). The electronic structure of such systems can be well described with coarse-grained Frenkel exciton Hamiltonian approaches.[691−694] Strong coupling typically results in delocalized electronic states and gives rise to spectroscopic signatures of excitonic bands,[695] which are also manifested in the intermediate coupling regime characterized by partially localized excitations.[696−698] In this case, the methodology for interpreting vibronic spectra in terms of splitting due to both intra- and intermolecular vibrations has already been demonstrated.[696,699,700] In the case of weak coupling, electronic excitations are localized on individual chromophores. Here the excitation energy transfer (EET) can be modeled using the Förster resonance energy transfer (FRET) framework.

Experimentally, EET dynamics is commonly studied using a variety of time-resolved spectroscopies, such as 2-D electron spectroscopy (2DES)[701−703] or pump−probe and transient absorption experiments.[549,704−706] For example, time-resolved fluorescence anisotropy can be used to detect changes in polarization resulting from excitation localization and migration. Such measurements have been used to investigate energy migration and electronic relaxation in light harvesting systems[707,708] such as chromophore rings,[683,684,709] dendrimers,[710] conjugated polymers,[711−713] and chromophore dimers.[714,715] Such spectroscopic probes are very precise and provide detailed information on EET. These need to be met by the corresponding NAMD simulations at the atomistic level. Besides NAMD, semiclassical kinetic/Marcus/Fermi's golden rule approaches have also been successfully applied to describe the photoinduced charge- and energy-transfer processes (see reviews in refs 716−718).

In the NAMD modeling, the excited-state electronic wavefunction typically undergoes multiple delocalization and localization cycles in the course of ET. Specific nuclear vibrations are frequently responsible for bringing electronic states into resonance and promoting the energy exchange between them. The coherent evolution of electronic and vibrational degrees of freedom is well established across an array of theoretical and experimental studies.[50,719−722] Notably, in multichromophore systems, the energy levels and excitation localization can be very sensitive to geometry distortions and morphology changes[310,549,579,588,697,723−729] and trivial unavoided crossings are common during dynamics. Therefore, properly accounting for trivial unavoided crossings when modeling photophysics in such systems is critical (see section 3.4.3). We will illustrate the essential EET aspects appearing in the NAMD simulation of multichromophore aggregates in the subsequent subsections.

5.1. Interactions in Weakly Coupled Chromophores

Dimers composed of two identical chromophore units are the simplest multichromophore systems making them excellent models for studying complex photophysics involving the interplay between intra- and intermolecular interactions and effects of vibrational motions on electronic dynamics. Different interaction regimes, based on the relative intermolecular coupling strength between chromophores in a dimer, produce a variety of electronic effects. In weakly coupled dimers, a stochastic hopping mechanism can occur where excitations move between localized sites. Exciton hopping is characterized by short-range interchromophore energy migration between adjacent localized sites (chromophores).[730−733] If geometric distortions are not sufficient to bring electronic states into resonance, then exciton hopping will be absent, and the complete relaxation can occur within a single chromophore unit. In that case, localization persists in a single unit, where the choice of chromophore is randomly distributed. The variation in the strength of the NACs, which modulate the interaction between the electronic and vibrational degrees of freedom, and the extent of exciton localization, both contribute to the final electronic distribution among different chromophore units following EET.

https://dx.doi.org/10.1021/acs.chemrev.9b00447
Chem. Rev. 2020, 120, 2215−2287

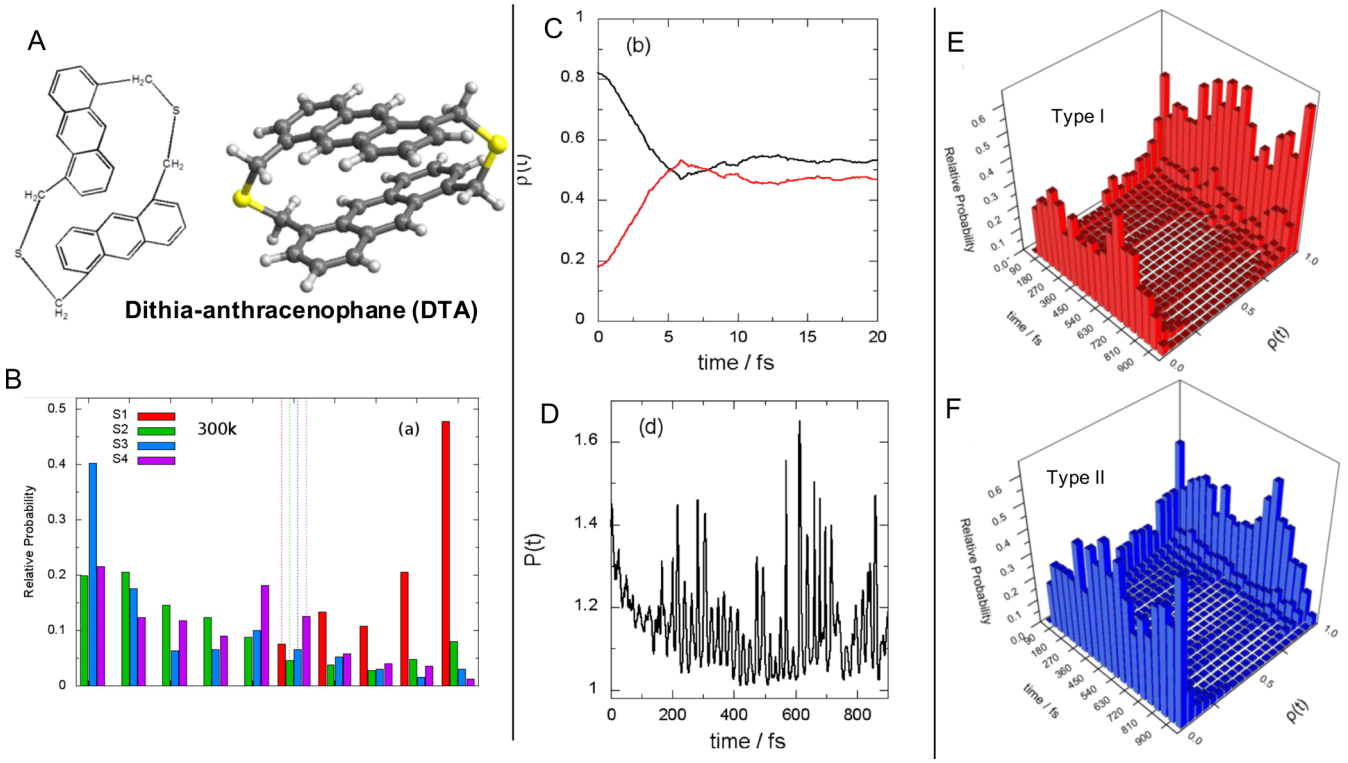

Figure 18. Fewest-switches surface-hopping simulations at room temperature of excited-state NAMD in dithia-anthracenophane (DTA) bichromophore. (A) Chemical structure and optimal ground-state geometry of the weakly coupled DTA. (B) Equilibrated ensemble of the transition density (TD) of the four lowest energy excited states in the monomer where S_1 is initially localized (bottom). The dashed lines correspond to the equilibrium geometry. S_1 and S_3 are localized on different monomers, and S_2 and S_4 are more delocalized between the two monomers. (C) Time evolution during non-radiative relaxation of the average fraction of TD localized on either DTA monomer. The black line corresponds to the monomer where S_1 is initially localized. (D) Corresponding evolution of the participation number (defined taking the monomers as units), where a value of 1 indicates localization to a single monomer unit and a value of 2 indicates complete delocalization (see section 3.5). (E) Histogram of the TD evolution in DTA during non-radiative relaxation for type I trajectories (final TD primarily localized on the same monomer as the initial TD). (F) Same as panel E but for type II trajectories (final TD primarily localized on the opposite monomer as the initial TD). Reproduced with permission from ref 734. Copyright 2015 American Chemical Society.

These effects have been demonstrated in NAMD simulations of ET in numerous dimers and systems with equivalent chromophores.[246,310,549,588,636,734] As an example, we revisit the dithia-anthracenophane (DTA) dimer shown in Figure 18A, composed of two weakly coupled anthracene units. At the ground-state optimized geometry, excitonic coupling between the chromophore units induces delocalization of the four lowest energy excited states over both anthracenes. The delocalization does not persist during room temperature ground-state dynamics due to thermal fluctuations that break the structural symmetry[735−737] overcoming electronic interactions. At room temperature, S_1 and S_3 states are strongly localized in different monomers while S_2 and S_4 are more delocalized, as seen in the histogram in Figure 18B. S_1 and S_3 dimer excitations correspond to the antisymmetric Davydov component of the S_1 and S_2 monomer states, respectively. Similarly, S_2 and S_4 dimer states arise from the symmetric combinations of monomer states. Thermally induced geometry distortions along the center of mass coordinate and the angle between the anthracene planes causes the TD of the four lowest energy excited states to sample regions of configuration space where strong localization occurs, consistent with the localization observed in the ensemble at room temperature (Figure 18B). These coordinates involve collective relative displacements between the anthracene units and are thus expected to be related to low frequency normal modes of the dimer.

The evolution of the average TD localized in each anthracene unit (Figure 18C) provides a picture of the exciton dynamics of the ensemble. The anthracene units are distinguished based on the TD localization of the initial excited state with monomer A having the larger initial fraction of TD. The decay of the TD of A coincides with the rise in the TD of B, such that both arrive at 50% within 10 fs. Since this is an ensemble average, it does not reveal the actual distribution (or the actual underlying composition of the distribution) of the exciton localization. Instead, Figure 18C reveals that within 10 fs, monomers A and B are no longer distinguishable as the average fraction of TD in each unit becomes more or less equivalent on a very fast time scale. The evolution of the participation numbers (Figure 18D) suggests that fast localization to each monomer unit occurs with equal probability, opposite to the case of fully delocalized excitation across the anthracenes.

In surface hopping, there can be two types of trajectories: those whose final TD is primarily localized on the same monomer as the initial TD (type I), and those whose final TD is primarily localized in the monomer that initially had less TD (type II). That is, type II trajectories correspond to pathways that lead to an effective intermonomer ET at long times. Both types initially have 80% TD localized in monomer A. However, type I remains localized in the same monomer, while type II switches its localization to B. We find nearly half of the trajectories finish with the TD completely localized in the

https://dx.doi.org/10.1021/acs.chemrev.9b00447
Chem. Rev. 2020, 120, 2215−2287

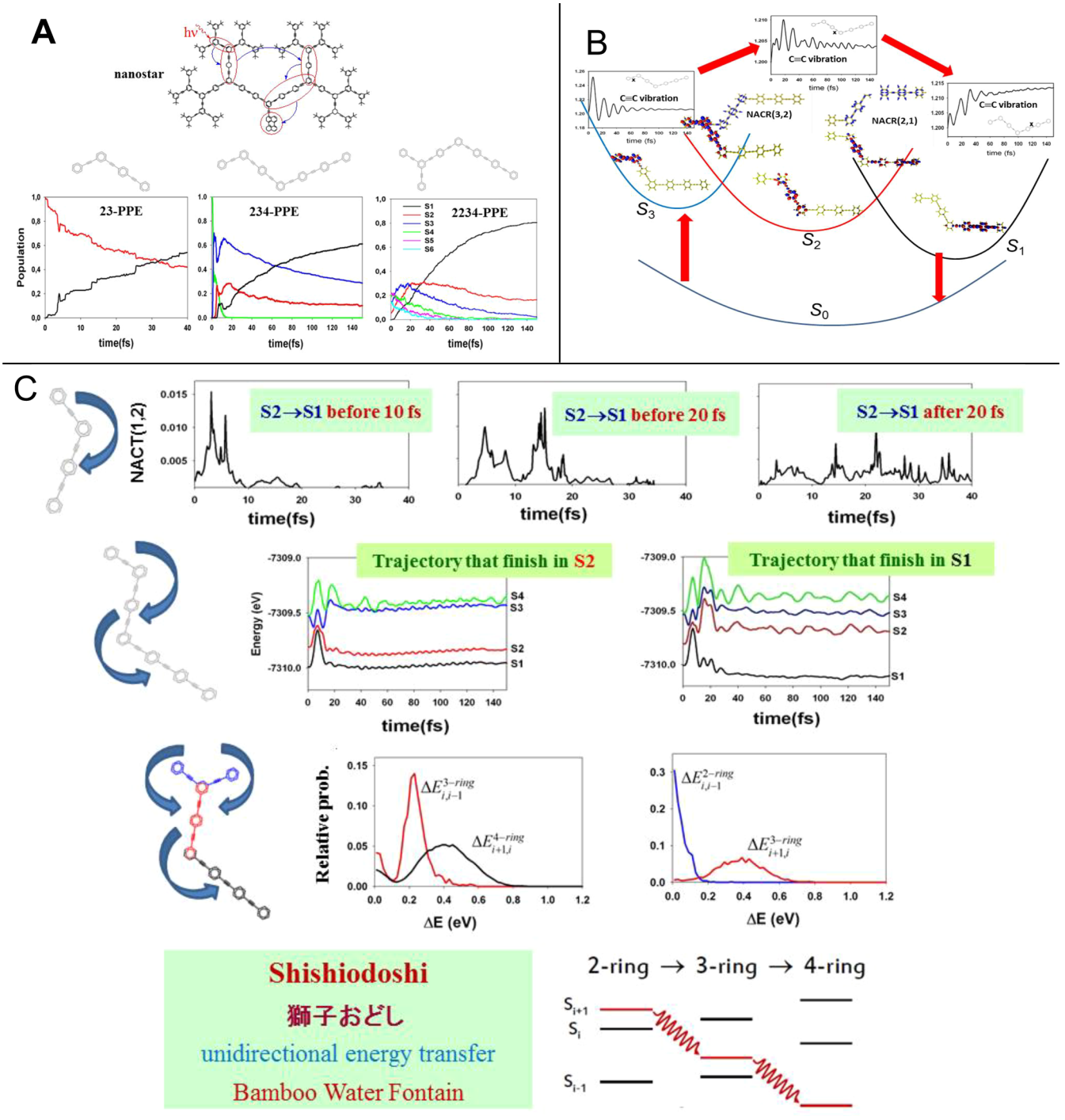

Figure 19. Fewest-switches surface-hopping simulations at room temperature of excited-state NAMD in various PPE dendrimers. (A) Scheme of the nanostar (top) and model PPE structures (bottom). Calculated evolution of the population of different adiabatic electronic excited states after initial photoexcitation at the absorption band corresponding to the 2-ring units, showing a gradual increase of S_1 population. (B) Unidirectional 2-ring → 3-ring → 4-ring electronic and vibrational energy transfer (ET) revealed by the transition density localization in PPE chromophores and excited C≡C stretching motion at each segment. Analysis of state-specific vibrations reveals excited-state normal modes responsible for ET and vibrational relaxation.[751,752] (C) Illustration of the Shishiodoshi mechanism that ensures the 2-ring → 3-ring → 4-ring unidirectional ET. Adapted with permission from ref 546, copyright 2018 AIP Publishing; ref 745, copyright 1994 American Chemical Society; ref 747, copyright 2003 American Chemical Society; and ref 748, copyright 2010 American Chemical Society.

initially excited monomer, while the other half of the trajectories finish with the TD completely localized in the opposite monomer. Figure 18E,F shows a constant transfer of the exciton from one monomer to the other, where the exciton is localized in one anthracene unit or the other but rarely delocalized between both. The initial damping is fast and is followed by persistent hops due to thermal fluctuations which can change the dynamics to incoherent resonance ET.

https://dx.doi.org/10.1021/acs.chemrev.9b00447
Chem. Rev. 2020, 120, 2215−2287

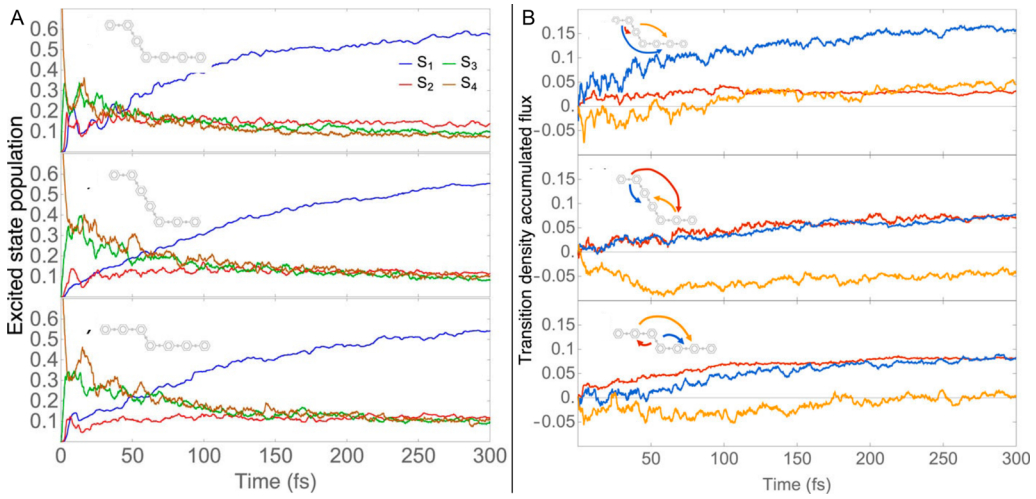

Figure 20. Ab initio multiple cloning−multiconfigurational Ehrenfest simulations at room temperature of excited-state NAMD in model PPE dendrimers. (A) Time-evolution of the average populations of different adiabatic electronic states obtained for 234-PPE (top panel), 243-PPE (middle panel), and 324-PPE (bottom panel). (B) The corresponding accumulated fluxes calculated for 234-PPE (top panel), 243-PPE (middle panel), and 324-PPE (bottom panel). Colored arrows in the sketch show the direction of the different fluxes, matching the colored curves. Reproduced with permission from ref 753. Copyright 2019 AIP Publishing.

5.2. Dynamics of Energy Transfer in Conjugated Dendritic Structures

Dendrimers are highly branched conjugated molecules with exceptional light harvesting capabilities over a broad region of the solar spectrum.[738−740] Their well-defined architecture guarantees highly efficient intramolecular ET between many different chromophore units. In particular, the family of dendrimers comprised of PPE units has been the subject of several theoretical and experimental studies.[741−743] Among them, the perylene-terminated dendrimer called the nanostar is perhaps the most studied compound.[744−746] It has a branched structure composed of four generations of linear PPE segments with decreasing lengths toward the periphery, creating an efficient energy funnel toward the perylene trap (Figure 19A). The different PPE segments are linked by meta-substitutions at the branching phenylene nodes where conjugation is broken and excitons are localized within each linear fragment. Therefore, the nanostar can be understood as an ensemble of linear chromophore PPE units with relatively weak coupling between them.[747,748] It exhibits a highly efficient light harvesting due to an efficient energy funneling from the periphery chromophores (2-ring units, high-energy spectrum) through the dendritic branches (3-ring and 4-ring units) to the perylene core.

5.2.1. Shishiodoshi Unidirectional Energy-Transfer Mechanism. Following the interpretation of the nanostar as an ensemble of individual coupled chromophore units, NAMD simulations helped develop a clear picture of its photoinduced dynamics providing a detailed description of the underlying photophysical processes such as exciton formation, localization/delocalization, NACs, ET between chromophore units, and efficient energy funneling. For this purpose, different structural building blocks have been addressed as model systems.[547,749−751] In all of them, internal conversion leads to an ultrafast highly efficient and unidirectional ET from the shortest PPE units (2-ring units) to the largest PPE units (3-ring or 4-ring units) as illustrated in Figure 19A. While the sequential *through-bond* pathway 2-ring → 3-ring → 4-ring represents the main mechanism of intramolecular ET, a significant contribution of the intramolecular *through-space* pathway 2-ring → 4-ring has been confirmed in the case of the 234-PPE building block.[547]

These NAMD simulations are schematically summarized in Figure 19B showing the internal conversion process of the 234-PPE building block.[751,752] The dynamics starts by photoexcitation of the molecule to a high-energy electronic state (S_3), leading to excess electronic and vibrational energy on the 2-ring unit. The vibrational energy can be tracked by monitoring the C≡C stretching motion on the 2-ring unit. During passages of the molecule through phase space domains close to the crossing seam with the lower S_2 state, the strong NAC promotes transient exciton delocalization. The main direction of ET is dictated by the NACR ($\boldsymbol{d}_{32}$) that in turn can be associated with specific excited-state normal modes. This leads to a $S_3 \rightarrow S_2$ transfer of electronic population, a localization of the exciton mainly in the 3-ring unit, and the concomitant excitation of the C≡C stretching motions across the 3-ring unit. The subsequent passage through the crossing seam between S_2 and S_1 leads to a new transient delocalization guided by normal modes aligned with the corresponding NACR ($\boldsymbol{d}_{21}$) direction. Once the molecule reaches the lowest S_1 state, the exciton becomes localized in the 4-ring unit and the corresponding C≡C stretches are excited. The results highlight the importance of using native excited-state gradients in the simulations directing energy flow into specific vibrations.

Accumulated data from studies on different systems underscores a common *shishiodoshi* mechanism behind an efficient unidirectional ET in PPE dendrimers (see Figure 19C). NAMD simulations of the 23-PPE system[749,750] reveal that after crossing the S_2/S_1 seam, the trajectories follow different pathways on either the S_1 or S_2 PES. Trajectories reaching the S_1 state move away to regions of low NAC, while trajectories remaining on S_2 continue lingering in the regions of strong NAC, which facilitates subsequent relaxation to S_1. This is shown in Figure 19C where the NACT averages are depicted for trajectories that hop at different times during relaxation emphasizing decreasing non-adiabaticity. That is, quantitative differences in the vibrational dynamics on the S_1 and S_2 states enhance the funneling ET mechanism. Figure 19C further highlights the time-evolution of excited-state energies for typical trajectories

https://dx.doi.org/10.1021/acs.chemrev.9b00447
Chem. Rev. 2020, 120, 2215−2287

performed on the 234-PPE molecule[751,752] that, after photoexcitation to S_3, relaxes to S_2 and S_1 states. While the trajectory that hops to S_1 moves in a phase space with a large energy difference between S_1 and S_2, the trajectory staying on S_2 remains in regions with a small S_1-S_2 energy gap (ΔE_{12}). This favors the $S_2 \rightarrow S_1$ transition since the NAC $\approx 1/\Delta E_{12}$, eq 2.6. This is reinforced by the analysis of the role of the nuclear differential motion on the different PESs performed for the internal conversion process in the 2234-PPE molecule.[547] Figure 19C displays histograms of the energy gap $\Delta E^{X\text{-ring}}_{a,a-1}$ between the S_a and S_{a-1} states and the energy gap $\Delta E^{X\text{-ring}}_{a+1,a}$ between the S_{a+1} and S_a states, while nuclei are moving on the ath state whose TD is more than 90% localized in the X-ring linear PPE unit (X = 2, 3, and 4). $\Delta E^{2\text{-ring}}_{a+1,a} < \Delta E^{3\text{-ring}}_{a+1,a}$ and $\Delta E^{3\text{-ring}}_{a,a-1} < \Delta E^{4\text{-ring}}_{a+1,a}$ ensure the unidirectional 2-ring → 3-ring → 4-ring ET, reminiscent of the stepwise water flow in a Japanese bamboo water fountain (Shishiodoshi).

5.2.2. AIMC-MCE Energy-Transfer Pathways in Dendrimer Building Blocks. Across this Review, we have shown that Ehrenfest and surface-hopping-like methods (section 2.2) remain the most popular approaches for NAMD simulations of large systems owing to their simplicity, straightforward implementation, low computational cost, and facile interpretation of the numerical results. On the other hand, these approaches are subject to multiple approximations as illustrated in sections 2.2 and 2.3. This raises a question of assessing the NAMD error bar for specific molecular families, which is difficult to answer given imperfect underlying electronic structure methodology and insufficiently detailed experimental data. The recent implementation of the accurate AIMC-MCE approach (section 2.5.4)[350] allows this problem to be addressed via direct comparisons. Notably, compared to Ehrenfest and surface hopping, the AIMC-MCE methodology more adequately samples the phase space through the trajectory trains, where decoherence corrections come naturally at the cloning events. The preliminary studies indicate that, for the PPE dendrimer class, the AIMC-MCE approach results in nonadiabatic transition rates, ET, induced vibrational dynamics, and evolution of electronic wavefunctions generally similar to the counterparts obtained from Ehrenfest and surface-hopping simulations. Moreover the machinery for analysis of physical processes and dynamics (section 3.5) remains directly applicable to the AIMC-MCE simulations.

To demonstrate, 234-PPE, 243-PPE, and 324-PPE molecules shown in the insets of Figure 20A were studied using AIMC-MCE and Ehrenfest approaches.[753] Here 100 snapshots were collected as initial geometries and momenta for both simulations (section 3.3.1). The NAMD simulations were then started by an instantaneous excitation of all systems to the S_4 state. On the time scale of about 10 fs, this state undergoes an ultrafast electronic energy relaxation to the lower excited states. In 234-PPE, this process is faster causing S_3 and S_4 states to show coherent in-phase oscillations that are out-of-phase with respect to S_2 and S_1 oscillations, which are attributed to C≡C stretching motions as mentioned in section 5.2.1. Such coherent electron-vibrational dynamics for the ensemble will be discussed in detail in section 5.4. After about 50 fs, these oscillations gradually disappear, while population on S_1 increases to 50% on the time scale of about 200 fs. S_2 seems to participate more actively in the electronic relaxation of 234-PPE than 243-PPE and 324-PPE, in agreement with the through-bond sequential transfer via $S_4/S_3 \rightarrow S_2 \rightarrow S_1$ mechanism observed with surface hopping and discussed in section 5.2.1. ET pathways between units can be further distinguished using the TD flux analysis described in section 3.5. Figure 20B illustrates the time evolution of the TD accumulated fluxes for each molecular system. In the case of 234-PPE, all intramolecular through-space and through-bond transfers go in the same direction for the relaxation process. The ET pathways in 243-PPE and 324-PPE are different from the ones observed in 234-PPE. In both cases, equivalent effective 2-ring → 3-ring and 2-ring → 4-ring fluxes are observed. However, due to geometries, the energy fluxes in 243-PPE and 324-PPE can be constructive or destructive, leading to the lower overall rate and efficiency compared to 243-PPE.

Overall, all methodologies (Ehrenfest, AIMC-MCE, FSSH) used for PPE dendrimers depict very similar non-radiative relaxation dynamics and are able to distinguish all dissipative pathways present in the systems. The relaxation rates to S_1 can be further compared by monitoring the rise of population in the S_1 state across an ensemble of trajectories. While the overall dynamics is comparable, we observe that AIMC-MCE rates are faster than those from Ehrenfest by about 15%, whereas the FSSH rates are faster compared to that of AIMC-MCE by roughly another 15%. This trend can be rationalized by recalling that the Ehrenfest dynamics uses an average force across the states (eq 2.18), which is effectively lower than the forces experienced by the cloned wavepackets in AIMC-MCE.[349,353] Furthermore, pristine FSSH relaxation dynamics is very fast. Empirical decoherence corrections slow it down significantly. The observed ∼15% difference in rates between FSSH and AIMC-MCE is likely dominated by the particular decoherence algorithm used in the simulation (in our case, the ID approach, section 2.4). Another practical consideration is the numerical expense underpinning these methods. For the PPE family of molecules, an Ehrenfest trajectory is about 5−10 times more computationally involved compared to its FSSH analog. Even though both simulations use the same on-the-fly calculations, Ehrenfest propagation requires shorter dynamical time steps ($\Delta t \approx 0.05$ fs compared to $\Delta t \approx 0.1$ fs for FSSH simulations) and calculation of gradients for all the excited states involved in the process (compared to the gradient of a single state in FSSH). The shorter time step arises due to the spiky behavior of the nonadiabatic contribution to the Ehrenfest force (second term of eq 2.18). The AIMC-MCE is about 5 times more expensive compared to the Ehrenfest analog, depending on the frequency of cloning events, which can drastically increase in the cases of dense excited-state manifolds. A significant advantage of all these approaches is parallel propagation of a swarm of trajectories allowing for a favorable scaling of computational resources.

5.2.3. Energy-Harvesting in Conjugated Dendrimers. Parallel experimental and theoretical investigations of photoexcited dynamics reveal unprecedented insights into the nature of physical processes. Moreover, a direct comparison with time-resolved spectroscopic measurements constitutes yet another critical evaluation of NAMD performance. Such experimental probes have been performed[310,549] for more complex PPE dendrimers denoted as 2g1m and ph3pg1[310,549] (see insets in Figure 21B,D). These are LHCs composed of multiple chromophore units. These systems can contain an explicit inherent energy gradient, as presented by 2g1m. Alternatively, if they are comprised of identical chromophore units, there are no internal energy gradients and the electronic states are differentiated only by thermal fluctuations, as in ph3pg1. In either case, the ET can involve excitations delocalized over multiple chromophores. For both 2g1m and ph3pg1,[310,549] good

https://dx.doi.org/10.1021/acs.chemrev.9b00447
Chem. Rev. 2020, 120, 2215−2287

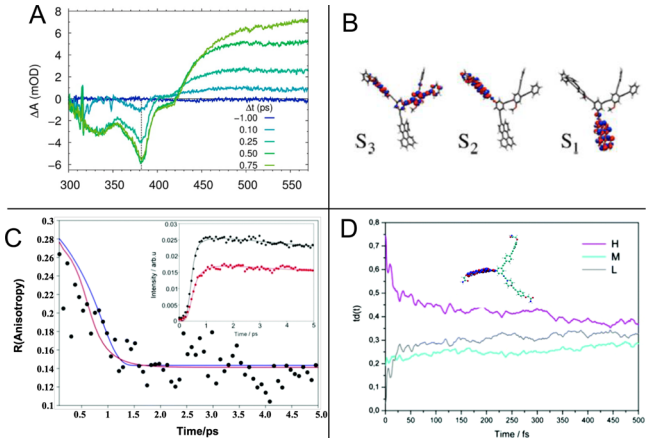

Figure 21. Experimental time-resolved spectroscopy and fewest-switches surface-hopping simulations of excited-state NAMD. (A) Room-temperature transient absorption spectra of the 2g1m dendrimer at different time delays following excitation at 315 nm, suggesting involvement of the intermediate localized transition in the backbone dendrimer. (B) Snapshot of the orbital representation of a typical transition density matrix for one NAMD trajectory. S_i ($i \geq 3$) states are spread over both branches, the S_2 state is localized in one phenylene-ethynylene branch, and S_1 is localized over the perylene fragment. (C) Fluorescence anisotropy data for the ph3pg1 dendrimer in THF solvent. Experimental decay, its fit, and simulations are shown in black, red, and blue, respectively. The inset shows time-resolved fluorescence data at parallel polarization (black dots) and perpendicular polarization (red dots), with their fitting given in solid lines. (D) Calculated time evolution of the fraction of transition density in the different ph3pg1 branches. The branches are assigned as high (H), medium (M), and low (L) according to the highest, intermediate, and lowest fractions of initial transition densities, respectively. Panels A and B: Reproduced with permission from ref 549. Copyright 2015 American Chemical Society. Panels C and D: Reproduced with permission from ref 310. Copyright 2016 The Royal Society of Chemistry.

agreements between surface-hopping NAMD simulations and experiments have been achieved.

In particular, transient absorption spectroscopy performed on 2g1m after photoexcitation at 315 nm, shows two main features:[549] the broad bleach signal extended over the whole absorption spectrum indicating the delocalization of excitation energy on the initially excited state; and a negative signal that appears with a maximum at 382 nm (light blue) and reaches a maximum at ∼500 fs and points to the participation of a transient localized state during energy relaxation (Figure 21A). The analysis of NAMD results for 2g1m[549] confirms that the initial excited states ($S_{\geq 3}$) are delocalized between both phenylene-ethynylene (PE) branches (Figure 21B). Thereafter, when S_2 becomes populated, the photoexcited wavefunction undergoes an ultrafast spatial collapse onto a single branch. This collapse is reminiscent of the slower exciton self-trapping process occurring on the picosecond time scale discussed in this Review, for example, in section 4.1. In the present case, this localization occurs due to non-adiabatic transitions between excited states driven by strong coupling to high-frequency vibrational modes. The differential nuclear motion on the PESs (discussed in section 5.2.1) modulates the energy difference between states and promotes a unidirectional downhill mechanism. The triple bond excitations in the PE dendrimer coincide with the localization of the electronic transition densities, meaning that the ET dynamics is a concerted electronic and vibrational ET process. This effect is captured in simulation by using the "native" excited-state forces which differ on each surface and promote vibrational relaxation toward the excited-state energy minimum. Finally, the molecule reaches the perylene sink in the lower part of the molecule where S_1 is localized and from where fluorescence occurs.

In another example, time-resolved fluorescence anisotropy measurements (Figure 21C) performed on the ph3pg1 dendrimer (inset in Figure 21D) have been reproduced using NAMD simulations. The agreement between NAMD and experiment has allowed further analysis of simulation results in order to elucidate the origin of the fast anisotropy decay. While initial photoexcitation localizes the exciton mainly in two chromophore units (∼80% in one branch and ∼20% in the other), the internal conversion process involves an intramolecular energy redistribution that leads to an equivalent final energy spread among all three chromophore units. This final distribution can be achieved either by a complete delocalization of the wavefunction among the three units or by one-third of the ensemble having the localization on each of the three different branches. Our simulations reveal that, as the excited-state dynamics evolves, a random distribution of self-trapped excitons on different units appears. Therefore, the experimental anisotropy decay can be assigned to the confinement of the electronic states with random probability in any of the individual units (similar to the distribution described in DTA in section 5.1). The NAMD simulations of ph3pg1 have been performed in vacuum so that the ultrafast self-trapping observed in this system cannot be caused by solvent interactions. It is interesting to note that the same effect has also been attributed to interactions with polar solvent.[754]

5.3. Energy Transfer beyond Förster Theory

EET is generally a specific case of internal conversion when transition between donor and acceptor excited states leads to a change of spatial localization of the wavefunction as was illustrated in the previous sections (sections 4.2 and 5.2). Nuclear motions, such as torsions and bond stretches, can lead to quasi-degeneracy of electronic states that are close in energy, and facilitate transition (such as the Shishiodoshi example in section 5.2.1). Beyond PPE, such structural reorganization after photoexcitation is a notoriously common case for a broad class of conjugated systems such as PPV,[618,755] poly(phenylene-ethynylene-butadiynylene),[756] MEH-PPV,[757,758] and polyfluorene.[759,760] The resulting geometry changes, mainly planarization, occur through torsional relaxation in the excited state. While planarization of conjugated oligomers is generally taking place on the picosecond time scale,[755] ultrafast ∼100 fs torsional relaxation in polyfluorene oligomers has been observed experimentally and confirmed with NAMD simulations.[759] This ultrafast torsional reorganization introduces large geometrical distortions on the same time scale as electronic relaxation (Figure 22A). Moreover, thermal fluctuations can help bring states into resonance, albeit the case of uncoupled states or trivial crossings (section 3.4.3) should be carefully distinguished. In any case, resulting resonant- or near-resonant proximity between coupled states in multichromophoric systems leads to non-adiabatic transitions changing the electronic character and localization of states. Because of the diverse conformational landscape accessible, ET in systems composed of multiple soft organic polymers and chromophores of similar conjugation length can rarely be described by a single well-defined pathway due to conformational variety involving multiple units.[579,712]

https://dx.doi.org/10.1021/acs.chemrev.9b00447
Chem. Rev. 2020, 120, 2215−2287

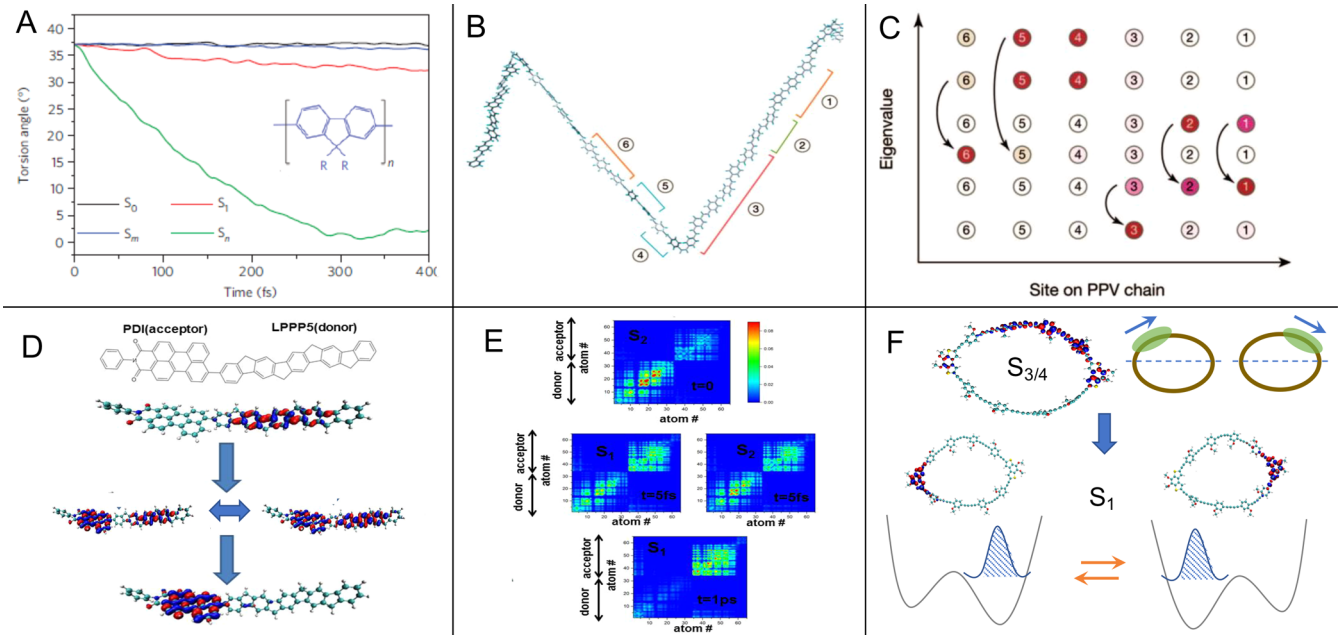

Figure 22. (A) Evolution of the average torsion angle between fluorene units on an oligomer during non-radiative relaxation from various initial states: S_0 and S_m (both B_u symmetry) show no time dependence; S_1 (B_u symmetry) shows weak torsional relaxation over the first 400 fs, whereas torsional relaxation from S_n (A_g symmetry) results in ultrafast local planarization within 100 fs. (B) Conjugated PPV polymer chain where torsion-induced conjugation breaks introduce conformational subunits. (C) Schematic representation of exciton states formed by interaction among the subunits shown in panel B. Arrows indicate favorable transitions based on both energetic and overlap conditions within a FRET model, revealing multiple ET pathways. (D) Photoexcited dynamics of ET in a molecular dyad system comprising a ladder-type poly(para-phenylene) oligomer donor unit (LPPP5) covalently linked with a perylenemonoimide acceptor unit (PMI). The plot shows localization of the electronic transition densities at different stages during the energy migration process. (E) The 2-D plots of transition density matrix elements for the S_1 and S_2 states on the basis of donor and acceptor atomic orbitals (AOs). The x and y axes denote spatial positioning of an electron and a hole in respective AOs for atoms ordered along the molecular backbone. Block diagonal quadrants correspond to excitation localized on the donor (lower quadrant) or acceptor (upper quadrant), while off-diagonal blocks correspond to charge-transfer contributions. (F) NAMD simulations of a bichromophore molecular polygon (digon) with bent chromophore chains showing competition of multiple ET pathways and completely depolarized excitations. Panel A: Reproduced with permission from ref 759. Copyright 2012 Springer Nature. Panels B and C: Reproduced with permission from ref 712. Copyright 2009 American Chemical Society. Panels D and E: Reproduced with permission from ref 255. Copyright 2017 American Chemical Society. Panel F: Reproduced with permission from ref 728. Copyright 2018 American Chemical Society.

As long as the donor and acceptor sites are separated in space, a rate description based on the FRET theory can be applied. FRET relies on the point dipole approximation, that requires sufficiently large donor−acceptor separation distances,[622,761−763] donor−acceptor coupling through long-range Coulomb interactions, and significant overlap between donor emission and acceptor absorption spectra.[764−767] However, identification of donor and acceptor sites in soft systems is challenging. Here static disorder can introduce kinks that break the conjugation forming so-called conformational subunits[712,768] (Figure 22B) which can significantly impact the rate of excitation energy migration and electronic relaxation. Such arrangements were experimentally observed, for example, by photoluminescence anisotropy decay in the PPV family of conjugated polymers[712] and porphyrin nanorings.[769] As a consequence, such kinks can lead to excited-state energy reordering and random (non-unidirectional) ET,[579] varying spectral overlap of donor and acceptor units, interference between multiple pathways (Figure 22C),[246,712] and competing rates that cannot be described by a Förster model based on a single rate. Multichromophoric Förster resonance energy transfer (MC-FRET) theories[634,770−774] overcome some of these limitations and were successfully applied, for example, to the study of ET in the photosynthetic LHC2 of purple bacteria revealing a collective enhancement effect.[774,775] However, even sophisticated MC-FRET theories can only treat static energy disorder,[634] and the distance dependence can vary with disorder[776] and temperature.[771]

In this sense, NAMD simulations go well beyond the Förster theories by permitting non-empirical insights into the nature of dynamical processes and specific conformational disorder. For example, bridged Donor−Acceptor dyads, such as LPPP5-PMI depicted in Figure 22D, are suitable molecular systems to explore structural, functional, and environmental effects on the efficiency of donor → acceptor intramolecular ET. Here short-range interactions cannot be neglected[772,777] and the absence of spectral overlap between the donor and acceptor moieties is not a hindrance for efficient ET.[778,779]

An atomistic description of the intramolecular ET that takes place in such bridged Donor−Acceptor dyads requires not only an adequate treatment of long-range through-space ET,[780,781] short-range wavefunction overlaps,[782] but also effects of the environment and vibrational dynamics.[783] Nuclear vibrations actually induce couplings between donor and acceptor electronic states and, therefore, are responsible for the efficiency of the intramolecular ET. Moreover, donor → acceptor vibrational ET can occur concomitant to electronic ET. NAMD simulations bring forward the analysis of the donor → acceptor electronic and vibrational energy relaxation via the conventional display of orbitals, TD, and vibrational motions in LPPP5-PMI (Figure 22D).[255] The exciton, initially localized on the donor moiety, experiences an ultrafast delocalization over

https://dx.doi.org/10.1021/acs.chemrev.9b00447
Chem. Rev. 2020, 120, 2215−2287

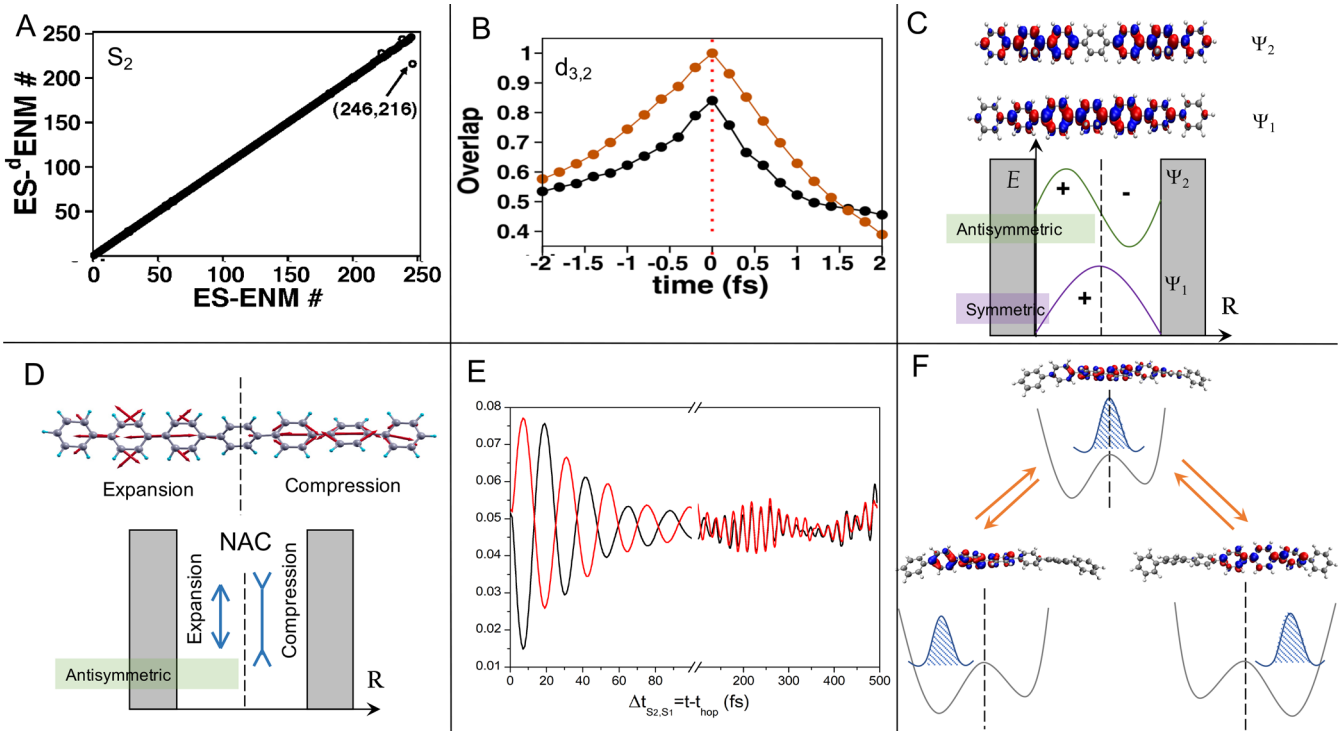

Figure 23. (A) Comparison of adiabatic excited-state equilibrium normal modes (ES-ENM) computed at the S_2 minimum of the 234-PPE molecule (Figure 19) and the transformed diabatic ES^d-ESM reveals high-frequency modes that are perturbed by non-adiabaticity. (B) Time-dependent overlap between the non-adiabatic coupling vector (NACR) $\boldsymbol{d}_{32}(t^{hop})$ and $\boldsymbol{d}_{32}(t - t^{hop})$ (brown) and the overlap between $\boldsymbol{d}_{32}(t^{hop})$ and $\mathbf{Q}_3^{max}(t - t^{hop})$ (black) the ES-INM that most strongly matches $\boldsymbol{d}_{32}(t)$ in 234-PPE. Plots span the 2 fs before and after the $S_3 \rightarrow S_2$ transition ($t = 0$). The average maximum values occur at the moment of hop with very short lifetimes. (C) Symmetric and antisymmetric forms of the wavefunction for the two lowest energy excited states in the PE oligomer. (D) Antisymmetric form of the NACR $\mathbf{d}_{12}$ for the two lowest energy excited states in the PE oligomer (spanel E) giving rise to expansion and compression vibrational motions. (E) After non-adiabatic transition in the PE oligomer, antisymmetric nuclear motions excited by the NACR are evident in out-of-phase oscillations in bond length alternation for right (black) and left (red) sides of the oligomer (panels C and D). (F) Change in transition density localization between the left and right halves of a PE oligomer corresponds to sloshing of the wavefunction between quasi-degenerate electronic states with intermittent delocalization. Panel A: Reproduced with permission from ref 798. Copyright 2014 American Chemical Society. Panel B: Reproduced with permission from ref 752. Copyright 2012 American Chemical Society. Panels C–F: Reproduced with permission from ref 795. Copyright 2018 Springer Nature.

the entire dyad before its final localization on the acceptor moiety. This intermittent delocalization is common (see section 5.4) and here is a result of through-bond ET mechanisms modulated by vibrations in the direction of the NACR. These vibrations are commonly restricted to a small subspace of normal modes and can be fully delocalized between the donor and acceptor units.[784] Additionally, monitoring changes and fluctuations in the localization of the electronic TD during the donor → acceptor ET (Figure 22E) allows potential charge-transfer contributions to be distinguished. In the case of the model LPPP5-PMI dyad system,[255] a very minor cross-delocalization is observed. It is very important that off-diagonal quadrants indicating charge-transfer character between the donor and the acceptor (i.e., positioning of the electron and the hole on different units) are not activated in all cases. Thus, this TDM analysis emphasizes a dominance of the Frenkel character of the excitation during the entire ET event.

Finally, Figure 22F illustrates distinct ET pathways in a multichomophore system where geometry and strain controls the efficiency in the bichromophore molecular polygon (digon) with bent chromophore chains. Here, bending strain localizes an exciton on individual chromophore units of the conjugated chains. NAMD modeling shows an ultrafast intramolecular energy redistribution that spreads the exciton equally among spatially separated chromophore fragments within the molecular system along with quenching of the excitation at the terminal units.[728] In this way, digons become unpolarized absorbers and emitters, in agreement with recent experimental studies on the single-molecule level.[785]

5.4. Non-adiabatic Dynamics and Excited-State Coherent Vibrational Motions

In a discussion of ET processes, a common hypothesis is that extended electronic and vibrational coupling leading to oscillatory evolution of delocalized electronic wavefunctions can improve transport of energy and charge carriers for photobiology, light-harvesting, lighting, and other optoelectronic applications.[50,786−790] Consequently, there has recently been a large amount of work to understand the vibronic effects in promoting efficient energy and electron transfer in biological and artificial systems.[50,786,791−794] Since such processes are specific cases of non-radiative relaxation, NAMD modeling can clarify the specific role of concomitant non-adiabatic transitions in initiating such coupled electron-vibrational dynamics[795,796] following the energy and charge carrier transport.[797]

Interaction between electronic and nuclear motions is the defining feature of NAMD, where the NACR is related to specific excited-state vibrations[752,798] and typically defines the direction of ET. The direction of the NACR represents the non-adiabatic contribution to the forces on the nuclei during electronic transitions, and the nuclear velocities in the direction

https://dx.doi.org/10.1021/acs.chemrev.9b00447
Chem. Rev. 2020, 120, 2215−2287

of the NACR have a strong effect on the NAC strength. In contrast, during dynamics near a level crossing, both the Pechukas force and excess electronic energy redistribution following quantum transitions effectively increase the classical nuclear momenta in the direction of the NACR. This promotes flow of electronic energy into vibrational modes aligned with the NACR. The correspondence of a set of adiabatic excited-state equilibrium normal modes (ES-ENMs) and diabatic ES^{d}-ENMs (Figure 23A) reveals typically one or two high frequency modes that are perturbed by mode mixing due to non-adiabatic coupling.[798] Furthermore, NACRs during electronic transitions strongly overlap with the normal modes participating in electronic relaxation processes, as demonstrated in ChlA[548] (section 4.2) and PPE dendrimers[752,798] (section 5.2). The relevance of NACR is illustrated in Figure 23B showing the NACR identity and correspondence between NACR and the excited-state instantaneous normal mode (ES-INM) with the strongest overlap.[752] The identity of $\boldsymbol{d}_{32}(t^{\mathrm{hop}})$ decays more quickly after the transition (positive time) when the system is moving on the lower surface. The maximum overlap between NACR and the ES-INM occurs at the exact moment of non-adiabatic transition and exhibits a short lifetime.

To demonstrate the appearance of coherent electronic-vibrational dynamics, we recall that excited states on conjugated molecular structures are standing waves[586] with alternating symmetry between the neighboring states. For example, the wavefunctions of the lowest energy S_1 and S_2 states in the model PE oligomer (visualized via orbital plots of the TDs in Figure 23C) depict $S_2 \rightarrow S_1$ as transition from an initial asymmetric state S_2 with a single node to the symmetric S_1 state with no node. As a result, the NACR $\boldsymbol{d}_{21}$ driving the non-adiabatic transition (and resulting vibrational excitation) is asymmetric and characterized by the left and right side of the PE oligomer undergoing expansion and compression, respectively, of nuclear coordinates (Figure 23D). This interaction between the form of the electronic wavefunction, NACR, and nuclear vibrations is manifested in excited-state NAMD simulations of the PE oligomer in the time evolution of bond length alternation (BLA)[799] for left and right halves of the oligomer (plotted in Figure 23E in red and black lines, respectively) showing out of phase oscillations consistent with sloshing of the wavefunction between left and right halves of the system pictured in Figure 23F. Thus, the wavefunctions of neighboring states define an asymmetric form of the NAC that drives the quantum transitions between excited states, and leads to a collective asymmetric vibrational excitation coupled to the electronic system. This promotes oscillatory evolution of the wavefunctions undergoing periodic dynamical localizations in the different segments of the molecule and intermittent delocalizations (Figure 23F). In fact, specific phase and amplitude relations are preserved across the entire ensemble of trajectories on time scales of hundreds of femtoseconds.[795] For several decades, empirical observations have suggested the role of coherent electron-vibrational dynamics in energy-transfer processes. In the light-harvesting complex LH-1, coherent vibrational motion during energy transfer plays an active role in the quantum beats in emission signals,[800] and oscillations in the fluorescence of LH-1 are understood to arise from excited-state wavepacket motions originating from vibrations.[707] Besides energy-transfer processes, oscillations in excited-state absorption features observed experimentally via transient absorption spectroscopy have been investigated using NAMD simulations that reveal the presence of vibrational coherences that play a central role in photoisomerization and excited-state deactivation involving non-adiabatic passage through a conical intersection.[259,801] Such coherent exciton-vibrational dynamics is ubiquitous and is observed across multiple molecular systems.[50,52,719,720,768,802−806]

6. SUMMARY, OUTLOOK, AND PERSPECTIVES

Excited-state dynamics are at the heart of many critical processes in chemistry and materials science including photochemical reactivity, fluorescence, light harvesting, and photocatalysis. Over the years, electronic structure theory became an indispensable tool used to model, analyze, predict, and ultimately guide experiment through its ability to quantitatively capture a variety of electronic properties such as band structure, excited-state energetics, dipoles, and UV−vis absorption and emission spectra.[7,132,386,402,428,430,492,807−810] However, simulation of electronic dynamics in large molecular systems, particularly beyond the BO regime as reviewed here, is a much more demanding task, which has yet to achieve the same level of quantitative prediction already witnessed for its static counterpart. One part of this challenge is the broad diversity of unique electronic features, such as excitonic phenomena, which become more complicated with coupling to the nuclear degrees of freedom beyond their classical treatment.[120,125,796,811] Further complicating the problem is the underlying numerical expense of performing NAMD simulations, as accurate excited-state quantum simulations must be performed at every time step for an ensemble of MD trajectories, each propagated for a picosecond or longer.[10,437,625,792] Subsequently, the NAMD modeling of a realistically large system always requires some compromises to find the right balance between precision and numerical cost. This makes it extremely difficult to evaluate the accuracy of NAMD simulations due to the superposition of two distinct sources of errors: numerical dynamics algorithms and electronic structure methodology.

The first is related to the NAMD algorithm allowing for an approximate solution of the time-dependent Schrödinger equation (section 2.1). Beyond specific few-state models suitable for analytic solutions (such as the early LZ framework for simulating 1-D reaction coordinates), numerical calculations are typically required based on the chosen model electronic structure method. Here, the family of mixed quantum-classical (MQC) techniques provides practical approaches for performing NAMD simulations on large systems.[136,607,812] In particular, Ehrenfest dynamics and the FSSH methods (section 2.2) are very robust and relatively simple algorithms that heavily dominate the field of NAMD simulations of molecular systems and materials.[74,76,121,550,813] These are, however, both subject to severe approximations in the way that electron−nuclear correlation is treated, being the mean field for Ehrenfest and ad hoc for FSSH. The limitations of these theories can be clearly identified on a set of model problems for non-adiabatic algorithms (section 2.3). For example, inconsistent treatment of electron−nuclear correlation in FSSH leads to decoherence and recoherence/interference problems, calling for respective empirical (e.g., ID, CSDM[82,814]) or non-empirical (e.g., A-FSSH[96]) corrections (section 2.4) making it a largely solved problem.[78] The next step in improvement of accuracy is the use of more rigorously derived (and slightly more complicated) dynamics methods such as AIMC-MCE[350] or the CW[351] algorithms. Here the NAMD error can be well controlled, however, at much larger numerical expense compared to simpler approaches. The development of numerically stable and

https://dx.doi.org/10.1021/acs.chemrev.9b00447
Chem. Rev. 2020, 120, 2215−2287

computationally tractable algorithms remains an active field that continues to evolve and improve.

We also mention that most of the MQC methods involve propagation of an ensemble of trajectories. This samples two distinct distributions, namely molecular conformations at a given temperature and environment, as well as nondeterministic evolution of the wavepackets on the excited-state manifold. For example, in the FSSH approach, these are sampled simultaneously by starting the dynamics from different initial conditions and propagating trajectories in a Monte Carlo-like stochastic fashion.[74,76,437,550] Such an approach necessarily assumes the need for an adequate statistical sampling, including exhaustive sampling of molecular conformations and convergence of the results with an increasing number of trajectories (section 3.3). Tests to verify sufficient statistical sampling and convergence are rarely done due to limitations of computational resources. We further note that, in the case of FSSH, the convergence is typically achieved for more than 500 trajectories. Thus, simulations limited by propagation of only tens of trajectories provide just a qualitative picture. Finally, one needs to be aware of numerical issues related to the appearance of trivial unavoided crossings (section 3.4.3), which are ubiquitous in extended molecules with many excited states.[104,105,107]

The second source of error is due to the electronic structure methodology underlying the NAMD method. Described in this Review, the family of TD-SCF methods[118,430] seems to be sufficiently accurate while providing a reasonable compromise for numerical expense (section 3.1). This framework is superior, for example, to the lower level monoelectronic approximation[815−819] since it is capable of naturally describing excitonic charge-transfer and spin states abundant in molecular chromophores. On the other hand, TD-SCF cannot address doubly excited and multiconfigurational electronic states such as those controlling singlet fission processes,[820−823] or cases of crossing between the excited- and ground-state PESs.[43] While significantly more expensive, there are a variety of more accurate correlated electronic structure methods (such as coupled cluster theory) capable of computing these quantities,[1,2,282] which are beyond the scope of this Review. We further note that, due to strong coupling of electronic and vibrational degrees of freedom, calculations of the native excited-state gradients (going beyond the classical path approximation[815]) is necessary for quality NAMD simulations in systems where ground and excited PESs differ considerably.[10,437,625] Consequently, on-the-fly calculations of gradients and non-adiabatic couplings are essential. These are all available within TD-SCF approaches (section 3.1.3).[434,435] Another important consideration is the choice of the electronic Hamiltonian for TD-SCF techniques. In the land of DFT, there is a plethora of functionals available. Here, hybrid and range-corrected functionals seem to be a more sensible choice for molecular simulations[379,824] since they overcome the inability of pure and semilocal models to treat charge-transfer and delocalized states.[410] In the present Review, we have shown multiple NAMD applications using tried-and-true semiempirical model Hamiltonians. Their simplistic form significantly lowers numerical cost, albeit providing only qualitative accuracy.

It is important to realize that the requirements for electronic structure theory when performing NAMD simulations may be significantly more stringent compared to those for static simulations. For example, errors on the order of 0.1 eV for transition energies are considered as "good" and "quantitatively adequate" for modeling of UV-spectra using TD-SCF approaches.[825−827] In contrast, since the NAC critically depends on the energy gap between states ($\sim 1/\Delta E$, eqs 2.6), a seemingly innocent 0.1 eV deviation (which is barely noticeable when comparing experimental and theoretical spectra at ambient conditions), may lead to orders of magnitude differences when simulating non-radiative relaxation rates. This is one of the reasons why these rates are very sensitive to the presence of the dielectric environment such as solvent or a solid-state matrix. Subsequently, solvent and environmental effects are critical to a wide range of excited-state dynamics.[502,828−830] However, treatment of solvent effects adds to the numerical overhead and leads to additional computational problems (section 3.2). Here, the use of polarizable continuum models[137,470,472,492] is a basic approximation. Importantly, the solvent should respond to the charge density of excited states, as in state-specific solvent models, to produce a set of self-consistent equations, which are difficult to solve iteratively and lack analytic gradients.[506] Other models, such as the VE[507] or cLR[493] models remove the dependence of the ground-state density on the excited-state solvent model, simplifying the iterative procedure (section 3.2.1). Intuitively, solvent relaxation will occur over a variety of time scales in NAMD simulations, posing another challenge for solvation models (section 3.2.2).[529−532]

Our examples of applications of excited-state NAMD methods to a variety of molecular systems (sections 4 and 5) demonstrate potential utility of such simulations. A variety of photoinduced phenomena, such as internal conversion, energy transfer, and molecular decompositions, can be modeled and analyzed with NAMD. The analysis using the transition density matrix (section 3.5) or its derivatives such as transition charge density or natural transition orbitals, provides a very convenient way to monitor the evolution of photoexcited wavefunctions. Here coupling of electronic and vibrational degrees of freedom drives non-radiative relaxation dynamics ultimately resulting in irreversible transformation of electronic energy into heat (internal molecular vibrations and finally bath degrees of freedom). This is a non-equilibrium process with multiple time scales, which can be probed by experiment, for example, by time-resolved spectroscopies.[722,831,832] While the current NAMD methods for large systems can provide only qualitative agreement with spectroscopic data, they complement experiment with an unmatchable level of atomistic details. For example, there are a limited number of vibrational motions (such as bond stretching or torsions) that are coupled to electrons (e.g., section 5.2). Subsequently, there is a concerted evolution of only a few variables on the ultrafast time scale of hundreds of femtoseconds leading to coherent exciton-vibrational dynamics driven by non-adiabatic transitions (section 5.4),[795] potentially providing additional ways to manipulate excited-state dynamics and energy-transfer pathways in molecular materials.

Having summarized the current state of methodologies, numerical algorithms, and applications of NAMD to large systems, the next questions to address are the outstanding challenges in the field and future directions. Putting a firm error bar on NAMD simulation is an important target, given the appearance of newer and more accurate NAMD approaches. For example, the problems of the Ehrenfest and FSSH methods for synthetic models are well understood.[78,221,226,264,833,834] On the other hand, do these drawbacks necessarily preclude the application of these simplified methods to realistic molecules? Stated another way, would any qualitatively different scenario of photoinduced dynamics appear when applying more accurate and numerically involved methods such as multiple cloning?

https://dx.doi.org/10.1021/acs.chemrev.9b00447
Chem. Rev. 2020, 120, 2215−2287

Notably, such quantitative differences may not show up in the integrated variables such as relaxation rates averaged over the trajectory ensemble, but may appear in sophisticated evolutions of time-dependent wavefunctions including phase information, which can be probed by modern spectroscopies. Our example of comparisons points to a consistency among results obtained using these three methods for a simple dendrimer system (section 5.2.2).[753] This is just a single point, facilitating exhaustive comparisons between different methodologies in the realistic setting. Next, further development of state-specific solvation methods is an important direction. Here, explicit solvent models such as QM/MM approaches provide a conceptually appealing future framework promising significant improvements in accuracy. Accelerated MD approaches, such as extended Lagrangian dynamics, already proved their utility for ground-state ab initio MD. Extending these to excited-state adiabatic MD (section 3.3.3) and particularly to excited-state NAMD modeling, is an attractive way of reducing the numerical expense. Other research focuses on making NAMD simulations faster by using tight-binding and effective Hamiltonian models, allowing for longer simulations of larger systems.[137,835,836] Additionally, machine learning techniques, which have made a significant impact across the field of theoretical chemistry demonstrated success at accelerating or even bypassing the underlying QM calculations in NAMD simulations.[837−840]

In conclusion, over the past decade, we have witnessed the merging and interfacing of NAMD algorithms (such as MQC techniques) with electronic structure methods for excited states (such as the TD-SCF family). This advance led to the development of multiple computational packages[136,449,488,605,606,841] allowing us to address photoexcited dynamics in realistic molecular systems and materials. While a unified methodology for NAMD simulations is difficult, if not impossible to construct, the actively developing ladder of increasingly accurate NAMD algorithms along with the counterpart for electronic structure theory (e.g., Jacobs's DFT ladder) would enable errors in simulations to be quantified and ultimately allow treatment of more complex and larger systems. This opens an exciting future prospect where NAMD simulations would play a pivotal role not only in guiding and analyzing experiments, but also as an interdisciplinary computational tool that is able to reach far beyond normal experimental conditions.

ASSOCIATED CONTENT

Special Issue Paper

This paper is an additional Review for *Chem. Rev.* **2018**, *118*, issue 15, "Theoretical Modeling of Excited State Processes".

AUTHOR INFORMATION

Corresponding Authors

Adrian E. Roitberg − *Department of Chemistry, University of Florida, Gainesville, Florida 32611, United States;* orcid.org/0000-0003-3963-8784; Email: roitberg@ufl.edu

Sergei Tretiak − *Theoretical Division, Los Alamos National Laboratory, Los Alamos, New Mexico 87545, United States;* orcid.org/0000-0001-5547-3647; Email: serg@lanl.gov

Authors

Tammie R. Nelson − *Theoretical Division, Los Alamos National Laboratory, Los Alamos, New Mexico 87545, United States;* orcid.org/0000-0002-3173-5291

Alexander J. White − *Theoretical Division, Los Alamos National Laboratory, Los Alamos, New Mexico 87545, United States;* orcid.org/0000-0002-7771-3899

Josiah A. Bjorgaard − *Theoretical Division, Los Alamos National Laboratory, Los Alamos, New Mexico 87545, United States;* orcid.org/0000-0003-3679-2487

Andrew E. Sifain − *Theoretical Division, Los Alamos National Laboratory, Los Alamos, New Mexico 87545, United States; U.S. Army Research Laboratory, Aberdeen Proving Ground, Maryland 21005, United States;* orcid.org/0000-0002-2964-1923

Yu Zhang − *Theoretical Division, Los Alamos National Laboratory, Los Alamos, New Mexico 87545, United States;* orcid.org/0000-0001-8938-1927

Benjamin Nebgen − *Theoretical Division, Los Alamos National Laboratory, Los Alamos, New Mexico 87545, United States*

Sebastian Fernandez-Alberti − *Universidad Nacional de Quilmes/CONICET, B1876BXD Bernal, Argentina;* orcid.org/0000-0002-0916-5069

Dmitry Mozyrsky − *Theoretical Division, Los Alamos National Laboratory, Los Alamos, New Mexico 87545, United States*

Complete contact information is available at: https://pubs.acs.org/10.1021/acs.chemrev.9b00447

Notes

The authors declare no competing financial interest.

Biographies

Tammie R. Nelson is a Staff Scientist at Los Alamos National Laboratory. She received her undergraduate degrees in Chemistry and Biochemistry from California Polytechnic State University San Luis Obispo in 2008 and her Ph.D. (2013) in Physical Chemistry from the University of Rochester, NY. Her research interests include the development of efficient methods for modeling photoinduced processes in realistic molecular systems and the application of excited-state NAMD to model photochemistry in nanomaterials.

Alexander J. White is a Staff Scientist in the Physics and Chemistry of Materials group of the Theoretical Division at Los Alamos National Laboratory. He received his undergraduate degree in Chemistry from California Polytechnic State University San Luis Obispo in 2008 and his Ph.D. in Chemistry from the University of California San Diego in 2014. He is interested in the development of computational and theoretical approaches to model material behavior from organic molecules to degenerate plasmas (warm dense matter), including non-equilibrium quantum transport, open-quantum systems, time-dependent density functional theory, and non-adiabatic and equilibrium molecular dynamics.

Josiah A. Bjorgaard is an independent consultant working on cloud infrastructure and machine learning projects. He was a Postdoctoral Fellow at Los Alamos National Laboratory in the Center for Nonlinear Studies and Computational Physics Division, where he worked on implicit solvent models for time-dependent density functional theory. He received his undergraduate degree in Chemistry at Minnesota State University Moorhead in 2010 and his Ph.D. in Physical Chemistry at North Dakota State University in 2014. Some of his interests are quantum chemistry, matter at extreme conditions, high-performance computing, and distributed systems.

Andrew E. Sifain is a Postdoctoral Fellow at the U.S. Army Research Laboratory. He received undergraduate degrees in Mathematics and Physics from the University of Rochester (2011) and his Ph.D. in Chemical Physics from the University of Southern California (2018) under the guidance of Oleg V. Prezhdo (USC) and Sergei Tretiak

https://dx.doi.org/10.1021/acs.chemrev.9b00447
Chem. Rev. 2020, 120, 2215−2287

(LANL). His research interests are modeling photoinduced electronic processes in molecules and nanomaterials, including optical spectroscopy and non-adiabatic excited-state molecular dynamics. Other interests include the use of machine learning algorithms for predicting quantum and physicochemical properties of materials.

Yu Zhang is a Staff Scientist at Los Alamos National Laboratory. He received his Bachelor's degree in physics from Sun Yat-Sen University in 2010 and his Ph.D. in chemical physics from the University of Hong Kong in 2014. His research interests are the development and application of theoretical models and computational methods for problems of scientific importance, including non-adiabatic dynamics, photoinduced complex processes, light−matter interaction, charge transport, and energy transfer and conversion.

Benjamin Nebgen is a Staff Scientist at Los Alamos National Laboratory. He received his undergraduate degree in 2010 from Cornell University and his Ph.D. in 2014 from Purdue University. His research interests focus on the use of machine learning in the fields of chemistry, materials science, and seismology.

Sebastian Fernandez-Alberti is a Full Professor at National University of Quilmes (UNQ, Argentina) and Principal Researcher at the National Council for Scientific and Technical Research (CONICET, Argentina). He received his undergraduate degree in 1993 from the National University of La Plata (UNLP, Argentina) and his Ph.D. in Molecular Physics in 1999 from the University of Paul Sabatier (Toulouse, France). His research interests include excited-state non-adiabatic dynamics simulations in extended conjugated molecules, electronic and vibrational relaxation, intramolecular energy redistribution in polyatomic molecules, and protein dynamics analysis using collective coordinates.

Dmitry Mozyrsky is a Staff Scientist at Los Alamos National Laboratory. He received his Master's degree in Physics from Moscow Institute of Physics and Technology (Russia) in 1995 and Ph.D. degree in Physics from Clarkson University (Potsdam, NY) in 1999. His research interests are primarily in quantum condensed matter physics and quantum chemistry, particularly in the theory of non-equilibrium processes and modeling non-adiabatic dynamics.

Adrian E. Roitberg is a Full Professor in the Chemistry Department at the University of Florida. He received his undergraduate degree from the University of Buenos Aires, Argentina, in 1987, and his Ph.D. from the University of Illinois at Chicago in 1992. He joined the University of Florida in 2001. His research interests are molecular modeling of molecules and materials and studying the effects of dynamics and conformational diversity on experimental observables.

Sergei Tretiak is a Staff Scientist at Los Alamos National Laboratory. He received his M.Sc. degree from Moscow Institute of Physics and Technology (Russia) in 1994 and his Ph.D. degree in 1998 from the University of Rochester (US). Since 2006 Tretiak has been a member of the DOE-funded Center for Integrated Nanotechnologies (CINT). He also serves as an Adjunct Professor at the University of California Santa Barbara (2015−present) and at the Skolkovo Institute of Science and Technology, Moscow, Russia (2013−present). His research interests include development of modern computational methods for molecular optical properties, nonlinear optical response of organic chromophores, adiabatic and non-adiabatic molecular dynamics of excited states, optical response of confined excitons in conjugated polymers, carbon nanotubes, semiconductor nanoparticles, halide perovskites, and molecular aggregates.

ACKNOWLEDGMENTS

We acknowledge support from the Center for Integrated Nanotechnology (CINT), a U.S. Department of Energy, Office of Basic Energy Sciences user facility. S.F.-A. is supported by CONICET, UNQ, ANPCyT (PICT-2018-02360). We acknowledge support from Los Alamos National Laboratory (LANL) Directed Research and Development Funds (LDRD). This research used resources provided by the LANL Institutional Computing (IC) Program. LANL is operated by Triad National Security, LLC, for the National Nuclear Security Administration of the U.S. Department of Energy (Contract No. 89233218NCA000001).

LIST OF SYMBOLS USED

Ψ	full wavefunction
$\hat{H}$	Hamiltonian
$\boldsymbol{R}$	nuclear position vector (a variable)
$\boldsymbol{P}$	nuclear momentum vector (a variable)
$\hat{\boldsymbol{m}}_{\boldsymbol{R}}$	nuclear mass matrix (typically diagonal)
m_e	electron mass
$\hat{T}$	nuclear kinetic energy operator
$\hat{H}_{el}$	electronic Hamiltonian
$\hat{V}$	potential operator
ϕ	diabatic electronic wavefunction
χ	nuclear wavefunction
ψ	adiabatic electronic wavefunction
∇	gradient operator
$a, b, \ldots$	many-body eigenstate index
E_a	adiabatic eigenstate of the ath eigenstate
$\boldsymbol{d}_{ab}(\boldsymbol{R})$	non-adiabatic coupling of the ath and bth eigenstates, NACR
H_{ab}	ath, bth diabatic element of electronic Hamiltonian operator
g	Gaussian wavepacket
$\hat{\alpha}$	Gaussian wavepacket width
γ_t	Gaussian wavepacket phase
$\boldsymbol{R}_t, \boldsymbol{P}_t$	classical nuclear position and momentum vectors
S	classical action
$c_a(t)$	time-dependent adiabatic expansion coefficient
$d^{(n)}$	configurational wavefunction expansion coefficient
V_{ab}	ath, bth matrix element of effective electronic Hamiltonian
$i, j, \ldots$	molecular orbital index
σ, σ'	orbital spin index
$\hat{\boldsymbol{\rho}}$	single particle density matrix
θ_i	molecular orbital (single particle eigenstate)
$\hat{\boldsymbol{F}}(\hat{\boldsymbol{\rho}})$	Fock operator
$\hat{\boldsymbol{V}}(\hat{\boldsymbol{\rho}})$	Coulomb operator
$\hat{\boldsymbol{t}}$	electron single particle operator
$\hat{\boldsymbol{V}}^{xc}(\hat{\boldsymbol{\rho}})$	exchange-correlation operator
$\hat{\boldsymbol{L}}$	Liouvillian supermatrix
$\hat{\boldsymbol{\xi}}$	transition density matrix (linear response eigenvector)
Ω	linear response excitation energy (eigenvalue)
$\hat{\boldsymbol{\mu}}$	dipole operator
ε	dielectric constant
α, β	nuclear coordinates
T	temperature
$\mathcal{L}^{ES}$	excited-state Lagrangian
$\mathcal{L}^{XES}$	extended excited-state Lagrangian
P_X	participation number of unit X

Note: symbol with "hat" (not bold) indicates an operator;

https://dx.doi.org/10.1021/acs.chemrev.9b00447
Chem. Rev. 2020, 120, 2215−2287

bold symbol indicates a vector in nuclear, orbital, or many-body state basis;
bold symbol with "hat" indicates a matrix in any basis

ABBREVIATIONS AND ACRONYMS

1-D	one-dimensional (sec. 2.1)
2-D	two-dimensional (sec. 2.3)
2DES	two-dimensional electronic spectroscopy (sec. 5)
A-FSSH	augmented fewest-switches surface hopping (sec. 2.4)
AIMC	ab initio multiple cloning (secs. 1 and 2.5.4)
AIMS	ab initio multiple spawning (sec. 1)
AO	atomic orbital (sec. 3.11)
BAB	bisazobenzene (sec. 2.2.2)
BO	Born−Oppenheimer (sec. 1)
BOMD	Born−Oppenheimer molecular dynamics (sec. 3.3.3)
CAS-CI	complete active space configuration interaction (sec. 2.2.2)
CASPT2	complete active space second-order perturbation theory (sec. 2.2.2)
CASSCF	complete active space self-consistent field (sec. 2.2.2)
CC	complete coupling (sec. 3.4.1)
Chl	chlorophyll (sec. 1)
CI	configuration interaction (sec. 3.1)
CIS	configuration interaction singles (sec. 3.1.2)
CISD	configuration interaction singles and doubles (sec. 2.2.1)
cLR	corrected linear response (sec. 3.2.1)
COSMO	conductor-like screening model (sec. 3.2)
CPCM	conductor-like polarizable continuum model (sec. 3.2)
CPMD	Car−Parrinello molecular dynamics (sec. 3.3.3)
CS	coherent state (sec. 2.5.4)
CSDM	coherent switching with decay of mixing (sec. 2.4)
CSH	consensus surface hopping (sec. 2.5.2)
CW	coupled-wavepacket (sec. 2.5.5)
DFT	density functional theory (sec. 1)
DFTB	density functional tight binding (sec. 2.2.1)
DISH	decoherence-induced surface hopping (sec. 2.4)
DTA	dithia-anthracenophane (sec. 5.1)
DTSH	direct trajectories with surface hopping (sec. 3.4.3)
DVR	discrete variable representation (sec. 2.1)
E-Z	zusammen and entgegen (sec. 2.2.2)
EDC	energy-based decoherence correction (sec. 2.4)
EET	excitation energy transfer (sec. 5)
EOM	equation of motion (sec. 2.1.1)
EP	Ehrenfest-plus (sec. 2.5.5)
ES-ENM	excited-state equilibrium normal mode (sec. 5.4)
ES-INM	excited-state instantaneous normal mode (sec. 5.4)
ESMD	excited-state molecular dynamics (sec. 1)
ET	energy transfer (sec. 1)
FMO	Fenna−Mathews−Olson, photosynthetic complex (sec. 2.5.1)
FRET	Förster resonance energy transfer (sec. 5)
FSH	flexible surface hopping (sec. 3.4.3)
FSSH	fewest-switches surface hopping (sec. 2.2.2)
fwhm	full width at half-maximum (sec. 3.3.1)
GFSH	global flux surface hopping (sec. 2.4)
GGA	generalized gradient approximation (sec. 3.3.1)
GWD	Gaussian wavepacket dynamics (sec. 2.1.1)
HF	Hartree−Fock (sec. 3.1)
HK	Herman−Kluk (sec. 2.1.1)
ID	instantaneous decoherence (sec. 2.4)
KS	Kohn−Sham (sec. 3.1)
LDA	local density approximation (sec. 3.1.1)
LHC	light-harvesting complex (sec. 3.6)
LR	linear response (sec. 3.1.3)
LZ	Landau and Zener (sec. 2.1.1)
MC-FRET	multichromophoric Förster resonance energy transfer (sec. 5.3)
MC-TDH	multiconfigurational time-dependent Hartree (sec. 1)
MCE	multiconfigurational Ehrenfest (sec. 1)
MD	molecular dynamics (sec. 1)
MMST	Miller−Meyer−Stock−Thoss (sec. 2.1.1)
MO	molecular orbital (sec. 3.1.1)
MQC	mixed quantum-classical (sec. 1)
MRCI	multireference configuration interaction (sec. 4.3)
NAC	non-adiabatic coupling (sec. 1)
NACR	non-adiabatic coupling vector (sec. 2.1)
NACT	non-adiabatic coupling scalar (sec. 2.1)
NAMD	non-adiabatic molecular dynamics (sec. 1)
NEXMD	non-adiabatic excited-state molecular dynamics (sec. 1)
NPI	norm-preserving interpolation (sec. 3.4.3)
NTO	natural transition orbital (sec. 3.5)
PBME	Poisson-bracket mapping equation (sec. 2.5.2)
PC	partial coupling (sec. 3.4.1)
PCM	polarizable continuum model (sec. 3.2)
PDE	partial differential equation (sec. 2.1)
PETN	pentaerythritol tetranitrate (sec. 4.3)
PetrinTzCl	pentaerythritol tetranitrate chlorotetrazine (sec. 4.3)
PES	potential energy surface (sec. 1)
PPE	poly(phenylene-ethynylene) (sec. 2.4)
PPV	poly(phenylene-vinylene) (sec. 2.4)
QCLE	quantum-classical Liouville equation (sec. 2.5.2)
QM	quantum mechanical (sec. 2.1.1)
QM/MM	quantum mechanics/molecular mechanics (sec. 3.2)
RKS	restricted Kohn−Sham (sec. 4.3)
RPMD	ring-polymer molecular dynamics (sec. 2.5.1)
SAC	single avoided crossing (sec. 2.3)
SCC-DFTB	self-consistent charge density functional tight binding (sec. 3.6)
SC-FSSH	self-consistent fewest-switches surface hopping (sec. 3.4.3)
SC-IVR	semiclassical initial value representation (sec. 2.1.1)
SCMC	semiclassical Monte Carlo (sec. 2.5.5)
SHLS	surface hopping in Liouville space (sec. 2.4)
SMF	statistical minimum flow (sec. 3.5)
SREDA	spin-resolved electronic dynamics approach (sec. 4.3)
SS	state-specific (sec. 1)
TD	transition density (sec. 3.2.1)
TDA	Tamm−Dancoff approximation (sec. 3.1.2)
TDDB	time-dependent diabatic basis (sec. 2.5.4)
TD-DFT	time-dependent density functional theory (sec. 1)
TD-HF	time-dependent Hartree−Fock (sec. 1)
TDM	transition density matrix (sec. 1)
TD-SCF	time-dependent self-consistent field (sec. 1)

https://dx.doi.org/10.1021/acs.chemrev.9b00447
Chem. Rev. 2020, 120, 2215−2287

TDSE	time-dependent Schrödinger equation (sec. 2.1)
TS	two-state (sec. 2.5.5)
u-TDESMD	spin-unrestricted DFT-based time-dependent excited-state molecular dynamics (sec. 4.3)
VE	vertical excitation (sec. 3.2.1)
v-MCG	variational multiconfigurational Gaussian (sec. 2.5.4)
WKB	Wentzel−Kramers−Brillouin (sec. 2.1.1)
XL-BOMD	extended Lagrangian methods for Born−Oppenheimer molecular dynamics (sec. 3.3.3)
XL-ESMD	extended Lagrangian methods for excited-state molecular dynamics (sec. 3.3.3)
ZPE	zero-point energy (sec. 2.2.1)

REFERENCES

(1) Baeck, K. K.; Martinez, T. J. Ab Initio Molecular Dynamics with Equation-of-Motion Coupled-Cluster Theory: Electronic Absorption Spectrum of Ethylene. *Chem. Phys. Lett.* **2003**, *375*, 299−308.

(2) Faraji, S.; Matsika, S.; Krylov, A. I. Calculations of Non-Adiabatic Couplings within Equation-of-Motion Coupled-Cluster Framework: Theory, Implementation, and Validation against Multi-Reference Methods. *J. Chem. Phys.* **2018**, *148*, 044103.

(3) Gonzalez, L.; Escudero, D.; Serrano-Andres, L. Progress and Challenges in the Calculation of Electronic Excited States. *ChemPhysChem* **2012**, *13*, 28−51.

(4) Plasser, F.; Mewes, S. A.; Dreuw, A.; Gonzalez, L. Detailed Wave Function Analysis for Multireference Methods: Implementation in the Molcas Program Package and Applications to Tetracene. *J. Chem. Theory Comput.* **2017**, *13*, 5343−5353.

(5) Aquilante, F.; Autschbach, J.; Carlson, R. K.; Chibotaru, L. F.; Delcey, M. G.; De Vico, L.; Fdez. Galvan, I.; Ferre, N.; Frutos, L. M.; Gagliardi, L.; et al. Molcas 8: New Capabilities for Multiconfigurational Quantum Chemical Calculations across the Periodic Table. *J. Comput. Chem.* **2016**, *37*, 506−541.

(6) Marques, M. A.; Gross, E. K. Time-Dependent Density Functional Theory. *Annu. Rev. Phys. Chem.* **2004**, *55*, 427−455.

(7) Adamo, C.; Jacquemin, D. The Calculations of Excited-State Properties with Time-Dependent Density Functional Theory. *Chem. Soc. Rev.* **2013**, *42*, 845−856.

(8) Maitra, N. T. Perspective: Fundamental Aspects of Time-Dependent Density Functional Theory. *J. Chem. Phys.* **2016**, *144*, 220901.

(9) Agostini, F.; Curchod, B. F. E.; Vuilleumier, R.; Tavernelli, I.; Gross, E. K. U. *TDDFT and Quantum-Classical Dynamics: A Universal Tool Describing the Dynamics of Matter*; Springer: Cham, 2018.

(10) Tapavicza, E.; Bellchambers, G. D.; Vincent, J. C.; Furche, F. Ab Initio Non-Adiabatic Molecular Dynamics. *Phys. Chem. Chem. Phys.* **2013**, *15*, 18336−18348.

(11) Dewar, M. J. S.; Zoebisch, E. G.; Healy, E. F.; Stewart, J. J. P. Development and Use of Quantum Mechanical Molecular Models. 76. Am1: A New General Purpose Quantum Mechanical Molecular Model. *J. Am. Chem. Soc.* **1985**, *107*, 3902−3909.

(12) Thiel, W. Semiempirical Quantum−Chemical Methods. *Wiley Interdiscip. Rev.: Comput. Mol. Sci.* **2014**, *4*, 145−157.

(13) Christensen, A. S.; Kubař, T.; Cui, Q.; Elstner, M. Semiempirical Quantum Mechanical Methods for Noncovalent Interactions for Chemical and Biochemical Applications. *Chem. Rev.* **2016**, *116*, 5301−5337.

(14) *Conical Intersections*; Domcke, W., Yarkony, D. R., Koppel, H., Eds. World Scientific, 2004; Vol. *15*.

(15) Olivucci, M. *Theoretical and Computational Chemistry*; Elsevier: New York, 2005.

(16) Klessinger, M.; Michl, J. *Excited States and Photochemistry of Molecules*; Wiley VCH: Berlin, 1995.

(17) Turro, N. J.; Ramamurthy, V.; Scaiano, J. C. *Principles of Molecular Photochemistry: An Introduction*; University Science Books, 2009.

(18) Baer, M. *Beyond Born-Oppenheimer. Electronic Nonadiabatic Coupling Terms and Conical Intersections*; Wiley-Interscience: Hoboken, NJ, 2006.

(19) Hartschuh, A.; Pedrosa, H. N.; Novotny, L.; Krauss, T. D. Simultaneous Fluorescence and Raman Scattering from Single Carbon Nanotubes. *Science* **2003**, *301*, 1354−1356.

(20) Giessen, H.; Lippitz, M. Directing Light Emission from Quantum Dots. *Science* **2010**, *329*, 910−911.

(21) Shirasaki, Y.; Supran, G. J.; Bawendi, M. G.; Bulović, V. Emergence of Colloidal Quantum-Dot Light-Emitting Technologies. *Nat. Photonics* **2013**, *7*, 13−23.

(22) Saha, A.; Gifford, B. J.; He, X.; Ao, G.; Zheng, M.; Kataura, H.; Htoon, H.; Kilina, S.; Tretiak, S.; Doorn, S. K. Narrow-Band Single-Photon Emission through Selective Aryl Functionalization of Zigzag Carbon Nanotubes. *Nat. Chem.* **2018**, *10*, 1089−1095.

(23) Terenziani, F.; Katan, C.; Badaeva, E.; Tretiak, S.; Blanchard-Desce, M. Enhanced Two-Photon Absorption of Organic Chromophores: Theoretical and Experimental Assessments. *Adv. Mater.* **2008**, *20*, 4641−4678.

(24) Franco, I.; Tretiak, S. Electron-Vibrational Dynamics of Photoexcited Polyfluorenes. *J. Am. Chem. Soc.* **2004**, *126*, 12130−12140.

(25) Park, Y. I.; Postupna, O.; Zhugayevych, A.; Shin, H.; Park, Y. S.; Kim, B.; Yen, H. J.; Cheruku, P.; Martinez, J. S.; Park, J. W.; et al. A New Ph Sensitive Fluorescent and White Light Emissive Material through Controlled Intermolecular Charge Transfer. *Chem. Sci.* **2015**, *6*, 789−797.

(26) Silva, G. L.; Ediz, V.; Yaron, D.; Armitage, B. A. Experimental and Computational Investigation of Unsymmetrical Cyanine Dyes: Understanding Torsionally Responsive Fluorogenic Dyes. *J. Am. Chem. Soc.* **2007**, *129*, 5710−5718.

(27) Romero, E.; Novoderezhkin, V. I.; van Grondelle, R. Quantum Design of Photosynthesis for Bio-Inspired Solar-Energy Conversion. *Nature* **2017**, *543*, 355−365.

(28) Gratzel, M. Solar Energy Conversion by Dye-Sensitized Photovoltaic Cells. *Inorg. Chem.* **2005**, *44*, 6841−6851.

(29) Fassioli, F.; Dinshaw, R.; Arpin, P. C.; Scholes, G. D. Photosynthetic Light Harvesting: Excitons and Coherence. *J. R. Soc., Interface* **2014**, *11*, 20130901.

(30) Ponseca, C. S., Jr.; Chabera, P.; Uhlig, J.; Persson, P.; Sundstrom, V. Ultrafast Electron Dynamics in Solar Energy Conversion. *Chem. Rev.* **2017**, *117*, 10940−11024.

(31) Provencher, F.; Berube, N.; Parker, A. W.; Greetham, G. M.; Towrie, M.; Hellmann, C.; Cote, M.; Stingelin, N.; Silva, C.; Hayes, S. C. Direct Observation of Ultrafast Long-Range Charge Separation at Polymer-Fullerene Heterojunctions. *Nat. Commun.* **2014**, *5*, 4288.

(32) Hallermann, M.; Haneder, S.; Da Como, E. Charge-Transfer States in Conjugated Polymer/Fullerene Blends: Below-Gap Weakly Bound Excitons for Polymer Photovoltaics. *Appl. Phys. Lett.* **2008**, *93*, 053307.

(33) Hallermann, M.; Kriegel, I.; Da Como, E.; Berger, J. M.; von Hauff, E.; Feldmann, J. Charge Transfer Excitons in Polymer/Fullerene Blends: The Role of Morphology and Polymer Chain Conformation. *Adv. Funct. Mater.* **2009**, *19*, 3662−3668.

(34) Deschler, F.; Da Como, E.; Limmer, T.; Tautz, R.; Godde, T.; Bayer, M.; von Hauff, E.; Yilmaz, S.; Allard, S.; Scherf, U.; et al. Reduced Charge Transfer Exciton Recombination in Organic Semiconductor Heterojunctions by Molecular Doping. *Phys. Rev. Lett.* **2011**, *107*, 127402.

(35) Leveillee, J.; Katan, C.; Zhou, L.; Mohite, A. D.; Even, J.; Tretiak, S.; Schleife, A.; Neukirch, A. J. Influence of Π-Conjugated Cations and Halogen Substitution on the Optoelectronic and Excitonic Properties of Layered Hybrid Perovskites. *Phys. Rev. Mater.* **2018**, *2*, 105406.

(36) Corrales, M. E.; Gonzalez-Vazquez, J.; Balerdi, G.; Sola, I. R.; de Nalda, R.; Banares, L. Control of Ultrafast Molecular Photodissociation by Laser-Field-Induced Potentials. *Nat. Chem.* **2014**, *6*, 785−790.

(37) Saveant, J. M. Electron Transfer, Bond Breaking, and Bond Formation. *Acc. Chem. Res.* **1993**, *26*, 455−461.

https://dx.doi.org/10.1021/acs.chemrev.9b00447
Chem. Rev. 2020, 120, 2215−2287

(38) Greenfield, M.; Guo, Y. Q.; Bernstein, E. R. Ultrafast Photodissociation Dynamics of Hmx and Rdx from Their Excited Electronic States Via Femtosecond Laser Pump−Probe Techniques. *Chem. Phys. Lett.* **2006**, *430*, 277−281.
(39) Guo, Y. Q.; Greenfield, M.; Bhattacharya, A.; Bernstein, E. R. On the Excited Electronic State Dissociation of Nitramine Energetic Materials and Model Systems. *J. Chem. Phys.* **2007**, *127*, 154301.
(40) Ern, J.; Bens, A. T.; Martin, H. D.; Mukamel, S.; Tretiak, S.; Tsyganenko, K.; Kuldova, K.; Trommsdorff, H. P.; Kryschi, C. Reaction Dynamics of a Photochromic Fluorescing Dithienylethene. *J. Phys. Chem. A* **2001**, *105*, 1741−1749.
(41) Yang, J.; Zhu, X.; Wolf, T. J. A.; Li, Z.; Nunes, J. P. F.; Coffee, R.; Cryan, J. P.; Guhr, M.; Hegazy, K.; Heinz, T. F.; et al. Imaging Cf3i Conical Intersection and Photodissociation Dynamics with Ultrafast Electron Diffraction. *Science* **2018**, *361*, 64−67.
(42) Lee, M. H.; Dunietz, B. D.; Geva, E. Calculation from First Principles of Intramolecular Golden-Rule Rate Constants for Photo-Induced Electron Transfer in Molecular Donor−Acceptor Systems. *J. Phys. Chem. C* **2013**, *117*, 23391−23401.
(43) Levine, B. G.; Martinez, T. J. Isomerization through Conical Intersections. *Annu. Rev. Phys. Chem.* **2007**, *58*, 613−634.
(44) Dugave, C.; Demange, L. Cis-Trans Isomerization of Organic Molecules and Biomolecules: Implications and Applications. *Chem. Rev.* **2003**, *103*, 2475−2532.
(45) Wang, Q.; Schoenlein, R. W.; Peteanu, L. A.; Mathies, R. A.; Shank, C. V. Vibrationally Coherent Photochemistry in the Femtosecond Primary Event of Vision. *Science* **1994**, *266*, 422−424.
(46) Peteanu, L. A.; Schoenlein, R. W.; Wang, Q.; Mathies, R. A.; Shank, C. V. The First Step in Vision Occurs in Femtoseconds: Complete Blue and Red Spectral Studies. *Proc. Natl. Acad. Sci. U. S. A.* **1993**, *90*, 11762−11766.
(47) Schnedermann, C.; Yang, X.; Liebel, M.; Spillane, K. M.; Lugtenburg, J.; Fernandez, I.; Valentini, A.; Schapiro, I.; Olivucci, M.; Kukura, P.; et al. Evidence for a Vibrational Phase-Dependent Isotope Effect on the Photochemistry of Vision. *Nat. Chem.* **2018**, *10*, 449−455.
(48) Wasielewski, M. R. Photoinduced Electron Transfer in Supramolecular Systems for Artificial Photosynthesis. *Chem. Rev.* **1992**, *92*, 435−461.
(49) Song, Y.; Schubert, A.; Maret, E.; Burdick, R. K.; Dunietz, B.; Geva, E.; Ogilvie, J. Vibronic Structure of Photosynthetic Pigments Probed by Polarized Two-Dimensional Electronic Spectroscopy and Ab Initio Calculations. *Chem. Sci.* **2019**, *10*, 8143−8153.
(50) Scholes, G. D.; Fleming, G. R.; Chen, L. X.; Aspuru-Guzik, A.; Buchleitner, A.; Coker, D. F.; Engel, G. S.; van Grondelle, R.; Ishizaki, A.; Jonas, D. M.; et al. Using Coherence to Enhance Function in Chemical and Biophysical Systems. *Nature* **2017**, *543*, 647−656.
(51) Romero, E.; Augulis, R.; Novoderezhkin, V. I.; Ferretti, M.; Thieme, J.; Zigmantas, D.; van Grondelle, R. Quantum Coherence in Photosynthesis for Efficient Solar Energy Conversion. *Nat. Phys.* **2014**, *10*, 676−682.
(52) Collini, E.; Wong, C. Y.; Wilk, K. E.; Curmi, P. M.; Brumer, P.; Scholes, G. D. Coherently Wired Light-Harvesting in Photosynthetic Marine Algae at Ambient Temperature. *Nature* **2010**, *463*, 644−647.
(53) Beljonne, D.; Pourtois, G.; Silva, C.; Hennebicq, E.; Herz, L. M.; Friend, R. H.; Scholes, G. D.; Setayesh, S.; Mullen, K.; Bredas, J. L. Interchain Vs. Intrachain Energy Transfer in Acceptor-Capped Conjugated Polymers. *Proc. Natl. Acad. Sci. U. S. A.* **2002**, *99*, 10982−10987.
(54) Henriksen, N. E. Laser Control of Chemical Reactions. *Chem. Soc. Rev.* **2002**, *31*, 37−42.
(55) Zare, R. N. Laser Control of Chemical Reactions. *Science* **1998**, *279*, 1875−1879.
(56) Brumer, P.; Shapiro, M. Coherence Chemistry: Controlling Chemical Reactions [with Lasers]. *Acc. Chem. Res.* **1989**, *22*, 407−413.
(57) Pan, X.; Fang, C.; Fantin, M.; Malhotra, N.; So, W. Y.; Peteanu, L. A.; Isse, A. A.; Gennaro, A.; Liu, P.; Matyjaszewski, K. Mechanism of Photoinduced Metal-Free Atom Transfer Radical Polymerization: Experimental and Computational Studies. *J. Am. Chem. Soc.* **2016**, *138*, 2411−2425.
(58) Chen, L.; Zhang, Y.; Chen, G.; Franco, I. Stark Control of Electrons Along Nanojunctions. *Nat. Commun.* **2018**, *9*, 2070−2082.
(59) Scholes, G. D.; Rumbles, G. Excitons in Nanoscale Systems. *Nat. Mater.* **2006**, *5*, 683−696.
(60) Bernardi, F.; Olivucci, M.; Robb, M. A. Potential Energy Surface Crossings in Organic Photochemistry. *Chem. Soc. Rev.* **1996**, *25*, 321−328.
(61) Beck, M. H.; Jäckle, A.; Worth, G. A.; Meyer, H. D. The Multiconfiguration Time-Dependent Hartree (Mctdh) Method: A Highly Efficient Algorithm for Propagating Wavepackets. *Phys. Rep.* **2000**, *324*, 1−105.
(62) Ben-Nun, M.; Martínez, T. J. Ab Initio Quantum Molecular Dynamics. *Adv. Chem. Phys.* **2002**, *121*, 439−512.
(63) Stock, G.; Thoss, M. Semiclassical Description of Nonadiabatic Quantum Dynamics. *Phys. Rev. Lett.* **1997**, *78*, 578−581.
(64) Thoss, M.; Stock, G. Mapping Approach to the Semiclassical Description of Nonadiabatic Quantum Dynamics. *Phys. Rev. A: At., Mol., Opt. Phys.* **1999**, *59*, 64−79.
(65) Thoss, M.; Miller, W. H.; Stock, G. Semiclassical Description of Nonadiabatic Quantum Dynamics: Application to the S1−S2 Conical Intersection in Pyrazine. *J. Chem. Phys.* **2000**, *112*, 10282−10292.
(66) Lee, M. K.; Huo, P.; Coker, D. F. Semiclassical Path Integral Dynamics: Photosynthetic Energy Transfer with Realistic Environment Interactions. *Annu. Rev. Phys. Chem.* **2016**, *67*, 639−668.
(67) Chowdhury, S. N.; Huo, P. State Dependent Ring Polymer Molecular Dynamics for Investigating Excited Nonadiabatic Dynamics. *J. Chem. Phys.* **2019**, *150*, 244102.
(68) Makhov, D. V.; Symonds, C.; Fernandez-Alberti, S.; Shalashilin, D. V. Ab Initio Quantum Direct Dynamics Simulations of Ultrafast Photochemistry with Multiconfigurational Ehrenfest Approach. *Chem. Phys.* **2017**, *493*, 200−218.
(69) McLachlan, A. D. A Variational Solution of the Time-Dependent Schrodinger Equation. *Mol. Phys.* **1964**, *8*, 39−44.
(70) Micha, D. A. A Self-Consistent Eikonal Treatment of Electronic Transitions in Molecular Collisions. *J. Chem. Phys.* **1983**, *78*, 7138−7145.
(71) Kirson, Z.; Gerber, R. B.; Nitzan, A.; Ratner, M. A. Dynamics of Metal Electron Excitation in Atom-Surface Collisions: A Quantum Wave Packet Approach. *Surf. Sci.* **1984**, *137*, 527−550.
(72) Sawada, S.-I.; Nitzan, A.; Metiu, H. Mean-Trajectory Approximation for Charge- and Energy-Transfer Processes at Surfaces. *Phys. Rev. B: Condens. Matter Mater. Phys.* **1985**, *32*, 851−867.
(73) Billing, G. D. *The Quantum Classical Theory*; Oxford University Press: Oxford, UK, 2003.
(74) Wang, L.; Akimov, A.; Prezhdo, O. V. Recent Progress in Surface Hopping: 2011−2015. *J. Phys. Chem. Lett.* **2016**, *7*, 2100−2112.
(75) *Nonadiabatic Dynamics: Mean-Field and Surface Hopping, Nikos L. Doltsinis, Quantum Simulations of Complex Many-Body Systems: From Theory to Algorithms, Lecture Notes*, NIC Series; Grotendorst, J., Marx, D., Muramatsu, A., Eds.; John von Neumann Institute for Computing: Jülich, 2002; Vol. *10*.
(76) Tully, J. C. Perspective: Nonadiabatic Dynamics Theory. *J. Chem. Phys.* **2012**, *137*, 22A301.
(77) Joos, E.; Zeh, H. D.; Kiefer, C.; Giulini, D. J. W.; Kupsch, J.; Stamatescu, I.-O. *Decoherence and the Appearance of a Classical World in Quantum Theory*; Springer-Verlag: Berlin/Heidelberg, 2003.
(78) Subotnik, J. E.; Jain, A.; Landry, B.; Petit, A.; Ouyang, W.; Bellonzi, N. Understanding the Surface Hopping View of Electronic Transitions and Decoherence. *Annu. Rev. Phys. Chem.* **2016**, *67*, 387−417.
(79) Landry, B. R.; Subotnik, J. E. Communication: Standard Surface Hopping Predicts Incorrect Scaling for Marcus' Golden-Rule Rate: The Decoherence Problem Cannot Be Ignored. *J. Chem. Phys.* **2011**, *135*, 191101.
(80) Prezhdo, O. V.; Rossky, P. J. Evaluation of Quantum Transition Rates from Quantum-Classical Molecular Dynamics Simulations. *J. Chem. Phys.* **1997**, *107*, 5863−5878.

https://dx.doi.org/10.1021/acs.chemrev.9b00447
Chem. Rev. 2020, 120, 2215−2287

(81) Hack, M. D.; Truhlar, D. G. A Natural Decay of Mixing Algorithm for Non-Born−Oppenheimer Trajectories. *J. Chem. Phys.* **2001**, *114*, 9305−9314.
(82) Zhu, C.; Nangia, S.; Jasper, A. W.; Truhlar, D. G. Coherent Switching with Decay of Mixing: An Improved Treatment of Electronic Coherence for Non-Born-Oppenheimer Trajectories. *J. Chem. Phys.* **2004**, *121*, 7658−7670.
(83) Granucci, G.; Persico, M. Critical Appraisal of the Fewest Switches Algorithm for Surface Hopping. *J. Chem. Phys.* **2007**, *126*, 134114.
(84) Granucci, G.; Persico, M.; Zoccante, A. Including Quantum Decoherence in Surface Hopping. *J. Chem. Phys.* **2010**, *133*, 134111.
(85) Barbatti, M.; Lischka, H. Nonadiabatic Deactivation of 9h-Adenine: A Comprehensive Picture Based on Mixed Quantum−Classical Dynamics. *J. Am. Chem. Soc.* **2008**, *130*, 6831−6839.
(86) Barbatti, M.; Lan, Z.; Crespo-Otero, R.; Szymczak, J. J.; Lischka, H.; Thiel, W. Critical Appraisal of Excited State Nonadiabatic Dynamics Simulations of 9h-Adenine. *J. Chem. Phys.* **2012**, *137*, 22A503.
(87) Plasser, F.; Granucci, G.; Pittner, J.; Barbatti, M.; Persico, M.; Lischka, H. Surface Hopping Dynamics Using a Locally Diabatic Formalism: Charge Transfer in the Ethylene Dimer Cation and Excited State Dynamics in the 2-Pyridone Dimer. *J. Chem. Phys.* **2012**, *137*, 22A514.
(88) Webster, F.; Rossky, P. J.; Friesner, R. A. Nonadiabatic Processes in Condensed Matter: Semi-Classical Theory and Implementation. *Comput. Phys. Commun.* **1991**, *63*, 494−522.
(89) Habenicht, B. F.; Prezhdo, O. V. Nonradiative Quenching of Fluorescence in a Semiconducting Carbon Nanotube: A Time-Domain Ab Initio Study. *Phys. Rev. Lett.* **2008**, *100*, 197402.
(90) Habenicht, B. F.; Prezhdo, O. V. Time-Domain Ab Initio Study of Nonradiative Decay in a Narrow Graphene Ribbon. *J. Phys. Chem. C* **2009**, *113*, 14067−14070.
(91) Prezhdo, O. V.; Rossky, P. J. Relationship between Quantum Decoherence Times and Solvation Dynamics in Condensed Phase Chemical Systems. *Phys. Rev. Lett.* **1998**, *81*, 5294−5297.
(92) Webster, F.; Wang, E. T.; Rossky, P. J.; Friesner, R. A. Stationary Phase Surface Hopping for Nonadiabatic Dynamics: Two-State Systems. *J. Chem. Phys.* **1994**, *100*, 4835−4847.
(93) Nelson, T.; Fernandez-Alberti, S.; Roitberg, A. E.; Tretiak, S. Nonadiabatic Excited-State Molecular Dynamics: Treatment of Electronic Decoherence. *J. Chem. Phys.* **2013**, *138*, 224111.
(94) Shenvi, N.; Yang, W. Achieving Partial Decoherence in Surface Hopping through Phase Correction. *J. Chem. Phys.* **2012**, *137*, 22A528.
(95) Subotnik, J. E.; Shenvi, N. A New Approach to Decoherence and Momentum Rescaling in the Surface Hopping Algorithm. *J. Chem. Phys.* **2011**, *134*, 024105.
(96) Subotnik, J. E. Fewest-Switches Surface Hopping and Decoherence in Multiple Dimensions. *J. Phys. Chem. A* **2011**, *115*, 12083−12096.
(97) Larsen, R. E.; Bedard-Hearn, M. J.; Schwartz, B. J. Exploring the Role of Decoherence in Condensed-Phase Nonadiabatic Dynamics: A Comparison of Different Mixed Quantum/Classical Simulation Algorithms for the Excited Hydrated Electron. *J. Phys. Chem. B* **2006**, *110*, 20055−20066.
(98) Bedard-Hearn, M. J.; Larsen, R. E.; Schwartz, B. J. Mean-Field Dynamics with Stochastic Decoherence (MF-SD): A New Algorithm for Nonadiabatic Mixed Quantum/Classical Molecular-Dynamics Simulations with Nuclear-Induced Decoherence. *J. Chem. Phys.* **2005**, *123*, 234106.
(99) Jaeger, H. M.; Fischer, S.; Prezhdo, O. V. Decoherence-Induced Surface Hopping. *J. Chem. Phys.* **2012**, *137*, 22A545.
(100) Neria, E.; Nitzan, A. Semiclassical Evaluation of Nonadiabatic Rates in Condensed Phases. *J. Chem. Phys.* **1993**, *99*, 1109−1123.
(101) Schwartz, B. J.; Bittner, E. R.; Prezhdo, O. V.; Rossky, P. J. Quantum Decoherence and the Isotope Effect in Condensed Phase Nonadiabatic Molecular Dynamics Simulations. *J. Chem. Phys.* **1996**, *104*, 5942−5955.
(102) Bittner, E. R.; Rossky, P. J. Decoherent Histories and Nonadiabatic Quantum Molecular Dynamics Simulations. *J. Chem. Phys.* **1997**, *107*, 8611−8618.
(103) Fang, J.-Y.; Hammes-Schiffer, S. Improvement of the Internal Consistency in Trajectory Surface Hopping. *J. Phys. Chem. A* **1999**, *103*, 9399−9407.
(104) Fernandez-Alberti, S.; Roitberg, A. E.; Nelson, T.; Tretiak, S. Identification of Unavoided Crossings in Nonadiabatic Photoexcited Dynamics Involving Multiple Electronic States in Polyatomic Conjugated Molecules. *J. Chem. Phys.* **2012**, *137*, 014512.
(105) Nelson, T.; Fernandez-Alberti, S.; Roitberg, A. E.; Tretiak, S. Artifacts Due to Trivial Unavoided Crossings in the Modeling of Photoinduced Energy Transfer Dynamics in Extended Conjugated Molecules. *Chem. Phys. Lett.* **2013**, *590*, 208−213.
(106) Granucci, G.; Persico, M.; Toniolo, A. Direct Semiclassical Simulation of Photochemical Processes with Semiempirical Wave Functions. *J. Chem. Phys.* **2001**, *114*, 10608−10615.
(107) Wang, L.; Prezhdo, O. V. A Simple Solution to the Trivial Crossing Problem in Surface Hopping. *J. Phys. Chem. Lett.* **2014**, *5*, 713−719.
(108) Virshup, A. M.; Levine, B. G.; Martínez, T. J. Steric and Electrostatic Effects on Photoisomerization Dynamics Using QM/MM Ab Initio Multiple Spawning. *Theor. Chem. Acc.* **2014**, *133*, 1506.
(109) Plasser, F.; Ruckenbauer, M.; Mai, S.; Oppel, M.; Marquetand, P.; González, L. Efficient and Flexible Computation of Many-Electron Wave Function Overlaps. *J. Chem. Theory Comput.* **2016**, *12*, 1207−1219.
(110) Wang, L.; Beljonne, D. Flexible Surface Hopping Approach to Model the Crossover from Hopping to Band-Like Transport in Organic Crystals. *J. Phys. Chem. Lett.* **2013**, *4*, 1888−1894.
(111) Fabiano, E.; Keal, T. W.; Thiel, W. Implementation of Surface Hopping Molecular Dynamics Using Semiempirical Methods. *Chem. Phys.* **2008**, *349*, 334−347.
(112) Fabiano, E.; Groenhof, G.; Thiel, W. Approximate Switching Algorithms for Trajectory Surface Hopping. *Chem. Phys.* **2008**, *351*, 111−116.
(113) Spörkel, L.; Thiel, W. Adaptive Time Steps in Trajectory Surface Hopping Simulations. *J. Chem. Phys.* **2016**, *144*, 194108.
(114) Wang, L.; Trivedi, D.; Prezhdo, O. V. Global Flux Surface Hopping Approach for Mixed Quantum-Classical Dynamics. *J. Chem. Theory Comput.* **2014**, *10*, 3598−3605.
(115) Meek, G. A.; Levine, B. G. Evaluation of the Time-Derivative Coupling for Accurate Electronic State Transition Probabilities from Numerical Simulations. *J. Phys. Chem. Lett.* **2014**, *5*, 2351−2356.
(116) Meek, G. A.; Levine, B. G. Accurate and Efficient Evaluation of Transition Probabilities at Unavoided Crossings in Ab Initio Multiple Spawning. *Chem. Phys.* **2015**, *460*, 117−124.
(117) Jain, A.; Alguire, E.; Subotnik, J. E. An Efficient, Augmented Surface Hopping Algorithm That Includes Decoherence for Use in Large-Scale Simulations. *J. Chem. Theory Comput.* **2016**, *12*, 5256−5268.
(118) McLachlan, A. D.; Ball, M. A. Time-Dependent Hartree—Fock Theory for Molecules. *Rev. Mod. Phys.* **1964**, *36*, 844−855.
(119) Jorgensen, P. Molecular and Atomic Applications of Time-Dependent Hartree-Fock Theory. *Annu. Rev. Phys. Chem.* **1975**, *26*, 359−380.
(120) Curchod, B. F. E.; Martinez, T. J. Ab Initio Nonadiabatic Quantum Molecular Dynamics. *Chem. Rev.* **2018**, *118*, 3305−3336.
(121) Crespo-Otero, R.; Barbatti, M. Recent Advances and Perspectives on Nonadiabatic Mixed Quantum-Classical Dynamics. *Chem. Rev.* **2018**, *118*, 7026−7068.
(122) Bredas, J. L.; Beljonne, D.; Coropceanu, V.; Cornil, J. Charge-Transfer and Energy-Transfer Processes in Pi-Conjugated Oligomers and Polymers: A Molecular Picture. *Chem. Rev.* **2004**, *104*, 4971−5004.
(123) Goings, J. J.; Lestrange, P. J.; Li, X. Real-Time Time-Dependent Electronic Structure Theory. *WIREs Comput. Mol. Sci.* **2018**, *8*, e1341.
(124) Yeager, D. L.; Jørgensen, P. A Multiconfigurational Time-Dependent Hartree-Fock Approach. *Chem. Phys. Lett.* **1979**, *65*, 77−80.

https://dx.doi.org/10.1021/acs.chemrev.9b00447
Chem. Rev. 2020, 120, 2215−2287

(125) Ben-Nun, M.; Quenneville, J.; Martínez, T. J. Ab Initio Multiple Spawning: Photochemistry from First Principles Quantum Molecular Dynamics. *J. Phys. Chem. A* **2000**, *104*, 5161−5175.
(126) Min, S. K.; Agostini, F.; Tavernelli, I.; Gross, E. K. U. Ab Initio Nonadiabatic Dynamics with Coupled Trajectories: A Rigorous Approach to Quantum (De)Coherence. *J. Phys. Chem. Lett.* **2017**, *8*, 3048−3055.
(127) Kapral, R. Progress in the Theory of Mixed Quantum-Classical Dynamics. *Annu. Rev. Phys. Chem.* **2006**, *57*, 129−157.
(128) Habershon, S.; Manolopoulos, D. E.; Markland, T. E.; Miller, T. F., III Ring-Polymer Molecular Dynamics: Quantum Effects in Chemical Dynamics from Classical Trajectories in an Extended Phase Space. *Annu. Rev. Phys. Chem.* **2013**, *64*, 387−413.
(129) Manthe, U. Wavepacket Dynamics and the Multi-Configurational Time-Dependent Hartree Approach. *J. Phys.: Condens. Matter* **2017**, *29*, 253001.
(130) Markland, T. E.; Ceriotti, M. Nuclear Quantum Effects Enter the Mainstream. *Nat. Rev. Chem.* **2018**, *2*, 0109.
(131) Zhugayevych, A.; Tretiak, S. Theoretical Description of Structural and Electronic Properties of Organic Photovoltaic Materials. *Annu. Rev. Phys. Chem.* **2015**, *66*, 305−330.
(132) Bartlett, R. J.; Musiał, M. Coupled-Cluster Theory in Quantum Chemistry. *Rev. Mod. Phys.* **2007**, *79*, 291−352.
(133) Bartlett, R. J. Many-Body Perturbation Theory and Coupled Cluster Theory for Electron Correlation in Molecules. *Annu. Rev. Phys. Chem.* **1981**, *32*, 359−401.
(134) Lyakh, D. I.; Musial, M.; Lotrich, V. F.; Bartlett, R. J. Multireference Nature of Chemistry: The Coupled-Cluster View. *Chem. Rev.* **2012**, *112*, 182−243.
(135) Reining, L. The Gw Approximation: Content, Successes and Limitations. *WIREs Comput. Mol. Sci.* **2018**, *8*, e1344.
(136) Akimov, A. V.; Prezhdo, O. V. The Pyxaid Program for Non-Adiabatic Molecular Dynamics in Condensed Matter Systems. *J. Chem. Theory Comput.* **2013**, *9*, 4959−4972.
(137) Sifain, A. E.; Bjorgaard, J. A.; Nelson, T. R.; Nebgen, B. T.; White, A. J.; Gifford, B. J.; Gao, D. W.; Prezhdo, O. V.; Fernandez-Alberti, S.; Roitberg, A. E.; et al. Photoexcited Nonadiabatic Dynamics of Solvated Push−Pull Π-Conjugated Oligomers with the Nexmd Software. *J. Chem. Theory Comput.* **2018**, *14*, 3955−3966.
(138) Born, M.; K, H. *Dynamical Theory of Crystal Lattices*; Oxford University Press, 1955.
(139) Born, M.; Oppenheimer, R. Zur Quantentheorie Der Molekeln. *Ann. Phys.* **1927**, *389*, 457−484.
(140) Subotnik, J. E.; Alguire, E. C.; Ou, Q.; Landry, B. R.; Fatehi, S. The Requisite Electronic Structure Theory to Describe Photoexcited Nonadiabatic Dynamics: Nonadiabatic Derivative Couplings and Diabatic Electronic Couplings. *Acc. Chem. Res.* **2015**, *48*, 1340−1350.
(141) Piryatinski, A.; Stepanov, M.; Tretiak, S.; Chernyak, V. Semiclassical Scattering on Conical Intersections. *Phys. Rev. Lett.* **2005**, *95*, 223001.
(142) Chen, L.; Shao, K.; Chen, J.; Yang, M.; Zhang, D. H. Full-Dimensional Quantum Dynamics Study of the $H_2 + C_2H \rightarrow H + C_2H_2$ Reaction on an Ab Initio Potential Energy Surface. *J. Chem. Phys.* **2016**, *144*, 194309.
(143) Zhang, D. H.; Guo, H. Recent Advances in Quantum Dynamics of Bimolecular Reactions. *Annu. Rev. Phys. Chem.* **2016**, *67*, 135−158.
(144) Ren, Y.; Li, B.; Bian, W. Full-Dimensional Quantum Dynamics Study of Vinylidene-Acetylene Isomerization: A Scheme Using the Normal Mode Hamiltonian. *Phys. Chem. Chem. Phys.* **2011**, *13*, 2052−2061.
(145) Jiang, B.; Xie, D.; Guo, H. State-to-State Photodissociation Dynamics of Triatomic Molecules: H_2O in the B Band. *J. Chem. Phys.* **2012**, *136*, 034302.
(146) DeVine, J. A.; Weichman, M. L.; Zhou, X. Y.; Ma, J. Y.; Jiang, B.; Guo, H.; Neumark, D. M. Non-Adiabatic Effects on Excited States of Vinylidene Observed with Slow Photoelectron Velocity-Map Imaging. *J. Am. Chem. Soc.* **2016**, *138*, 16417−16425.
(147) Guo, H.; Ma, J. Y.; Jiang, B.; Xie, D. Q. Quantum Non-Adiabatic Dynamics in Polyatomic Photodissociation. *Abstr. Pap. Am. Chem. Soc.* **2013**, *245*.
(148) Ma, J. Y.; Xie, C. J.; Zhu, X. L.; Yarkony, D. R.; Xie, D. Q.; Guo, H. Full-Dimensional Quantum Dynamics of Vibrationally Mediated Photodissociation of NH_3 and ND_3 on Coupled Ab Initio Potential Energy Surfaces: Absorption Spectra and $NH_2(\tilde{A}^2A_1)/NH_2(\tilde{X}^2B_1)$ Branching Ratios. *J. Phys. Chem. A* **2014**, *118*, 11926−11934.
(149) Ma, J. Y.; Zhu, X. L.; Guo, H.; Yarkony, D. R. First Principles Determination of the Nh2/Nd2((a)over-Tilde,(X)over-Tilde) Branching Ratios for Photodissociation of Nh3/Nd3 Via Full-Dimensional Quantum Dynamics Based on a New Quasi-Diabatic Representation of Coupled Ab Initio Potential Energy Surfaces. *J. Chem. Phys.* **2012**, *137*, 22A541.
(150) Tao, G. Electronically Nonadiabatic Dynamics in Singlet Fission: A Quasi-Classical Trajectory Simulation. *J. Phys. Chem. C* **2014**, *118*, 17299−17305.
(151) Tao, G.; Miller, W. H. Semiclassical Description of Electronic Excitation Population Transfer in a Model Photosynthetic System. *J. Phys. Chem. Lett.* **2010**, *1*, 891−894.
(152) Van Wyngarden, A. L.; Mar, K. A.; Quach, J.; Nguyen, A. P. Q.; Wiegel, A. A.; Lin, S. Y.; Lendvay, G.; Guo, H.; Lin, J. J.; Lee, Y. T.; et al. The Non-Statistical Dynamics of the $^{18}O + {}^{32}O_2$ Isotope Exchange Reaction at Two Energies. *J. Chem. Phys.* **2014**, *141*, 064311.
(153) Xie, C. J.; Hu, X. X.; Zhou, L. S.; Xie, D. Q.; Guo, H. Ab Initio Determination of Potential Energy Surfaces for the First Two Uv Absorption Bands of SO_2. *J. Chem. Phys.* **2013**, *139*, 014305.
(154) Xie, C. J.; Zhu, X. L.; Ma, J. Y.; Yarkony, D. R.; Xie, D. Q.; Guo, H. Communication: On the Competition between Adiabatic and Nonadiabatic Dynamics in Vibrationally Mediated Ammonia Photodissociation in Its a Band. *J. Chem. Phys.* **2015**, *142*, 091101.
(155) Zhou, L.; Jiang, B.; Xie, D.; Guo, H. State-to-State Photodissociation Dynamics of H_2O in the B-Band: Competition between Two Coexisting Nonadiabatic Pathways. *J. Phys. Chem. A* **2013**, *117*, 6940−6947.
(156) Zhou, L. S.; Xie, D. Q.; Guo, H. Signatures of Non-Adiabatic Dynamics in the Fine-Structure State Distributions of the $OH(\tilde{X}/\tilde{A})$ Products in the B-Band Photodissociation of H_2O. *J. Chem. Phys.* **2015**, *142*, 124317.
(157) Zhou, Z.; Liu, J.; Long, R.; Li, L.; Guo, L.; Prezhdo, O. V. Control of Charge Carriers Trapping and Relaxation in Hematite by Oxygen Vacancy Charge: Ab Initio Non-Adiabatic Molecular Dynamics. *J. Am. Chem. Soc.* **2017**, *139*, 6707−6717.
(158) Ma, J.; Guo, H. *Advances in Chemical Physics*; John Wiley & Sons, Inc., 2018; Vol. *163*.
(159) Goldberg, A.; Schey, H. M.; Schwartz, J. L. Computer-Generated Motion Pictures of One-Dimensional Quantum-Mechanical Transmission and Reflection Phenomena. *Am. J. Phys.* **1967**, *35*, 177−186.
(160) Askar, A.; Cakmak, A. S. Explicit Integration Method for the Time-Dependent Schrodinger Equation for Collision Problems. *J. Chem. Phys.* **1978**, *68*, 2794−2798.
(161) Gray, S. K. Wave Packet Dynamics of Resonance Decay: An Iterative Equation Approach with Application to HCP→H+CO. *J. Chem. Phys.* **1992**, *96*, 6543−6554.
(162) Kosloff, R. Propagation Methods for Quantum Molecular-Dynamics. *Annu. Rev. Phys. Chem.* **1994**, *45*, 145−178.
(163) McCullough, E. A.; Wyatt, R. E. Dynamics of the Collinear H $+H_2$ Reaction. I. Probability Density and Flux. *J. Chem. Phys.* **1971**, *54*, 3578−3591.
(164) Colbert, D. T.; Miller, W. H. A Novel Discrete Variable Representation for Quantum-Mechanical Reactive Scattering Via the S-Matrix Kohn Method. *J. Chem. Phys.* **1992**, *96*, 1982−1991.
(165) Wu, Y.; Herman, M. F.; Batista, V. S. Matching-Pursuit/Split-Operator Fourier-Transform Simulations of Nonadiabatic Quantum Dynamics. *J. Chem. Phys.* **2005**, *122*, 114114.
(166) Wu, Y.; Batista, V. S. Matching-Pursuit for Simulations of Quantum Processes. *J. Chem. Phys.* **2003**, *118*, 6720−6724.

https://dx.doi.org/10.1021/acs.chemrev.9b00447
Chem. Rev. 2020, 120, 2215−2287

(167) Wu, Y.; Batista, V. S. Semiclassical Molecular Dynamics Simulations of the Excited State Photodissociation Dynamics of H_2O in the A^1B_1 Band. *J. Phys. Chem. B* **2002**, *106*, 8271−8277.
(168) Chen, X.; Batista, V. S. Matching-Pursuit/Split-Operator-Fourier-Transform Simulations of Excited-State Nonadiabatic Quantum Dynamics in Pyrazine. *J. Chem. Phys.* **2006**, *125*, 124313.
(169) Worth, G. A.; Meyer, H. D.; Köppel, H.; Cederbaum, L. S.; Burghardt, I. Using the Mctdh Wavepacket Propagation Method to Describe Multimode Non-Adiabatic Dynamics. *Int. Rev. Phys. Chem.* **2008**, *27*, 569−606.
(170) Tamura, H.; Burghardt, I. Ultrafast Charge Separation in Organic Photovoltaics Enhanced by Charge Delocalization and Vibronically Hot Exciton Dissociation. *J. Am. Chem. Soc.* **2013**, *135*, 16364−16367.
(171) Meyer, H. D.; Manthe, U.; Cederbaum, L. S. The Multi-Configurational Time-Dependent Hartree Approach. *Chem. Phys. Lett.* **1990**, *165*, 73−78.
(172) Landau, L. D. Zur Theorie Der Energieübertragung Bei StöSsen. *Phys. Z. Sowjetunion* **1932**, *1*, 88−98.
(173) Landau, L. D. Zur Theorie Der Energieübertragung II. *Phys. Z. Sowjetunion* **1932**, *2*, 46−51.
(174) Zener, C. Non-Adiabatic Crossing of Energy Levels. *Proc. R. Soc. London, Ser. A* **1932**, *137*, 696−702.
(175) Wittig, C. The Landau-Zener Formula. *J. Phys. Chem. B* **2005**, *109*, 8428−8430.
(176) Massey, H. S. W. Collisions between Atoms and Molecules at Ordinary Temperatures. *Rep. Prog. Phys.* **1949**, *12*, 248−269.
(177) Stueckelberg, E. C. G. Theorie Der Unelastischen StöSse Zwischen Atomen. *Helv. Phys. Acta* **1932**, *5*, 369−422.
(178) Rosen, N.; Zener, C. Double Stern-Gerlach Experiment and Related Collision Phenomena. *Phys. Rev.* **1932**, *40*, 502−507.
(179) Demkov, Y. N. Charge Transfer at Small Resonance Defects. *Soviet Phys. JETP-USSR* **1964**, *18*, 138−142.
(180) Teller, E. The Crossing of Potential Surfaces. *J. Phys. Chem.* **1937**, *41*, 109−116.
(181) Kaliakin, D. S.; Zaari, R. R.; Varganov, S. A. Effect of H_2 Binding on the Nonadiabatic Transition Probability between Singlet and Triplet States of the [Nife]-Hydrogenase Active Site. *J. Phys. Chem. A* **2015**, *119*, 1066−1073.
(182) Tapavicza, E.; Tavernelli, I.; Rothlisberger, U. Ab Initio Excited State Properties and Dynamics of a Prototype Σ-Bridged-Donor-Acceptor Molecule. *J. Phys. Chem. A* **2009**, *113*, 9595−9602.
(183) Zaari, R. R.; Varganov, S. A. Nonadiabatic Transition State Theory and Trajectory Surface Hopping Dynamics: Intersystem Crossing between ^{3}B1 and ^{1}A1 States of SiH_2. *J. Phys. Chem. A* **2015**, *119*, 1332−1338.
(184) Delos, J. B.; Thorson, W. R. Studies of the Potential-Curve-Crossing Problem. Ii. General Theory and a Model for Close Crossings. *Phys. Rev. A: At., Mol., Opt. Phys.* **1972**, *6*, 728−745.
(185) Nikitin, E. E. Nonadiabatic Vibrational Excitation of Molecules During Molecular Collisions. *Opt. Spectrosc.* **1960**, *9*, 16−21.
(186) Nikitin, E. E. Probability of Nonadiabatic Transitions in the Case of Non-Separating Terms. *Opt. Spectrosc.* **1962**, *13*, 761−765.
(187) Nikitin, E. E.; Bykhovsk, Vk Nonadiabatic Transitions During Atomic Collisions. Quenching of Resonance Fluorescence of Sodium Vapors by Argon. *Opt. Spectrosc.* **1964**, *17*, 444.
(188) Nikitin, E. E. Nonadiabatic Transitions between Fine-Structure Components of Alkali Metal Atoms During Atomic Collisions. *Opt. Spectrosc.* **1965**, *19*, 91.
(189) Nikitin, E. E. Methods for Calculation of Nonadiabatic Transition Probabilities. *Opt. Spectrosc.* **1965**, *18*, 431.
(190) Nikitin, E. E. Nonadiabatic Transitions between Fine-Structure Components of Alkali Atoms Upon Collision with Inert-Gas Atoms. *J. Chem. Phys.* **1965**, *43*, 744−750.
(191) Zhu, C. Y.; Nakamura, H. Numerical-Method for the 2-State Linear Curve Crossing - Nonadiabatic Tunneling Case. *Comput. Phys. Commun.* **1993**, *74*, 9−17.
(192) Zhu, C. Y.; Nakamura, H. The 2-State Linear Curve Crossing Problems Revisited 0.3. Analytical Approximations for Stokes Constant and Scattering Matrix - Nonadiabatic Tunneling Case. *J. Chem. Phys.* **1993**, *98*, 6208−6222.
(193) Zhu, C.; Nakamura, H. Theory of Nonadiabatic Transition for General Two-State Curve Crossing Problems. *J. Chem. Phys.* **1994**, *101*, 10630−10647.
(194) Zhu, C.; Nakamura, H. Theory of Nonadiabatic Transition for General Two-State Curve Crossing Problems. Ii. Landau−Zener Case. *J. Chem. Phys.* **1995**, *102*, 7448−7461.
(195) Ishida, T.; Nanbu, S.; Nakamura, H. Clarification of Nonadiabatic Chemical Dynamics by the Zhu-Nakamura Theory of Nonadiabatic Transition: From Tri-Atomic Systems to Reactions in Solutions. *Int. Rev. Phys. Chem.* **2017**, *36*, 229−285.
(196) Nikitin, E. E. Nonadiabatic Transitions: What We Learned from Old Masters and How Much We Owe Them. *Annu. Rev. Phys. Chem.* **1999**, *50*, 1−21.
(197) Nakamura, H. *Nonadiabatic Transition: Concepts, Basic Theories and Applications*; World Scientific, 2012.
(198) Delos, J. B. Reactions of N2 with O. *J. Chem. Phys.* **1973**, *59*, 2365−2369.
(199) Littlejohn, R. G. The Van Vleck Formula, Maslov Theory, and Phase Space Geometry. *J. Stat. Phys.* **1992**, *68*, 7−50.
(200) Meyer, H. D.; Miller, W. H. A Classical Analog for Electronic Degrees of Freedom in Nonadiabatic Collision Processes. *J. Chem. Phys.* **1979**, *70*, 3214−3223.
(201) Miller, W. H. The Semiclassical Initial Value Representation: A Potentially Practical Way for Adding Quantum Effects to Classical Molecular Dynamics Simulations. *J. Phys. Chem. A* **2001**, *105*, 2942−2955.
(202) Sun, X.; Miller, W. H. Mixed Semiclassical−Classical Approaches to the Dynamics of Complex Molecular Systems. *J. Chem. Phys.* **1997**, *106*, 916−927.
(203) Miller, W. H. Electronically Nonadiabatic Dynamics Via Semiclassical Initial Value Methods. *J. Phys. Chem. A* **2009**, *113*, 1405−1415.
(204) Heller, E. J. Time-Dependent Approach to Semiclassical Dynamics. *J. Chem. Phys.* **1975**, *62*, 1544−1555.
(205) Heller, E. J. Frozen Gaussians: A Very Simple Semiclassical Approximation. *J. Chem. Phys.* **1981**, *75*, 2923−2931.
(206) Huber, D.; Heller, E. J. Generalized Gaussian Wave Packet Dynamics. *J. Chem. Phys.* **1987**, *87*, 5302−5311.
(207) Kong, X. M.; Markmann, A.; Batista, V. S. Time-Sliced Thawed Gaussian Propagation Method for Simulations of Quantum Dynamics. *J. Phys. Chem. A* **2016**, *120*, 3260−3269.
(208) Kluk, E.; Herman, M. F.; Davis, H. L. Comparison of the Propagation of Semiclassical Frozen Gaussian Wave Functions with Quantum Propagation for a Highly Excited Anharmonic Oscillator. *J. Chem. Phys.* **1986**, *84*, 326−334.
(209) Herman, M. F. Nonadiabatic Semiclassical Scattering. I. Analysis of Generalized Surface Hopping Procedures. *J. Chem. Phys.* **1984**, *81*, 754−763.
(210) Yang, G.; Herman, M. F. Semiclassical Surface Hopping H−K Propagator: Application to Two-Dimensional, Two-Surface Problems. *J. Phys. Chem. B* **2001**, *105*, 6562−6569.
(211) Wu, Y.; Herman, M. F. On the Properties of a Primitive Semiclassical Surface Hopping Propagator for Nonadiabatic Quantum Dynamics. *J. Chem. Phys.* **2007**, *127*, 044109.
(212) Wu, Y.; Herman, M. F. A Justification for a Nonadiabatic Surface Hopping Herman-Kluk Semiclassical Initial Value Representation of the Time Evolution Operator. *J. Chem. Phys.* **2006**, *125*, 154116.
(213) Wu, Y.; Herman, M. F. Nonadiabatic Surface Hopping Herman-Kluk Semiclassical Initial Value Representation Method Revisited: Applications to Tully's Three Model Systems. *J. Chem. Phys.* **2005**, *123*, 144106.
(214) Herman, M. F. Toward an Accurate and Efficient Semiclassical Surface Hopping Procedure for Nonadiabatic Problems. *J. Phys. Chem. A* **2005**, *109*, 9196−9205.
(215) Loh, E. Y.; Gubernatis, J. E.; Scalettar, R. T.; White, S. R.; Scalapino, D. J.; Sugar, R. L. Sign Problem in the Numerical Simulation

https://dx.doi.org/10.1021/acs.chemrev.9b00447
Chem. Rev. 2020, 120, 2215−2287

of Many-Electron Systems. *Phys. Rev. B: Condens. Matter Mater. Phys.* **1990**, *41*, 9301−9307.
(216) Teh, H. H.; Cheng, Y. C. On the Accuracy of the Lsc-Ivr Approach for Excitation Energy Transfer in Molecular Aggregates. *J. Chem. Phys.* **2017**, *146*, 144105.
(217) Huo, P.; Coker, D. F. Semi-Classical Path Integral Non-Adiabatic Dynamics: A Partial Linearized Classical Mapping Hamiltonian Approach. *Mol. Phys.* **2012**, *110*, 1035−1052.
(218) Ananth, N.; Venkataraman, C.; Miller, W. H. Semiclassical Description of Electronically Nonadiabatic Dynamics Via the Initial Value Representation. *J. Chem. Phys.* **2007**, *127*, 084114.
(219) Ehrenfest, P. Bemerkung Uber Die Angenaherte Gultigkeit Der Klassischen Mechanik Innerhalb Der Quantenmechanik. *Eur. Phys. J. A* **1927**, *45*, 455−457.
(220) Nitzan, A. *Chemical Dynamics in Condensed Phases: Relaxation, Transfer, and Reactions in Condensed Molecular Systems*, 1st ed.; Oxford University Press, 2014.
(221) Tully, J. C. Mixed Quantum−Classical Dynamics. *Faraday Discuss.* **1998**, *110*, 407−419.
(222) Nagashima, K.; Takatsuka, K. Early-Stage Dynamics in Coupled Proton-Electron Transfer from the $\pi-\pi^*$ State of Phenol to Solvent Ammonia Clusters: A Nonadiabatic Electron Dynamics Study. *J. Phys. Chem. A* **2012**, *116*, 11167−11179.
(223) Gao, X.; Geng, H.; Peng, Q.; Ren, J.; Yi, Y.; Wang, D.; Shuai, Z. Nonadiabatic Molecular Dynamics Modeling of the Intrachain Charge Transport in Conjugated Diketopyrrolo-Pyrrole Polymers. *J. Phys. Chem. C* **2014**, *118*, 6631−6640.
(224) da Silva Oliboni, R.; Bortolini, G.; Torres, A.; Rego, L. G. C. A Nonadiabatic Excited State Molecular Mechanics/Extended Hückel Ehrenfest Method. *J. Phys. Chem. C* **2016**, *120*, 27688−27698.
(225) Ichikawa, H.; Takatsuka, K. Chemical Modification of Conical Intersections in Photoisomerization Dynamics of Butadiene Derivatives. *J. Phys. Chem. A* **2017**, *121*, 315−325.
(226) Parandekar, P. V.; Tully, J. C. Detailed Balance in Ehrenfest Mixed Quantum-Classical Dynamics. *J. Chem. Theory Comput.* **2006**, *2*, 229−235.
(227) Schmidt, J. R.; Parandekar, P. V.; Tully, J. C. Mixed Quantum-Classical Equilibrium: Surface Hopping. *J. Chem. Phys.* **2008**, *129*, 044104.
(228) Xie, B.; Cui, G.; Fang, W. H. Multiple-State Nonadiabatic Dynamics Simulation of Photoisomerization of Acetylacetone with the Direct Ab Initio Qtmf Approach. *J. Chem. Theory Comput.* **2017**, *13*, 2717−2729.
(229) Donati, G.; Lingerfelt, D. B.; Petrone, A.; Rega, N.; Li, X. "Watching" Polaron Pair Formation from First-Principles Electron-Nuclear Dynamics. *J. Phys. Chem. A* **2016**, *120*, 7255−7261.
(230) Lee, D.; Forsuelo, M. A.; Kocherzhenko, A. A.; Whaley, K. B. Higher-Energy Charge Transfer States Facilitate Charge Separation in Donor−Acceptor Molecular Dyads. *J. Phys. Chem. C* **2017**, *121*, 13043−13051.
(231) Ribeiro, L. A.; da Cunha, W. F.; de Oliveria Neto, P. H.; Gargano, R.; e Silva, G. M. Effects of Temperature and Electric Field Induced Phase Transitions on the Dynamics of Polarons and Bipolarons. *New J. Chem.* **2013**, *37*, 2829−2836.
(232) Meng, S.; Kaxiras, E. Electron and Hole Dynamics in Dye-Sensitized Solar Cells: Influencing Factors and Systematic Trends. *Nano Lett.* **2010**, *10*, 1238−1247.
(233) Ding, F.; Goings, J. J.; Liu, H.; Lingerfelt, D. B.; Li, X. Ab Initio Two-Component Ehrenfest Dynamics. *J. Chem. Phys.* **2015**, *143*, 114105.
(234) Tully, J. C. Molecular Dynamics with Electronic Transitions. *J. Chem. Phys.* **1990**, *93*, 1061−1071.
(235) Tully, J. C.; Preston, R. K. Trajectory Surface Hopping Approach to Nonadiabatic Molecular Collisions: The Reaction of H^+ with D_2. *J. Chem. Phys.* **1971**, *55*, 562−572.
(236) Jasper, A. W.; Truhlar, D. G. Improved Treatment of Momentum at Classically Forbidden Electronic Transitions in Trajectory Surface Hopping Calculations. *Chem. Phys. Lett.* **2003**, *369*, 60−67.
(237) Jasper, A. W.; Stechmann, S. N.; Truhlar, D. G. Fewest-Switches with Time Uncertainty: A Modified Trajectory Surface-Hopping Algorithm with Better Accuracy for Classically Forbidden Electronic Transitions. *J. Chem. Phys.* **2002**, *116*, 5424−5431.
(238) Perkins, T.; Herraez-Aguilar, D.; McCrudden, G.; Klos, J.; Aoiz, F. J.; Brouard, M. Surface-Hopping Trajectories for $OH(A^2\Sigma^+)$ + Kr: Extension to the 1A″ State. *J. Chem. Phys.* **2015**, *142*, 144307.
(239) Akimov, A. V.; Prezhdo, O. V. Second-Quantized Surface Hopping. *Phys. Rev. Lett.* **2014**, *113*, 153003.
(240) Martens, C. C. Surface Hopping by Consensus. *J. Phys. Chem. Lett.* **2016**, *7*, 2610−2615.
(241) Martens, C. C. Nonadiabatic Dynamics in the Semiclassical Liouville Representation: Locality, Transformation Theory, and the Energy Budget. *Chem. Phys.* **2016**, *481*, 60−68.
(242) Cardozo, T. M.; Galliez, A. P.; Borges, I.; Plasser, F.; Aquino, A. J. A.; Barbatti, M.; Lischka, H. Dynamics of Benzene Excimer Formation from the Parallel-Displaced Dimer. *Phys. Chem. Chem. Phys.* **2019**, *21*, 13916−13924.
(243) Atkins, A. J.; Gonzalez, L. Trajectory Surface-Hopping Dynamics Including Intersystem Crossing in [Ru(Bpy)3]2. *J. Phys. Chem. Lett.* **2017**, *8*, 3840−3845.
(244) Muuronen, M.; Parker, S. M.; Berardo, E.; Le, A.; Zwijnenburg, M. A.; Furche, F. Mechanism of Photocatalytic Water Oxidation on Small TiO2 Nanoparticles. *Chem. Sci.* **2017**, *8*, 2179−2183.
(245) Floss, G.; Saalfrank, P. The Photoinduced E–> Z Isomerization of Bisazobenzenes: A Surface Hopping Molecular Dynamics Study. *J. Phys. Chem. A* **2015**, *119*, 5026−5037.
(246) Alfonso Hernandez, L.; Nelson, T.; Gelin, M. F.; Lupton, J. M.; Tretiak, S.; Fernandez-Alberti, S. Interference of Interchromophoric Energy-Transfer Pathways in Pi-Conjugated Macrocycles. *J. Phys. Chem. Lett.* **2016**, *7*, 4936−4944.
(247) Sporkel, L.; Cui, G.; Thiel, W. Photodynamics of Schiff Base Salicylideneaniline: Trajectory Surface-Hopping Simulations. *J. Phys. Chem. A* **2013**, *117*, 4574−4583.
(248) Akimov, A. V. Nonadiabatic Molecular Dynamics with Tight-Binding Fragment Molecular Orbitals. *J. Chem. Theory Comput.* **2016**, *12*, 5719−5736.
(249) Park, J. W.; Shiozaki, T. On-the-Fly Caspt2 Surface-Hopping Dynamics. *J. Chem. Theory Comput.* **2017**, *13*, 3676−3683.
(250) Wei, Y.; Li, L.; Fang, W.; Long, R.; Prezhdo, O. V. Weak Donor-Acceptor Interaction and Interface Polarization Define Photoexcitation Dynamics in the MoS_2/TiO_2 Composite: Time-Domain Ab Initio Simulation. *Nano Lett.* **2017**, *17*, 4038−4046.
(251) Wiebeler, C.; Plasser, F.; Hedley, G. J.; Ruseckas, A.; Samuel, I. D.; Schumacher, S. Ultrafast Electronic Energy Transfer in an Orthogonal Molecular Dyad. *J. Phys. Chem. Lett.* **2017**, *8*, 1086−1092.
(252) Prlj, A.; Curchod, B. F.; Corminboeuf, C. Excited State Dynamics of Thiophene and Bithiophene: New Insights into Theoretically Challenging Systems. *Phys. Chem. Chem. Phys.* **2015**, *17*, 14719−14730.
(253) Akimov, A. V.; Prezhdo, O. V. Nonadiabatic Dynamics of Charge Transfer and Singlet Fission at the Pentacene/C_{60} Interface. *J. Am. Chem. Soc.* **2014**, *136*, 1599−1608.
(254) Rauer, C.; Nogueira, J. J.; Marquetand, P.; Gonzalez, L. Cyclobutane Thymine Photodimerization Mechanism Revealed by Nonadiabatic Molecular Dynamics. *J. Am. Chem. Soc.* **2016**, *138*, 15911−15916.
(255) Athanasopoulos, S.; Alfonso Hernandez, L.; Beljonne, D.; Fernandez-Alberti, S.; Tretiak, S. Ultrafast Non-Forster Intramolecular Donor-Acceptor Excitation Energy Transfer. *J. Phys. Chem. Lett.* **2017**, *8*, 1688−1694.
(256) Plasser, F.; Gomez, S.; Menger, M.; Mai, S.; Gonzalez, L. Highly Efficient Surface Hopping Dynamics Using a Linear Vibronic Coupling Model. *Phys. Chem. Chem. Phys.* **2019**, *21*, 57−69.
(257) Kasha, M. Characterization of Electronic Transitions in Complex Molecules. *Discuss. Faraday Soc.* **1950**, *9*, 14−19.
(258) Iyer, E. S. S.; Sadybekov, A.; Lioubashevski, O.; Krylov, A. I.; Ruhman, S. Rewriting the Story of Excimer Formation in Liquid Benzene. *J. Phys. Chem. A* **2017**, *121*, 1962−1975.

https://dx.doi.org/10.1021/acs.chemrev.9b00447
Chem. Rev. 2020, 120, 2215−2287

(259) Nenov, A.; Borrego-Varillas, R.; Oriana, A.; Ganzer, L.; Segatta, F.; Conti, I.; Segarra-Marti, J.; Omachi, J.; Dapor, M.; Taioli, S.; et al. Uv-Light-Induced Vibrational Coherences: The Key to Understand Kasha Rule Violation in Trans-Azobenzene. *J. Phys. Chem. Lett.* **2018**, *9*, 1534−1541.
(260) El-Tahawy, M. M. T.; Nenov, A.; Weingart, O.; Olivucci, M.; Garavelli, M. Relationship between Excited State Lifetime and Isomerization Quantum Yield in Animal Rhodopsins: Beyond the One-Dimensional Landau−Zener Model. *J. Phys. Chem. Lett.* **2018**, *9*, 3315−3322.
(261) Rego, L. G. C.; Bortolini, G. Modulating the Photoisomerization Mechanism of Semiconductor-Bound Azobenzene-Functionalized Compounds. *J. Phys. Chem. C* **2019**, *123*, 5692−5698.
(262) Torres, A.; Prado, L. R.; Bortolini, G.; Rego, L. G. C. Charge Transfer Driven Structural Relaxation in a Push−Pull Azobenzene Dye−Semiconductor Complex. *J. Phys. Chem. Lett.* **2018**, *9*, 5926−5933.
(263) Shalashilin, D. V. Nonadiabatic Dynamics with the Help of Multiconfigurational Ehrenfest Method: Improved Theory and Fully Quantum 24d Simulation of Pyrazine. *J. Chem. Phys.* **2010**, *132*, 244111.
(264) Shenvi, N.; Subotnik, J. E.; Yang, W. Phase-Corrected Surface Hopping: Correcting the Phase Evolution of the Electronic Wavefunction. *J. Chem. Phys.* **2011**, *135*, 024101.
(265) White, A. J.; Gorshkov, V. N.; Tretiak, S.; Mozyrsky, D. Non-Adiabatic Molecular Dynamics by Accelerated Semiclassical Monte Carlo. *J. Chem. Phys.* **2015**, *143*, 014115.
(266) Schneider, R.; Domcke, W. S_1-S_2 Conical Intersection and Ultrafast $S_2 \rightarrow S_1$ Internal-Conversion in Pyrazine. *Chem. Phys. Lett.* **1988**, *150*, 235−242.
(267) Stock, G.; Schneider, R.; Domcke, W. Theoretical Studies on the Femtosecond Real-Time Measurement of Ultrafast Electronic Decay in Polyatomic Molecules. *J. Chem. Phys.* **1989**, *90*, 7184−7194.
(268) Schneider, R.; Domcke, W.; Köppel, H. Aspects of Dissipative Electronic and Vibrational Dynamics of Strongly Vibronically Coupled Systems. *J. Chem. Phys.* **1990**, *92*, 1045−1061.
(269) Worth, G. A.; Meyer, H. D.; Cederbaum, L. S. The Effect of a Model Environment on Thes2absorption Spectrum of Pyrazine: A Wave Packet Study Treating All 24 Vibrational Modes. *J. Chem. Phys.* **1996**, *105*, 4412−4426.
(270) Zimmermann, T.; Vanicek, J. Efficient on-the-Fly Ab Initio Semiclassical Method for Computing Time-Resolved Nonadiabatic Electronic Spectra with Surface Hopping or Ehrenfest Dynamics. *J. Chem. Phys.* **2014**, *141*, 134102.
(271) Raab, A.; Worth, G. A.; Meyer, H. D.; Cederbaum, L. S. Molecular Dynamics of Pyrazine after Excitation to the S_2 Electronic State Using a Realistic 24-Mode Model Hamiltonian. *J. Chem. Phys.* **1999**, *110*, 936−946.
(272) Shalashilin, D. V.; Child, M. S. Real Time Quantum Propagation on a Monte Carlo Trajectory Guided Grids of Coupled Coherent States: 26D Simulation of Pyrazine Absorption Spectrum. *J. Chem. Phys.* **2004**, *121*, 3563−3568.
(273) Burghardt, I.; Giri, K.; Worth, G. A. Multimode Quantum Dynamics Using Gaussian Wavepackets: The Gaussian-Based Multi-configuration Time-Dependent Hartree (G-MCTDH) Method Applied to the Absorption Spectrum of Pyrazine. *J. Chem. Phys.* **2008**, *129*, 174104.
(274) Webster, F. J.; Schnitker, J.; Friedrichs, M. S.; Friesner, R. A.; Rossky, P. J. Solvation Dynamics of the Hydrated Electron: A Nonadiabatic Quantum Simulation. *Phys. Rev. Lett.* **1991**, *66*, 3172−3175.
(275) Bittner, E. R.; Rossky, P. J. Quantum Decoherence in Mixed Quantum-Classical Systems: Nonadiabatic Processes. *J. Chem. Phys.* **1995**, *103*, 8130−8143.
(276) Sellner, B.; Ruckenbauer, M.; Stambolic, I.; Barbatti, M.; Aquino, A. J.; Lischka, H. Photodynamics of Azomethane: A Nonadiabatic Surface-Hopping Study. *J. Phys. Chem. A* **2010**, *114*, 8778−8785.
(277) Xie, B. B.; Xia, S. H.; Liu, L. H.; Cui, G. Surface-Hopping Dynamics Simulations of Malachite Green: A Triphenylmethane Dye. *J. Phys. Chem. A* **2015**, *119*, 5607−5617.
(278) Fazzi, D.; Barbatti, M.; Thiel, W. Unveiling the Role of Hot Charge-Transfer States in Molecular Aggregates Via Nonadiabatic Dynamics. *J. Am. Chem. Soc.* **2016**, *138*, 4502−4511.
(279) Wang, J.; Huang, J.; Du, L.; Lan, Z. Photoinduced Ultrafast Intramolecular Excited-State Energy Transfer in the Silylene-Bridged Biphenyl and Stilbene (SBS) System: A Nonadiabatic Dynamics Point of View. *J. Phys. Chem. A* **2015**, *119*, 6937−6948.
(280) Nachtigallova, D.; Aquino, A. J.; Szymczak, J. J.; Barbatti, M.; Hobza, P.; Lischka, H. Nonadiabatic Dynamics of Uracil: Population Split among Different Decay Mechanisms. *J. Phys. Chem. A* **2011**, *115*, 5247−5255.
(281) Pereira Rodrigues, G.; Ventura, E.; do Monte, S. A.; Barbatti, M. Photochemical Deactivation Process of HCFC-133a ($C_2H_2F_3Cl$): A Nonadiabatic Dynamics Study. *J. Phys. Chem. A* **2014**, *118*, 12041−12049.
(282) Plasser, F.; Crespo-Otero, R.; Pederzoli, M.; Pittner, J.; Lischka, H.; Barbatti, M. Surface Hopping Dynamics with Correlated Single-Reference Methods: 9H-Adenine as a Case Study. *J. Chem. Theory Comput.* **2014**, *10*, 1395−1405.
(283) Ruckenbauer, M.; Barbatti, M.; Muller, T.; Lischka, H. Nonadiabatic Excited-State Dynamics with Hybrid Ab Initio Quantum-Mechanical/Molecular-Mechanical Methods: Solvation of the Pentadieniminium Cation in Apolar Media. *J. Phys. Chem. A* **2010**, *114*, 6757−6765.
(284) Benassi, E.; Granucci, G.; Persico, M.; Corni, S. Can Azobenzene Photoisomerize When Chemisorbed on a Gold Surface? An Analysis of Steric Effects Based on Nonadiabatic Dynamics Simulations. *J. Phys. Chem. C* **2015**, *119*, 5962−5974.
(285) Huang, J.; Du, L.; Wang, J.; Lan, Z. Photoinduced Excited-State Energy-Transfer Dynamics of a Nitrogen-Cored Symmetric Dendrimer: From the Perspective of the Jahn−Teller Effect. *J. Phys. Chem. C* **2015**, *119*, 7578−7589.
(286) Marchand, G.; Eng, J.; Schapiro, I.; Valentini, A.; Frutos, L. M.; Pieri, E.; Olivucci, M.; Leonard, J.; Gindensperger, E. Directionality of Double-Bond Photoisomerization Dynamics Induced by a Single Stereogenic Center. *J. Phys. Chem. Lett.* **2015**, *6*, 599−604.
(287) Chaiwongwattana, S.; Sapunar, M.; Ponzi, A.; Decleva, P.; Doslic, N. Exploration of Excited State Deactivation Pathways of Adenine Monohydrates. *J. Phys. Chem. A* **2015**, *119*, 10637−10644.
(288) Weingart, O.; Lan, Z.; Koslowski, A.; Thiel, W. Chiral Pathways and Periodic Decay Incis-Azobenzene Photodynamics. *J. Phys. Chem. Lett.* **2011**, *2*, 1506−1509.
(289) Liu, X. Y.; Chang, X. P.; Xia, S. H.; Cui, G.; Thiel, W. Excited-State Proton-Transfer-Induced Trapping Enhances the Fluorescence Emission of a Locked Gfp Chromophore. *J. Chem. Theory Comput.* **2016**, *12*, 753−764.
(290) Sporkel, L.; Jankowska, J.; Thiel, W. Photoswitching of Salicylidene Methylamine: A Theoretical Photodynamics Study. *J. Phys. Chem. B* **2015**, *119*, 2702−2710.
(291) Favero, L.; Granucci, G.; Persico, M. Surface Hopping Investigation of Benzophenone Excited State Dynamics. *Phys. Chem. Chem. Phys.* **2016**, *18*, 10499−10506.
(292) Barbatti, M.; Aquino, A. J.; Szymczak, J. J.; Nachtigallova, D.; Lischka, H. Photodynamical Simulations of Cytosine: Characterization of the Ultrafast Bi-Exponential Uv Deactivation. *Phys. Chem. Chem. Phys.* **2011**, *13*, 6145−6155.
(293) Richter, M.; Mai, S.; Marquetand, P.; Gonzalez, L. Ultrafast Intersystem Crossing Dynamics in Uracil Unravelled by Ab Initio Molecular Dynamics. *Phys. Chem. Chem. Phys.* **2014**, *16*, 24423−24436.
(294) Crespo-Otero, R.; Mardykov, A.; Sanchez-Garcia, E.; Sander, W.; Barbatti, M. Photo-Stability of Peptide-Bond Aggregates: N-Methylformamide Dimers. *Phys. Chem. Chem. Phys.* **2014**, *16*, 18877−18887.
(295) Cao, J. Photoinduced Reactions of Both 2-Formyl-2h-Azirine and Isoxazole: A Theoretical Study Based on Electronic Structure

https://dx.doi.org/10.1021/acs.chemrev.9b00447
Chem. Rev. 2020, 120, 2215−2287

Calculations and Nonadiabatic Dynamics Simulations. *J. Chem. Phys.* **2015**, *142*, 244302.
(296) Assmann, M.; Weinacht, T.; Matsika, S. Surface Hopping Investigation of the Relaxation Dynamics in Radical Cations. *J. Chem. Phys.* **2016**, *144*, 034301.
(297) Kazaryan, A.; Lan, Z.; Schafer, L. V.; Thiel, W.; Filatov, M. Surface Hopping Excited-State Dynamics Study of the Photoisomerization of a Light-Driven Fluorene Molecular Rotary Motor. *J. Chem. Theory Comput.* **2011**, *7*, 2189−2199.
(298) Lan, Z.; Lu, Y.; Weingart, O.; Thiel, W. Nonadiabatic Decay Dynamics of a Benzylidene Malononitrile. *J. Phys. Chem. A* **2012**, *116*, 1510−1518.
(299) Ruckenbauer, M.; Barbatti, M.; Sellner, B.; Muller, T.; Lischka, H. Azomethane: Nonadiabatic Photodynamical Simulations in Solution. *J. Phys. Chem. A* **2010**, *114*, 12585−12590.
(300) Ruckenbauer, M.; Barbatti, M.; Muller, T.; Lischka, H. Nonadiabatic Photodynamics of a Retinal Model in Polar and Nonpolar Environment. *J. Phys. Chem. A* **2013**, *117*, 2790−2799.
(301) Subotnik, J. E. Augmented Ehrenfest Dynamics Yields a Rate for Surface Hopping. *J. Chem. Phys.* **2010**, *132*, 134112.
(302) Subotnik, J. E.; Ouyang, W.; Landry, B. R. Can We Derive Tully's Surface-Hopping Algorithm from the Semiclassical Quantum Liouville Equation? Almost, but Only with Decoherence. *J. Chem. Phys.* **2013**, *139*, 214107.
(303) Ouyang, W.; Subotnik, J. E. Estimating the Entropy and Quantifying the Impurity of a Swarm of Surface-Hopping Trajectories: A New Perspective on Decoherence. *J. Chem. Phys.* **2014**, *140*, 204102.
(304) Landry, B. R.; Subotnik, J. E. How to Recover Marcus Theory with Fewest Switches Surface Hopping: Add Just a Touch of Decoherence. *J. Chem. Phys.* **2012**, *137*, 22A513.
(305) Shenvi, N.; Subotnik, J. E.; Yang, W. Simultaneous-Trajectory Surface Hopping: A Parameter-Free Algorithm for Implementing Decoherence in Nonadiabatic Dynamics. *J. Chem. Phys.* **2011**, *134*, 144102.
(306) Akimov, A. V.; Long, R.; Prezhdo, O. V. Coherence Penalty Functional: A Simple Method for Adding Decoherence in Ehrenfest Dynamics. *J. Chem. Phys.* **2014**, *140*, 194107.
(307) Garcia-Iriepa, C.; Marazzi, M.; Zapata, F.; Valentini, A.; Sampedro, D.; Frutos, L. M. Chiral Hydrogen Bond Environment Providing Unidirectional Rotation in Photoactive Molecular Motors. *J. Phys. Chem. Lett.* **2013**, *4*, 1389−1396.
(308) Senanayake, R. D.; Akimov, A. V.; Aikens, C. M. Theoretical Investigation of Electron and Nuclear Dynamics in the $[Au_{25}(SH)_{18}]^{-1}$ Thiolate-Protected Gold Nanocluster. *J. Phys. Chem. C* **2017**, *121*, 10653−10662.
(309) Parlant, G.; Gislason, E. A. An Exact Trajectory Surface Hopping Procedure: Comparison with Exact Quantal Calculations. *J. Chem. Phys.* **1989**, *91*, 4416−4418.
(310) Ondarse-Alvarez, D.; Komurlu, S.; Roitberg, A. E.; Pierdominici-Sottile, G.; Tretiak, S.; Fernandez-Alberti, S.; Kleiman, V. D. Ultrafast Electronic Energy Relaxation in a Conjugated Dendrimer Leading to Inter-Branch Energy Redistribution. *Phys. Chem. Chem. Phys.* **2016**, *18*, 25080−25089.
(311) Franklin-Mergarejo, R.; Nelson, T.; Tretiak, S.; Fernandez-Alberti, S. Phonon Bottleneck and Long-Lived Excited States in Pi-Conjugated Pyrene Hoop. *Phys. Chem. Chem. Phys.* **2017**, *19*, 9478−9484.
(312) Fischer, S. A.; Lingerfelt, D. B.; May, J. W.; Li, X. Non-Adiabatic Molecular Dynamics Investigation of Photoionization State Formation and Lifetime in Mn^{2+}-Doped ZnO Quantum Dots. *Phys. Chem. Chem. Phys.* **2014**, *16*, 17507−17514.
(313) Sifain, A. E.; Wang, L.; Prezhdo, O. V. Mixed Quantum-Classical Equilibrium in Global Flux Surface Hopping. *J. Chem. Phys.* **2015**, *142*, 224102.
(314) Wang, L.; Sifain, A. E.; Prezhdo, O. V. Fewest Switches Surface Hopping in Liouville Space. *J. Phys. Chem. Lett.* **2015**, *6*, 3827−3833.
(315) Shakib, F. A.; Huo, P. Ring Polymer Surface Hopping: Incorporating Nuclear Quantum Effects into Nonadiabatic Molecular Dynamics Simulations. *J. Phys. Chem. Lett.* **2017**, *8*, 3073−3080.
(316) Yoshikawa, T.; Takayanagi, T. Application of Ring-Polymer Molecular Dynamics to Electronically Nonadiabatic Excess Electron Dynamics in Water Clusters: Importance of Nuclear Quantum Effects. *Chem. Phys. Lett.* **2013**, *564*, 1−5.
(317) Kapral, R. Surface Hopping from the Perspective of Quantum−Classical Liouville Dynamics. *Chem. Phys.* **2016**, *481*, 77−83.
(318) Kelly, A.; Rhee, Y. M. Mixed Quantum-Classical Description of Excitation Energy Transfer in a Model Fenna−Matthews−Olsen Complex. *J. Phys. Chem. Lett.* **2011**, *2*, 808−812.
(319) Kim, H. W.; Kelly, A.; Park, J. W.; Rhee, Y. M. All-Atom Semiclassical Dynamics Study of Quantum Coherence in Photosynthetic Fenna-Matthews-Olson Complex. *J. Am. Chem. Soc.* **2012**, *134*, 11640−11651.
(320) Menzeleev, A. R.; Bell, F.; Miller, T. F., 3rd Kinetically Constrained Ring-Polymer Molecular Dynamics for Non-Adiabatic Chemical Reactions. *J. Chem. Phys.* **2014**, *140*, 064103.
(321) Richardson, J. O.; Thoss, M. Communication: Nonadiabatic Ring-Polymer Molecular Dynamics. *J. Chem. Phys.* **2013**, *139*, 031102.
(322) Welsch, R.; Song, K.; Shi, Q.; Althorpe, S. C.; Miller, T. F., 3rd Non-Equilibrium Dynamics from Rpmd and Cmd. *J. Chem. Phys.* **2016**, *145*, 204118.
(323) Duke, J. R.; Ananth, N. Simulating Excited State Dynamics in Systems with Multiple Avoided Crossings Using Mapping Variable Ring Polymer Molecular Dynamics. *J. Phys. Chem. Lett.* **2015**, *6*, 4219−4223.
(324) Mulvihill, E.; Schubert, A.; Sun, X.; Dunietz, B. D.; Geva, E. A Modified Approach for Simulating Electronically Nonadiabatic Dynamics Via the Generalized Quantum Master Equation. *J. Chem. Phys.* **2019**, *150*, 034101.
(325) Kapral, R.; Ciccotti, G. Mixed Quantum-Classical Dynamics. *J. Chem. Phys.* **1999**, *110*, 8919−8929.
(326) Kapral, R. Quantum Dynamics in Open Quantum-Classical Systems. *J. Phys.: Condens. Matter* **2015**, *27*, 073201.
(327) Horenko, I.; Salzmann, C.; Schmidt, B.; Schütte, C. Quantum-Classical Liouville Approach to Molecular Dynamics: Surface Hopping Gaussian Phase-Space Packets. *J. Chem. Phys.* **2002**, *117*, 11075−11088.
(328) Bonella, S.; Ciccotti, G.; Kapral, R. Linearization Approximations and Liouville Quantum−Classical Dynamics. *Chem. Phys. Lett.* **2010**, *484*, 399−404.
(329) Hsieh, C.-Y.; Schofield, J.; Kapral, R. Forward−Backward Solution of Quantum-Classical Liouville Equation in the Adiabatic Mapping Basis. *Mol. Phys.* **2013**, *111*, 3546−3554.
(330) Dell'Angelo, D.; Hanna, G. Self-Consistent Filtering Scheme for Efficient Calculations of Observables Via the Mixed Quantum-Classical Liouville Approach. *J. Chem. Theory Comput.* **2016**, *12*, 477−485.
(331) Kananenka, A. A.; Hsieh, C. Y.; Cao, J.; Geva, E. Accurate Long-Time Mixed Quantum-Classical Liouville Dynamics Via the Transfer Tensor Method. *J. Phys. Chem. Lett.* **2016**, *7*, 4809−4814.
(332) Kim, H.; Nassimi, A.; Kapral, R. Quantum-Classical Liouville Dynamics in the Mapping Basis. *J. Chem. Phys.* **2008**, *129*, 084102.
(333) Duan, H.-G.; Prokhorenko, V. I.; Cogdell, R. J.; Ashraf, K.; Stevens, A. L.; Thorwart, M.; Miller, R. J. D. Nature Does Not Rely on Long-Lived Electronic Quantum Coherence for Photosynthetic Energy Transfer. *Proc. Natl. Acad. Sci. U. S. A.* **2017**, *114*, 8493−8498.
(334) Martens, C. C. Communication: Fully Coherent Quantum State Hopping. *J. Chem. Phys.* **2015**, *143*, 141101.
(335) Martens, C. C. Surface Hopping without Momentum Jumps: A Quantum-Trajectory-Based Approach to Nonadiabatic Dynamics. *J. Phys. Chem. A* **2019**, *123*, 1110−1128.
(336) Zamstein, N.; Tannor, D. J. Non-Adiabatic Molecular Dynamics with Complex Quantum Trajectories. *J. Chem. Phys.* **2012**, *137*, 22A517.
(337) Zamstein, N.; Tannor, D. J. Non-Adiabatic Molecular Dynamics with Complex Quantum Trajectories. Ii. The Adiabatic Representation. *J. Chem. Phys.* **2012**, *137*, 22A518.
(338) Rassolov, V. A.; Garashchuk, S. Semiclassical Nonadiabatic Dynamics with Quantum Trajectories. *Phys. Rev. A: At., Mol., Opt. Phys.* **2005**, *71*, 032511.

https://dx.doi.org/10.1021/acs.chemrev.9b00447
Chem. Rev. 2020, 120, 2215−2287

(339) Agostini, F.; Min, S. K.; Abedi, A.; Gross, E. K. Quantum-Classical Nonadiabatic Dynamics: Coupled- Vs Independent-Trajectory Methods. *J. Chem. Theory Comput.* **2016**, *12*, 2127−2143.
(340) Min, S. K.; Agostini, F.; Gross, E. K. Coupled-Trajectory Quantum-Classical Approach to Electronic Decoherence in Nonadiabatic Processes. *Phys. Rev. Lett.* **2015**, *115*, 073001.
(341) Curchod, B. F. E.; Agostini, F.; Tavernelli, I. Ct-Mqc − a Coupled-Trajectory Mixed Quantum/Classical Method Including Nonadiabatic Quantum Coherence Effects. *Eur. Phys. J. B* **2018**, *91*, 168−180.
(342) Gu, B.; Garashchuk, S. Quantum Dynamics with Gaussian Bases Defined by the Quantum Trajectories. *J. Phys. Chem. A* **2016**, *120*, 3023−3031.
(343) Child, M. S.; Shalashilin, D. V. Locally Coupled Coherent States and Herman−Kluk Dynamics. *J. Chem. Phys.* **2003**, *118*, 2061−2071.
(344) Worth, G. A.; Robb, M. A.; Burghardt, I. A Novel Algorithm for Non-Adiabatic Direct Dynamics Using Variational Gaussian Wavepackets. *Faraday Discuss.* **2004**, *127*, 307.
(345) Richings, G. W.; Polyak, I.; Spinlove, K. E.; Worth, G. A.; Burghardt, I.; Lasorne, B. Quantum Dynamics Simulations Using Gaussian Wavepackets: The Vmcg Method. *Int. Rev. Phys. Chem.* **2015**, *34*, 269−308.
(346) Saita, K.; Shalashilin, D. V. On-the-Fly Ab Initio Molecular Dynamics with Multiconfigurational Ehrenfest Method. *J. Chem. Phys.* **2012**, *137*, 22A506.
(347) Martinez, T. J. Insights for Light-Driven Molecular Devices from Ab Initio Multiple Spawning Excited-State Dynamics of Organic and Biological Chromophores. *Acc. Chem. Res.* **2006**, *39*, 119−126.
(348) Levine, B. G.; Coe, J. D.; Virshup, A. M.; Martínez, T. J. Implementation of Ab Initio Multiple Spawning in the Molpro Quantum Chemistry Package. *Chem. Phys.* **2008**, *347*, 3−16.
(349) Makhov, D. V.; Glover, W. J.; Martinez, T. J.; Shalashilin, D. V. Ab Initio Multiple Cloning Algorithm for Quantum Nonadiabatic Molecular Dynamics. *J. Chem. Phys.* **2014**, *141*, 054110.
(350) Fernandez-Alberti, S.; Makhov, D. V.; Tretiak, S.; Shalashilin, D. V. Non-Adiabatic Excited State Molecular Dynamics of Phenylene Ethynylene Dendrimer Using a Multiconfigurational Ehrenfest Approach. *Phys. Chem. Chem. Phys.* **2016**, *18*, 10028−10040.
(351) White, A.; Tretiak, S.; Mozyrsky, D. Coupled Wave-Packets for Non-Adiabatic Molecular Dynamics: A Generalization of Gaussian Wave-Packet Dynamics to Multiple Potential Energy Surfaces. *Chem. Sci.* **2016**, *7*, 4905−4911.
(352) White, A. J.; Gorshkov, V. N.; Wang, R.; Tretiak, S.; Mozyrsky, D. Semiclassical Monte Carlo: A First Principles Approach to Non-Adiabatic Molecular Dynamics. *J. Chem. Phys.* **2014**, *141*, 184101.
(353) Freixas, V. M.; Fernandez-Alberti, S.; Makhov, D. V.; Tretiak, S.; Shalashilin, D. An Ab Initio Multiple Cloning Approach for the Simulation of Photoinduced Dynamics in Conjugated Molecules. *Phys. Chem. Chem. Phys.* **2018**, *20*, 17762−17772.
(354) Makhov, D. V.; Martinez, T. J.; Shalashilin, D. V. Toward Fully Quantum Modelling of Ultrafast Photodissociation Imaging Experiments. Treating Tunnelling in the Ab Initio Multiple Cloning Approach. *Faraday Discuss.* **2016**, *194*, 81−94.
(355) Fedorov, D. A.; Levine, B. G. Nonadiabatic Quantum Molecular Dynamics in Dense Manifolds of Electronic States. *J. Phys. Chem. Lett.* **2019**, *10*, 4542−4548.
(356) Baskov, R.; White, A. J.; Mozyrsky, D. Improved Ehrenfest Approach to Model Correlated Electron−Nuclear Dynamics. *J. Phys. Chem. Lett.* **2019**, *10*, 433−440.
(357) Gorshkov, V. N.; Tretiak, S.; Mozyrsky, D. Semiclassical Monte-Carlo Approach for Modelling Non-Adiabatic Dynamics in Extended Molecules. *Nat. Commun.* **2013**, *4*, 2144.
(358) Szabo, A.; Ostlund, N. S. *Modern Quantum Chemistry: Introduction to Advanced Electronic Structure Theory*; McGraw-Hill: New York, 1989.
(359) Raghavachari, K.; Pople, J. A.; Replogle, E. S.; Head-Gordon, M. Fifth Order Moeller-Plesset Perturbation Theory: Comparison of Existing Correlation Methods and Implementation of New Methods Correct to Fifth Order. *J. Phys. Chem.* **1990**, *94*, 5579−5586.
(360) Krishnan, R.; Pople, J. A. Approximate Fourth-Order Perturbation Theory of the Electron Correlation Energy. *Int. J. Quantum Chem.* **1978**, *14*, 91−100.
(361) Pople, J. A.; Seeger, R.; Krishnan, R. Variational Configuration Interaction Methods and Comparison with Perturbation Theory. *Int. J. Quantum Chem.* **1977**, *12*, 149−163.
(362) Pople, J. A.; Binkley, J. S.; Seeger, R. Theoretical Models Incorporating Electron Correlation. *Int. J. Quantum Chem.* **1976**, *10*, 1−19.
(363) Head-Gordon, M.; Pople, J. A.; Frisch, M. J. Mp2 Energy Evaluation by Direct Methods. *Chem. Phys. Lett.* **1988**, *153*, 503−506.
(364) Frisch, M. J.; Head-Gordon, M.; Pople, J. A. A Direct Mp2 Gradient Method. *Chem. Phys. Lett.* **1990**, *166*, 275−280.
(365) Bartlett, R. J.; Purvis, G. D. Many-Body Perturbation Theory, Coupled-Pair Many-Electron Theory, and the Importance of Quadruple Excitations for the Correlation Problem. *Int. J. Quantum Chem.* **1978**, *14*, 561−581.
(366) Pople, J. A.; Krishnan, R.; Schlegel, H. B.; Binkley, J. S. Electron Correlation Theories and Their Application to the Study of Simple Reaction Potential Surfaces. *Int. J. Quantum Chem.* **1978**, *14*, 545−560.
(367) Purvis, G. D.; Bartlett, R. J. A. Full Coupled-Cluster Singles and Doubles Model: The Inclusion of Disconnected Triples. *J. Chem. Phys.* **1982**, *76*, 1910−1918.
(368) Koch, H.; Jorgensen, P. Coupled Cluster Response Functions. *J. Chem. Phys.* **1990**, *93*, 3333−3344.
(369) Kállay, M.; Gauss, J. Calculation of Excited-State Properties Using General Coupled-Cluster and Configuration-Interaction Models. *J. Chem. Phys.* **2004**, *121*, 9257−9269.
(370) Levchenko, S. V.; Krylov, A. I. Equation-of-Motion Spin-Flip Coupled-Cluster Model with Single and Double Substitutions: Theory and Application to Cyclobutadiene. *J. Chem. Phys.* **2004**, *120*, 175−185.
(371) Hohenberg, P.; Kohn, W. Inhomogeneous Electron Gas. *Phys. Rev.* **1964**, *136*, B864−B871.
(372) Kohn, W.; Sham, L. J. Self-Consistent Equations Including Exchange and Correlation Effects. *Phys. Rev.* **1965**, *140*, A1133−A1138.
(373) Parr, R. G. *Horizons of Quantum Chemistry*; Springer, 1980; pp 5−15.
(374) Perdew, J. P.; Burke, K.; Ernzerhof, M. Generalized Gradient Approximation Made Simple. *Phys. Rev. Lett.* **1996**, *77*, 3865−3868.
(375) Zhao, Y.; Truhlar, D. G. The M06 Suite of Density Functionals for Main Group Thermochemistry, Thermochemical Kinetics, Noncovalent Interactions, Excited States, and Transition Elements: Two New Functionals and Systematic Testing of Four M06-Class Functionals and 12 Other Functionals. *Theor. Chem. Acc.* **2008**, *120*, 215−241.
(376) Yu, H. S.; He, X.; Li, S. L.; Truhlar, D. G. Mn15: A Kohn−Sham Global-Hybrid Exchange−Correlation Density Functional with Broad Accuracy for Multi-Reference and Single-Reference Systems and Noncovalent Interactions. *Chem. Sci.* **2016**, *7*, 5032−5051.
(377) Henderson, T. M.; Izmaylov, A. F.; Scalmani, G.; Scuseria, G. E. Can Short-Range Hybrids Describe Long-Range-Dependent Properties? *J. Chem. Phys.* **2009**, *131*, 044108.
(378) Yanai, T.; Tew, D. P.; Handy, N. C. A New Hybrid Exchange-Correlation Functional Using the Coulomb-Attenuating Method (Cam-B3lyp). *Chem. Phys. Lett.* **2004**, *393*, 51−57.
(379) Chai, J.-D.; Head-Gordon, M. Long-Range Corrected Hybrid Density Functionals with Damped Atom−Atom Dispersion Corrections. *Phys. Chem. Chem. Phys.* **2008**, *10*, 6615−6620.
(380) Becke, A. D. Density-Functional Thermochemistry. Iii. The Role of Exact Exchange. *J. Chem. Phys.* **1993**, *98*, 5648−5652.
(381) Perdew, J. P.; Chevary, J. A.; Vosko, S. H.; Jackson, K. A.; Pederson, M. R.; Singh, D. J.; Fiolhais, C. Atoms, Molecules, Solids, and Surfaces: Applications of the Generalized Gradient Approximation for Exchange and Correlation. *Phys. Rev. B: Condens. Matter Mater. Phys.* **1992**, *46*, 6671−6687.
(382) Perdew, J. P.; Wang, Y. Accurate and Simple Analytic Representation of the Electron-Gas Correlation Energy. *Phys. Rev. B: Condens. Matter Mater. Phys.* **1992**, *45*, 13244−13249.

https://dx.doi.org/10.1021/acs.chemrev.9b00447
Chem. Rev. 2020, 120, 2215−2287

(383) Pople, J. A.; Gill, P. M. W.; Johnson, B. G. Kohn—Sham Density-Functional Theory within a Finite Basis Set. *Chem. Phys. Lett.* **1992**, *199*, 557−560.
(384) Frauenheim, T.; Seifert, G.; Elsterner, M.; Hajnal, Z.; Jungnickel, G.; Porezag, D.; Suhai, S.; Scholz, R. A Self-Consistent Charge Density-Functional Based Tight-Binding Method for Predictive Materials Simulations in Physics, Chemistry and Biology. Phys. *Phys. Status Solidi B* **2000**, *217*, 41−62.
(385) Frauenheim, T.; Seifert, G.; Elstner, M.; Niehaus, T.; Köhler, C.; Amkreutz, M.; Sternberg, M.; Hajnal, Z.; Carlo, A. D.; Suhai, S. Atomistic Simulations of Complex Materials: Ground-State and Excited-State Properties. *J. Phys.: Condens. Matter* **2002**, *14*, 3015−3047.
(386) Elstner, M.; Porezag, D.; Jungnickel, G.; Elsner, J.; Haugk, M.; Frauenheim, T.; Suhai, S.; Seifert, G. Self-Consistent-Charge Density-Functional Tight-Binding Method for Simulations of Complex Materials Properties. *Phys. Rev. B: Condens. Matter Mater. Phys.* **1998**, *58*, 7260−7268.
(387) Elstner, M. The SCC-DFTB Method and Its Application to Biological Systems. *Theor. Chem. Acc.* **2006**, *116*, 316−325.
(388) Gaus, M.; Cui, Q.; Elstner, M. DFTB3: Extension of the Self-Consistent-Charge Density-Functional Tight-Binding Method (SCC-DFTB). *J. Chem. Theory Comput.* **2011**, *7*, 931−948.
(389) Aradi, B.; Hourahine, B.; Frauenheim, T. DFTB+, a Sparse Matrix-Based Implementation of the DFTB Method. *J. Phys. Chem. A* **2007**, *111*, 5678−5684.
(390) Stewart, J. J. P. Optimization of Parameters for Semiempirical Methods I. *J. Comput. Chem.* **1989**, *10*, 209−220.
(391) Stewart, J. J. P. Optimization of Parameters for Semiempirical Methods V: Modification of Nddo Approximations and Application to 70 Elements. *J. Mol. Model.* **2007**, *13*, 1173−1213.
(392) Stewart, J. J. P. Optimization of Parameters for Semiempirical Methods Vi: More Modifications to the Nddo Approximations and Re-Optimization of Parameters. *J. Mol. Model.* **2013**, *19*, 1−32.
(393) Gieseking, R. L. M. Third-Order Nonlinear Optical Properties of Ag Nanoclusters: Connecting Molecule-Like and Nanoparticle-Like Behavior. *Chem. Mater.* **2019**, *31*, 6850−6859.
(394) VandeVondele, J.; Borštnik, U.; Hutter, J. Linear Scaling Self-Consistent Field Calculations with Millions of Atoms in the Condensed Phase. *J. Chem. Theory Comput.* **2012**, *8*, 3565−3573.
(395) Mniszewski, S. M.; Cawkwell, M. J.; Wall, M. E.; Mohd-Yusof, J.; Bock, N.; Germann, T. C.; Niklasson, A. M. N. Efficient Parallel Linear Scaling Construction of the Density Matrix for Born−Oppenheimer Molecular Dynamics. *J. Chem. Theory Comput.* **2015**, *11*, 4644−4654.
(396) Negre, C. F. A.; Mniszewski, S. M.; Cawkwell, M. J.; Bock, N.; Wall, M. E.; Niklasson, A. M. N. Recursive Factorization of the Inverse Overlap Matrix in Linear-Scaling Quantum Molecular Dynamics Simulations. *J. Chem. Theory Comput.* **2016**, *12*, 3063−3073.
(397) Szalay, P. G.; Müller, T.; Gidofalvi, G.; Lischka, H.; Shepard, R. Multiconfiguration Self-Consistent Field and Multireference Configuration Interaction Methods and Applications. *Chem. Rev.* **2012**, *112*, 108−181.
(398) Grout, P. J.; Maruani, J.; Delgado-Barrio, G.; Piecuch, P. *Frontiers in Quantum Systems in Chemistry and Physics*; Springer: Netherlands, 2008.
(399) Cramer, C. J. *Essentials of Computational Chemistry: Theories and Models*; Wiley, 2005.
(400) Chen, G. P.; Voora, V. K.; Agee, M. M.; Balasubramani, S. G.; Furche, F. Random-Phase Approximation Methods. *Annu. Rev. Phys. Chem.* **2017**, *68*, 421−445.
(401) Tretiak, S.; Mukamel, S. Density Matrix Analysis and Simulation of Electronic Excitations in Conjugated and Aggregated Molecules. *Chem. Rev.* **2002**, *102*, 3171−3212.
(402) Dreuw, A.; Head-Gordon, M. Single-Reference Ab Initio Methods for the Calculation of Excited States of Large Molecules. *Chem. Rev.* **2005**, *105*, 4009−4037.
(403) Tretiak, S.; Chernyak, V. Resonant Nonlinear Polarizabilities in the Time-Dependent Density Functional Theory. *J. Chem. Phys.* **2003**, *119*, 8809−8823.
(404) Aiken, J. G.; Jonassen, H. B.; Aldrich, H. S. Löwdin Orthogonalization as a Minimum Energy Perturbation. *J. Chem. Phys.* **1975**, *62*, 2745−2746.
(405) Casida, M. Time-Dependent Density-Functional Theory for Molecules and Molecular Solids. *J. Mol. Struct.: THEOCHEM* **2009**, *914*, 3−18.
(406) Becke, A. D. A. New Mixing of Hartree−Fock and Local Density-Functional Theories. *J. Chem. Phys.* **1993**, *98*, 1372−1377.
(407) Ceperley, D. M.; Alder, B. J. Ground State of the Electron Gas by a Stochastic Method. *Phys. Rev. Lett.* **1980**, *45*, 566−569.
(408) Becke, A. D. Density-Functional Exchange-Energy Approximation with Correct Asymptotic Behavior. *Phys. Rev. A: At., Mol., Opt. Phys.* **1988**, *38*, 3098−3100.
(409) Adamo, C.; Barone, V. Toward Reliable Density Functional Methods without Adjustable Parameters: The Pbe0Model. *J. Chem. Phys.* **1999**, *110*, 6158−6170.
(410) Mardirossian, N.; Head-Gordon, M. Thirty Years of Density Functional Theory in Computational Chemistry: An Overview and Extensive Assessment of 200 Density Functionals. *Mol. Phys.* **2017**, *115*, 2315−2372.
(411) Badaeva, E. A.; Timofeeva, T. V.; Masunov, A.; Tretiak, S. Role of Donor−Acceptor Strengths and Separation on the Two-Photon Absorption Response of Cytotoxic Dyes: A TD-DFT Study. *J. Phys. Chem. A* **2005**, *109*, 7276−7284.
(412) Masunov, A.; Tretiak, S. Prediction of Two-Photon Absorption Properties for Organic Chromophores Using Time-Dependent Density-Functional Theory. *J. Phys. Chem. B* **2004**, *108*, 899−907.
(413) Magyar, R. J.; Tretiak, S. Dependence of Spurious Charge-Transfer Excited States on Orbital Exchange in TDDFT: Large Molecules and Clusters. *J. Chem. Theory Comput.* **2007**, *3*, 976−987.
(414) Dreuw, A.; Head-Gordon, M. Failure of Time-Dependent Density Functional Theory for Long-Range Charge-Transfer Excited States: The Zincbacteriochlorin-Bacteriochlorin and Bacteriochlorophyll-Spheroidene Complexes. *J. Am. Chem. Soc.* **2004**, *126*, 4007−4016.
(415) Dreuw, A.; Weisman, J. L.; Head-Gordon, M. Long-Range Charge-Transfer Excited States in Time-Dependent Density Functional Theory Require Non-Local Exchange. *J. Chem. Phys.* **2003**, *119*, 2943−2946.
(416) Rohrdanz, M. A.; Martins, K. M.; Herbert, J. M. A Long-Range-Corrected Density Functional That Performs Well for Both Ground-State Properties and Time-Dependent Density Functional Theory Excitation Energies, Including Charge-Transfer Excited States. *J. Chem. Phys.* **2009**, *130*, 054112.
(417) Li, H.; Nieman, R.; Aquino, A. J. A.; Lischka, H.; Tretiak, S. Comparison of LC-TDDFT and ADC(2) Methods in Computations of Bright and Charge Transfer States in Stacked Oligothiophenes. *J. Chem. Theory Comput.* **2014**, *10*, 3280−3289.
(418) Kronik, L.; Stein, T.; Refaely-Abramson, S.; Baer, R. Excitation Gaps of Finite-Sized Systems from Optimally Tuned Range-Separated Hybrid Functionals. *J. Chem. Theory Comput.* **2012**, *8*, 1515−1531.
(419) Zheng, Z.; Egger, D. A.; Brédas, J.-L.; Kronik, L.; Coropceanu, V. Effect of Solid-State Polarization on Charge-Transfer Excitations and Transport Levels at Organic Interfaces from a Screened Range-Separated Hybrid Functional. *J. Phys. Chem. Lett.* **2017**, *8*, 3277−3283.
(420) Manna, A. K.; Refaely-Abramson, S.; Reilly, A. M.; Tkatchenko, A.; Neaton, J. B.; Kronik, L. Quantitative Prediction of Optical Absorption in Molecular Solids from an Optimally Tuned Screened Range-Separated Hybrid Functional. *J. Chem. Theory Comput.* **2018**, *14*, 2919−2929.
(421) Bhandari, S.; Dunietz, B. D. Quantitative Accuracy in Calculating Charge Transfer State Energies in Solvated Molecular Complexes Using a Screened Range Separated Hybrid Functional within a Polarized Continuum Model. *J. Chem. Theory Comput.* **2019**, *15*, 4305−4311.

https://dx.doi.org/10.1021/acs.chemrev.9b00447
Chem. Rev. 2020, 120, 2215−2287

(422) Liu, L. T.; Yaron, D.; Sluch, M. I.; Berg, M. A. Modeling the Effects of Torsional Disorder on the Spectra of Poly- and Oligo-(P-Phenyleneethynylenes). *J. Phys. Chem. B* **2006**, *110*, 18844−18852.
(423) Mueller, C. M.; Gieseking, R. L. M.; Schatz, G. C. *Molecular Spectroscopy: A Quantum Chemistry Approach*; Wiley: New York, 2019.
(424) Silva-Junior, M. R.; Thiel, W. Benchmark of Electronically Excited States for Semiempirical Methods: MNDO, AM1, PM3, OM1, OM2, OM3, INDO/S, and INDO/S2. *J. Chem. Theory Comput.* **2010**, *6*, 1546−1564.
(425) Moran, A. M.; Kelley, A. M.; Tretiak, S. Excited State Molecular Dynamics Simulations of Nonlinear Push−Pull Chromophores. *Chem. Phys. Lett.* **2003**, *367*, 293−307.
(426) Bowler, D. R.; Miyazaki, T.; Gillan, M. J. Recent Progress in Linear Scalingab Initioelectronic Structure Techniques. *J. Phys.: Condens. Matter* **2002**, *14*, 2781−2798.
(427) Cawkwell, M. J.; Niklasson, A. M. N. Energy Conserving, Linear Scaling Born-Oppenheimer Molecular Dynamics. *J. Chem. Phys.* **2012**, *137*, 134105.
(428) Yarkony, D. R. *Modern Electronic Structure Theory*; World Scientific 1995.
(429) Hirata, S.; Head-Gordon, M. Time-Dependent Density Functional Theory within the Tamm−Dancoff Approximation. *Chem. Phys. Lett.* **1999**, *314*, 291−299.
(430) Casida, M. E. *Recent Advances in Density Functional Methods*; World Scientific, 1995; Vol. *1*.
(431) Chernyak, V.; Schulz, M. F.; Mukamel, S.; Tretiak, S.; Tsiper, E. V. Krylov-Space Algorithms for Time-Dependent Hartree−Fock and Density Functional Computations. *J. Chem. Phys.* **2000**, *113*, 36−43.
(432) Furche, F.; Krull, B. T.; Nguyen, B. D.; Kwon, J. Accelerating Molecular Property Calculations with Nonorthonormal Krylov Space Methods. *J. Chem. Phys.* **2016**, *144*, 174105.
(433) Stener, M.; Fronzoni, G.; de Simone, M. Time Dependent Density Functional Theory of Core Electrons Excitations. *Chem. Phys. Lett.* **2003**, *373*, 115−123.
(434) Tavernelli, I.; Curchod, B. F. E.; Laktionov, A.; Rothlisberger, U. Nonadiabatic Coupling Vectors for Excited States within Time-Dependent Density Functional Theory in the Tamm−Dancoff Approximation and Beyond. *J. Chem. Phys.* **2010**, *133*, 194104.
(435) Tommasini, M.; Chernyak, V.; Mukamel, S. Electronic Density-Matrix Algorithm for Nonadiabatic Couplings in Molecular Dynamics Simulations. *Int. J. Quantum Chem.* **2001**, *85*, 225−238.
(436) Chernyak, V.; Mukamel, S. Density-Matrix Representation of Nonadiabatic Couplings in Time-Dependent Density Functional (TDDFT) Theories. *J. Chem. Phys.* **2000**, *112*, 3572−3579.
(437) Nelson, T.; Fernandez-Alberti, S.; Chernyak, V.; Roitberg, A. E.; Tretiak, S. Nonadiabatic Excited-State Molecular Dynamics Modeling of Photoinduced Dynamics in Conjugated Molecules. *J. Phys. Chem. B* **2011**, *115*, 5402−5414.
(438) Tavernelli, I.; Tapavicza, E.; Rothlisberger, U. Nonadiabatic Coupling Vectors within Linear Response Time-Dependent Density Functional Theory. *J. Chem. Phys.* **2009**, *130*, 124107.
(439) Ou, Q.; Bellchambers, G. D.; Furche, F.; Subotnik, J. E. First-Order Derivative Couplings between Excited States from Adiabatic TDDFT Response Theory. *J. Chem. Phys.* **2015**, *142*, 064114.
(440) Ou, Q.; Fatehi, S.; Alguire, E.; Shao, Y.; Subotnik, J. E. Derivative Couplings between TDDFT Excited States Obtained by Direct Differentiation in the Tamm-Dancoff Approximation. *J. Chem. Phys.* **2014**, *141*, 024114.
(441) Hu, C.; Hirai, H.; Sugino, O. Nonadiabatic Couplings from Time-Dependent Density Functional Theory: Formulation in the Casida Formalism and Practical Scheme within Modified Linear Response. *J. Chem. Phys.* **2007**, *127*, 064103.
(442) Billeter, S. R.; Curioni, A. Calculation of Nonadiabatic Couplings in Density-Functional Theory. *J. Chem. Phys.* **2005**, *122*, 034105.
(443) Gross, E. K. U.; Oliveira, L. N.; Kohn, W. Rayleigh-Ritz Variational Principle for Ensembles of Fractionally Occupied States. *Phys. Rev. A: At., Mol., Opt. Phys.* **1988**, *37*, 2805−2808.
(444) Schaefer, H. F., III *Methods of Electronic Structure Theory*; Springer: US, 1977.
(445) Goddard, W. A.; Dunning, T. H.; Hunt, W. J. The Proper Treatment of Off-Diagonal Lagrange Multipliers and Coupling Operators in Self-Consistent Field Equations. *Chem. Phys. Lett.* **1969**, *4*, 231−234.
(446) Furche, F.; Ahlrichs, R. Adiabatic Time-Dependent Density Functional Methods for Excited State Properties. *J. Chem. Phys.* **2002**, *117*, 7433−7447.
(447) Furche, F. On the Density Matrix Based Approach to Time-Dependent Density Functional Response Theory. *J. Chem. Phys.* **2001**, *114*, 5982−5992.
(448) Barbatti, M.; Ruckenbauer, M.; Plasser, F.; Pittner, J.; Granucci, G.; Persico, M.; Lischka, H. Newton-X: A Surface-Hopping Program for Nonadiabatic Molecular Dynamics. *WIREs Comput. Mol. Sci.* **2014**, *4*, 26−33.
(449) Barbatti, M.; Granucci, G.; Ruckenbauer, M.; Plasser, F.; Pittner, J.; Persico, M.; Lischka, H. *Newton-X: A Package for Newtonian Dynamics Close to the Crossing Seam*, 2012.
(450) Pulay, P. Ab Initio Calculation of Force Constants and Equilibrium Geometries in Polyatomic Molecules. *Mol. Phys.* **1969**, *17*, 197−204.
(451) Malmqvist, P. Å. Calculation of Transition Density Matrices by Nonunitary Orbital Transformations. *Int. J. Quantum Chem.* **1986**, *30*, 479−494.
(452) Li, Y.; Ullrich, C. A. Time-Dependent Transition Density Matrix. *Chem. Phys.* **2011**, *391*, 157−163.
(453) Liang, W.; Fischer, S. A.; Frisch, M. J.; Li, X. Energy-Specific Linear Response TDHF/TDDFT for Calculating High-Energy Excited States. *J. Chem. Theory Comput.* **2011**, *7*, 3540−3547.
(454) Tretiak, S.; Chernyak, V.; Mukamel, S. Collective Electronic Oscillators for Nonlinear Optical Response of Conjugated Molecules. *Chem. Phys. Lett.* **1996**, *259*, 55−61.
(455) Tretiak, S.; Chernyak, V.; Mukamel, S. Recursive Density-Matrix-Spectral-Moment Algorithm for Molecular Nonlinear Polarizabilities. *J. Chem. Phys.* **1996**, *105*, 8914−8928.
(456) Tretiak, S.; Chernyak, V.; Mukamel, S. Chemical Bonding and Size Scaling of Nonlinear Polarizabilities of Conjugated Polymers. *Phys. Rev. Lett.* **1996**, *77*, 4656−4659.
(457) Hu, C.; Sugino, O.; Hirai, H.; Tateyama, Y. Nonadiabatic Couplings from the Kohn-Sham Derivative Matrix: Formulation by Time-Dependent Density-Functional Theory and Evaluation in the Pseudopotential Framework. *Phys. Rev. A: At., Mol., Opt. Phys.* **2010**, *82*, 062508.
(458) Send, R.; Furche, F. First-Order Nonadiabatic Couplings from Time-Dependent Hybrid Density Functional Response Theory: Consistent Formalism, Implementation, and Performance. *J. Chem. Phys.* **2010**, *132*, 044107.
(459) Li, Z.; Liu, W. First-Order Nonadiabatic Coupling Matrix Elements between Excited States: A Lagrangian Formulation at the CIS, RPA, TD-HF, and TD-DFT Levels. *J. Chem. Phys.* **2014**, *141*, 014110.
(460) Ou, Q.; Alguire, E. C.; Subotnik, J. E. Derivative Couplings between Time-Dependent Density Functional Theory Excited States in the Random-Phase Approximation Based on Pseudo-Wavefunctions: Behavior around Conical Intersections. *J. Phys. Chem. B* **2015**, *119*, 7150−7161.
(461) Yarkony, D. R. On the Reaction $Na(^2p)+H_2 \rightarrow Na(^2s)+H_2$ Nonadiabatic Effects. *J. Chem. Phys.* **1986**, *84*, 3206−3211.
(462) Thorson, W. R.; Delos, J. B. Theory of near-Adiabatic Collisions. I. Electron Translation Factor Method. *Phys. Rev. A: At., Mol., Opt. Phys.* **1978**, *18*, 117.
(463) Fatehi, S.; Subotnik, J. E. Derivative Couplings with Built-in Electron-Translation Factors: Application to Benzene. *J. Phys. Chem. Lett.* **2012**, *3*, 2039−2043.
(464) Marcus, R. A. Electrostatic Free Energy and Other Properties of States Having Nonequilibrium Polarization. *J. Chem. Phys.* **1956**, *24*, 979−989.

https://dx.doi.org/10.1021/acs.chemrev.9b00447
Chem. Rev. 2020, 120, 2215−2287

(465) Martin, R. L.; Hay, P. J.; Pratt, L. R. Hydrolysis of Ferric Ion in Water and Conformational Equilibrium. *J. Phys. Chem. A* **1998**, *102*, 3565−3573.
(466) Park, Y. I.; Kuo, C.-Y.; Martinez, J. S.; Park, Y.-S.; Postupna, O.; Zhugayevych, A.; Kim, S.; Park, J.; Tretiak, S.; Wang, H.-L. Tailored Electronic Structure and Optical Properties of Conjugated Systems through Aggregates and Dipole−Dipole Interactions. *ACS Appl. Mater. Interfaces* **2013**, *5*, 4685−4695.
(467) Schwartz, B. J.; Peteanu, L. A.; Harris, C. B. Direct Observation of Fast Proton Transfer: Femtosecond Photophysics of 3-Hydroxyflavone. *J. Phys. Chem.* **1992**, *96*, 3591−3598.
(468) Bayliss, N. S.; McRae, E. G. Solvent Effects in Organic Spectra: Dipole Forces and the Franck−Condon Principle. *J. Phys. Chem.* **1954**, *58*, 1002−1006.
(469) Tomasi, J.; Mennucci, B.; Cammi, R. Quantum Mechanical Continuum Solvation Models. *Chem. Rev.* **2005**, *105*, 2999−3094.
(470) Cramer, C. J.; Truhlar, D. G. Implicit Solvation Models: Equilibria, Structure, Spectra, and Dynamics. *Chem. Rev.* **1999**, *99*, 2161−2200.
(471) Barone, V.; Cossi, M. Quantum Calculation of Molecular Energies and Energy Gradients in Solution by a Conductor Solvent Model. *J. Phys. Chem. A* **1998**, *102*, 1995−2001.
(472) Mennucci, B. Polarizable Continuum Model. *WIREs Comput. Mol. Sci.* **2012**, *2*, 386−404.
(473) Klamt, A.; Schüürmann, G. Cosmo: A New Approach to Dielectric Screening in Solvents with Explicit Expressions for the Screening Energy and Its Gradient. *J. Chem. Soc., Perkin Trans. 2* **1993**, *2*, 799−805.
(474) Onsager, L. Electric Moments of Molecules in Liquids. *J. Am. Chem. Soc.* **1936**, *58*, 1486−1493.
(475) Kirkwood, J. G. Theory of Solutions of Molecules Containing Widely Separated Charges with Special Application to Zwitterions. *J. Chem. Phys.* **1934**, *2*, 351−361.
(476) Warshel, A.; Levitt, M. Theoretical Studies of Enzymic Reactions: Dielectric, Electrostatic and Steric Stabilization of the Carbonium Ion in the Reaction of Lysozyme. *J. Mol. Biol.* **1976**, *103*, 227−249.
(477) Gao, J. Energy Components of Aqueous Solution: Insight from Hybrid QM/MM Simulations Using a Polarizable Solvent Model. *J. Comput. Chem.* **1997**, *18*, 1061−1071.
(478) Brunk, E.; Rothlisberger, U. Mixed Quantum Mechanical/Molecular Mechanical Molecular Dynamics Simulations of Biological Systems in Ground and Electronically Excited States. *Chem. Rev.* **2015**, *115*, 6217−6263.
(479) Senn, H. M.; Thiel, W. QM/MM Methods for Biomolecular Systems. *Angew. Chem., Int. Ed.* **2009**, *48*, 1198−1229.
(480) Marin, M. D. C.; De Vico, L.; Dong, S. S.; Gagliardi, L.; Truhlar, D. G.; Olivucci, M. Assessment of MC-PDFT Excitation Energies for a Set of QM/MM Models of Rhodopsins. *J. Chem. Theory Comput.* **2019**, *15*, 1915−1923.
(481) Dokukina, I.; Nenov, A.; Garavelli, M.; Marian, C. M.; Weingart, O. QM/MM Photodynamics of Retinal in the Channelrhodopsin Chimera C1C2 with OM3/MRCI. *ChemPhotoChem.* **2019**, *3*, 107−116.
(482) Vreven, T.; Bernardi, F.; Garavelli, M.; Olivucci, M.; Robb, M. A.; Schlegel, H. B. Ab Initio Photoisomerization Dynamics of a Simple Retinal Chromophore Model. *J. Am. Chem. Soc.* **1997**, *119*, 12687−12688.
(483) Garavelli, M.; Bernardi, F.; Olivucci, M.; Bearpark, M. J.; Klein, S.; Robb, M. A. Product Distribution in the Photolysis of S-Cis Butadiene: A Dynamics Simulation. *J. Phys. Chem. A* **2001**, *105*, 11496−11504.
(484) Bearpark, M. J.; Bernardi, F.; Olivucci, M.; Robb, M. A.; Smith, B. R. Can Fulvene S_1 Decay Be Controlled? A CASSCF Study with MMVB Dynamics. *J. Am. Chem. Soc.* **1996**, *118*, 5254−5260.
(485) Bearpark, M. J.; Bernardi, F.; Clifford, S.; Olivucci, M.; Robb, M. A.; Smith, B. R.; Vreven, T. The Azulene S1 State Decays Via a Conical Intersection: A CasSCF Study with Mmvb Dynamics. *J. Am. Chem. Soc.* **1996**, *118*, 169−175.
(486) Weingart, O.; Garavelli, M. Modelling Vibrational Coherence in the Primary Rhodopsin Photoproduct. *J. Chem. Phys.* **2012**, *137*, 22A523.
(487) Demoulin, B.; Altavilla, S. F.; Rivalta, I.; Garavelli, M. Fine Tuning of Retinal Photoinduced Decay in Solution. *J. Phys. Chem. Lett.* **2017**, *8*, 4407−4412.
(488) Weingart, O.; Nenov, A.; Altoè, P.; Rivalta, I.; Segarra-Martí, J.; Dokukina, I.; Garavelli, M. Cobramm 2.0 — a Software Interface for Tailoring Molecular Electronic Structure Calculations and Running Nanoscale (QM/MM). *J. Mol. Model.* **2018**, *24*, 271.
(489) Borrego-Varillas, R.; Teles-Ferreira, D. C.; Nenov, A.; Conti, I.; Ganzer, L.; Manzoni, C.; Garavelli, M.; Maria de Paula, A.; Cerullo, G. Observation of the Sub-100 fs Population of a Dark State in a Thiobase Mediating Intersystem Crossing. *J. Am. Chem. Soc.* **2018**, *140*, 16087−16093.
(490) Polli, D.; Altoè, P.; Weingart, O.; Spillane, K. M.; Manzoni, C.; Brida, D.; Tomasello, G.; Orlandi, G.; Kukura, P.; Mathies, R. A.; et al. Conical Intersection Dynamics of the Primary Photoisomerization Event in Vision. *Nature* **2010**, *467*, 440−443.
(491) Polli, D.; Weingart, O.; Brida, D.; Poli, E.; Maiuri, M.; Spillane, K. M.; Bottoni, A.; Kukura, P.; Mathies, R. A.; Cerullo, G.; et al. Wavepacket Splitting and Two-Pathway Deactivation in the Photoexcited Visual Pigment Isorhodopsin. *Angew. Chem., Int. Ed.* **2014**, *53*, 2504−2507.
(492) Scalmani, G.; Frisch, M. J.; Mennucci, B.; Tomasi, J.; Cammi, R.; Barone, V. Geometries and Properties of Excited States in the Gas Phase and in Solution: Theory and Application of a Time-Dependent Density Functional Theory Polarizable Continuum Model. *J. Chem. Phys.* **2006**, *124*, 094107.
(493) Caricato, M.; Mennucci, B.; Tomasi, J.; Ingrosso, F.; Cammi, R.; Corni, S.; Scalmani, G. Formation and Relaxation of Excited States in Solution: A New Time Dependent Polarizable Continuum Model Based on Time Dependent Density Functional Theory. *J. Chem. Phys.* **2006**, *124*, 124520.
(494) Bjorgaard, J. A.; Kuzmenko, V.; Velizhanin, K. A.; Tretiak, S. Solvent Effects in Time-Dependent Self-Consistent Field Methods. I. Optical Response Calculations. *J. Chem. Phys.* **2015**, *142*, 044103.
(495) Cammi, R.; Mennucci, B. Linear Response Theory for the Polarizable Continuum Model. *J. Chem. Phys.* **1999**, *110*, 9877−9886.
(496) Cossi, M.; Barone, V. Solvent Effect on Vertical Electronic Transitions by the Polarizable Continuum Model. *J. Chem. Phys.* **2000**, *112*, 2427−2435.
(497) Bagchi, B.; Oxtoby, D. W.; Fleming, G. R. Theory of the Time Development of the Stokes Shift in Polar Media. *Chem. Phys.* **1984**, *86*, 257−267.
(498) Zheng, S.; Geva, E.; Dunietz, B. D. Solvated Charge Transfer States of Functionalized Anthracene and Tetracyanoethylene Dimers: A Computational Study Based on a Range Separated Hybrid Functional and Charge Constrained Self-Consistent Field with Switching Gaussian Polarized Continuum Models. *J. Chem. Theory Comput.* **2013**, *9*, 1125−1131.
(499) Zheng, S.; Phillips, H.; Geva, E.; Dunietz, B. D. Ab Initio Study of the Emissive Charge-Transfer States of Solvated Chromophore-Functionalized Silsesquioxanes. *J. Am. Chem. Soc.* **2012**, *134*, 6944−6947.
(500) Bittner, E. R.; Silva, C. Noise-Induced Quantum Coherence Drives Photo-Carrier Generation Dynamics at Polymeric Semiconductor Heterojunctions. *Nat. Commun.* **2014**, *5*, 3119−3126.
(501) Improta, R.; Scalmani, G.; Frisch, M. J.; Barone, V. Toward Effective and Reliable Fluorescence Energies in Solution by a New State Specific Polarizable Continuum Model Time Dependent Density Functional Theory Approach. *J. Chem. Phys.* **2007**, *127*, 074504.
(502) Bagchi, B. Dynamics of Solvation and Charge Transfer Reactions in Dipolar Liquids. *Annu. Rev. Phys. Chem.* **1989**, *40*, 115−141.
(503) Sneskov, K.; Schwabe, T.; Christiansen, O.; Kongsted, J. Scrutinizing the Effects of Polarization in QM/MM Excited State Calculations. *Phys. Chem. Chem. Phys.* **2011**, *13*, 18551−18560.

https://dx.doi.org/10.1021/acs.chemrev.9b00447
Chem. Rev. 2020, 120, 2215−2287

(504) Caricato, M. A Comparison between State-Specific and Linear-Response Formalisms for the Calculation of Vertical Electronic Transition Energy in Solution with the Ccsd-Pcm Method. *J. Chem. Phys.* **2013**, *139*, 044116.
(505) Corni, S.; Cammi, R.; Mennucci, B.; Tomasi, J. Electronic Excitation Energies of Molecules in Solution within Continuum Solvation Models: Investigating the Discrepancy between State-Specific and Linear-Response Methods. *J. Chem. Phys.* **2005**, *123*, 134512.
(506) Improta, R.; Barone, V.; Scalmani, G.; Frisch, M. J. A State-Specific Polarizable Continuum Model Time Dependent Density Functional Theory Method for Excited State Calculations in Solution. *J. Chem. Phys.* **2006**, *125*, 054103.
(507) Marenich, A. V.; Cramer, C. J.; Truhlar, D. G.; Guido, C. A.; Mennucci, B.; Scalmani, G.; Frisch, M. J. Practical Computation of Electronic Excitation in Solution: Vertical Excitation Model. *Chem. Sci.* **2011**, *2*, 2143−2161.
(508) Caricato, M. Absorption and Emission Spectra of Solvated Molecules with the EOM−CCSD−PCM Method. *J. Chem. Theory Comput.* **2012**, *8*, 4494−4502.
(509) Caricato, M. Exploring Potential Energy Surfaces of Electronic Excited States in Solution with the EOM-CCSD-PCM Method. *J. Chem. Theory Comput.* **2012**, *8*, 5081−5091.
(510) Cammi, R.; Fukuda, R.; Ehara, M.; Nakatsuji, H. Symmetry-Adapted Cluster and Symmetry-Adapted Cluster-Configuration Interaction Method in the Polarizable Continuum Model: Theory of the Solvent Effect on the Electronic Excitation of Molecules in Solution. *J. Chem. Phys.* **2010**, *133*, 024104.
(511) Cammi, R. Coupled-Cluster Theories for the Polarizable Continuum Model. II. Analytical Gradients for Excited States of Molecular Solutes by the Equation of Motion Coupled-Cluster Method. *Int. J. Quantum Chem.* **2010**, *110*, 3040−3052.
(512) Slipchenko, L. V. Solvation of the Excited States of Chromophores in Polarizable Environment: Orbital Relaxation Versus Polarization. *J. Phys. Chem. A* **2010**, *114*, 8824−8830.
(513) Bjorgaard, J. A.; Velizhanin, K. A.; Tretiak, S. Solvent Effects in Time-Dependent Self-Consistent Field Methods. Ii. Variational Formulations and Analytical Gradients. *J. Chem. Phys.* **2015**, *143*, 054305.
(514) Bjorgaard, J. A.; Velizhanin, K. A.; Tretiak, S. Nonequilibrium Solvent Effects in Born-Oppenheimer Molecular Dynamics for Ground and Excited Electronic States. *J. Chem. Phys.* **2016**, *144*, 154104.
(515) Nieman, R.; Tsai, H.; Nie, W.; Aquino, A. J. A.; Mohite, A. D.; Tretiak, S.; Li, H.; Lischka, H. The Crucial Role of a Spacer Material on the Efficiency of Charge Transfer Processes in Organic Donor−Acceptor Junction Solar Cells. *Nanoscale* **2018**, *10*, 451−459.
(516) Guido, C. A.; Mennucci, B.; Scalmani, G.; Jacquemin, D. Excited State Dipole Moments in Solution: Comparison between State-Specific and Linear-Response TD-DFT Values. *J. Chem. Theory Comput.* **2018**, *14*, 1544−1553.
(517) Menger, M. F. S. J.; Caprasecca, S.; Mennucci, B. Excited-State Gradients in Polarizable QM/MM Models: An Induced Dipole Formulation. *J. Chem. Theory Comput.* **2017**, *13*, 3778−3786.
(518) Fried, L. E.; Mukamel, S. Solvation Structure and the Time-Resolved Stokes Shift in Non-Debye Solvents. *J. Chem. Phys.* **1990**, *93*, 932−946.
(519) Mennucci, B.; Scalmani, G.; Jacquemin, D. Excited-State Vibrations of Solvated Molecules: Going Beyond the Linear-Response Polarizable Continuum Model. *J. Chem. Theory Comput.* **2015**, *11*, 847−850.
(520) van der Zwan, G.; Hynes, J. T. Nonequilibrium Solvation Dynamics in Solution Reactions. *J. Chem. Phys.* **1983**, *78*, 4174−4185.
(521) Van der Zwan, G.; Hynes, J. T. Time-Dependent Fluorescence Solvent Shifts, Dielectric Friction, and Nonequilibrium Solvation in Polar Solvents. *J. Phys. Chem.* **1985**, *89*, 4181−4188.
(522) Calef, D. F.; Wolynes, P. G. Classical Solvent Dynamics and Electron Transfer. 1. Continuum Theory. *J. Phys. Chem.* **1983**, *87*, 3387−3400.
(523) Cammi, R.; Tomasi, J. Nonequilibrium Solvation Theory for the Polarizable Continuum Model: A New Formulation at the SCF Level with Application to the Case of the Frequency-Dependent Linear Electric Response Function. *Int. J. Quantum Chem.* **1995**, *56*, 465−474.
(524) Simon, J. D. Time-Resolved Studies of Solvation in Polar Media. *Acc. Chem. Res.* **1988**, *21*, 128−134.
(525) Scaife, B. K. P. *Principles of Dielectrics*; Oxford University Press: New York, 1989.
(526) Bottcher, C. J. F. *Theory of Electric Polarization*; Elsevier: Amsterdam, 1973.
(527) Loring, R. F.; Mukamel, S. Molecular Theory of Solvation and Dielectric Response in Polar Fluids. *J. Chem. Phys.* **1987**, *87*, 1272−1283.
(528) Hsu, C.-P.; Song, X.; Marcus, R. A. Time-Dependent Stokes Shift and Its Calculation from Solvent Dielectric Dispersion Data. *J. Phys. Chem. B* **1997**, *101*, 2546−2551.
(529) Ingrosso, F.; Mennucci, B.; Tomasi, J. Quantum Mechanical Calculations Coupled with a Dynamical Continuum Model for the Description of Dielectric Relaxation: Time Dependent Stokes Shift of Coumarin C153 in Polar Solvents. *J. Mol. Liq.* **2003**, *108*, 21−46.
(530) Caricato, M.; Ingrosso, F.; Mennucci, B.; Tomasi, J. A Time-Dependent Polarizable Continuum Model: Theory and Application. *J. Chem. Phys.* **2005**, *122*, 154501.
(531) Ding, F.; Lingerfelt, D. B.; Mennucci, B.; Li, X. Time-Dependent Non-Equilibrium Dielectric Response in Qm/Continuum Approaches. *J. Chem. Phys.* **2015**, *142*, 034120.
(532) Corni, S.; Pipolo, S.; Cammi, R. Equation of Motion for the Solvent Polarization Apparent Charges in the Polarizable Continuum Model: Application to Real-Time TDDFT. *J. Phys. Chem. A* **2015**, *119*, 5405−5416.
(533) Barbatti, M.; Sen, K. Effects of Different Initial Condition Samplings on Photodynamics and Spectrum of Pyrrole. *Int. J. Quantum Chem.* **2016**, *116*, 762−771.
(534) Allen, M. P.; Tildesley, D. J. *Computer Simulation of Liquids*; Oxford University Press: USA, 1990.
(535) van Gunsteren, W. F.; Berendsen, H. J. C. Algorithms for Brownian Dynamics. *Mol. Phys.* **1982**, *45*, 637−647.
(536) Paterlini, M. G.; Ferguson, D. M. Constant Temperature Simulations Using the Langevin Equation with Velocity Verlet Integration. *Chem. Phys.* **1998**, *236*, 243−252.
(537) Andersen, H. C. Molecular Dynamics Simulations at Constant Pressure and/or Temperature. *J. Chem. Phys.* **1980**, *72*, 2384−2393.
(538) Tanaka, H.; Nakanishi, K.; Watanabe, N. Constant Temperature Molecular Dynamics Calculation on Lennard-Jones Fluid and Its Application to Watera. *J. Chem. Phys.* **1983**, *78*, 2626−2634.
(539) Nosé, S. A. Unified Formulation of the Constant Temperature Molecular Dynamics Methods. *J. Chem. Phys.* **1984**, *81*, 511−519.
(540) Thijssen, J. M. *Computational Physics*, 2nd ed.; Cambridge University Press: UK, 2007.
(541) Berendsen, H. J. C.; Postma, J. P. M.; van Gunsteren, W. F.; DiNola, A.; Haak, J. R. Molecular Dynamics with Coupling to an External Bath. *J. Chem. Phys.* **1984**, *81*, 3684−3690.
(542) Mor, A.; Ziv, G.; Levy, Y. Simulations of Proteins with Inhomogeneous Degrees of Freedom: The Effect of Thermostats. *J. Comput. Chem.* **2008**, *29*, 1992−1998.
(543) Tuckerman, M. *Statistical Mechanics: Theory and Molecular Simulation*; Oxford University Press, 2001.
(544) Nelson, T.; Fernandez-Alberti, S.; Chernyak, V.; Roitberg, A. E.; Tretiak, S. Nonadiabatic Excited-State Molecular Dynamics: Numerical Tests of Convergence and Parameters. *J. Chem. Phys.* **2012**, *136*, 054108.
(545) Monticelli, L.; Tieleman, D. P. Force Fields for Classical Molecular Dynamics. *Methods Mol. Biol.* **2013**, *924*, 197−213.
(546) Ondarse-Alvarez, D.; Oldani, N.; Roitberg, A. E.; Kleiman, V.; Tretiak, S.; Fernandez-Alberti, S. Energy Transfer and Spatial Scrambling of an Exciton in a Conjugated Dendrimer. *Phys. Chem. Chem. Phys.* **2018**, *20*, 29648−29660.
(547) Fernandez-Alberti, S.; Roitberg, A. E.; Kleiman, V. D.; Nelson, T.; Tretiak, S. Shishiodoshi Unidirectional Energy Transfer Mechanism

https://dx.doi.org/10.1021/acs.chemrev.9b00447
Chem. Rev. 2020, 120, 2215−2287

in Phenylene Ethynylene Dendrimers. *J. Chem. Phys.* **2012**, *137*, 22A526.
(548) Shenai, P. M.; Fernandez-Alberti, S.; Bricker, W. P.; Tretiak, S.; Zhao, Y. Internal Conversion and Vibrational Energy Redistribution in Chlorophyll A. *J. Phys. Chem. B* **2016**, *120*, 49−58.
(549) Galindo, J. F.; Atas, E.; Altan, A.; Kuroda, D. G.; Fernandez-Alberti, S.; Tretiak, S.; Roitberg, A. E.; Kleiman, V. D. Dynamics of Energy Transfer in a Conjugated Dendrimer Driven by Ultrafast Localization of Excitations. *J. Am. Chem. Soc.* **2015**, *137*, 11637−11644.
(550) Barbatti, M. Nonadiabatic Dynamics with Trajectory Surface Hopping Method. *WIREs Comput. Mol. Sci.* **2011**, *1*, 620−633.
(551) Bjorgaard, J. A.; Sheppard, D.; Tretiak, S.; Niklasson, A. M. N. Extended Lagrangian Excited State Molecular Dynamics. *J. Chem. Theory Comput.* **2018**, *14*, 799−806.
(552) Remler, D. K.; Madden, P. A. Molecular Dynamics without Effective Potentials Via the Car-Parrinello Approach. *Mol. Phys.* **1990**, *70*, 921−966.
(553) Pulay, P.; Fogarasi, G. Fock Matrix Dynamics. *Chem. Phys. Lett.* **2004**, *386*, 272−278.
(554) Niklasson, A. M. N.; Tymczak, C. J.; Challacombe, M. Time-Reversible Born-Oppenheimer Molecular Dynamics. *Phys. Rev. Lett.* **2006**, *97*, 123001.
(555) Marx, D.; Hutter, J. *Modern Methods and Algorithms of Quantum Chemistry*; John von Neumann Institute for Computing Forschungszentrum: Julich, Germany, 2000.
(556) Kirchner, B.; di Dio, P. J.; Hutter, J. In *Multiscale Molecular Methods in Applied Chemistry*; Kirchner, B., Vrabec, J., Eds.; Springer: Berlin/Heidelberg, 2012.
(557) Liberatore, E.; Meli, R.; Rothlisberger, U. A Versatile Multiple Time Step Scheme for Efficient Ab Initio Molecular Dynamics Simulations. *J. Chem. Theory Comput.* **2018**, *14*, 2834−2842.
(558) Moret, M.-E.; Tapavicza, E.; Guidoni, L.; Röhrig, U. F.; Sulpizi, M.; Tavernelli, I.; Rothlisberger, U. Quantum Mechanical/Molecular Mechanical (QM/MM) Car-Parrinello Simulations in Excited States. *Chimia* **2005**, *59*, 493−498.
(559) Markwick, P. R. L.; Doltsinis, N. L.; Schlitter, J. Probing Irradiation Induced DNA Damage Mechanisms Using Excited State Car-Parrinello Molecular Dynamics. *J. Chem. Phys.* **2007**, *126*, 045104.
(560) Niklasson, A. M. N. Next Generation Extended Lagrangian First Principles Molecular Dynamics. *J. Chem. Phys.* **2017**, *147*, 054103.
(561) Niklasson, A. M. N.; Steneteg, P.; Odell, A.; Bock, N.; Challacombe, M.; Tymczak, C. J.; Holmström, E.; Zheng, G.; Weber, V. Extended Lagrangian Born−Oppenheimer Molecular Dynamics with Dissipation. *J. Chem. Phys.* **2009**, *130*, 214109.
(562) Steneteg, P.; Abrikosov, I. A.; Weber, V.; Niklasson, A. M. N. Wave Function Extended Lagrangian Born-Oppenheimer Molecular Dynamics. *Phys. Rev. B: Condens. Matter Mater. Phys.* **2010**, *82*, 075110.
(563) Pittner, J.; Lischka, H.; Barbatti, M. Optimization of Mixed Quantum-Classical Dynamics: Time-Derivative Coupling Terms and Selected Couplings. *Chem. Phys.* **2009**, *356*, 147−152.
(564) Nelson, T.; Naumov, A.; Fernandez-Alberti, S.; Tretiak, S. Nonadiabatic Excited-State Molecular Dynamics: On-the-Fly Limiting of Essential Excited States. *Chem. Phys.* **2016**, *481*, 84−90.
(565) Hack, M. D.; Jasper, A. W.; Volobuev, Y. L.; Schwenke, D. W.; Truhlar, D. G. Quantum Mechanical and Quasiclassical Trajectory Surface Hopping Studies of the Electronically Nonadiabatic Predissociation of the Ã State of NaH_2. *J. Phys. Chem. A* **1999**, *103*, 6309−6326.
(566) Hammes-Schiffer, S.; Tully, J. C. Proton Transfer in Solution: Molecular Dynamics with Quantum Transitions. *J. Chem. Phys.* **1994**, *101*, 4657−4667.
(567) Mead, C. A.; Truhlar, D. G. Conditions for the Definition of a Strictly Diabatic Electronic Basis for Molecular Systems. *J. Chem. Phys.* **1982**, *77*, 6090−6098.
(568) Subotnik, J. E.; Yeganeh, S.; Cave, R. J.; Ratner, M. A. Constructing Diabatic States from Adiabatic States: Extending Generalized Mulliken−Hush to Multiple Charge Centers with Boys Localization. *J. Chem. Phys.* **2008**, *129*, 244101.
(569) Yang, C.-H.; Hsu, C.-P. A Multi-State Fragment Charge Difference Approach for Diabatic States in Electron Transfer: Extension and Automation. *J. Chem. Phys.* **2013**, *139*, 154104.
(570) Richter, M.; Marquetand, P.; González-Vázquez, J.; Sola, I.; González, L. Sharc: Ab Initio Molecular Dynamics with Surface Hopping in the Adiabatic Representation Including Arbitrary Couplings. *J. Chem. Theory Comput.* **2011**, *7*, 1253−1258.
(571) Mai, S.; Marquetand, P.; González, L. A General Method to Describe Intersystem Crossing Dynamics in Trajectory Surface Hopping. *Int. J. Quantum Chem.* **2015**, *115*, 1215−1231.
(572) Schnappinger, T.; Marazzi, M.; Mai, S.; Monari, A.; Gonzalez, L.; de Vivie-Riedle, R. Intersystem Crossing as a Key Component of the Nonadiabatic Relaxation Dynamics of Bithiophene and Terthiophene. *J. Chem. Theory Comput.* **2018**, *14*, 4530−4540.
(573) Mai, S.; Atkins, A. J.; Plasser, F.; Gonzalez, L. The Influence of the Electronic Structure Method on Intersystem Crossing Dynamics. The Case of Thioformaldehyde. *J. Chem. Theory Comput.* **2019**, *15*, 3470−3480.
(574) Fang, D.; Lu, J. A Diabatic Surface Hopping Algorithm Based on Time Dependent Perturbation Theory and Semiclassical Analysis. *Multiscale Model. Simul.* **2018**, *16*, 1603−1622.
(575) Yamada, A.; Okazaki, S. A Surface Hopping Method for Chemical Reaction Dynamics in Solution Described by Diabatic Representation: An Analysis of Tunneling and Thermal Activation. *J. Chem. Phys.* **2006**, *124*, 094110.
(576) Gadéa, F. X.; Berriche, H.; Roncero, O.; Villarreal, P.; Delgado Barrio, G. Nonradiative Lifetimes for Lih in the a State Using Adiabatic and Diabatic Schemes. *J. Chem. Phys.* **1997**, *107*, 10515−10522.
(577) Alguire, E. C.; Fatehi, S.; Shao, Y.; Subotnik, J. E. Analysis of Localized Diabatic States Beyond the Condon Approximation for Excitation Energy Transfer Processes. *J. Phys. Chem. A* **2014**, *118*, 11891−11900.
(578) Swope, W. C.; Andersen, H. C.; Berens, P. H.; Wilson, K. R. A Computer Simulation Method for the Calculation of Equilibrium Constants for the Formation of Physical Clusters of Molecules: Application to Small Water Clusters. *J. Chem. Phys.* **1982**, *76*, 637−649.
(579) Nelson, T.; Fernandez-Alberti, S.; Roitberg, A. E.; Tretiak, S. Conformational Disorder in Energy Transfer: Beyond Forster Theory. *Phys. Chem. Chem. Phys.* **2013**, *15*, 9245−9256.
(580) Shu, Y.; Levine, B. G. First-Principles Study of Nonradiative Recombination in Silicon Nanocrystals: The Role of Surface Silanol. *J. Phys. Chem. C* **2016**, *120*, 23246−23253.
(581) Szczepanik, D.; Mrozek, J. On Several Alternatives for Löwdin Orthogonalization. *Comput. Theor. Chem.* **2013**, *1008*, 15−19.
(582) Prezhdo, O. V.; Rossky, P. J. Mean-Field Molecular Dynamics with Surface Hopping. *J. Chem. Phys.* **1997**, *107*, 825−834.
(583) Evenhuis, C.; Martinez, T. J. A Scheme to Interpolate Potential Energy Surfaces and Derivative Coupling Vectors without Performing a Global Diabatization. *J. Chem. Phys.* **2011**, *135*, 224110.
(584) Torres, A.; Oliboni, R. S.; Rego, L. G. C. Vibronic and Coherent Effects on Interfacial Electron Transfer Dynamics. *J. Phys. Chem. Lett.* **2015**, *6*, 4927−4935.
(585) Tretiak, S.; Isborn, C. M.; Niklasson, A. M. N.; Challacombe, M. Representation Independent Algorithms for Molecular Response Calculations in Time-Dependent Self-Consistent Field Theories. *J. Chem. Phys.* **2009**, *130*, 054111.
(586) Wu, C.; Malinin, S. V.; Tretiak, S.; Chernyak, V. Y. Exciton Scattering and Localization in Branched Dendrimeric Structures. *Nat. Phys.* **2006**, *2*, 631−635.
(587) Tretiak, S.; Chernyak, V.; Mukamel, S. Two-Dimensional Real-Space Analysis of Optical Excitations in Acceptor-Substituted Carotenoids. *J. Am. Chem. Soc.* **1997**, *119*, 11408−11419.
(588) Ondarse-Alvarez, D.; Oldani, N.; Tretiak, S.; Fernandez-Alberti, S. Computational Study of Photoexcited Dynamics in Bichromophoric Cross-Shaped Oligofluorene. *J. Phys. Chem. A* **2014**, *118*, 10742−10753.
(589) Oldani, N.; Tretiak, S.; Bazan, G.; Fernandez-Alberti, S. Modeling of Internal Conversion in Photoexcited Conjugated

https://dx.doi.org/10.1021/acs.chemrev.9b00447
Chem. Rev. 2020, 120, 2215−2287

Molecular Donors Used in Organic Photovoltaics. *Energy Environ. Sci.* **2014**, *7*, 1175−1184.
(590) Tretiak, S.; Igumenshchev, K.; Chernyak, V. Exciton Sizes of Conducting Polymers Predicted by Time-Dependent Density Functional Theory. *Phys. Rev. B: Condens. Matter Mater. Phys.* **2005**, *71*, 033201.
(591) Igumenshchev, K. I.; Tretiak, S.; Chernyak, V. Y. Excitonic Effects in a Time-Dependent Density Functional Theory. *J. Chem. Phys.* **2007**, *127*, 114902.
(592) Plasser, F.; Lischka, H. Analysis of Excitonic and Charge Transfer Interactions from Quantum Chemical Calculations. *J. Chem. Theory Comput.* **2012**, *8*, 2777−2789.
(593) Martin, R. L. Natural Transition Orbitals. *J. Chem. Phys.* **2003**, *118*, 4775−4777.
(594) Nogueira, J. J.; Plasser, F.; González, L. Electronic Delocalization, Charge Transfer and Hypochromism in the Uv Absorption Spectrum of Polyadenine Unravelled by Multiscale Computations and Quantitative Wavefunction Analysis. *Chem. Sci.* **2017**, *8*, 5682−5691.
(595) Luzanov, A. V.; Zhikol, O. A. Electron Invariants and Excited State Structural Analysis for Electronic Transitions within Cis, Rpa, and Tddft Models. *Int. J. Quantum Chem.* **2009**, *110*, 902−924.
(596) Davydov, A. S. The Theory of Molecular Excitons. *Phys.-Uspekhi* **1964**, *7*, 145−178.
(597) Rashba, E. I., Sturge, M. D., Eds. *Excitons*, Vol. 2; Modern Problems in Condensed Matter Sciences; North-Holland, Amsterdam/New York, 1982.
(598) Broude, V. L.; Rashba, E. I.; Sheka, E. *Spectroscopy of Molecular Excitons*; Springer-Verlag: Berlin/Heidelberg, 1985. DOI: 10.1007/978-1-4020-8707-3.
(599) Tautz, R.; Da Como, E.; Wiebeler, C.; Soavi, G.; Dumsch, I.; Frohlich, N.; Grancini, G.; Allard, S.; Scherf, U.; Cerullo, G.; et al. Charge Photogeneration in Donor-Acceptor Conjugated Materials: Influence of Excess Excitation Energy and Chain Length. *J. Am. Chem. Soc.* **2013**, *135*, 4282−4290.
(600) Bell, R. J.; Dean, P.; Hibbins-Butler, D. C. Localization of Normal Modes in Vitreous Silica, Germania and Beryllium Fluoride. *J. Phys. C: Solid State Phys.* **1970**, *3*, 2111−2118.
(601) Taraskin, S.; Elliott, S. R. Anharmonicity and Localization of Atomic Vibrations in Vitreous Silica. *Phys. Rev. B: Condens. Matter Mater. Phys.* **1999**, *59*, 8572−8585.
(602) Oldani, N.; Doorn, S. K.; Tretiak, S.; Fernandez-Alberti, S. Photoinduced Dynamics in Cycloparaphenylenes: Planarization, Electron−Phonon Coupling, Localization and Intra-Ring Migration of the Electronic Excitation. *Phys. Chem. Chem. Phys.* **2017**, *19*, 30914−30924.
(603) Soler, M. A.; Bastida, A.; Farag, M. H.; Zúñiga, J.; Requena, A. A Method for Analyzing the Vibrational Energy Flow in Biomolecules in Solution. *J. Chem. Phys.* **2011**, *135*, 204106.
(604) Akimov, A. V.; Prezhdo, O. V. Advanced Capabilities of the Pyxaid Program: Integration Schemes, Decoherence Effects, Multi-excitonic States, and Field-Matter Interaction. *J. Chem. Theory Comput.* **2014**, *10*, 789−804.
(605) Mai, S.; Marquetand, P.; Gonzalez, L. Nonadiabatic Dynamics: The Sharc Approach. *WIREs Comput. Mol. Sci.* **2018**, *8*, e1370.
(606) Shao, Y.; Gan, Z.; Epifanovsky, E.; Gilbert, A. T. B.; Wormit, M.; Kussmann, J.; Lange, A. W.; Behn, A.; Deng, J.; Feng, X.; et al. Advances in Molecular Quantum Chemistry Contained in the Q-Chem 4 Program Package. *Mol. Phys.* **2015**, *113*, 184−215.
(607) Pal, S.; Trivedi, D. J.; Akimov, A. V.; Aradi, B.; Frauenheim, T.; Prezhdo, O. V. Nonadiabatic Molecular Dynamics for Thousand Atom Systems: A Tight-Binding Approach toward Pyxaid. *J. Chem. Theory Comput.* **2016**, *12*, 1436−1448.
(608) Valiev, M.; Bylaska, E. J.; Govind, N.; Kowalski, K.; Straatsma, T. P.; Van Dam, H. J. J.; Wang, D.; Nieplocha, J.; Apra, E.; Windus, T. L.; et al. Nwchem: A Comprehensive and Scalable Open-Source Solution for Large Scale Molecular Simulations. *Comput. Phys. Commun.* **2010**, *181*, 1477−1489.
(609) Frisch, M. J.; Trucks, G. W.; Schlegel, H. B.; Scuseria, G. E.; Robb, M. A.; Cheeseman, J. R.; Scalmani, G.; Barone, V.; Petersson, G. A.; Nakatsuji, H..et al. *Gaussian 16*; Gaussian Inc., Wallingford, CT, 2016.
(610) Mukamel, S.; Tretiak, S.; Wagersreiter, T.; Chernyak, V. Electronic Coherence and Collective Optical Excitations of Conjugated Molecules. *Science* **1997**, *277*, 781−787.
(611) Ridley, J.; Zerner, M. An Intermediate Neglect of Differential Overlap Technique for Spectroscopy: Pyrrole and the Azines. *Theor. Chim. Acta* **1973**, *32*, 111−134.
(612) Case, D.; Cerutti, D. S.; Cheatham, T.; Darden, T.; Duke, R.; Giese, T. J.; Gohlke, H.; Götz, A.; Greene, D.; Homeyer, N..et al. *Amber 2017*; University of California, San Francisco, 2017.
(613) Thouless, D. J. *The Quantum Mechanics of Many-Body Systems*; Academic Press: New York, 1972.
(614) Tretiak, S.; Saxena, A.; Martin, R. L.; Bishop, A. R. Ceo/Semiempirical Calculations of Uv−Visible Spectra in Conjugated Molecules. *Chem. Phys. Lett.* **2000**, *331*, 561−568.
(615) Tretiak, S.; Saxena, A.; Martin, R. L.; Bishop, A. R. Collective Electronic Oscillator/Semiempirical Calculations of Static Nonlinear Polarizabilities in Conjugated Molecules. *J. Chem. Phys.* **2001**, *115*, 699−707.
(616) Meng, Z.; Dölle, A.; Robert Carper, W. Gas Phase Model of an Ionic Liquid: Semi-Empirical and Ab Initio Bonding and Molecular Structure. *J. Mol. Struct.: THEOCHEM* **2002**, *585*, 119−128.
(617) Stewart, J. J. P. Comparison of the Accuracy of Semiempirical and Some Dft Methods for Predicting Heats of Formation. *J. Mol. Model.* **2004**, *10*, 6−12.
(618) Tretiak, S.; Saxena, A.; Martin, R. L.; Bishop, A. R. Conformational Dynamics of Photoexcited Conjugated Molecules. *Phys. Rev. Lett.* **2002**, *89*, 097402.
(619) Franco, I.; Tretiak, S. Electron-Vibrational Relaxation of Photoexcited Polyfluorenes in the Presence of Chemical Defects: A Theoretical Study. *Chem. Phys. Lett.* **2003**, *372*, 403−408.
(620) Tretiak, S.; Chernyak, V.; Mukamel, S. Localized Electronic Excitations in Phenylacetylene Dendrimers. *J. Phys. Chem. B* **1998**, *102*, 3310−3315.
(621) Tretiak, S.; Middleton, C.; Chernyak, V.; Mukamel, S. Exciton Hamiltonian for the Bacteriochlorophyll System in the Lh2 Antenna Complex of Purple Bacteria. *J. Phys. Chem. B* **2000**, *104*, 4519−4528.
(622) Tretiak, S.; Middleton, C.; Chernyak, V.; Mukamel, S. Bacteriochlorophyll and Carotenoid Excitonic Couplings in the Lh2 System of Purple Bacteria. *J. Phys. Chem. B* **2000**, *104*, 9540−9553.
(623) Kilina, S.; Tretiak, S.; Doorn, S. K.; Luo, Z.; Papadimitrakopoulos, F.; Piryatinski, A.; Saxena, A.; Bishop, A. R. Cross-Polarized Excitons in Carbon Nanotubes. *Proc. Natl. Acad. Sci. U. S. A.* **2008**, *105*, 6797−6802.
(624) Kilina, S.; Tretiak, S. Excitonic and Vibrational Properties of Single-Walled Semiconducting Carbon Nanotubes. *Adv. Funct. Mater.* **2007**, *17*, 3405−3420.
(625) Nelson, T.; Fernandez-Alberti, S.; Roitberg, A. E.; Tretiak, S. Nonadiabatic Excited-State Molecular Dynamics: Modeling Photophysics in Organic Conjugated Materials. *Acc. Chem. Res.* **2014**, *47*, 1155−1164.
(626) Lewis, S. E. Cycloparaphenylenes and Related Nanohoops. *Chem. Soc. Rev.* **2015**, *44*, 2221−2304.
(627) Adamska, L.; Nayyar, I.; Chen, H.; Swan, A. K.; Oldani, N.; Fernandez-Alberti, S.; Golder, M. R.; Jasti, R.; Doorn, S. K.; Tretiak, S. Self-Trapping of Excitons, Violation of Condon Approximation, and Efficient Fluorescence in Conjugated Cycloparaphenylenes. *Nano Lett.* **2014**, *14*, 6539−6546.
(628) Evans, P. J.; Jasti, R. Molecular Belts. *Polyarenes I*, Topics in Current Chemistry *349*; Springer: Berlin, 2012; pp 249−290. DOI: 10.1007/128_2012_415
(629) Wong, B. M.; Lee, J. W. Anomalous Optoelectronic Properties of Chiral Carbon Nanorings···and One Ring to Rule Them All. *J. Phys. Chem. Lett.* **2011**, *2*, 2702−2706.
(630) Omachi, H.; Segawa, Y.; Itami, K. Synthesis and Racemization Process of Chiral Carbon Nanorings: A Step toward the Chemical

Synthesis of Chiral Carbon Nanotubes. *Org. Lett.* **2011**, *13*, 2480−2483.
(631) Franklin-Mergarejo, R.; Alvarez, D. O.; Tretiak, S.; Fernandez-Alberti, S. Carbon Nanorings with Inserted Acenes: Breaking Symmetry in Excited State Dynamics. *Sci. Rep.* **2016**, *6*, 31253.
(632) Iwamoto, T.; Kayahara, E.; Yasuda, N.; Suzuki, T.; Yamago, S. Synthesis, Characterization, and Properties of [4]Cyclo-2,7-Pyrenylene: Effects of Cyclic Structure on the Electronic Properties of Pyrene Oligomers. *Angew. Chem., Int. Ed.* **2014**, *53*, 6430−6434.
(633) Fidler, A. F.; Singh, V. P.; Long, P. D.; Dahlberg, P. D.; Engel, G. S. Dynamic Localization of Electronic Excitation in Photosynthetic Complexes Revealed with Chiral Two-Dimensional Spectroscopy. *Nat. Commun.* **2014**, *5*, 3286.
(634) Scholes, G. D.; Fleming, G. R. On the Mechanism of Light Harvesting in Photosynthetic Purple Bacteria: B800 to B850 Energy Transfer. *J. Phys. Chem. B* **2000**, *104*, 1854−1868.
(635) Fenna, R. E.; Matthews, B. W. Chlorophyll Arrangement in a Bacteriochlorophyll Protein from Chlorobium Limicola. *Nature* **1975**, *258*, 573−577.
(636) Zheng, F.; Fernandez-Alberti, S.; Tretiak, S.; Zhao, Y. Photoinduced Intra- and Intermolecular Energy Transfer in Chlorophyll a Dimer. *J. Phys. Chem. B* **2017**, *121*, 5331−5339.
(637) Kelley, R. F.; Tauber, M. J.; Wilson, T. M.; Wasielewski, M. R. Controlling Energy and Charge Transfer in Linear Chlorophyll Dimers. *Chem. Commun.* **2007**, 4407−4409.
(638) Lee, S. H.; Matula, A. J.; Hu, G.; Troiano, J. L.; Karpovich, C. J.; Crabtree, R. H.; Batista, V. S.; Brudvig, G. W. Strongly Coupled Phenazine-Porphyrin Dyads: Light-Harvesting Molecular Assemblies with Broad Absorption Coverage. *ACS Appl. Mater. Interfaces* **2019**, *11*, 8000−8008.
(639) Milder, M. T. W.; Brüggemann, B.; van Grondelle, R.; Herek, J. L. Revisiting the Optical Properties of the Fmo Protein. *Photosynth. Res.* **2010**, *104*, 257−274.
(640) Blankenship, R. E. *Molecular Mechanisms of Photosynthesis*; Blackwell Publishing: Williston, VT, USA, 2002.
(641) Croce, R.; van Amerongen, H. Natural Strategies for Photosynthetic Light Harvesting. *Nat. Chem. Biol.* **2014**, *10*, 492−501.
(642) Scholes, G. D.; Fleming, G. R.; Olaya-Castro, A.; van Grondelle, R. Lessons from Nature About Solar Light Harvesting. *Nat. Chem.* **2011**, *3*, 763−774.
(643) Nguyen, K. A.; Day, P. N.; Pachter, R.; Tretiak, S.; Chernyak, V.; Mukamel, S. Analysis of Absorption Spectra of Zinc Porphyrin, Zinc Meso-Tetraphenylporphyrin, and Halogenated Derivatives. *J. Phys. Chem. A* **2002**, *106*, 10285−10293.
(644) Bricker, W. P.; Shenai, P. M.; Ghosh, A.; Liu, Z.; Enriquez, M. G. M.; Lambrev, P. H.; Tan, H.-S.; Lo, C. S.; Tretiak, S.; Fernandez-Alberti, S.; et al. Non-Radiative Relaxation of Photoexcited Chlorophylls: Theoretical and Experimental Study. *Sci. Rep.* **2015**, *5*, 13625−13640.
(645) Wang, N.; Tong, X.; Burlingame, Q.; Yu, J.; Forrest, S. R. Photodegradation of Small-Molecule Organic Photovoltaics. *Sol. Energy Mater. Sol. Cells* **2014**, *125*, 170−175.
(646) Zhugayevych, A.; Postupna, O.; Bakus, R. C., II; Welch, G. C.; Bazan, G. C.; Tretiak, S. Ab Initio Study of a Molecular Crystal for Photovoltaics: Light Absorption, Exciton and Charge Carrier Transport. *J. Phys. Chem. C* **2013**, *117*, 4920−4930.
(647) Zhang, K.; Cao, W.; Zhang, J. Solid-Phase Photocatalytic Degradation of Pvc by Tungstophosphoric Acid—a Novel Method for Pvc Plastic Degradation. *Appl. Catal., A* **2004**, *276*, 67−73.
(648) Shang, J.; Chai, M.; Zhu, Y. Solid-Phase Photocatalytic Degradation of Polystyrene Plastic with Tio2 as Photocatalyst. *J. Solid State Chem.* **2003**, *174*, 104−110.
(649) Greenfield, M. T.; McGrane, S. D.; Bolme, C. A.; Bjorgaard, J. A.; Nelson, T. R.; Tretiak, S.; Scharff, R. J. Photoactive High Explosives: Linear and Nonlinear Photochemistry of Petrin Tetrazine Chloride. *J. Phys. Chem. A* **2015**, *119*, 4846−4855.
(650) Nelson, T.; Bjorgaard, J.; Greenfield, M.; Bolme, C.; Brown, K.; McGrane, S.; Scharff, R. J.; Tretiak, S. Ultrafast Photodissociation Dynamics of Nitromethane. *J. Phys. Chem. A* **2016**, *120*, 519−526.
(651) McBee, J. K.; Kuksa, V.; Alvarez, R.; de Lera, A. R.; Prezhdo, O.; Haeseleer, F.; Sokal, I.; Palczewski, K. Isomerization of All-Trans-Retinol to Cis-Retinols in Bovine Retinal Pigment Epithelial Cells: Dependence on the Specificity of Retinoid-Binding Proteins. *Biochemistry* **2000**, *39*, 11370−11380.
(652) Weingart, O. The Twisted C11═C12 Bond of the Rhodopsin Chromophorea Photochemical Hot Spot. *J. Am. Chem. Soc.* **2007**, *129*, 10618−10619.
(653) George, C.; Ammann, M.; D'Anna, B.; Donaldson, D. J.; Nizkorodov, S. A. Heterogeneous Photochemistry in the Atmosphere. *Chem. Rev.* **2015**, *115*, 4218−4258.
(654) Grannas, A. M.; Pagano, L. P.; Pierce, B. C.; Bobby, R.; Fede, A. Role of Dissolved Organic Matter in Ice Photochemistry. *Environ. Sci. Technol.* **2014**, *48*, 10725−10733.
(655) Kim, S. K.; Zewail, A. H. Femtosecond Elementary Dynamics of Transition States and Asymmetric A-Cleavage in Norrish Reactions. *Chem. Phys. Lett.* **1996**, *250*, 279−286.
(656) Lee, J.; Jadhav, P.; Reusswig, P. D.; Yost, S. R.; Thompson, N. J.; Congreve, D. N.; Hontz, E.; Van Voorhis, T.; Baldo, M. A. Singlet Exciton Fission Photovoltaics. *Acc. Chem. Res.* **2013**, *46*, 1300−1311.
(657) Ni, M.; Leung, M. K. H.; Leung, D. Y. C.; Sumathy, K. A Review and Recent Developments in Photocatalytic Water-Splitting Using Tio2 for Hydrogen Production. *Renewable Sustainable Energy Rev.* **2007**, *11*, 401−425.
(658) Maeda, K.; Domen, K. Photocatalytic Water Splitting: Recent Progress and Future Challenges. *J. Phys. Chem. Lett.* **2010**, *1*, 2655−2661.
(659) Ismail, A. A.; Bahnemann, D. W. Photochemical Splitting of Water for Hydrogen Production by Photocatalysis: A Review. *Sol. Energy Mater. Sol. Cells* **2014**, *128*, 85−101.
(660) Castro, A. L.; Nunes, M. R.; Carvalho, M. D.; Ferreira, L. P.; Jumas, J. C.; Costa, F. M.; Florêncio, M. H. Doped Titanium Dioxide Nanocrystalline Powders with High Photocatalytic Activity. *J. Solid State Chem.* **2009**, *182*, 1838−1845.
(661) Gole, J. L.; Prokes, S. M.; Glembocki, O. J. Efficient Room-Temperature Conversion of Anatase to Rutile Tio2 Induced by High-Spin Ion Doping. *J. Phys. Chem. C* **2008**, *112*, 1782−1788.
(662) Brown, H. W.; Pimentel, G. C. Photolysis of Nitromethane and of Methyl Nitrite in an Argon Matrix; Infrared Detection of Nitroxyl, Hno. *J. Chem. Phys.* **1958**, *29*, 883−888.
(663) Wodtke, A. M.; Hintsa, E. J.; Lee, Y. T. The Observation of CH_3O in the Collision Free Multiphoton Dissociation of CH_3NO_2. *J. Chem. Phys.* **1986**, *84*, 1044−1045.
(664) Guo, Y. Q.; Bhattacharya, A.; Bernstein, E. R. Photodissociation Dynamics of Nitromethane at 226 and 271 nm at Both Nanosecond and Femtosecond Time Scales. *J. Phys. Chem. A* **2009**, *113*, 85−96.
(665) Lystrom, L.; Zhang, Y.; Tretiak, S.; Nelson, T. Site-Specific Photodecomposition in Conjugated Energetic Materials. *J. Phys. Chem. A* **2018**, *122*, 6055−6061.
(666) Myers, T. W.; Bjorgaard, J. A.; Brown, K. E.; Chavez, D. E.; Hanson, S. K.; Scharff, R. J.; Tretiak, S.; Veauthier, J. M. Energetic Chromophores: Low-Energy Laser Initiation in Explosive Fe(II) Tetrazine Complexes. *J. Am. Chem. Soc.* **2016**, *138*, 4685−4692.
(667) Gräfenstein, J.; Kraka, E.; Filatov, M.; Cremer, D. Can Unrestricted Density-Functional Theory Describe Open Shell Singlet Biradicals? *Int. J. Mol. Sci.* **2002**, *3*, 360−394.
(668) Grimme, S. Towards First Principles Calculation of Electron Impact Mass Spectra of Molecules. *Angew. Chem., Int. Ed.* **2013**, *52*, 6306−6312.
(669) Bauernschmitt, R.; Ahlrichs, R. Stability Analysis for Solutions of the Closed Shell Kohn−Sham Equation. *J. Chem. Phys.* **1996**, *104*, 9047−9052.
(670) Vincent, J. C.; Muuronen, M.; Pearce, K. C.; Mohanam, L. N.; Tapavicza, E.; Furche, F. That Little Extra Kick: Nonadiabatic Effects in Acetaldehyde Photodissociation. *J. Phys. Chem. Lett.* **2016**, *7*, 4185−4190.
(671) Jensen, S. J.; Inerbaev, T. M.; Kilin, D. S. Spin Unrestricted Excited State Relaxation Study of Vanadium(IV)-Doped Anatase. *J. Phys. Chem. C* **2016**, *120*, 5890−5905.

https://dx.doi.org/10.1021/acs.chemrev.9b00447
Chem. Rev. 2020, 120, 2215−2287

(672) Jensen, S. J.; Inerbaev, T. M.; Abuova, A. U.; Kilin, D. S. Spin Unrestricted Nonradiative Relaxation Dynamics of Cobalt-Doped Anatase Nanowire. *J. Phys. Chem. C* **2017**, *121*, 16110−16125.
(673) Han, Y.; Kilin, D. S.; May, P. S.; Berry, M. T.; Meng, Q. Photofragmentation Pathways for Gas-Phase Lanthanide Tris-(Isopropylcyclopentadienyl) Complexes. *Organometallics* **2016**, *35*, 3461−3473.
(674) Han, Y.; Rasulev, B.; Kilin, D. S. Photofragmentation of Tetranitromethane: Spin-Unrestricted Time-Dependent Excited-State Molecular Dynamics. *J. Phys. Chem. Lett.* **2017**, *8*, 3185−3192.
(675) Ben-Nun, M.; Molnar, F.; Schulten, K.; Martínez, T. J. The Role of Intersection Topography in Bond Selectivity of *cis-trans* Photoisomerization. *Proc. Natl. Acad. Sci. U. S. A.* **2002**, *99*, 1769−1773.
(676) Faraji, S.; Vazdar, M.; Reddy, V. S.; Eckert-Maksic, M.; Lischka, H.; Köppel, H. Ab Initio Quantum Dynamical Study of the Multi-State Nonadiabatic Photodissociation of Pyrrole. *J. Chem. Phys.* **2011**, *135*, 154310.
(677) Lefler, K. M.; Kim, C. H.; Wu, Y.-L.; Wasielewski, M. R. Self-Assembly of Supramolecular Light-Harvesting Arrays from Symmetric Perylene-3,4-Dicarboximide Trefoils. *J. Phys. Chem. Lett.* **2014**, *5*, 1608−1615.
(678) Uetomo, A.; Kozaki, M.; Suzuki, S.; Yamanaka, K.-i.; Ito, O.; Okada, K. Efficient Light-Harvesting Antenna with a Multi-Porphyrin Cascade. *J. Am. Chem. Soc.* **2011**, *133*, 13276−13279.
(679) Leishman, C. W.; McHale, J. L. Light-Harvesting Properties and Morphology of Porphyrin Nanostructures Depend on Ionic Species Inducing Aggregation. *J. Phys. Chem. C* **2015**, *119*, 28167−28181.
(680) Ishida, Y.; Shimada, T.; Masui, D.; Tachibana, H.; Inoue, H.; Takagi, S. Efficient Excited Energy Transfer Reaction in Clay/Porphyrin Complex toward an Artificial Light-Harvesting System. *J. Am. Chem. Soc.* **2011**, *133*, 14280−14286.
(681) Ziessel, R.; Ulrich, G.; Haefele, A.; Harriman, A. An Artificial Light-Harvesting Array Constructed from Multiple Bodipy Dyes. *J. Am. Chem. Soc.* **2013**, *135*, 11330−11344.
(682) Lee, C. Y.; Farha, O. K.; Hong, B. J.; Sarjeant, A. A.; Nguyen, S. T.; Hupp, J. T. Light-Harvesting Metal−Organic Frameworks (MOFs): Efficient Strut-to-Strut Energy Transfer in Bodipy and Porphyrin-Based Mofs. *J. Am. Chem. Soc.* **2011**, *133*, 15858−15861.
(683) Johnson, J. M.; Chen, R.; Chen, X.; Moskun, A. C.; Zhang, X.; Hogen-Esch, T. E.; Bradforth, S. E. Investigation of Macrocyclic Polymers as Artificial Light Harvesters: Subpicosecond Energy Transfer in Poly(9,9-Dimethyl-2-Vinylfluorene). *J. Phys. Chem. B* **2008**, *112*, 16367−16381.
(684) Aggarwal, A. V.; Thiessen, A.; Idelson, A.; Kalle, D.; Würsch, D.; Stangl, T.; Steiner, F.; Jester, S.-S.; Vogelsang, J.; Höger, S.; et al. Fluctuating Exciton Localization in Giant Π-Conjugated Spoked-Wheel Macrocycles. *Nat. Chem.* **2013**, *5*, 964−970.
(685) Swallen, S. F.; Kopelman, R.; Moore, J. S.; Devadoss, C. Dendrimer Photoantenna Supermolecules: Energetic Funnels, Exciton Hopping and Correlated Excimer Formation. *J. Mol. Struct.* **1999**, *485*−*486*, 585−597.
(686) Andrews, D. L. Light Harvesting in Dendrimer Materials: Designer Photophysics and Electrodynamics. *J. Mater. Res.* **2012**, *27*, 627−638.
(687) Franco, I.; Shapiro, M.; Brumer, P. Femtosecond Dynamics and Laser Control of Charge Transport in Trans-Polyacetylene. *J. Chem. Phys.* **2008**, *128*, 244905.
(688) Kippelen, B.; Brédas, J.-L. Organic Photovoltaics. *Energy Environ. Sci.* **2009**, *2*, 251.
(689) Burroughes, J. H.; Bradley, D. D. C.; Brown, A. R.; Marks, R. N.; Mackay, K.; Friend, R. H.; Burns, P. L.; Holmes, A. B. Light-Emitting Diodes Based on Conjugated Polymers. *Nature* **1990**, *347*, 539−541.
(690) Schroeder, V.; Savagatrup, S.; He, M.; Lin, S.; Swager, T. M. Carbon Nanotube Chemical Sensors. *Chem. Rev.* **2019**, *119*, 599−663.
(691) Spano, F. C. The Spectral Signatures of Frenkel Polarons in H- and J-Aggregates. *Acc. Chem. Res.* **2010**, *43*, 429−439.
(692) Hestand, N. J.; Spano, F. C. Expanded Theory of H- and J-Molecular Aggregates: The Effects of Vibronic Coupling and Intermolecular Charge Transfer. *Chem. Rev.* **2018**, *118*, 7069−7163.
(693) Knoester, J. Modeling the Optical Properties of Excitons in Linear and Tubular J-Aggregates. *Int. J. Photoenergy* **2006**, *2006*, 1−10.
(694) Spano, F. C.; Silva, C. H- and J-Aggregate Behavior in Polymeric Semiconductors. *Annu. Rev. Phys. Chem.* **2014**, *65*, 477−500.
(695) Ottiger, P.; Koppel, H.; Leutwyler, S. Excitonic Splittings in Molecular Dimers: Why Static Ab Initio Calculations Cannot Match Them. *Chem. Sci.* **2015**, *6*, 6059−6068.
(696) Nebgen, B.; Emmert, F. L.; Slipchenko, L. V. Vibronic Coupling in Asymmetric Bichromophores: Theory and Application to Diphenylmethane. *J. Chem. Phys.* **2012**, *137*, 084112.
(697) Nayyar, I. H.; Batista, E. R.; Tretiak, S.; Saxena, A.; Smith, D. L.; Martin, R. L. Role of Geometric Distortion and Polarization in Localizing Electronic Excitations in Conjugated Polymers. *J. Chem. Theory Comput.* **2013**, *9*, 1144−1154.
(698) Lai, L. F.; Love, J. A.; Sharenko, A.; Coughlin, J. E.; Gupta, V.; Tretiak, S.; Nguyen, T.-Q.; Wong, W.-Y.; Bazan, G. C. Topological Considerations for the Design of Molecular Donors with Multiple Absorbing Units. *J. Am. Chem. Soc.* **2014**, *136*, 5591−5594.
(699) Buchanan, E. G.; Walsh, P. S.; Plusquellic, D. F.; Zwier, T. S. Excitonic Splitting and Vibronic Coupling in 1,2-Diphenoxyethane: Conformation-Specific Effects in the Weak Coupling Limit. *J. Chem. Phys.* **2013**, *138*, 204313.
(700) Beil, A.; Hollenstein, H.; Monti, O. L. A.; Quack, M.; Stohner, J. Vibrational Spectra and Intramolecular Vibrational Redistribution in Highly Excited Deuterobromochlorofluoromethane CDBrClF: Experiment and Theory. *J. Chem. Phys.* **2000**, *113*, 2701−2718.
(701) Ostroumov, E. E.; Mulvaney, R. M.; Cogdell, R. J.; Scholes, G. D. Broadband 2D Electronic Spectroscopy Reveals a Carotenoid Dark State in Purple Bacteria. *Science* **2013**, *340*, 52−56.
(702) Thyrhaug, E.; Žídek, K.; Dostál, J.; Bína, D.; Zigmantas, D. Exciton Structure and Energy Transfer in the Fenna−Matthews−Olson Complex. *J. Phys. Chem. Lett.* **2016**, *7*, 1653−1660.
(703) Piryatinski, A.; Tretiak, S.; Chernyak, V.; Mukamel, S. Simulations of Two-Dimensional Femtosecond Infrared Photon Echoes of Glycine Dipeptide. *J. Raman Spectrosc.* **2000**, *31*, 125−135.
(704) Soavi, G.; Scotognella, F.; Lanzani, G.; Cerullo, G. Ultrafast Photophysics of Single-Walled Carbon Nanotubes. *Adv. Opt. Mater.* **2016**, *4*, 1670−1688.
(705) Dean, J. C.; Zhang, R.; Hallani, R. K.; Pensack, R. D.; Sanders, S. N.; Oblinsky, D. G.; Parkin, S. R.; Campos, L. M.; Anthony, J. E.; Scholes, G. D. Photophysical Characterization and Time-Resolved Spectroscopy of a Anthradithiophene Dimer: Exploring the Role of Conformation in Singlet Fission. *Phys. Chem. Chem. Phys.* **2017**, *19*, 23162−23175.
(706) Dean, J. C.; Oblinsky, D. G.; Rafiq, S.; Scholes, G. D. Methylene Blue Exciton States Steer Nonradiative Relaxation: Ultrafast Spectroscopy of Methylene Blue Dimer. *J. Phys. Chem. B* **2016**, *120*, 440−454.
(707) Bradforth, S. E.; Jimenez, R.; van Mourik, F.; van Grondelle, R.; Fleming, G. R. Excitation Transfer in the Core Light-Harvesting Complex (Lh-1) of Rhodobacter Sphaeroides: An Ultrafast Fluorescence Depolarization and Annihilation Study. *J. Phys. Chem.* **1995**, *99*, 16179−16191.
(708) Camacho, R.; Tubasum, S.; Southall, J.; Cogdell, R. J.; Sforazzini, G.; Anderson, H. L.; Pullerits, T.; Scheblykin, I. G. Fluorescence Polarization Measures Energy Funneling in Single Light-Harvesting Antennas—LH2 vs Conjugated Polymers. *Sci. Rep.* **2015**, *5*, 15080−15090.
(709) Yong, C.-K.; Parkinson, P.; Kondratuk, D. V.; Chen, W.-H.; Stannard, A.; Summerfield, A.; Sprafke, J. K.; O'Sullivan, M. C.; Beton, P. H.; Anderson, H. L.; et al. Ultrafast Delocalization of Excitation in Synthetic Light-Harvesting Nanorings. *Chem. Sci.* **2015**, *6*, 181−189.
(710) Varnavski, O.; Samuel, I. D. W.; Pålsson, L. O.; Beavington, R.; Burn, P. L.; Goodson, T. Investigations of Excitation Energy Transfer and Intramolecular Interactions in a Nitrogen Corded Distrylbenzene Dendrimer System. *J. Chem. Phys.* **2002**, *116*, 8893−8903.
(711) Schmid, S. A.; Yim, K. H.; Chang, M. H.; Zheng, Z.; Huck, W. T. S.; Friend, R. H.; Kim, J. S.; Herz, L. M. Polarization Anisotropy Dynamics for Thin Films of a Conjugated Polymer Aligned by

https://dx.doi.org/10.1021/acs.chemrev.9b00447
Chem. Rev. 2020, 120, 2215−2287

Nanoimprinting. *Phys. Rev. B: Condens. Matter Mater. Phys.* **2008**, *77*, 115338.
(712) Dykstra, T. E.; Hennebicq, E.; Beljonne, D.; Gierschner, J.; Claudio, G.; Bittner, E. R.; Knoester, J.; Scholes, G. D. Conformational Disorder and Ultrafast Exciton Relaxation in Ppv-Family Conjugated Polymers. *J. Phys. Chem. B* **2009**, *113*, 656−667.
(713) De Sio, A.; Troiani, F.; Maiuri, M.; Rehault, J.; Sommer, E.; Lim, J.; Huelga, S. F.; Plenio, M. B.; Rozzi, C. A.; Cerullo, G.; et al. Tracking the Coherent Generation of Polaron Pairs in Conjugated Polymers. *Nat. Commun.* **2016**, *7*, 13742.
(714) Yamazaki, I.; Akimoto, S.; Yamazaki, T.; Sato, S.-i.; Sakata, Y. Oscillatory Excitation Transfer in Dithiaanthracenophane: Quantum Beat in a Coherent Photochemical Process in Solution. *J. Phys. Chem. A* **2002**, *106*, 2122−2128.
(715) Zhu, F.; Galli, C.; Hochstrasser, R. M. The Real-Time Intramolecular Electronic Excitation Transfer Dynamics of 9',9-Bifluorene and 2',2-Binaphthyl in Solution. *J. Chem. Phys.* **1993**, *98*, 1042−1057.
(716) Laborda, E.; Henstridge, M. C.; Batchelor-McAuley, C.; Compton, R. G. Asymmetric Marcus−Hush Theory for Voltammetry. *Chem. Soc. Rev.* **2013**, *42*, 4894−4905.
(717) Hammes-Schiffer, S.; Stuchebrukhov, A. A. Theory of Coupled Electron and Proton Transfer Reactions. *Chem. Rev.* **2010**, *110*, 6939−6960.
(718) Natali, M.; Campagna, S.; Scandola, F. Photoinduced Electron Transfer across Molecular Bridges: Electron- and Hole-Transfer Superexchange Pathways. *Chem. Soc. Rev.* **2014**, *43*, 4005−4018.
(719) Mirkovic, T.; Ostroumov, E. E.; Anna, J. M.; van Grondelle, R.; Govindjee; Scholes, G. D. Light Absorption and Energy Transfer in the Antenna Complexes of Photosynthetic Organisms. *Chem. Rev.* **2017**, *117*, 249−293.
(720) Engel, G. S.; Calhoun, T. R.; Read, E. L.; Ahn, T.-K.; Mančal, T.; Cheng, Y.-C.; Blankenship, R. E.; Fleming, G. R. Evidence for Wavelike Energy Transfer through Quantum Coherence in Photosynthetic Systems. *Nature* **2007**, *446*, 782−786.
(721) Huo, P.; Coker, D. F. Theoretical Study of Coherent Excitation Energy Transfer in Cryptophyte Phycocyanin 645 at Physiological Temperature. *J. Phys. Chem. Lett.* **2011**, *2*, 825−833.
(722) Falke, S. M.; Rozzi, C. A.; Brida, D.; Maiuri, M.; Amato, M.; Sommer, E.; De Sio, A.; Rubio, A.; Cerullo, G.; Molinari, E.; et al. Coherent Ultrafast Charge Transfer in an Organic Photovoltaic Blend. *Science* **2014**, *344*, 1001−1005.
(723) Hestand, N. J.; Spano, F. C. The Effect of Chain Bending on the Photophysical Properties of Conjugated Polymers. *J. Phys. Chem. B* **2014**, *118*, 8352−8363.
(724) Shi, T.; Li, H.; Tretiak, S.; Chernyak, V. Y. How Geometric Distortions Scatter Electronic Excitations in Conjugated Macromolecules. *J. Phys. Chem. Lett.* **2014**, *5*, 3946−3952.
(725) Becker, K.; Da Como, E.; Feldmann, J.; Scheliga, F.; Thorn Csányi, E.; Tretiak, S.; Lupton, J. M. How Chromophore Shape Determines the Spectroscopy of Phenylene−Vinylenes: Origin of Spectral Broadening in the Absence of Aggregation. *J. Phys. Chem. B* **2008**, *112*, 4859−4864.
(726) Van Averbeke, B.; Beljonne, D. Conformational Effects on Excitation Transport Along Conjugated Polymer Chains. *J. Phys. Chem. A* **2009**, *113*, 2677−2682.
(727) Nguyen, T.-Q.; Martini, I. B.; Liu, J.; Schwartz, B. J. Controlling Interchain Interactions in Conjugated Polymers: The Effects of Chain Morphology on Exciton−Exciton Annihilation and Aggregation in Meh−Ppv Films. *J. Phys. Chem. B* **2000**, *104*, 237−255.
(728) Ondarse-Alvarez, D.; Nelson, T.; Lupton, J. M.; Tretiak, S.; Fernandez-Alberti, S. Let Digons Be Bygones: The Fate of Excitons in Curved Π-Systems. *J. Phys. Chem. Lett.* **2018**, *9*, 7123−7129.
(729) Tretiak, S.; Saxena, A.; Martin, R. L.; Bishop, A. R. Interchain Electronic Excitations in Poly(Phenylenevinylene) (Ppv) Aggregates. *J. Phys. Chem. B* **2000**, *104*, 7029−7037.
(730) Müller, J. G.; Atas, E.; Tan, C.; Schanze, K. S.; Kleiman, V. D. The Role of Exciton Hopping and Direct Energy Transfer in the Efficient Quenching of Conjugated Polyelectrolytes. *J. Am. Chem. Soc.* **2006**, *128*, 4007−4016.
(731) Ikeda, T.; Lee, B.; Kurihara, S.; Tazuke, S.; Ito, S.; Yamamoto, M. Time-Resolved Observation of Excitation Hopping between Two Identical Chromophores Attached to Both Ends of Alkanes. *J. Am. Chem. Soc.* **1988**, *110*, 8299−8304.
(732) Bazan, G. C.; Oldham, W. J.; Lachicotte, R. J.; Tretiak, S.; Chernyak, V.; Mukamel, S. Stilbenoid Dimers: Dissection of a Paracyclophane Chromophore. *J. Am. Chem. Soc.* **1998**, *120*, 9188−9204.
(733) Tretiak, S.; Zhang, W. M.; Chernyak, V.; Mukamel, S. Excitonic Couplings and Electronic Coherence in Bridged Naphthalene Dimers. *Proc. Natl. Acad. Sci. U. S. A.* **1999**, *96*, 13003.
(734) Alfonso Hernandez, L.; Nelson, T.; Tretiak, S.; Fernandez-Alberti, S. Photoexcited Energy Transfer in a Weakly Coupled Dimer. *J. Phys. Chem. B* **2015**, *119*, 7242−7252.
(735) Beljonne, D.; Yamagata, H.; Brédas, J. L.; Spano, F. C.; Olivier, Y. Charge-Transfer Excitations Steer the Davydov Splitting and Mediate Singlet Exciton Fission in Pentacene. *Phys. Rev. Lett.* **2013**, *110*, 226402.
(736) Silbey, R.; Jortner, J.; Rice, S. A. On the Singlet-Exciton States of Crystalline Anthracene. *J. Chem. Phys.* **1965**, *42*, 1515−1534.
(737) Kurik, M. V.; Piryatinskii, Y. P.; Popel, O. M.; Frolova, E. K. Temperature Dependence of the Davydov Splitting in Anthracene. *Phys. Status Solidi B* **1970**, *37*, 803−806.
(738) Tomalia, D. A.; Fréchet, J. M. J. *Dendrimers and Other Dendritic Polymers*; John Wiley & Sons Ltd.: West Sussex, 2001.
(739) Balzani, B.; Venturi, M.; Credi, A. *Molecular Devices and Machines: A Journey into the Nanoworld*; Wiley-VCH Verlag GmbH & Co. KGaA: Weinheim, Germany, 2003.
(740) Katan, C.; Terenziani, F.; Mongin, O.; Werts, M. H. V.; Porrès, L.; Pons, T.; Mertz, J.; Tretiak, S.; Blanchard-Desce, M. Effects of (Multi)Branching of Dipolar Chromophores on Photophysical Properties and Two-Photon Absorption. *J. Phys. Chem. A* **2005**, *109*, 3024−3037.
(741) Mukamel, S. Trees to Trap Photons. *Nature* **1997**, *388*, 425−427.
(742) Frechet, J. M. Functional Polymers and Dendrimers: Reactivity, Molecular Architecture, and Interfacial Energy. *Science* **1994**, *263*, 1710−1715.
(743) Magyar, R. J.; Tretiak, S.; Gao, Y.; Wang, H. L.; Shreve, A. P. A Joint Theoretical and Experimental Study of Phenylene−Acetylene Molecular Wires. *Chem. Phys. Lett.* **2005**, *401*, 149−156.
(744) Shortreed, M. R.; Swallen, S. F.; Shi, Z.-Y.; Tan, W.; Xu, Z.; Devadoss, C.; Moore, J. S.; Kopelman, R. Directed Energy Transfer Funnels in Dendrimeric Antenna Supermolecules. *J. Phys. Chem. B* **1997**, *101*, 6318−6322.
(745) Xu, Z.; Kahr, M.; Walker, K. L.; Wilkins, C. L.; Moore, J. S. Phenylacetylene Dendrimers by the Divergent, Convergent, and Double-Stage Convergent Methods. *J. Am. Chem. Soc.* **1994**, *116*, 4537−4550.
(746) Devadoss, C.; Bharathi, P.; Moore, J. S. Energy Transfer in Dendritic Macromolecules: Molecular Size Effects and the Role of an Energy Gradient. *J. Am. Chem. Soc.* **1996**, *118*, 9635−9644.
(747) Tada, T.; Nozaki, D.; Kondo, M.; Yoshizawa, K. Molecular Orbital Interactions in the Nanostar Dendrimer. *J. Phys. Chem. B* **2003**, *107*, 14204−14210.
(748) Palma, J. L.; Atas, E.; Hardison, L.; Marder, T. B.; Collings, J. C.; Beeby, A.; Melinger, J. S.; Krause, J. L.; Kleiman, V. D.; Roitberg, A. E. Electronic Spectra of the Nanostar Dendrimer: Theory and Experiment. *J. Phys. Chem. C* **2010**, *114*, 20702−20712.
(749) Fernandez-Alberti, S.; Kleiman, V. D.; Tretiak, S.; Roitberg, A. E. Nonadiabatic Molecular Dynamics Simulations of the Energy Transfer between Building Blocks in a Phenylene Ethynylene Dendrimer. *J. Phys. Chem. A* **2009**, *113*, 7535−7542.
(750) Galindo, J. F.; Fernandez-Alberti, S.; Roitberg, A. E. Electronic Excited State Specific Ir Spectra for Phenylene Ethynylene Dendrimer Building Blocks. *J. Phys. Chem. C* **2013**, *117*, 26517−26528.

https://dx.doi.org/10.1021/acs.chemrev.9b00447
Chem. Rev. 2020, 120, 2215−2287

(751) Fernandez-Alberti, S.; Kleiman, V. D.; Tretiak, S.; Roitberg, A. E. Unidirectional Energy Transfer in Conjugated Molecules: The Crucial Role of High-Frequency C≡C Bonds. *J. Phys. Chem. Lett.* **2010**, *1*, 2699−2704.
(752) Soler, M. A.; Roitberg, A. E.; Nelson, T.; Tretiak, S.; Fernandez-Alberti, S. Analysis of State-Specific Vibrations Coupled to the Unidirectional Energy Transfer in Conjugated Dendrimers. *J. Phys. Chem. A* **2012**, *116*, 9802−9810.
(753) Freixas, V. M.; Ondarse-Alvarez, D.; Tretiak, S.; Makhov, D. V.; Shalashilin, D. V.; Fernandez-Alberti, S. Photoinduced Non-Adiabatic Energy Transfer Pathways in Dendrimer Building Blocks. *J. Chem. Phys.* **2019**, *150*, 124301.
(754) Hoff, D. A.; Silva, R.; Rego, L. G. C. Subpicosecond Dynamics of Metal-to-Ligand Charge-Transfer Excited States in Solvated [Ru(Bpy)3]2+ Complexes. *J. Phys. Chem. C* **2011**, *115*, 15617−15626.
(755) Wong, K. S.; Wang, H.; Lanzani, G. Ultrafast Excited-State Planarization of the Hexamethylsexithiophene Oligomer Studied by Femtosecond Time-Resolved Photoluminescence. *Chem. Phys. Lett.* **1998**, *288*, 59−64.
(756) Walter, M. J.; Lupton, J. M.; Becker, K.; Feldmann, J.; Gaefke, G.; Höger, S. Simultaneous Raman and Fluorescence Spectroscopy of Single Conjugated Polymer Chains. *Phys. Rev. Lett.* **2007**, *98*, 137401.
(757) Pullerits, T.; Mirzov, O.; Scheblykin, I. G. Conformational Fluctuations and Large Fluorescence Spectral Diffusion in Conjugated Polymer Single Chains at Low Temperatures. *J. Phys. Chem. B* **2005**, *109*, 19099−19107.
(758) Nayyar, I. H.; Batista, E. R.; Tretiak, S.; Saxena, A.; Smith, D. L.; Martin, R. L. Localization of Electronic Excitations in Conjugated Polymers Studied by Dft. *J. Phys. Chem. Lett.* **2011**, *2*, 566−571.
(759) Clark, J.; Nelson, T.; Tretiak, S.; Cirmi, G.; Lanzani, G. Femtosecond Torsional Relaxation. *Nat. Phys.* **2012**, *8*, 225−231.
(760) Kilina, S.; Batista, E. R.; Yang, P.; Tretiak, S.; Saxena, A.; Martin, R. L.; Smith, D. L. Electronic Structure of Self-Assembled Amorphous Polyfluorenes. *ACS Nano* **2008**, *2*, 1381−1388.
(761) Krueger, B. P.; Scholes, G. D.; Fleming, G. R. Calculation of Couplings and Energy-Transfer Pathways between the Pigments of Lh2 by the Ab Initio Transition Density Cube Method. *J. Phys. Chem. B* **1998**, *102*, 5378−5386.
(762) Ortiz, W.; Krueger, B. P.; Kleiman, V. D.; Krause, J. L.; Roitberg, A. E. Energy Transfer in the Nanostar: The Role of Coulombic Coupling and Dynamics. *J. Phys. Chem. B* **2005**, *109*, 11512−11519.
(763) Wong, C. Y.; Curutchet, C.; Tretiak, S.; Scholes, G. D. Ideal Dipole Approximation Fails to Predict Electronic Coupling and Energy Transfer between Semiconducting Single-Wall Carbon Nanotubes. *J. Chem. Phys.* **2009**, *130*, 081104.
(764) Kleima, F. J.; Hofmann, E.; Gobets, B.; van Stokkum, I. H.; van Grondelle, R.; Diederichs, K.; van Amerongen, H. Förster Excitation Energy Transfer in Peridinin-Chlorophyll-a-Protein. *Biophys. J.* **2000**, *78*, 344−353.
(765) Young, A. J.; Frank, H. A. Energy Transfer Reactions Involving Carotenoids: Quenching of Chlorophyll Fluorescence. *J. Photochem. Photobiol., B* **1996**, *36*, 3−15.
(766) Pullerits, T.; Hess, S.; Herek, J. L.; Sundström, V. Temperature Dependence of Excitation Transfer in LH2 of Rhodobacter Sphaeroides. *J. Phys. Chem. B* **1997**, *101*, 10560−10567.
(767) Sundström, V.; Pullerits, T.; van Grondelle, R. Photosynthetic Light-Harvesting: Reconciling Dynamics and Structure of Purple Bacterial LH2 Reveals Function of Photosynthetic Unit. *J. Phys. Chem. B* **1999**, *103*, 2327−2346.
(768) Collini, E.; Scholes, G. D. Coherent Intrachain Energy Migration in a Conjugated Polymer at Room Temperature. *Science* **2009**, *323*, 369−373.
(769) Gong, J. Q.; Favereau, L.; Anderson, H. L.; Herz, L. M. Breaking the Symmetry in Molecular Nanorings. *J. Phys. Chem. Lett.* **2016**, *7*, 332−338.
(770) Sumi, H. Theory on Rates of Excitation-Energy Transfer between Molecular Aggregates through Distributed Transition Dipoles with Application to the Antenna System in Bacterial Photosynthesis. *J. Phys. Chem. B* **1999**, *103*, 252−260.
(771) Jang, S.; Newton, M. D.; Silbey, R. J. Multichromophoric Förster Resonance Energy Transfer. *Phys. Rev. Lett.* **2004**, *92*, 218301.
(772) Scholes, G. D. Long-Range Resonancy Energy Transfer in Molecular Systems. *Annu. Rev. Phys. Chem.* **2003**, *54*, 57−87.
(773) Mukai, K.; Abe, S.; Sumi, H. Theory of Rapid Excitation-Energy Transfer from B800 to Optically-Forbidden Exciton States of B850 in the Antenna System Lh2 of Photosynthetic Purple Bacteria. *J. Phys. Chem. B* **1999**, *103*, 6096−6102.
(774) Jang, S.; Newton, M. D.; Silbey, R. J. Multichromophoric Förster Resonance Energy Transfer from B800 to B850 in the Light Harvesting Complex 2: Evidence for Subtle Energetic Optimization by Purple Bacteria. *J. Phys. Chem. B* **2007**, *111*, 6807−6814.
(775) Cleary, L.; Cao, J. Optimal Thermal Bath for Robust Excitation Energy Transfer in Disordered Light-Harvesting Complex 2 of Purple Bacteria. *New J. Phys.* **2013**, *15*, 125030.
(776) Coughlin, J. E.; Zhugayevych, A.; Bakus, R. C.; van der Poll, T. S.; Welch, G. C.; Teat, S. J.; Bazan, G. C.; Tretiak, S. A Combined Experimental and Theoretical Study of Conformational Preferences of Molecular Semiconductors. *J. Phys. Chem. C* **2014**, *118*, 15610−15623.
(777) Beljonne, D.; Curutchet, C.; Scholes, G. D.; Silbey, R. J. Beyond Förster Resonance Energy Transfer in Biological and Nanoscale Systems. *J. Phys. Chem. B* **2009**, *113*, 6583−6599.
(778) Becker, K.; Lupton, J. M.; Feldmann, J.; Setayesh, S.; Grimsdale, A. C.; Müllen, K. Efficient Intramolecular Energy Transfer in Single Endcapped Conjugated Polymer Molecules in the Absence of Appreciable Spectral Overlap. *J. Am. Chem. Soc.* **2006**, *128*, 680−681.
(779) Hinze, G.; Métivier, R.; Nolde, F.; Müllen, K.; Basché, T. Intramolecular Electronic Excitation Energy Transfer in Donor/Acceptor Dyads Studied by Time and Frequency Resolved Single Molecule Spectroscopy. *J. Chem. Phys.* **2008**, *128*, 124516.
(780) Marguet, S.; Markovitsi, D.; Millie, P.; Sigal, H.; Kumar, S. Influence of Disorder on Electronic Excited States: An Experimental and Numerical Study of Alkylthiotriphenylene Columnar Phases. *J. Phys. Chem. B* **1998**, *102*, 4697−4710.
(781) Beljonne, D.; Cornil, J.; Silbey, R.; Millié, P.; Brédas, J. L. Interchain Interactions in Conjugated Materials: The Exciton Model Versus the Supermolecular Approach. *J. Chem. Phys.* **2000**, *112*, 4749−4758.
(782) Dexter, D. L. A Theory of Sensitized Luminescence in Solids. *J. Chem. Phys.* **1953**, *21*, 836−850.
(783) Nalbach, P.; Pugliesi, I.; Langhals, H.; Thorwart, M. Noise-Induced Forster Resonant Energy Transfer between Orthogonal Dipoles in Photoexcited Molecules. *Phys. Rev. Lett.* **2012**, *108*, 218302.
(784) Singh, J.; Bittner, E. R. Isotopic Effect and Temperature Dependent Intramolecular Excitation Energy Transfer in a Model Donor−Acceptor Dyad. *Phys. Chem. Chem. Phys.* **2010**, *12*, 7418−7426.
(785) Wilhelm, P.; Vogelsang, J.; Poluektov, G.; Schönfelder, N.; Keller, T. J.; Jester, S.-S.; Höger, S.; Lupton, J. M. Molecular Polygons Probe the Role of Intramolecular Strain in the Photophysics of Π-Conjugated Chromophores. *Angew. Chem., Int. Ed.* **2017**, *56*, 1234−1238.
(786) Brédas, J.-L.; Sargent, E. H.; Scholes, G. D. Photovoltaic Concepts Inspired by Coherence Effects in Photosynthetic Systems. *Nat. Mater.* **2017**, *16*, 35−44.
(787) Huang, Y.; Sutter, E.; Sadowski, J. T.; Cotlet, M.; Monti, O. L.; Racke, D. A.; Neupane, M. R.; Wickramaratne, D.; Lake, R. K.; Parkinson, B. A.; et al. Tin Disulfide-an Emerging Layered Metal Dichalcogenide Semiconductor: Materials Properties and Device Characteristics. *ACS Nano* **2014**, *8*, 10743−10755.
(788) Di Nuzzo, D.; Fontanesi, C.; Jones, R.; Allard, S.; Dumsch, I.; Scherf, U.; von Hauff, E.; Schumacher, S.; Da Como, E. How Intermolecular Geometrical Disorder Affects the Molecular Doping of Donor-Acceptor Copolymers. *Nat. Commun.* **2015**, *6*, 6460.
(789) Schulz, P.; Kelly, L. L.; Winget, P.; Li, H.; Kim, H.; Ndione, P. F.; Sigdel, A. K.; Berry, J. J.; Graham, S.; Brédas, J.-L.; et al. Tailoring Electron-Transfer Barriers for Zinc Oxide/C60fullerene Interfaces. *Adv. Funct. Mater.* **2014**, *24*, 7381−7389.

https://dx.doi.org/10.1021/acs.chemrev.9b00447
Chem. Rev. 2020, 120, 2215−2287

(790) Kennehan, E. R.; Doucette, G. S.; Marshall, A. R.; Grieco, C.; Munson, K. T.; Beard, M. C.; Asbury, J. B. Electron-Phonon Coupling and Resonant Relaxation from 1d and 1p States in Pbs Quantum Dots. *ACS Nano* **2018**, *12*, 6263−6272.
(791) Huelga, S. F.; Plenio, M. B. Vibrations, Quanta and Biology. *Contemp. Phys.* **2013**, *54*, 181−207.
(792) Nelson, T.; Fernandez-Alberti, S.; Roitberg, A. E.; Tretiak, S. Electronic Delocalization, Vibrational Dynamics, and Energy Transfer in Organic Chromophores. *J. Phys. Chem. Lett.* **2017**, *8*, 3020−3031.
(793) Kolli, A.; O'Reilly, E. J.; Scholes, G. D.; Olaya-Castro, A. The Fundamental Role of Quantized Vibrations in Coherent Light Harvesting by Cryptophyte Algae. *J. Chem. Phys.* **2012**, *137*, 174109.
(794) Lingerfelt, D. B.; Lestrange, P. J.; Radler, J. J.; Brown-Xu, S. E.; Kim, P.; Castellano, F. N.; Chen, L. X.; Li, X. Can Excited State Electronic Coherence Be Tuned Via Molecular Structural Modification? A First-Principles Quantum Electronic Dynamics Study of Pyrazolate-Bridged Pt(Ii) Dimers. *J. Phys. Chem. A* **2017**, *121*, 1932−1939.
(795) Nelson, T. R.; Ondarse-Alvarez, D.; Oldani, N.; Rodriguez-Hernandez, B.; Alfonso-Hernandez, L.; Galindo, J. F.; Kleiman, V. D.; Fernandez-Alberti, S.; Roitberg, A. E.; Tretiak, S. Coherent Exciton-Vibrational Dynamics and Energy Transfer in Conjugated Organics. *Nat. Commun.* **2018**, *9*, 2316.
(796) Rozzi, C. A.; Falke, S. M.; Spallanzani, N.; Rubio, A.; Molinari, E.; Brida, D.; Maiuri, M.; Cerullo, G.; Schramm, H.; Christoffers, J.; et al. Quantum Coherence Controls the Charge Separation in a Prototypical Artificial Light-Harvesting System. *Nat. Commun.* **2013**, *4*, 1602.
(797) Eads, C. N.; Bandak, D.; Neupane, M. R.; Nordlund, D.; Monti, O. L. A. Anisotropic Attosecond Charge Carrier Dynamics and Layer Decoupling in Quasi-2D Layered SnS_2. *Nat. Commun.* **2017**, *8*, 1369.
(798) Soler, M. A.; Nelson, T.; Roitberg, A. E.; Tretiak, S.; Fernandez-Alberti, S. Signature of Nonadiabatic Coupling in Excited-State Vibrational Modes. *J. Phys. Chem. A* **2014**, *118*, 10372−10379.
(799) Gieseking, R. L.; Risko, C.; Bredas, J. L. Distinguishing the Effects of Bond-Length Alternation Versus Bond-Order Alternation on the Nonlinear Optical Properties of π-Conjugated Chromophores. *J. Phys. Chem. Lett.* **2015**, *6*, 2158−2162.
(800) Cina, J. A.; Fleming, G. R. Vibrational Coherence Transfer and Trapping as Sources for Long-Lived Quantum Beats in Polarized Emission from Energy Transfer Complexes. *J. Phys. Chem. A* **2004**, *108*, 11196−11208.
(801) Picchiotti, A.; Nenov, A.; Giussani, A.; Prokhorenko, V. I.; Miller, R. J. D.; Mukamel, S.; Garavelli, M. Pyrene, a Test Case for Deep-Ultraviolet Molecular Photophysics. *J. Phys. Chem. Lett.* **2019**, *10*, 3481−3487.
(802) Lee, H.; Cheng, Y.-C.; Fleming, G. R. Coherence Dynamics in Photosynthesis: Protein Protection of Excitonic Coherence. *Science* **2007**, *316*, 1462−1465.
(803) Hayes, D.; Griffin, G. B.; Engel, G. S. Engineering Coherence among Excited States in Synthetic Heterodimer Systems. *Science* **2013**, *340*, 1431−1434.
(804) Gambetta, A.; Manzoni, C.; Menna, E.; Meneghetti, M.; Cerullo, G.; Lanzani, G.; Tretiak, S.; Piryatinski, A.; Saxena, A.; Martin, R. L.; et al. Real-Time Observation of Nonlinear Coherent Phonon Dynamics in Single-Walled Carbon Nanotubes. *Nat. Phys.* **2006**, *2*, 515−520.
(805) Schulz, M.; Tretiak, S.; Chernyak, V.; Mukamel, S. Size Scaling of Third-Order Off-Resonant Polarizabilities. Electronic Coherence in Organic Oligomers. *J. Am. Chem. Soc.* **2000**, *122*, 452−459.
(806) Thouin, F.; Valverde-Chavez, D. A.; Quarti, C.; Cortecchia, D.; Bargigia, I.; Beljonne, D.; Petrozza, A.; Silva, C.; Srimath Kandada, A. R. Phonon Coherences Reveal the Polaronic Character of Excitons in Two-Dimensional Lead Halide Perovskites. *Nat. Mater.* **2019**, *18*, 349−356.
(807) Levine, B. G.; Ko, C.; Quenneville, J.; Martinez, T. J. Conical Intersections and Double Excitations in Time-Dependent Density Functional Theory. *Mol. Phys.* **2006**, *104*, 1039−1051.
(808) Gruenewald, M.; Schirra, L. K.; Winget, P.; Kozlik, M.; Ndione, P. F.; Sigdel, A. K.; Berry, J. J.; Forker, R.; Brédas, J.-L.; Fritz, T.; et al. Integer Charge Transfer and Hybridization at an Organic Semiconductor/Conductive Oxide Interface. *J. Phys. Chem. C* **2015**, *119*, 4865−4873.
(809) Kang, K.; Kononov, A.; Lee, C.-W.; Leveillee, J. A.; Shapera, E. P.; Zhang, X.; Schleife, A. Pushing the Frontiers of Modeling Excited Electronic States and Dynamics to Accelerate Materials Engineering and Design. *Comput. Mater. Sci.* **2019**, *160*, 207−216.
(810) Schleife, A.; Fuchs, F.; Furthmüller, J.; Bechstedt, F. First-Principles Study of Ground- and Excited-State Properties of MgO, ZnO, and CdO Polymorphs. *Phys. Rev. B: Condens. Matter Mater. Phys.* **2006**, *73*, 245212.
(811) Tuckerman, M.; Ceperley, D. Preface: Special Topic on Nuclear Quantum Effects. *J. Chem. Phys.* **2018**, *148*, 102001.
(812) Makri, N. Time-Dependent Quantum Methods for Large Systems. *Annu. Rev. Phys. Chem.* **1999**, *50*, 167−191.
(813) Wang, L.; Prezhdo, O. V.; Beljonne, D. Mixed Quantum-Classical Dynamics for Charge Transport in Organics. *Phys. Chem. Chem. Phys.* **2015**, *17*, 12395−12406.
(814) Jasper, A. W.; Nangia, S.; Zhu, C.; Truhlar, D. G. Non-Born-Oppenheimer Molecular Dynamics. *Acc. Chem. Res.* **2006**, *39*, 101−108.
(815) Akimov, A. V.; Neukirch, A. J.; Prezhdo, O. V. Theoretical Insights into Photoinduced Charge Transfer and Catalysis at Oxide Interfaces. *Chem. Rev.* **2013**, *113*, 4496−4565.
(816) Duncan, W. R.; Prezhdo, O. V. Theoretical Studies of Photoinduced Electron Transfer in Dye-Sensitized TiO_2. *Annu. Rev. Phys. Chem.* **2007**, *58*, 143−184.
(817) Long, R.; English, N. J.; Prezhdo, O. V. Photo-Induced Charge Separation across the Graphene-TiO_2 Interface Is Faster Than Energy Losses: A Time-Domain Ab Initio Analysis. *J. Am. Chem. Soc.* **2012**, *134*, 14238−14248.
(818) Prezhdo, O. V. Photoinduced Dynamics in Semiconductor Quantum Dots: Insights from Time-Domain Ab Initio Studies. *Acc. Chem. Res.* **2009**, *42*, 2005−2016.
(819) Prezhdo, O. V.; Duncan, W. R.; Prezhdo, V. V. Dynamics of the Photoexcited Electron at the Chromophore-Semiconductor Interface. *Acc. Chem. Res.* **2008**, *41*, 339−348.
(820) Casanova, D. Theoretical Modeling of Singlet Fission. *Chem. Rev.* **2018**, *118*, 7164−7207.
(821) Grieco, C.; Kennehan, E. R.; Kim, H.; Pensack, R. D.; Brigeman, A. N.; Rimshaw, A.; Payne, M. M.; Anthony, J. E.; Giebink, N. C.; Scholes, G. D.; et al. Direct Observation of Correlated Triplet Pair Dynamics During Singlet Fission Using Ultrafast Mid-IR Spectroscopy. *J. Phys. Chem. C* **2018**, *122*, 2012−2022.
(822) Grieco, C.; Doucette, G. S.; Pensack, R. D.; Payne, M. M.; Rimshaw, A.; Scholes, G. D.; Anthony, J. E.; Asbury, J. B. Dynamic Exchange During Triplet Transport in Nanocrystalline Tips-Pentacene Films. *J. Am. Chem. Soc.* **2016**, *138*, 16069−16080.
(823) Grieco, C.; Kennehan, E. R.; Rimshaw, A.; Payne, M. M.; Anthony, J. E.; Asbury, J. B. Harnessing Molecular Vibrations to Probe Triplet Dynamics During Singlet Fission. *J. Phys. Chem. Lett.* **2017**, *8*, 5700−5706.
(824) Vydrov, O. A.; Scuseria, G. E. Assessment of a Long-Range Corrected Hybrid Functional. *J. Chem. Phys.* **2006**, *125*, 234109.
(825) Jacquemin, D.; Perpete, E. A.; Ciofini, I.; Adamo, C.; Valero, R.; Zhao, Y.; Truhlar, D. G. On the Performances of the M06 Family of Density Functionals for Electronic Excitation Energies. *J. Chem. Theory Comput.* **2010**, *6*, 2071−2085.
(826) Caricato, M.; Trucks, G. W.; Frisch, M. J.; Wiberg, K. B. Electronic Transition Energies: A Study of the Performance of a Large Range of Single Reference Density Functional and Wave Function Methods on Valence and Rydberg States Compared to Experiment. *J. Chem. Theory Comput.* **2010**, *6*, 370−383.
(827) Sifain, A. E.; Bjorgaard, J. A.; Myers, T. W.; Veauthier, J. M.; Chavez, D. E.; Prezhdo, O. V.; Scharff, R. J.; Tretiak, S. Photoactive Excited States in Explosive Fe(II) Tetrazine Complexes: A Time-

https://dx.doi.org/10.1021/acs.chemrev.9b00447
Chem. Rev. 2020, 120, 2215−2287

Dependent Density Functional Theory Study. *J. Phys. Chem. C* **2016**, *120*, 28762−28773.
(828) So, W. Y.; Hong, J.; Kim, J. J.; Sherwood, G. A.; Chacon-Madrid, K.; Werner, J. H.; Shreve, A. P.; Peteanu, L. A.; Wildeman, J. Effects of Solvent Properties on the Spectroscopy and Dynamics of Alkoxy-Substituted Ppv Oligomer Aggregates. *J. Phys. Chem. B* **2012**, *116*, 10504−10513.
(829) Inoue, K.; Del Carmen Marin, M.; Tomida, S.; Nakamura, R.; Nakajima, Y.; Olivucci, M.; Kandori, H. Red-Shifting Mutation of Light-Driven Sodium-Pump Rhodopsin. *Nat. Commun.* **2019**, *10*, 1993.
(830) Barbara, P. F.; Jarzeba, W.Ultrafast Photochemical Intramolecular Charge and Excited State Solvation. *Advances in Photochemistry*, Vol. *22*; Wiley, 2007; pp 1−68.
(831) Zewail, A. H. Femtochemistry: Atomic-Scale Dynamics of the Chemical Bond. *J. Phys. Chem. A* **2000**, *104*, 5660−5694.
(832) Bakulin, A. A.; Silva, C.; Vella, E. Ultrafast Spectroscopy with Photocurrent Detection: Watching Excitonic Optoelectronic Systems at Work. *J. Phys. Chem. Lett.* **2016**, *7*, 250−258.
(833) Parandekar, P. V.; Tully, J. C. Mixed Quantum-Classical Equilibrium. *J. Chem. Phys.* **2005**, *122*, 094102.
(834) Sifain, A. E.; Wang, L.; Tretiak, S.; Prezhdo, O. V. Numerical Tests of Coherence-Corrected Surface Hopping Methods Using a Donor-Bridge-Acceptor Model System. *J. Chem. Phys.* **2019**, *150*, 194104.
(835) Lewis, J. P.; Jelínek, P.; Ortega, J.; Demkov, A. A.; Trabada, D. G.; Haycock, B.; Wang, H.; Adams, G.; Tomfohr, J. K.; Abad, E.; et al. Advances and Applications in the Fireballab Initio Tight-Binding Molecular-Dynamics Formalism. Phys. *Phys. Status Solidi B* **2011**, *248*, 1989−2007.
(836) Humeniuk, A.; Mitrić, R. DFTBaby: A Software Package for Non-Adiabatic Molecular Dynamics Simulations Based on Long-Range Corrected Tight-Binding TD-DFT(B). *Comput. Phys. Commun.* **2017**, *221*, 174−202.
(837) Hu, D.; Xie, Y.; Li, X.; Li, L.; Lan, Z. Inclusion of Machine Learning Kernel Ridge Regression Potential Energy Surfaces in on-the-Fly Nonadiabatic Molecular Dynamics Simulation. *J. Phys. Chem. Lett.* **2018**, *9*, 2725−2732.
(838) Häse, F.; Kreisbeck, C.; Aspuru-Guzik, A. Machine Learning for Quantum Dynamics: Deep Learning of Excitation Energy Transfer Properties. *Chem. Sci.* **2017**, *8*, 8419−8426.
(839) Dral, P. O.; Barbatti, M.; Thiel, W. Nonadiabatic Excited-State Dynamics with Machine Learning. *J. Phys. Chem. Lett.* **2018**, *9*, 5660−5663.
(840) Li, H.; Collins, C.; Tanha, M.; Gordon, G. J.; Yaron, D. J. A Density Functional Tight Binding Layer for Deep Learning of Chemical Hamiltonians. *J. Chem. Theory Comput.* **2018**, *14*, 5764−5776.
(841) Du, L.; Lan, Z. An on-the-Fly Surface-Hopping Program Jade for Nonadiabatic Molecular Dynamics of Polyatomic Systems: Implementation and Applications. *J. Chem. Theory Comput.* **2015**, *11*, 1360−1374.

https://dx.doi.org/10.1021/acs.chemrev.9b00447
Chem. Rev. 2020, 120, 2215−2287